GEORGIA DOT RESEARCH PROJECT 1134
FINAL REPORT

CORROSION-FREE PRECAST PRESTRESSED CONCRETE PILES MADE WITH STAINLESS STEEL REINFORCEMENT: CONSTRUCTION, TEST AND EVALUATION

OFFICE OF RESEARCH

GDOT Research Project No. 1134

Final Report

CORROSION-FREE PRECAST PRESTRESSED CONCRETE PILES MADE WITH STAINLESS STEEL REINFORCEMENT: CONSTRUCTION, TEST AND EVALUATION

By

Alvaro Paul, Lawrence F. Kahn, and Kimberly Kurtis
Georgia Institute of Technology

Contract with

Georgia Department of Transportation

In cooperation with

U.S. Department of Transportation

Federal Highway Administration

March 2015

1. Report No.: FHWA-GA-15-1134	2. Government Accession No.:	3. Recipient's Catalog No.:
4. Title and Subtitle: Corrosion-Free Precast Prestressed Concrete Piles Made with Stainless Steel Reinforcement: Construction, Test and Evaluation	5. Report Date: March 2015	
	6. Performing Organization Code:	
7. Author(s): Alvaro Paul, Lawrence F. Kahn, and Kimberly E. Kurtis	8. Performing Organ. Report No.:	
9. Performing Organization Name and Address: School of Civil & Environmental Engineering Georgia Institute of Technology Atlanta, GA 30332-0355	10. Work Unit No.:	
	11. Contract or Grant No.: 0010820 (RP 11-34)	
12. Sponsoring Agency Name and Address: Georgia Department of Transportation Office of Research 15 Kennedy Drive Forest Park, GA 30297-2534	13. Type of Report and Period Covered: Final; March 2012 – March 2015	
	14. Sponsoring Agency Code:	

15. Supplementary Notes: Prepared in cooperation with the U.S. Department of Transportation, Federal Highway Administration.

16. Abstract:

    The use of duplex high-strength stainless steel (HSSS) grade 2205 prestressing strand and austenitic stainless steel (SS) grade 304 spiral wire reinforcement is proposed as a replacement of conventional prestressing steel, in order to provide a 100+ year service life for prestressed concrete piles located in the Georgia coastal region. The study experimentally investigated 16-in. square, 70-ft. long piles constructed using duplex HSSS 2205 strands and SS 304 spiral wire reinforcement and compared their behavior with identical piles which were built using the conventional strands and spirals. The piles were successfully driven to refusal without visible damage, were extracted and tested in flexure and shear.

    Transfer and development length of piles using duplex HSSS 2205 strands were 57% and 55%, respectively, of the values predicted by AASHTO LRFD (2013). Transfer length of duplex HSSS 2205 strands was not affected by pile driving and extraction. Flexural and shear strength of piles using duplex HSSS 2205 strands were greater than predicted by ACI 318-11 and AASHTO LRFD (2013) specifications. Experimental prestress losses at 335 days for piles using duplex HSSS 2205 strands were 82% of the predicted losses by AASHTO LRFD refined method. Prestress losses were not affected by pile driving and extraction.

    It was concluded that duplex HSSS 2205 can be used for prestressing strands in combination with austenitic SS 304 for the transverse confinement and shear reinforcement for prestressed concrete piles, using the same design requirements and construction procedures used for conventional prestressing strand and wire reinforcement.

17. Key Words: Piles, corrosion, prestressed concrete, marine environment, stainless steel	18. Distribution Statement:		
19. Security Classification (of this report): Unclassified	20. Security Classification (of this page): Unclassified	21. Number of Pages: 306	22. Price:

EXECUTIVE SUMMARY

The use of duplex high-strength stainless steel (HSSS) grade 2205 prestressing strand and austenitic stainless steel (SS) grade 304 spiral wire reinforcement is proposed as a replacement of conventional prestressing steel, in order to provide a 100+ year service life for prestressed concrete piles located in the Georgia coastal region. The study experimentally investigated 16-in. square, 70-ft. long piles constructed using duplex HSSS 2205 strands and SS 304 spiral wire reinforcement and compared their behavior with identical piles which were built using the conventional strands and spirals. The piles were successfully driven to refusal without visible damage, were extracted and tested in flexure and shear.

Transfer and development length of piles using duplex HSSS 2205 strands were 57% and 55%, respectively, of the values predicted by AASHTO LRFD. Transfer length of duplex HSSS 2205 strands was not affected by pile driving and extraction.

Flexural and shear strength of piles using duplex HSSS 2205 strands were greater than predicted by ACI 318 and AASHTO LRFD specifications.

Experimental prestress losses at 335 days for piles using duplex HSSS 2205 strands were 82.3% of the predicted losses by AASHTO LRFD refined method. Prestress losses were not affected by pile driving and extraction.

It was concluded that duplex HSSS 2205 can be used for prestressing strands in combination with austenitic SS 304 for the transverse confinement and shear reinforcement for prestressed concrete piles, using the same design requirements and construction procedures used for conventional prestressing strand and wire reinforcement.

ACKNOWLEDGMENTS

TABLE OF CONTENTS

LIST OF FIGURES

LIST OF TABLES

xxiii

LIST OF SYMBOLS AND ABBREVIATIONS

AASHTO   American Association of State Highway and Transportation Officials

ACI   American Concrete Institute

AISI   American Iron and Steel Institute

APE   American Piledriving Equipment, Inc.

ASTM   American Society for Testing and Materials

CTL   Chloride threshold level

d_b Nominal diameter of strand

DEMEC   Detachable Mechanical Strain Gauge

EAC   Environmentally assisted cracking

E_c Concrete modulus of elasticity

E_{ci} Concrete modulus of elasticity at release

$f'_{c,28}$ Concrete compressive strength at 28 days

f'_{ci} Concrete compressive strength at release

f_{pe} (f_{se})   Effective stress in the prestressing steel after losses

f_{ps} Stress in the prestressing strand at nominal strength of member

f_{pu} Tensile strength of prestressing strand

f_{pt} Stress in the prestressing strand prior to transfer

f_{py} Yield strength of prestressing strand

f_{si} Stress in prestressing strand after strand release

f_{sp} Splitting tensile strength of concrete

FHWA   Federal Highway Administration

GDOT	Georgia Department of Transportation
HE	Hydrogen embrittlement
HPC	High-performance concrete
HSC	High-strength concrete
HSSS	High-strength stainless steel
l_d	Development length
l_e	Embedment length for development length testing
LRFD	Load and Resistance Factor Design
l_t	Transfer length
LVDT	Linear Variable Displacement Transformer
PREN	Pitting resistance equivalency number
SCC	Stress corrosion cracking
SCM	Supplementary cementitious material
SS	Stainless steel
UNS	Unified Numbering System
USGS	United States Geological Survey
UTS	Ultimate tensile strength
VWSG	Vibrating wire strain gauge
w/c	Water to cement mass ratio
w/cm	Water to cementitious material mass ratio
ε_u	Strain at ultimate state in prestressing strand

CHAPTER 1

INTRODUCTION

1.1 Research Purpose

The research presented in this report continued the research developed in two previous projects funded by Georgia Department of Transportation (GDOT); the global objective is to increase the service life of prestressed concrete piles in marine environments to 100 or more years.

The first project studied the environmental conditions at which bridges were exposed in marine environments of Georgia. The deterioration evidenced by precast prestressed concrete piles of eleven inspected bridges had service lives between 24 and 58 years at the time of the inspection, and corrosion damage of conventional steel prestressing strands and wires was evident (Moser et al., 2011). Based on the degradation mechanisms of prestressed concrete piles in marine environments found in the first project, the second project recommended two stainless steel alloys (duplex grades 2205 and 2304) and two high-performance concrete mixtures intended to improve the durability of prestressed concrete piles. The goal was to provide a service life for bridges of 100^+ years (Holland et al., 2012; Moser et al., 2012).

The main findings obtained in these two previous reports were:

- Precast prestressed concrete piles in Georgia coastal regions evidence accelerated chloride intrusion and significant cracking and damage due to corrosion of reinforcement, sulfate attack, surface abrasion, biological attack from boring sponges, and pile over-driving.

- Conventional steel AISI 1080 used in prestressing strands does not provide the necessary corrosion resistance to reach the required service life goal for bridges in marine environments.

- The presence of crevices and surface imperfections in prestressing strands generates additional sites for corrosion initiation that reduces the chloride threshold limit (CTL) compared to individual wires.

- Duplex high strength stainless steel grade 2205 (HSSS 2205) exhibited the best corrosion resistance among the analyzed, strain-hardened high strength stainless steels.

- Duplex high strength stainless steel grade 2205 and 2304 prestressing strands are able to be produced using the existing facilities and procedures used for conventional grade AISI 1080 prestressing strand production.

1.2 Objectives and Scope

The purpose of this research was to develop corrosion-free precast prestressed concrete piles which can be adopted for use in Georgia's coastal, marine environment.

The specific objectives were to evaluate if precast concrete piles constructed with high-strength stainless steel prestressing strand and spiral wire reinforcement and with high-durability concrete may be easily fabricated, driven without failure or cracking, had flexural and shear strength capacities exceeding those determined using standard AASHTO LRFD provisions, determine if the transfer and development lengths of stainless steel strand satisfied standard AASHTO LRFD provisions, examine the long-term durability of the strand and concrete under marine conditions, and provide

specifications and design recommendations for corrosion-free piles which may be implemented by the Georgia Department of Transportation (GDOT).

The scope of the research was limited to testing duplex high strength stainless steel grade 2205 (HSSS 2205, UNS grade S32205) and conventional A1080 steel for prestressing strand and using stainless steel grade 304 (SS 304, UNS grade S30400) and conventional plain wire (ASTM A 82).

The research took place over one and one-half years during which time the strength of the concrete increased. The important events in the research are listed over time in Table 1.1 below.

Table 1.1 Calendar dates of research events and age of concrete at those times.

Event	Dates	Concrete age (days)
Stress prestressing strands	June 26, 2013	
Place concrete	June 27, 2013	0
Cut-down prestressing strands	June 28, 2013	1
Drive piles	December 18, 2013	174
Extract piles	December 19, 2013	175
Development length tests	February 24 to April 21, 2014	242 to 298
Shear tests	June 17 to July 21, 2014	355 to 389
Flexure tests	August 5 to September 4, 2014	404 to 434

1.3 Organization of the Report

This report is comprised of twelve chapters.

Chapter 2 provides a theoretical background on the corrosion mechanisms of prestressed concrete structures in coastal regions, the characteristics of prestressing

reinforcement, and a description of stainless steel. Also, the factors that influence the prestress losses, development and transfer lengths are described, along with expressions proposed in the literature to predict the development and transfer lengths.

Chapter 3 describes the design of the prestressed concrete piles and the samples built for the study. The construction procedure of the piles is presented, including the instrumentation for prestress losses and transfer length monitoring, and the construction of the specimens for development length testing is detailed.

Chapter 4 summarizes the properties of the steel and concrete used in the piles. It includes the mechanical properties of duplex HSSS 2205 strand, conventional steel strand, and austenitic SS 304 wire, the evaluation of the galvanic corrosion of the couple HSSS 2205 – SS 304, concrete mixture composition, the mechanical properties of concrete over time (compressive strength, splitting tensile strength, elastic modulus of elasticity, and Poisson modulus), the variability of the concrete used in each pile, creep and shrinkage testing results, and the permeability of concrete to chloride ions.

Chapter 5 describes the pile driving operation in the Savannah River, at Savannah, Georgia, and the extraction by water-jet. Potential cracking and spalling damage by driving was especially monitored. The bearing capacity of piles is compared with required design capacity.

Chapter 6 presents the flexural capacity of the piles. Tests performed in piles with duplex HSSS 2205 and conventional steel strands are described, and the results are compared with predicted behavior by ACI 318 and AASHTO LRFD provisions. Chapter 7, which shows the shear capacity of piles, follows the same organization.

Chapter 8 shows the prestress losses measured in the piles during the first year after placement. The measured values are compared with the prediction from the AASHTO LRFD refined method.

Chapter 9 shows the transfer length calculated from concrete surface strains, for piles using duplex HSSS 2205 and conventional steel strands. The compliance with calculated values from AASHTO LRFD and ACI 318, and the prediction of expressions proposed by previous studies are evaluated. The effect of driving on the transfer length of piles is also assessed.

Chapter 10 presents the development length testing of piles using duplex HSSS 2205 and conventional steel strands. A flexure test using variable test embedment length to induce slip of the strands is described, and the results are compared with predictions from AASHTO LRFD, ACI 318, and expressions proposed in the literature.

Chapter 11 describes the evaluation of the long-term performance of piles using 30-inch long specimens located in the Savannah River. Preliminary evaluation of the specimens was performed to establish an "undamaged" state of the samples to be used for future assessment of deterioration.

Chapter 12 presents the conclusions of the study and provides recommendations for the use of duplex HSSS 2205 strands and austenitic SS 304 wire in prestressed concrete piles.

CHAPTER 2

BACKGROUND

2.1 Deterioration of Prestressed Concrete Piles

2.1.1 Characteristics of prestressing reinforcement

Conventional prestressing steel is a pearlitic (α-ferrite + Fe$_3$C [cementite]) eutectoid steel with approximate elemental composition of 0.75-0.88% C, 0.6-0.9% Mn, 0.05% S (max), 0.04% P (max), and traces of other elements, such as Si, Mo, Cr, and Ni (Moser et al., 2011a), conforming to specification of AISI 1080 steel. Microstructure of the longitudinal and transverse orientations of the prestressing steel is shown in Figure 2.1, where white plates correspond to the ferrite phase and black plates correspond to the cementite phase. The anisotropic microstructure is oriented in the direction of cold drawing.

(a)   (b)
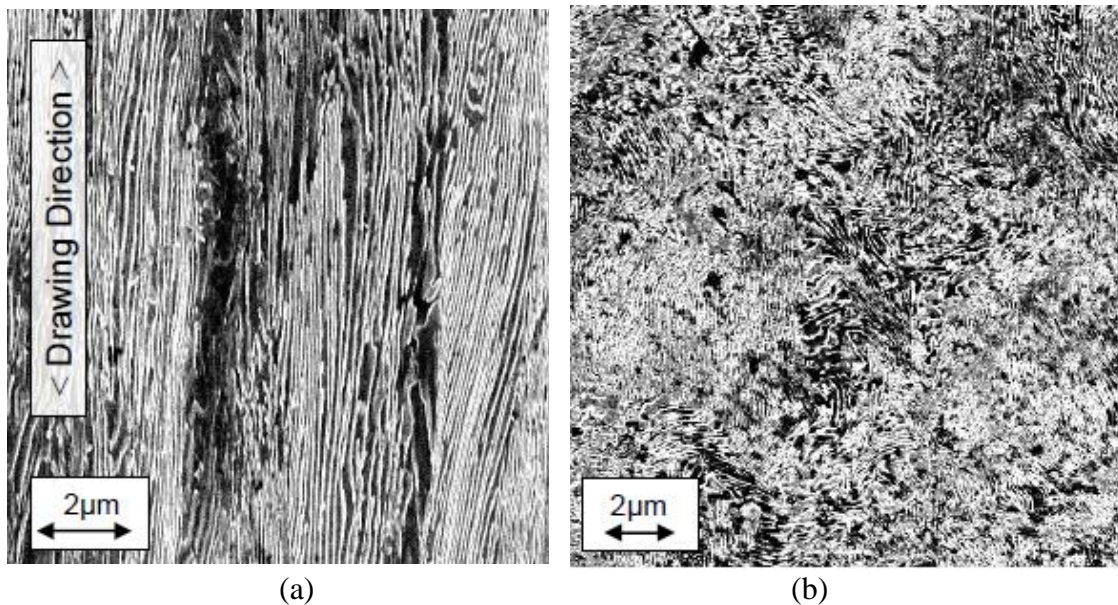
Figure 2.1 Microstructure of the (a) longitudinal and (b) transverse direction of prestressing steel (Moser et al., 2011a).

Prestressing steel reinforcement has higher yield and ultimate tensile strength than typical reinforced concrete reinforcement (Figure 2.2), in order to provide effective prestressing even after prestress losses reduce the magnitude of the prestressing force. Most common specified ultimate tensile strengths (UTS, often termed guaranteed ultimate tensile strengths, GUTS) are 250 and 270 ksi (1,724 and 1,862 MPa), and are typically stressed between 60% to 80% of the UTS; ultimate strain is about 7% and a modulus of elasticity of 29,000 ksi (200 GPa) is recommended by AASHTO (2013) and ACI 318 (2011) provisions.
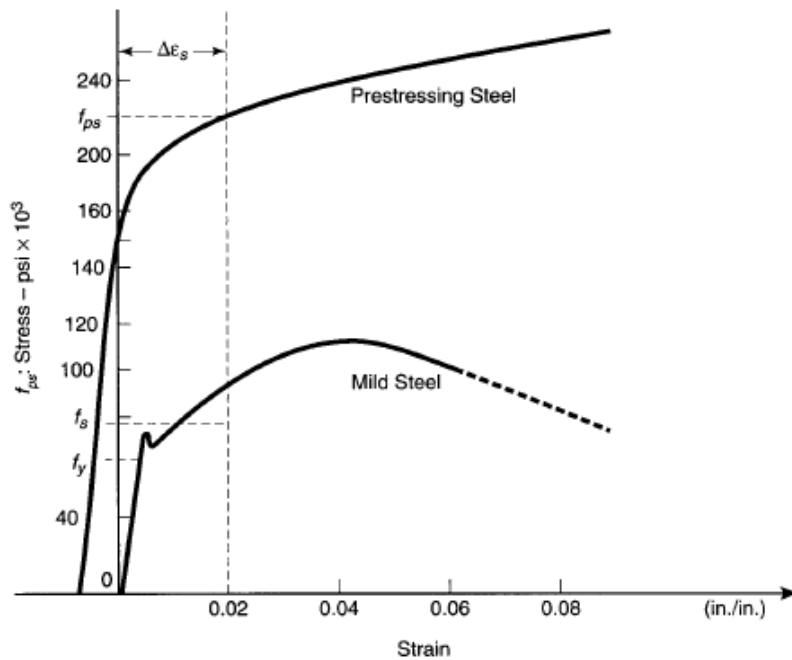
Figure 2.2 Stress-strain diagram of prestressing steel compared to mild steel (Nawy, 2009).

Prestressing steel is available in three forms: 1) uncoated wires (stress-relieved or low relaxation), 2) uncoated strands (stress-relieved or low relaxation), and 3) uncoated high-strength steel bars. Prestressing wires are cold-drawn to increase their tensile

7

strength, followed by a stress relieving process in which wires are exposed to temperatures of about 700 °F (371 °C) to remove residual stresses in steel. Low-relaxation wires and strands are subjected to the combined action of high temperature of stress relieving and stress approximately 40% of the UTS. Low-relaxation steel has a relaxation stress loss less than 2% to 3%, which is 25% of that of typical stress-relieved steel (Nawy, 2009; Moser et al., 2011a).

Standard strands are composed of seven wires; six of them twisted around one slightly larger central wire (Figure 2.3a). A compacted strand can also be formed to maximize the steel area of the 7-wire strand for a given nominal diameter (Figure 2.2b). The nominal diameter of the strand, d_b, ranges from 3/8 to 0.6-in. (9.5 to 15.2 mm).

(a)

(b)
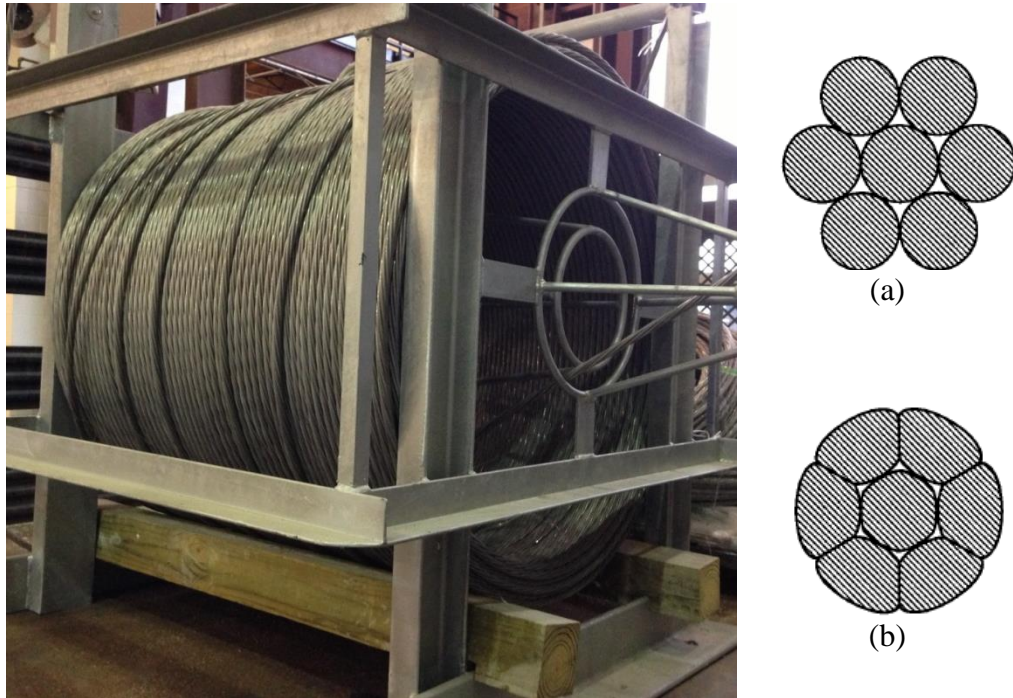
Figure 2.3 (a) Standard strand section and (b) compacted strand section (Nawy, 2009).

Prestressing wires are coated with $ZnPO_4$ to ease the cold working process and to provide a protective layer from the atmosphere before being placed in concrete. It has been shown that imperfections of this coating can be expected due to scratching, stranding, or cold-working. As a result, corrosion may initiate at these imperfection sites well before the breakdown of the $ZnPO_4$ layer (Moser et al., 2011b).

2.1.2 Corrosion of prestressed concrete structures

The failure mechanism due to corrosion of steel in prestressed concrete may differ significantly from conventional reinforced concrete. The nominal strength of prestressed concrete is dependent on the prestressing force. Thus, the corrosion of the prestressing steel and the subsequent reduction of the strand will have a higher impact compared to reinforced concrete structures. In extreme cases, corrosion of prestressing reinforcement can lead to catastrophic failure of prestressed concrete elements, which may occur without outward evidence (Nawy, 2009).

In the case of prestressed concrete piles exposed to marine environments, there are several mechanisms that contribute to the deterioration of these elements; the corrosion of the steel reinforcement is the most prevalent damage evidenced (Cannon et al., 2006). A survey of the condition of concrete bridges in the Georgia coastal region performed by Moser et al. (2011a) showed extensive damage of the substructure and superstructure. Most significant damage to piles was found in the submerged and tidal zones of bridges in contact with brackish water, where the most common deterioration features were abrasion of concrete, cracking and spalling of concrete, and corrosion staining. Analysis of water samples showed a pH between 5.88 and 7.47, and water

9

salinity and sulfate concentration consistent with brackish water (0.1-2.5% NaCl concentration and 1,000-2,700 mg/L SO_4^{2-}, respectively). Further examination of the piles identified chloride-induced corrosion and high chloride concentration in the tidal and splash zones, and evidence of concrete deterioration due to sulfate attack, carbonation, and the action of boring sponges.

These observations are consistent with the evaluation of prestressed concrete piles in the coast of Florida performed by Cannon et al. (2007). Half-cell potentials suggesting high probability of active corrosion of the reinforcement ($\leq$ -350 mV) were reported in the splash zone of piles, and higher chloride concentration was measured in submerged, splash, and tidal zones. Additionally, severe corrosion of the prestressing strands was observed at the pick-up points suggesting that accelerated chloride intrusion occurred at these regions.

The highest concentration of chloride in concrete piles partially submerged in seawater has been measured between 0 to 1 ft. (0 to 30.5 cm) above the waterline (Hartt and Rosemberg, 1980). Capillary flow of seawater and transverse evaporation of water from the sides of the piles explain the high concentration of residual salts in these regions (Chaix et al., 1995). Availability of moisture, chlorides, and oxygen at the splash and tidal regions can explain the higher corrosion rates and damage.

The accelerated deterioration of concrete structures in marine environments leads to a significant decrease of the predicted service life. Kurtis et al. (2013) estimated the predicted service life of reinforced concrete exposed to urban and marine environments. The diffusion coefficient of concrete was estimated from rapid chloride permeability tests (RCPT) performed on concrete mixtures with different water-to-cementitious material

ratios (*w/cm*) and varying additions of supplementary cementitious materials (SCMs), and then used as input for the service life modeling. Regardless of the concrete mixture used, life cycle analysis on Life-365® software (Ehlen et al., 2009) showed that the exposure of reinforced concrete elements to severe marine environments produce reductions of 68% to 78% in comparison with the service life of the same elements exposed to a mild urban environment (Figure 2.4).
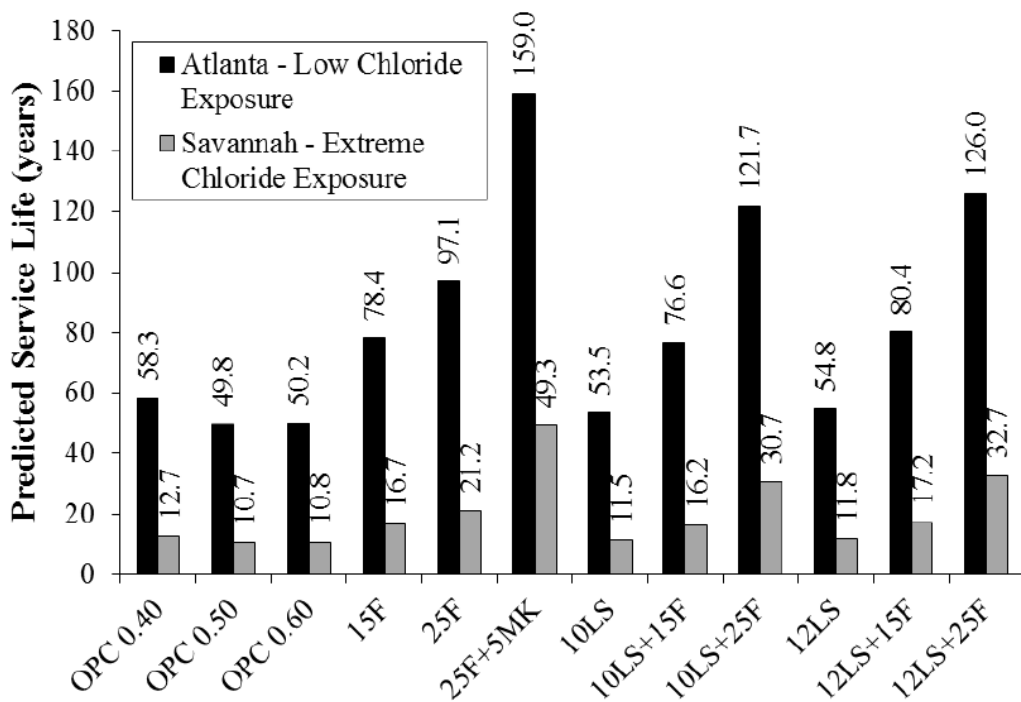
Figure 2.4 Impact of chloride exposure level on the predicted service life (Kurtis et al., 2013).

According to Georgia Department of Transportation (GDOT), some bridge sub-structures in the coastal area of Georgia are replaced after less than 40 years of service. The reduced service life of bridge structures generates higher maintenance and repair costs. Additionally, the Federal Highway Administration (FHWA) has instructed the increase of the service life of new bridges to 100 years or more (Moser et al., 2011a).

11

This objective cannot be reached in marine environments using conventional construction practices for prestressed concrete.

2.1.3 Corrosion of prestressing strand

The corrosion of prestressed concrete may be triggered by the action of different mechanisms. The two most common mechanisms are carbonation and chloride-induced corrosion; both of these involve the diffusion of deleterious elements through concrete, which eventually reach the depth of the prestressing strand and can initiate active corrosion. Additionally, environmentally-induced cracking can be produced in prestressing strands by two mechanisms: 1) stress corrosion cracking (SCC) and 2) hydrogen-assisted cracking (HAC) by hydrogen embrittlement (HE). These mechanisms of corrosion of prestressing steel strands are described below.

a) Carbonation-induced corrosion

Carbonation of concrete is initiated by the diffusion of airborne carbon dioxide (CO_2) through concrete porosity. CO_2 reaction with the alkaline components of cement paste (mainly calcium hydroxide ($Ca(OH)_2$, sodium hydroxide (NaOH), and potassium hydroxide (KOH)) and calcium silicate hydrate (C-S-H) may affect the service life of concrete structures (Bohni, 2005). The two main consequences of carbonation are: 1) the drop of pH due to the reduction in hydroxide concentration in the pore solution which is a process that induces the breakage of the passive layer of steel, and 2) the change of concrete permeability due to volume changes and microcracking caused by chemical reactions (Johanneson and Utgenannt, 2001). $Ca(OH)_2$ and alkali hydroxyls (NaOH and

KOH) are consumed due to the reaction with carbon dioxide and water, as shown in Equations 2.1 to 2.3. This consumption of hydroxyl ions lowers the pH of the pore solution from the original value (above 12.5) to values between 6 and 9 (Bohni, 2005).

$$Ca(OH)_2 + CO_2 + H_2O \rightarrow CaCO_3 + 2H_2O \qquad (2.1)$$

$$2NaOH + CO_2 + H_2O \rightarrow Na_2CO_3 + 2H_2O \qquad (2.2)$$

$$2KOH + CO_2 + H_2O \rightarrow K_2CO_3 + 2H_2O \qquad (2.3)$$
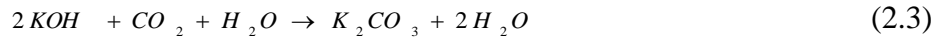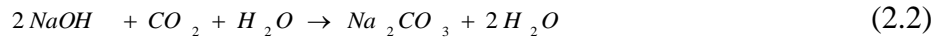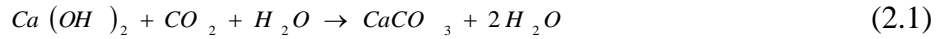
In concrete where $Ca(OH)_2$ becomes depleted, carbonation of C-S-H can also occur and lead to a further increase of porosity and permeability (Papadakis, et al, 1991; Neville, 1995; Johanneson and Utgenannt, 2001). Carbonation of C-S-H can be represented by Equation 2.4 (Papadakis, et al, 1991).

$$3CaO \cdot 2SiO_2 \cdot 3H_2O + 3CO_2 + H_2O \rightarrow 3CaCO_3 \cdot 2SiO_2 \cdot 4H_2O \qquad (2.4)$$
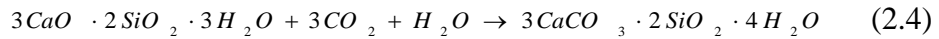
Carbonation of concrete begins at the exterior surface of concrete and infiltrates inward producing a low pH front (Bertolini et al., 2004). Once the carbonation front reaches the depth of the steel strand and the pH is reduced below 9, the protective oxide film is destroyed and active corrosion of the strand will initiate (Papadakis et al., 1991). Except for fully saturated concrete, a sufficient supply of oxygen can reach the steel surface. The availability of oxygen is important for the passive film development, but it also affects the corrosion rate and corrosion potential. In the absence of chlorides, the passive film will break down slowly according to Equation 2.5, where FeOOH is the passive film (Jones, 1996).

$$FeOOH + H_2O \rightarrow Fe^{3+} + 3OH^-$$

(2.5)

Carbonation ingress is at a maximum in the 50%-90% humidity range. Consequently, the most aggressive environments for carbonation-induced corrosion occur with alternating semi-dry and wet cycles. During the semi-dry periods, the carbonation rate increases and during the wet periods the steel corrosion rate increases (Rosenberg et al., 1989). High ambient CO_2 concentration, shallow cover, high permeability of concrete, and the presence of cracks are also factors that increase the rate of carbonation.

b) Chloride-induced corrosion.

Chloride-induced corrosion occurs when ingress of chlorides causes a breakdown of the protective, passive oxide film of steel, leading to active corrosion. While chlorides can come from internal or external sources, the corrosion of prestressing steel strands in non-carbonated concrete can only occur once the chloride content at the steel surface has reached a critical limit to initiate corrosion, called the chloride threshold level (CTL). Below the CTL, the passive film is thermodynamically stable and inhibits corrosion of the steel. Once corrosion is initiated, the corrosion rate depends on the source of chlorides, the transport mechanism involved, and several environmental factors.

Chloride ions exist in concrete in two forms, bound or free. Only the free chloride ions which are dissolved in the pore solution are able to participate in the corrosion process. As a result, free chloride concentration, and not the total chloride concentration in concrete, is critical for the CTL. Bound chlorides are those ions which react with other chemicals inside concrete and are no longer able to cause corrosion. For example, chloride ions can react with calcium aluminate (C_3A) present in cement paste to form

Friedel's salt ($C_3A \cdot CaCl_2 \cdot 15H_2O$). Studies have demonstrated that increasing the C_3A content of concrete from 2.43% to 14% increased the CTL by a factor of 2.85 (Kurtis and Mehta, 1997). However, sulfate present in Na_2SO_4 and $MgSO_4$ can affect the stability of bound chlorides, replacing Cl^- by SO_4^{2-} in Friedel's salt structure. This reaction that releases Cl^- and may increase the content of ettringite in concrete (Geng et al., 2015).

Currently, most design codes set limits on the amount of chloride content introduced from raw materials during the manufacturing of cement. The use of contaminated mixing water, unwashed aggregate or sand, or admixtures can also be sources of internal chlorides. In the past, calcium chloride was used extensively as an admixture before being forbidden because of its ties to corrosion. With internal chloride levels limited, the major source of chlorides is the ingress from the surrounding environment of the structure. The main sources of environmental chlorides are deicing salts and seawater (Bertolini et al., 2004).

Chloride penetration into concrete is a complex function of position, environment, and concrete properties (Bertolini *et al.*, 2004). Chloride permeation can occur due to a large pressure gradient such as in pressure vessels or piping. Chloride absorption can occur through capillary suction of a moisture gradient where cyclic wetting and drying occur, but absorption has been shown to be unable to penetrate to the depth of the steel (Holland et al., 2012). Thus, the primary transport mechanism for chlorides to penetrate concrete is diffusion.

Mathematical models are able to predict a chloride profile based on depth, time, apparent diffusion coefficient, and the surface chloride content. The apparent diffusion coefficient depends on the pore structure of the concrete and can vary based on *w/cm*,

15

compaction, curing, age, addition of SCMs, or type of cement. Often, the apparent

diffusion coefficient is used as a parameter to describe the resistance of concrete to

chloride penetration; the lower the coefficient value, the higher the resistance to chloride

penetration. This coefficient is also used to estimate the time a particular chloride

threshold will be reached at the depth of steel and corrosion will initiate (Bertolini et al.,

2004). However, if cracks are present, they allow a shorter path for deleterious material

to reach the steel.

When the CTL is reached, the protective oxide film is broken down and corrosion

is initiated. The chemical reactions responsible for the breakdown of the passive layer are

shown in Equations 2.6 and 2.7 (Jones, 1996).

$$FeOOH + Cl^- \rightarrow FeOCl + OH^- \tag{2.6}$$

$$FeOCl + H_2O \rightarrow Fe^{3+} + Cl^- + 2OH^- \tag{2.7}$$
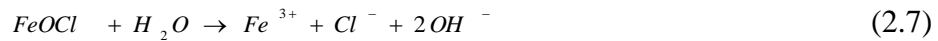
Equations 2.6 and 2.7 show that chloride ions are not consumed in this process,

and they are free to contribute to corrosion of the steel. This autocatalytic process

explains the accelerated corrosion of steel in chloride-induced corrosion.

Moser et al. (2011b) conducted a chloride-induced corrosion test on conventional

AISI 1080 7-wire prestressing strand and a wire. They found that the CTL for the

prestressing wire was similar to normal rebar. However, the CTL for prestressing strand

was significantly lower. In fact, the strand would initiate corrosion at one-third the level

of chlorides (Figure 2.5).
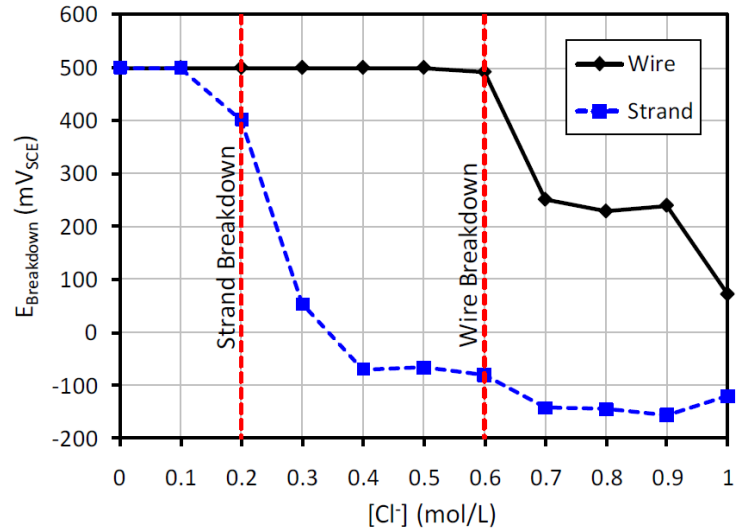
Figure 2.5 Breakdown potential versus chloride concentration for prestressing strand and wire (Moser et al., 2011b).

In carbonated concrete, the decrease in pH value and the presence of chloride ions act simultaneously. A lower pH will weaken or completely remove the passive protective layer of the steel. Therefore, chlorides can induce a more accelerated corrosion of steel. Moser et al. (2012) observed this effect in prestressing strands exposed to simulated carbonated concrete solution, where only a small addition of chlorides was necessary to initiate corrosion.

Corrosion will preferentially initiate on defect sites in the passive film. Film defects can be originated from grain boundaries, slip steps due to dislocations, or metal surface defects (Frankel, 1998). Moser et al. (2011b) showed that surface defects can also be originated during strand fabrication and stressing. Breakdown of the passive film is typically a localized phenomenon which results in the creation of a macro-galvanic cell (Rosenberg et al., 1989). Once the CTL is reached, localized pitting corrosion will likely occur.

b.1) Pitting corrosion

The mechanism of pitting corrosion on prestressing steel strands is similar to conventional steel reinforcement. Once the passive layer has been breached, the exposed areas undergo active corrosion. The local active area will act as an anode where the iron will readily dissolve, and the surrounding passive areas will act as a cathode (Rosenberg et al., 1989; Frankel, 1998). Meanwhile, the positively charged metal surface attracts the aggressive anions which will migrate to the site. The general corrosion reaction is given in Equation 2.8 (Jones, 1996; Frankel, 1998).

$$Fe^{2+} + 2H_2O + 2Cl^- \rightarrow Fe(OH)_2 + 2H^+ + 2Cl \qquad (2.8)$$
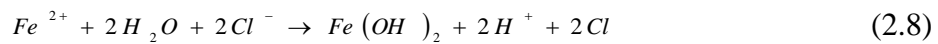
Analogous to equations 2.6 and 2.7, here the chloride ions are not consumed in the reaction. Instead, the chlorides dissolve the iron and then recycle to further react with more iron ions. Simultaneously, the pH inside the pit will drop because hydrogen ions are produced. As a result, pitting becomes an autocatalytic process, as shown in Figure 2.6 (Jones, 1996; Bertolini, et al, 2004; Frankel, 1998; Schmuki, 2002).
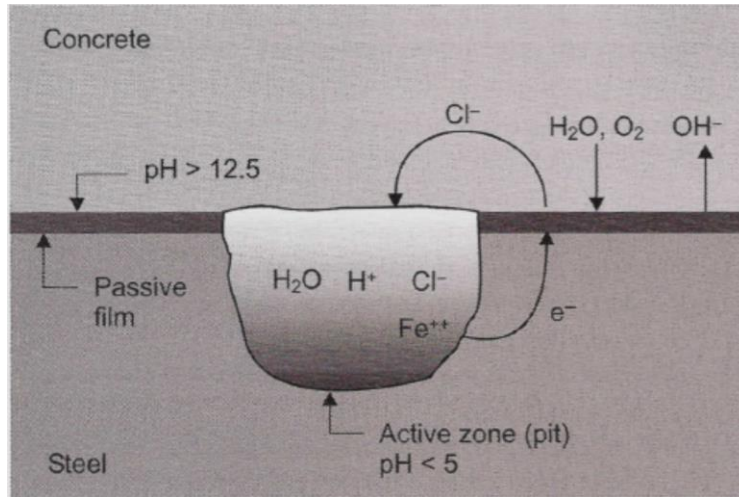
Figure 2.6 Schematic representation of pitting corrosion of steel in concrete (Bertolini et al., 2004).

b.2) Crevice corrosion

Although crevice corrosion of prestressing steel usually has not been considered a critical issue due to the closing of gaps between wires when strands are stressed, Moser et al. (2011a) showed that this type of corrosion can occur when imperfections on the protective coating provide preferential sites for corrosion initiation. A forensic analysis of a prestressed concrete bridge pile in the Georgia coastal region confirmed that crevice corrosion occurs, as seen in Figure 2.7 (Holland et al., 2012).

Figure 2.7 Core sample from corroded prestressed bridge pile evidencing crevice corrosion (Holland et al., 2012).

19

Moser et al. (2011a) also suggested that strand is more prone to initiate crevice corrosion because the alkaline cement paste is in contact with the outer surface of the strand wires. Once corrosion initiates in the crevices and acidifies the local area, a local concentration cell between the inner and outer portions of the strand develops and makes the environment more aggressive. After the initiation, the proposed mechanism of crevice corrosion propagation in chlorinated environments is very similar to the autocatalytic pitting mechanism.

At later ages, corrosion can spread to the strand surface due to a limited mass transport of reactants to the crevice regions. The model of initiation and propagation can be observed in Figure 2.8.
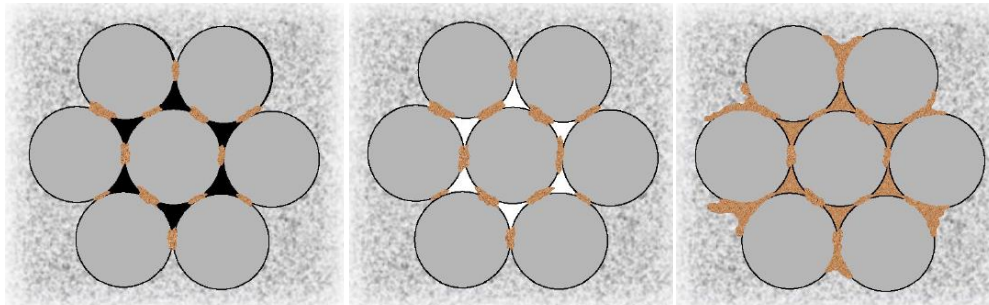
Figure 2.8 Crevice corrosion: initiation, propagation into the crevice regions and spread of the attack to strand surface (Moser et al., 2011a).

c) Environment-induced cracking (EIC)

While carbonation- and chloride-induced corrosion are observed on reinforced concrete and on prestressed concrete structures, high-strength prestressing steel also shows an increased susceptibility to environmentally-induced cracking (EIC). EIC results from the combination of susceptible material and a corrosive environment. Two common mechanisms of EIC are stress corrosion cracking (SCC) and hydrogen embrittlement

(HE), which can occur independently or simultaneously, and cause hydrogen-assisted cracking (HAC).

These three mechanisms may significantly reduce mechanical properties of prestressing steel. While prestressing steel is typically loaded to 60-80% of the UTS, the reduction of tensile stresses due to EIC can cause a catastrophic and brittle failure without even considering service loads. Because of their resulting brittle mode of failure, stress corrosion cracking, hydrogen embrittlement and hydrogen-assisted cracking are of great concern and are described below.

c.1) Stress corrosion cracking (SCC)

Stress corrosion cracking is the phenomena where a metal under tensile stresses forms sharp, defined cracks due to exposure to a certain environment. Commonly, cracking due to SCC takes the form of intergranular or transgranular cracking; that is, cracks form along the grain boundaries or through the grains. Cracks generally start at surface discontinuities like corrosion pits, grain boundaries, microstructure defects, or fabrication defects.

The two most common theories to explain the crack propagation phenomenon are electrochemical dissolution and stress sorption. The electrochemical dissolution theory proposes that galvanic cells are formed on the grain boundaries, and localized metal dissolution initiates a crack. Then, the stress disturbs the brittle oxide film over new anodic material, which is corroded. This process continues and the crack propagates within the material. The stress-sorption theory suggests that adsorbed deleterious elements reduce the cohesion between metal ions creating a weakened boundary, and the

applied stress causes crack growth along this boundary (ACI 222.2R, 2001; Jones, 1996). In the case of prestressing strands, hydrogen is generally the element that causes the brittle fracture of steel and thus, hydrogen assisted cracking (HAC) is the prevailing EIC mechanism.

Independent from the mechanism of initiation and propagation, SCC occurrence will depend on the type of metal or alloy used and the conditions of the environment. A stress field ahead of the crack tip can be characterized by a stress intensity factor, K_I. This parameter is related to both the stress level and crack size. When K_I reaches a critical threshold level, failure occurs. SCC will occur when $K_I = 43$ MPa·m$^{0.5}$ and a brittle fracture will occur when $K_I = 86$ MPa·m$^{0.5}$ (Darmawan and Stewart, 2007). Several tests have shown that present day prestressing strand has K_I values well above the SCC critical threshold in atmospheric and chloride environments. Thus, conventional steel strands are resistant to SCC in these environments (Nurnberger, 2002; Toribio and Ovejero, 2005; Darmawan and Stewart, 2007).

c.2) Hydrogen embrittlement (HE) and hydrogen-assisted cracking (HAC)

Hydrogen embrittlement (HE) is the reduction of ductility of metals and alloys due to the absorption of hydrogen atoms into the metal lattice (Fontana, 1986). HE does not require stress to occur, and hydrogen can be introduced during manufacturing of strand and strand storage, and during precast concrete pile construction and life of the pile. Some sources of hydrogen are welding, electroplating, hydrogen gas, cathodic polarization, and corrosion products. Hydrogen atoms present on the metal surface penetrate the metal lattice occupying different positions in the microstructure.

22

Hydrogen atoms trapped in the metal lattice are mainly responsible for the occurrence of HE on prestressing steel, because they deform the steel lattice. This deformation affects the mechanical properties of the steel, and straining the lattice limits the ductile slip mechanism and reduces toughness. The level of embrittlement increases with the amount of hydrogen trapped inside the steel (Recio et al., 2013), and some chemicals have been shown to accelerate HE, including hydrogen sulfide (H_2S), carbon dioxide (CO_2), chloride (Cl^-), cyanide (CN^-), and ammonium ions (NH_4^+).

Novokshchenov (1994) found that the susceptibility of steel to HE increases with increased carbon content, increased cold working, increased stress relieving, increased chloride concentration, and increased temperature. Additionally, forensics performed on structures affected by HE have revealed that embrittled steel presents the following characteristics: lower tensile strength reflects a loss of ductility due to hydrogen absorption, failure occurs over a broad range of applied stress, time to failure depends on the applied stress, and below a critical stress, failure does not occur (ACI 222.2R, 2001). However, hydrogen uptake is a function of environmental pH and HE is only observed with pH lower than 7. Thus, hydrogen absorption is not feasible when steel is in a passive state (Griess and Naus, 1980).

HE can act concurrently with SCC to form hydrogen-assisted cracking (HAC). Cracks are initiated by pitting corrosion which causes a local concentration of hydrogen ions and a lower pH. Simultaneously, hydrogen also has a tendency to concentrate where tensile stresses are the highest within the metal lattice, near the crack tip. The crack will propagate once the lattice is sufficiently embrittled, combined with an adequate tensile force (Figure 2.9). This process will continue to repeat itself and lead to steel failure as

long as hydrogen and stress remain present (Bertolini et al., 2004). Conventional AISI 1080 prestressing steel, tested using the Federation Internationale de la Precontrainte test (FIP-test), has showed high resistance, but not complete immunity to HAC susceptibility (Nurnberger, 2002; Toribio and Ovejero, 2005; Wu and Nurnberger, 2009).
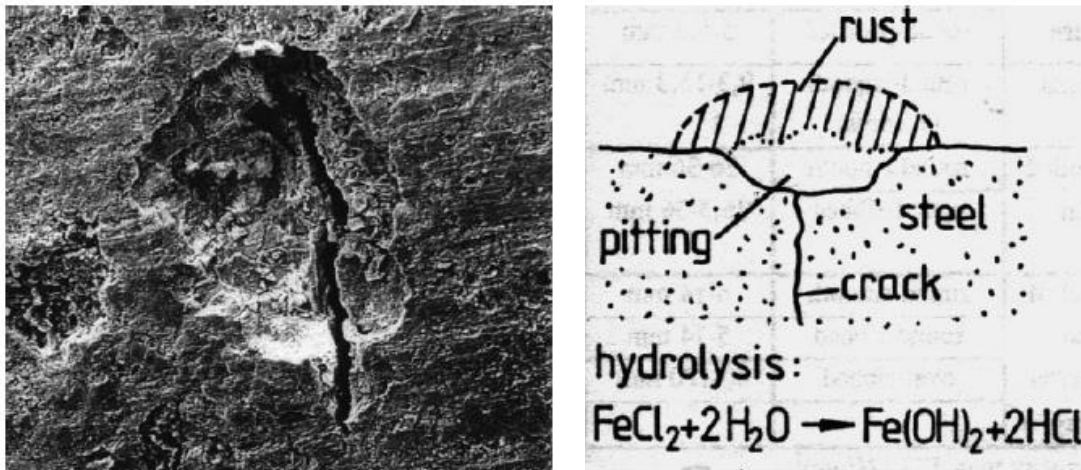
Figure 2.9 HAC of steel in concrete at a pit site (Nurnberger, 2002).

2.1.4 Alternative reinforcement for corrosion prevention

To prevent the high cost associated with maintenance, corrosion-resistant reinforcement has been proposed to reduce chloride-induced corrosion. These alternative reinforcement systems include galvanized reinforcement, epoxy-coated reinforcement, and stainless steel reinforcement.

Galvanized steel has a coating of zinc that protects steel, acting as an anode and increasing the time to corrosion initiation. Galvanized steel forms a passive layer in the alkaline environment of concrete, similar to the case of conventional steel. However, even when the corrosion initiation is delayed by the presence of a zinc coating, the durability of galvanized steel in marine environments is insufficient. It has been

24

estimated that galvanized steel can corrode in about 5 years when exposed to aggressive environments (Bautista and Gonzalez, 1996). Also, uncertainty of structural response of this material is introduced by the effect of galvanizing on the brittleness of bars with different composition and degrees of work hardening (Azizinamini et al., 2013).

Epoxy-coated bars reduce considerably the diffusion of oxygen and chloride through a barrier organic coating that protects reinforcing steel from corrosion. Studies have shown both great advantages provided by epoxy coating while others have shown potential weaknesses (Erdogdu et al., 2001; Weyers et al., 2006; Azizinamini et al., 2013).

Stainless steels are iron-chromium alloys that have a high corrosion resistance. Austenitic and austenitic-ferritic (duplex) stainless steel have shown more favorable potential to be used as reinforcement in concrete structures due to their excellent corrosion resistance when exposed to chloride-containing concrete (Wu and Nurnberger, 2009), and they have been effectively used in coastal bridges. However, the main concern in adopting this steel is the higher material cost. Moser et al. (2012) estimated in 2011 that austenitic grades 304 and 316 had a cost 6.9 and 9.6 times higher than conventional steel, respectively, while duplex grade 2205 had a cost 8.8 times higher than conventional carbon steel. Life cycle cost analysis has shown that the use of stainless steel reinforcement is cost-effective in marine environments, considering the extended service life and the minimal maintenance costs for structures made with stainless steel reinforcement (Azizinamini et al., 2013).

2.2 Properties of Stainless Steels

Stainless steel (SS) is a general denomination for ferrous alloys with a minimum chromium content of 10.5-11.0 wt. %. Presence of chromium allows the formation of a thin, self-healing chromium oxide layer that gives stainless steel a higher corrosion resistance than conventional steel, even in severe marine environments (Figure 2.10). The composition of stainless steels used in civil and mechanical engineering applications is highly variable, but commonly, elements such as Mn, P, S, Si, Ni, Mo, and N are present (ASTM A276, 2013). Consequently, a broad range of mechanical properties and corrosion resistance can be obtained. For instance, the addition of Mo enhances the resistance to pitting formation, while Ni addition increases the stability of austenite (Lo et al., 2009).
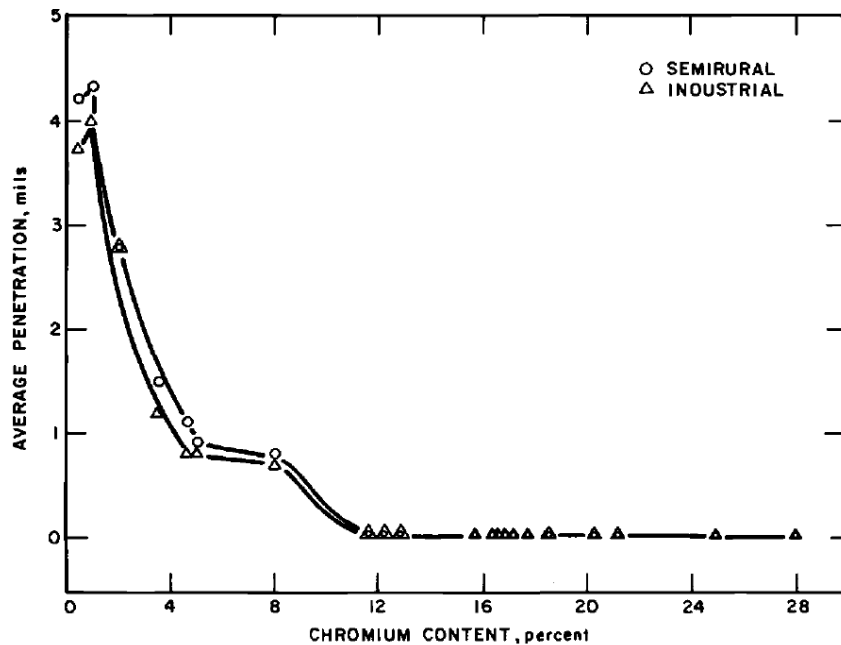
(a)

Figure 2.10 Effect of chromium content on corrosion depth of stainless steel on (a) industrial and semi-rural, and (b) marine environments (Schmitt and Mullen, 1969).

26
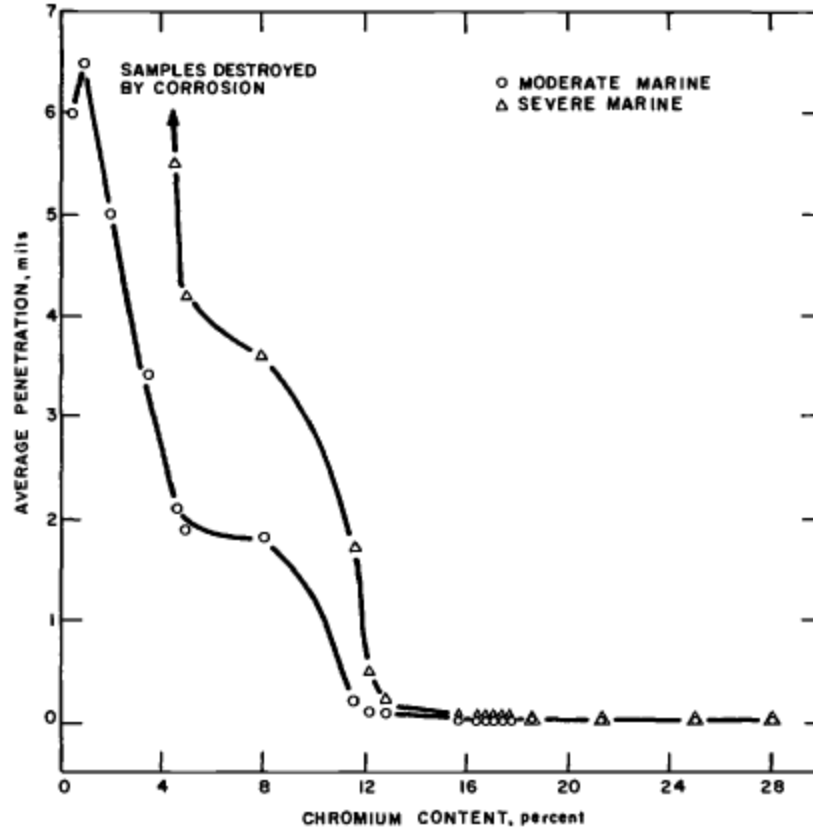
Figure 2.10 (cont.) Effect of chromium content on corrosion depth of stainless steel on (a) industrial and semi-rural, and (b) marine environments (Schmitt and Mullen, 1969).

Compared to conventional carbon steel used in structural applications, stainless steel exhibits a different stress-strain behavior. No clear yield point is appreciable and post-yield behavior cannot be modeled as a flat plateau (Gardner, 2005). Ramberg-Osgood expression (Equations 2.9) is often used to represent the stress-strain relation of SS before yield (Ramberg and Osgood, 1941).

$$\varepsilon = \frac{\sigma}{E_0} + 0.002 \left(\frac{\sigma}{\sigma_{0.2}} \right)^{n} \qquad \text{for } \sigma \leq \sigma_{0.2} \qquad (2.9)$$

27

where E_0 is the initial elastic modulus, $\sigma_{0.2}$ is the stress obtained by the 0.2% offset method, σ is the tensile strength, ε is the tensile strain, and n is a parameter calculated using Equation 2.10.

$$n = \frac{\ln(20)}{\ln\left(\dfrac{\sigma_{0.2}}{\sigma_{0.01}}\right)} \tag{2.10}$$

where $\sigma_{0.01}$ is the stress obtained by the 0.01% offset method.

Rasmussen (2003) proposed an expression for the stress-strain behavior after yield (Equation 2.11).

$$\varepsilon = \frac{\sigma - \sigma_{0.2}}{E_{0.2}} + \varepsilon_u \left(\frac{\sigma - \sigma_{0.2}}{\sigma_u - \sigma_{0.2}}\right)^m \qquad \text{for } \sigma > \sigma_{0.2} \tag{2.11}$$

where $E_{0.2}$ is the tangent elastic modulus at yield point, σ_u is the ultimate tensile strength, ε_u is the ultimate tensile strain, and m is a parameter calculated using Equation 2.12.

$$m = 1 + 3.5 \frac{\sigma_{0.2}}{\sigma_u} \tag{2.12}$$

Equations 2.9 and 2.11 showed good agreement with tensile test results performed on austenitic grades AISI 304, AISI 304L, and AISI 316L, duplex grade 2205, and ferritic grades AISI 430 and 3Cr12 (UNS 41050) (Rasmussen, 2003).

Additionally, stainless steels exhibit higher retention of strength and stiffness at elevated temperatures compared to conventional steel (Gardner, 2005).

2.2.1 Classification of stainless steels

Stainless steels can be classified as austenitic, ferritic, duplex (austenitic-ferritic), martensitic, and precipitation hardening.

Austenitic stainless steels are iron-chromium alloys that form face-centered cubic (FCC) austenite phase, with typical composition of Cr and Ni greater than 18% and 8%, respectively. They usually are non-magnetic and have high ductility, toughness, and work hardening during cold drawing. Also, nickel acting synergistically with chromium provides improved corrosion resistance compared with other stainless steels (Jones, 1996; Moser et al, 2012). Austenitic stainless steels are the most widely used stainless steels. Most common austenitic grades, AISI 304 and AISI 316, have been used in construction elements exposed to marine and urban environments, and also as reinforcement in concrete structures (Wallinder et al., 2002; Hartt, 2006). When austenitic SS is exposed to cold drawing higher than 40%, a process that affects the mechanical properties and reduces the corrosion resistance of steel, its microstructure can partially or fully transform to martensite (Wu and Nurnberger, 2009).

Ferritic stainless steels have a body-centered cubic (BCC) structure and they are alloyed mostly with 12-16% of chromium that acts as a ferrite stabilizer. Little amounts of Mo and Ni can also be incorporated. Ferritic SS grades have higher ultimate and yield strengths, and lower ductility, toughness, and corrosion resistance compared to austenitic grades (Moser et al., 2012).

Martensitic and precipitation hardening stainless steels usually have high strengths but, due to a lower corrosion resistance, they are more commonly used in mild environments (Jones, 1996).

Duplex stainless steels are composed of a ferrite-austenite dual microstructure, in roughly equal proportions. Duplex SS grades generally have a chromium content between 21% and 27%, and additions of Ni (1.5-24.5%), Mo (0.3-6.1%), and N (0.05-0.27%). Some duplex SS grades include minor contents of W and Cu (Alvarez-Armas, 2008). The dual-phase structure combines the superior mechanical properties of the ferrite phase with the high corrosion resistance of the austenite phase.

Duplex SS grades can be categorized by their pitting resistance equivalency number (PREN), calculated using the weight fraction of Cr, Mo, and N (Equation 2.13).

$$PREN = \% \, Cr + 3.3 \, \% \, Mo + \beta \cdot \% \, N \qquad (2.13)$$

where β is 30 for duplex grades, and 16 otherwise. This number provides a relative comparison of the expected resistance to pitting corrosion in marine environments, but it does not give a good measure of the corrosion resistance of stainless steel. Generally, duplex SS with PREN values lower than 30 are categorized as lean duplex grades, PREN numbers between 30 and 40 defines standard duplex grades, and SS with higher PREN numbers are considered superduplex alloys (Alvarez-Armas, 2008). The most common duplex grade is standard duplex 2205 (ASTM A276 grade UNS S31803). HSSS 2205 and lean duplex grades 2101 and 2304 (UNS 32101 and 32304, respectively)

have been tested as reinforcement in concrete structures due to the higher corrosion

resistance compared to austenitic grades (Moser et al., 2011; Hartt et al., 2006).

Characteristics of the most common stainless steel grades are given in Table 2.1.

Table 2.1 Composition and PREN values of the most common stainless steels (Moser et al., 2012).

| Grade | Type | Composition (wt. %) – Fe Balance | | | | | | PREN |
		C	N	Cr	Ni	Mo	Other	
304	Austenitic	0.04	0.06	18.2	8.1	------	------	19.2
316	Austenitic	0.04	0.06	17	11	2.8	------	27.2
430	Ferritic	0.04	------	16.5	------	------	------	16.5
2101	Duplex	0.03	0.22	21.5	1.5	0.3	5 Mn	29.1
2205	Duplex	0.02	0.17	22	5.5	3	------	37.0
2304	Duplex	0.02	0.10	23	4.8	0.3	------	27.0

2.2.2 Use of stainless steel in prestressing strands

Studies of the use of stainless steel to improve the corrosion resistance of

prestressing strands have been focused on austenitic grades, given their good corrosion

resistance. Cold-drawn strands and wires of grades 304, 316, and 316LN (low carbon,

nitrogen enhanced steel) have been produced with ultimate tensile strengths between 203

and 268 ksi (1,400 to 1,850 MPa) and stress relaxation of 7% (Moser et al., 2012). Good

resistance to chloride-induced corrosion has been reported, with no corrosion initiation at

Cl^- concentrations as high as 1.5 M, higher concentration than expected in seawater

(Hurley and Scully, 2006). Phase transformation to martensite when cold drawn higher

than 50% has been observed in production of grade 304 specimens (Milad et al., 2008),

which can explain a lower resistance to pitting corrosion and chloride-assisted SCC compared to grades 316 and 316 LN (Wu and Nurnberger, 2009). Application of austenitic stainless steel prestressing strands in full scale structures has not been reported.

Duplex high-strength stainless steel (HSSS) similar in composition to grade 2205, was analyzed as a replacement of carbon prestressing steel by Shirahama et al. (1999). Duplex HSSS was cold-drawn and stranded, the UTS was 237 ksi (1,636 MPa), the ultimate strain was 4.0%, and stress relaxation was 0.5% at an accelerated 10-hour test. Experimental analysis showed low susceptibility to chloride-induced corrosion, pitting corrosion, HE, and SCC.

Use of Nitronic 33 stainless steel (ASTM A580 grade XM-29), 3/16-in. (4.76 mm) diameter 7-wire prestressing strands in marine structures was reported by Jenkins (1987). Nitronic 33 strands had 17.7% Cr, 12.2% Mn, and 3.5% Ni. UTS and ultimate strain of wires were 136 ksi and 33.3%, respectively. The study included full scale piles, which showed enhanced corrosion protection compared to piles using carbon steel.

Moser et al. (2012) analyzed different HSSS grades to select the most promising to be used as a replacement of conventional AISI 1080 steel in prestressing strands. Low-relaxation wires of austenitic grades 304 and 316, martensitic grade 17-7, and duplex grades 2101, 2304, and 2205 were prepared using conventional practice. UTS of stainless steel wires varied from 181 to 225 ksi (1,250 to 1,550 MPa), and a lack of strain hardening after yielding was observed (Figure 2.11).

Analysis of the fracture surface showed a non-ductile failure in duplex HSSS 2205 samples. Corrosion testing of wires showed lower chloride-induced corrosion

susceptibility of duplex grades 2205 and 2304 in alkaline and carbonated simulated

environments.
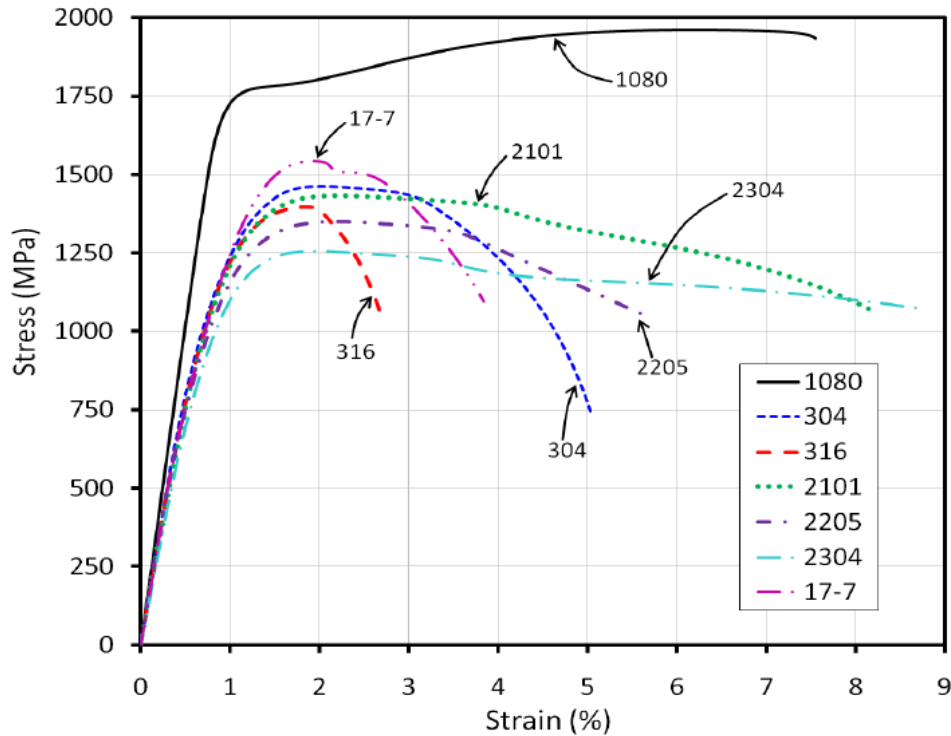
Figure 2.11 Stress-strain curves for conventional AISI 1080, austenitic 304 and 316, martensitic 17-7 and duplex 2101, 2205 and 2304 wires (Moser et al., 2013). 1 MPa = 145 psi.

Using traditional procedures of stranding and conditioning, 7- wire prestressing

strands were manufactured using duplex HSSS 2205 and 2304. Under the same testing

conditions used for the corrosion resistance of wires, duplex HSSS 2304 strands showed

pitting corrosion initiation for alkaline and carbonated formation with Cl^- concentration

of 0.5 M, the concentration level expected in seawater. Duplex HSSS 2205 strands

showed no corrosion evidence at Cl^- concentration of 1.00 M in alkaline and carbonated

solutions (Moser et al., 2012).

Schuetz (2013) tested the mechanical properties of duplex grades 2205 and 2304 prestressing strands. Duplex HSSS strands showed less ductility, elastic modulus, ultimate strain, and UTS than AISI 1080 steel strands (Figure 2.12).
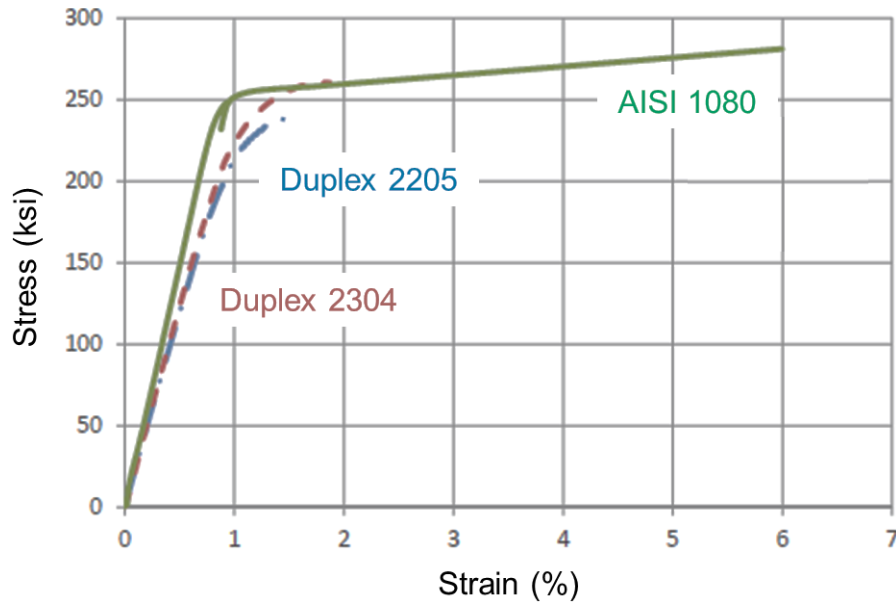
Figure 2.12 Stress-strain curves for conventional AISI 1080 steel, and duplex grades 2205 and 2304 prestressing strands (modified from Schuetz, 2013). 1 ksi = 6.9 MPa.

2.3 Prestress Losses

Prestressed concrete elements undergo losses of the initial prestressing force over time. The estimation of prestress losses allows the determination of the effective prestress acting on a prestressed concrete section, and to evaluate actual concrete stresses and deformation during the service life of a structure (Tadros et al., 2003).

Prestress losses in pretensioned members can be classified in two categories depending on the time when they occur (Nawy, 2009): immediate elastic shortening of concrete and time-dependent losses, which include creep and shrinkage of concrete and stress relaxation of steel. Elastic prestress gains can also be produced when live and

superimposed loads are applied to the prestressed element, but usually they are not

included explicitly in the estimation by codes (Figure 2.13).
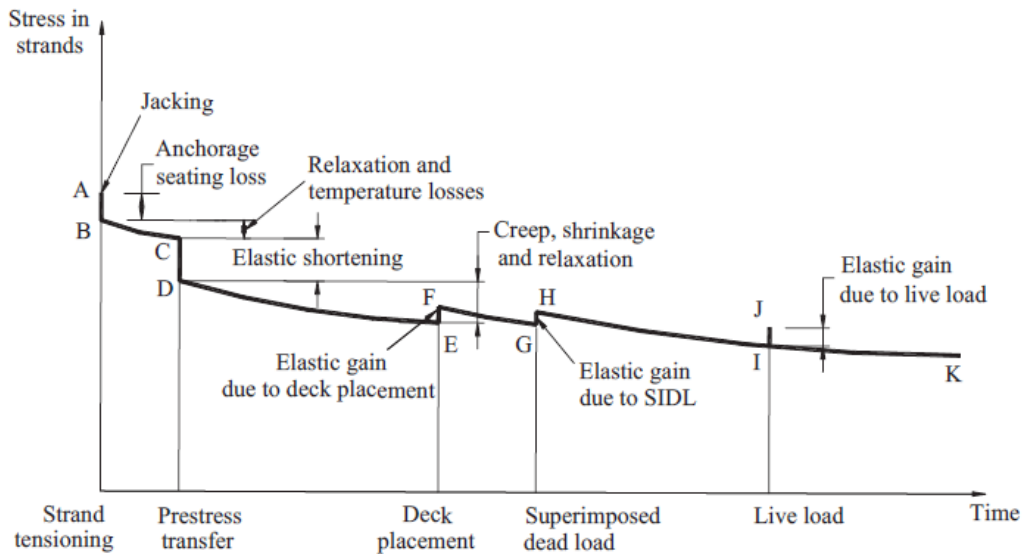
Figure 2.13 Change of stress on strands due to prestress losses (Tadros et al., 2003).

Due to the application of the prestressing force, concrete experiences elastic

shortening that simultaneously induces shortening of bonded strands. As the strands

shorten, a fraction of the prestressing force is lost. When additional forces are applied to

the element, the elongation of the strands produces elastic gains (Tadros et al., 2003).

Steel stresses are reduced over time due to the stress relaxation under a sustained

strain. Relaxation losses depend on the time that such strain is imposed to the strand and

the magnitude of the prestressing force that produces the elongation. ASTM A416 limits

relaxation losses in low-relaxation strands, after 1,000 hours of testing, to 2.5% of the

initial stress when axially loaded at 70% of the UTS, and to 3.5% when the load is 80%

of the UTS.

Prestress losses due to creep and shrinkage of concrete are commonly the principal source of losses in prestressed concrete elements (Bandyopadhyay and Sengupta, 1986; Tadros et al., 2003). Deformation of concrete due to creep and shrinkage produces the shortening of the prestressing strands and reduces the prestressing force applied to the member. Generally, the estimation of creep and shrinkage losses has a higher uncertainty compared with the other losses, given the number of factors that affect their magnitude. Creep losses depend on the environmental conditions, dimension and geometry of the element, the magnitude and duration of load application, mixture proportion and mechanical properties of concrete, time and method of curing, and age of concrete at transfer. Shrinkage losses are determined by environmental conditions, dimension and geometry of the element, mixture proportion of concrete, time and method of curing, and age of concrete at transfer.

AASHTO LRFD (2013) estimates the losses of pretensioned elements using Equation 2.14.

$$\Delta f_{pT} = \Delta f_{pES} + \Delta f_{pLT} \qquad (2.14)$$

where total losses, Δf_{pT}, are the sum of losses due to elastic shortening, Δf_{pES}, and long-term losses, Δf_{pLT}.

Δf_{pES} combines elastic losses and gains and is calculated using Equation 2.15.

$$\Delta f_{pES} = \frac{E_{ps}}{E_{ct}} f_{cgp} \qquad (2.15)$$

where E_{ps} is the elastic modulus of steel, E_{ct} is the elastic modulus of concrete at transfer, and f_{cgp} is the stress in concrete at the center of gravity of prestressing strands after transfer.

AASHTO estimates Δf_{pLT} by two different techniques: the approximate or lump-sum method, and the refined method. The lump-sum method calculates long-term losses using a single equation that combines creep, shrinkage and relaxation losses. The refined method estimates the contribution of every source of losses individually.

Examples of the use of both AASHTO methods for the estimation of prestress losses are given in Appendix K.

2.4 Transfer and Development Lengths: Code Provisions and Research Estimations

The transfer length of prestressing strand in pretensioned concrete elements is the distance, from the start of the bonded section, over which the strand transfers the initial tensile stress to compressive stress in concrete through bond stresses (Reutlinger, 1999). The flexural bond length is defined as the additional length of prestressing strand beyond the transfer length over which bond is developed to allow the strand to reach the stress at the nominal flexural strength of the member (Meyer, 2002). The development length is the sum of transfer and flexural bond length. Transfer of stress from strand to concrete along the development length can be represented by diagram in Figure 2.14.
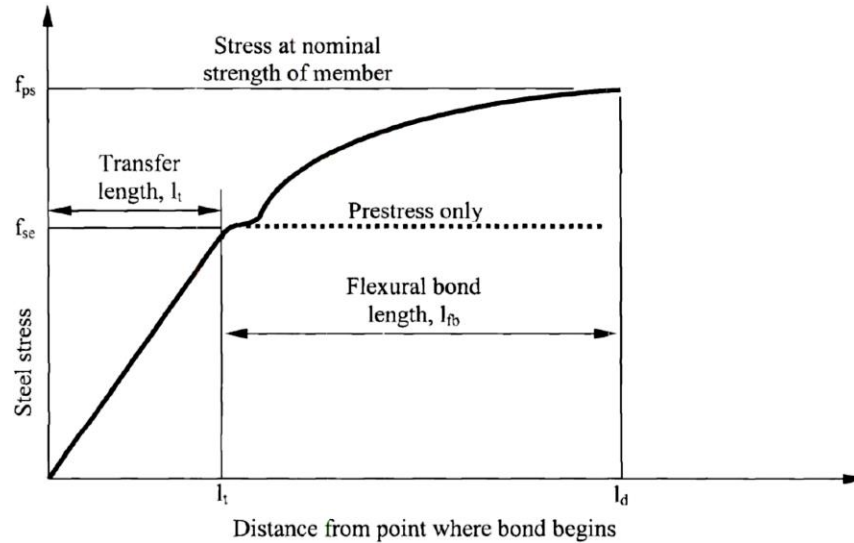
Figure 2.14 Strand stress along development length (Meyer, 2002).

The bond between the prestressing strand and concrete depends on three

mechanisms: 1) adhesion, 2) Hoyer's Effect, and 3) mechanical interlocking (Russell and

Burns, 1993).

Adhesion is the chemical bond between steel and concrete that prevents strand

slip as bond stresses increase to a critical stress level. After the critical stress is reached,

adhesion causes brittle failure, and resistance provided by the chemical bond is reduced

to zero. Adhesion has a small contribution to transfer bond and bond development under

applied loads (Russell and Burns, 1993; Reutlinger, 1999).

Hoyer's Effect was first described by Hoyer and Friedrich (1939) as a

consequence of the mechanical properties of steel and construction procedures of

pretensioned concrete elements. After the pretensioned load is applied, the diameter of

the strand is reduced by the Poisson's Effect. Then, when the strand is released in

hardened concrete, the strand expands laterally creating a normal force in concrete in

order to counteract the expansion. However, prestress along the strand in the transfer

38

region is not uniform, and the variation of the strand diameter will create a wedge action, which is greater closer to the end of the element. As a result, the normal force in concrete induces friction that anchors the strand and restrains its relative movement with respect to concrete. Hoyer's effect has a higher effect on bond in the transfer region and a negligible impact when additional loads are applied. Diagram in Figure 2.15 describes the wedge action produced by Hoyer's effect.
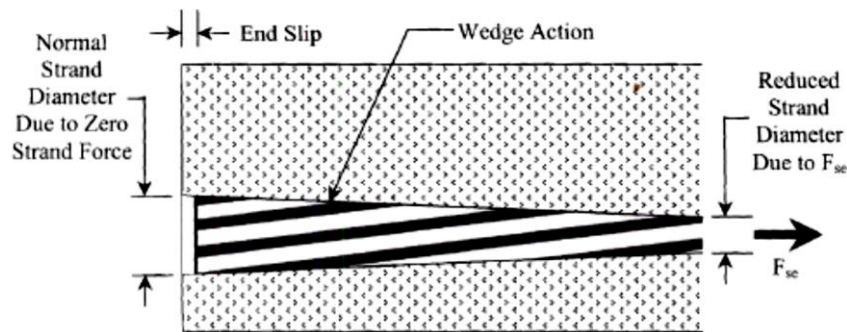
Figure 2.15 Hoyer's Effect in prestressing strand (Meyer, 2002).

Mechanical interlocking is a consequence of the physical characteristics of the pretensioned strand. Standard strand is composed of six wires wound around a central wire. The helical pattern of the strand creates deformities that are surrounded by concrete, creating an envelope. If the strand is pulled from concrete, ridges at the external wires restrict movement by mechanical interlock (Russell and Burns, 1993; Meyer, 2002). Mechanical interlocking is the dominant mechanism that enhances bond in the flexural bond region.

The expressions for development and transfer length calculation according to ACI 318 and AASHTO LRFD, and the proposed equations from previous studies are given below. Variables and units used in this section are detailed as follows:

l_t: transfer length, in inches.

l_d: development length, in inches.

d_b: nominal diameter of the prestressing strand, in inches.

f_{ps}: stress in prestressing steel at nominal flexural strength, in ksi.

f_{pt}: stress in prestressing strand, in ksi.

f_{si}: stress in prestressing strand after transfer, in ksi.

f_{se}: effective stress in prestressing strand after losses, in ksi.

f_{su}: ultimate strength of prestressing strand, in ksi.

E_{ci}: elastic modulus of concrete at release, in ksi.

f_c': design compressive strength of concrete, in ksi.

f_{ci}': compressive strength of concrete at release, in ksi.

M_{cr}: cracking moment, in kip-in.

M_n: nominal flexural resistance, in kip-in.

V_u: factored shear force, in kips.

V_{cw}: nominal shear resistance provided by tensile stresses in concrete in the web, in kips.

2.4.1 AASHTO and ACI estimations of transfer and development length

a) AASHTO LRFD (2013).

The determination of transfer and development lengths of prestressing strands is covered in Section 5.11.4 of the 6th Edition of AASHTO LRFD Bridge Design Specifications (2013). Equations 2.16 and 2.17 are proposed for l_t and l_d, respectively.

$$l_t = 60 \cdot d_b \tag{2.16}$$

$$l_d \geq \kappa \cdot \left(f_{ps} - \frac{2}{3} f_{pe} \right) \cdot d_b \tag{2.17}$$

where κ is 1.6 for pretensioned members with a depth greater than 24.0-in. (61.0 cm), and 1.0 otherwise. Units from expression in parenthesis in Equation 2.17 should be disregarded.

Expression for l_d was adopted mainly as a result of the experimental study of Hanson and Kaar (1959), while the addition of factor κ was adopted after a FHWA memorandum in 1988, based on poor transfer and development length test results at the University of North Carolina (Reutlinger, 1999).

b) ACI 318 (2011).

Equations 2.18 and 2.19 are proposed for l_t and l_d, respectively, in Section 12.9 of the Building Code Requirements for Structural Concrete (ACI 318-11).

$$l_t \geq \frac{f_{se} \cdot d_b}{3,000} \tag{2.18}$$

$$l_d \geq \left(\frac{f_{se}}{3,000} \right) \cdot d_b + \left(\frac{f_{ps} - f_{se}}{1,000} \right) \cdot d_b \tag{2.19}$$

where the stresses f_{se} and f_{ps} are expressed in psi, and the values calculated from expressions in parenthesis should be used as constants without units.

Transfer length expression in Equation 2.18 was established after experimental studies of Hanson and Kaar (1959) and Kaar et al. (1963), and it considered the calculated length in order to provide proper bond performance under an average transfer bond stress of 400 psi.

It should be noted that, when factor κ = 1.0 in Equation 2.17, the equations for development length provided by ACI 318 and AASHTO LRFD coincide.

41

2.4.2 Research estimation of transfer and development length

Equations for transfer and development length in AASHTO and ACI are based on limited test results. Expressions were developed from conditioned Grade 250 prestressing strands, with a maximum strand diameter of ½-in. (12.7 mm), and without the use or consideration of the traditional construction procedures in the prestressed concrete industry (Hanson and Kaar, 1959). Extensive research has been developed in order to propose better estimations of l_t and l_d (Reutlinger, 1999). Some of the equations proposed by previous studies for the estimation of transfer and development length of prestressed concrete elements are described below.

c) Martin and Scott (1976).

Martin and Scott (1976) reevaluated the results from Kaar et al. (1963) and proposed a conservative limit for l_t for strand diameters ranging from ¼-in (6.35 mm) to 0.6-in. (15.24 mm), shown in Equation 2.20. Additionally, a bi-linear relationship (Equation 2.21) was developed by fitting the experimental data of Hanson and Kaar (1959), in order to provide the maximum stress in the strand at ultimate condition, given an embedment length l_x. The use of the ultimate tensile strength of prestressing strand in Equation 2.21 can be used to estimate the development length.

$$l_t = 80 \cdot d_b \tag{2.20}$$

$$
\begin{aligned}
f_{ps} &\leq \left(\frac{135}{d_b^{1/6}} + 31 \right) \frac{l_x}{80 \cdot d_b} && for \ l_x \leq 80 \cdot d_b \\
\\
f_{ps} &\leq \frac{135}{d_b^{1/6}} + \frac{0.39 \cdot l_x}{d_b} && for \ l_x > 80 \cdot d_b
\end{aligned}
\tag{2.21}
$$

where l_x is the embedment length, in inches.

d) Zia and Mostafa (1977).

Estimations of l_t and l_d provided by Zia and Mostafa (1977) are empirical relationships based on a literature survey of bond development testing. The parameters considered in this study were: type of steel (strand or wire), prestress level, nominal diameter of strands, surface condition of strands, compressive strength of concrete, type of loading, type of strand release, and type of confining reinforcement.

Analysis of test data determined that transfer length depends on the initial stress in the strand and the compressive strength of concrete at transfer. As a result of the linear regression analysis of reported results, conservative equations for l_t and l_d were proposed for strands up to ½-in. (12.7 mm). It was suggested that the second term of Equation 2.19 from ACI Code, corresponding to the flexural bond length, should be increased by 25% to properly control bond failure of prestressing strands.

Equations 2.22 and 2.23 account for the effect of strand size, initial prestress level, and concrete strength at transfer; they are applicable for concrete strengths ranging from 2,000 to 8,000 psi (13.8 to 55.2 MPa).

$$l_t = 1.5 \frac{f_{si}}{f'_{ci}} d_b - 4.6 \tag{2.22}$$

$$l_d = \left(1.5 \frac{f_{si}}{f'_{ci}} d_b - 4.6 \right) + 1.25 \left(f_{su} - f_{se} \right) \cdot d_b \tag{2.23}$$

e) Deatherage, Burdette, and Chew (1989).

An experimental study performed on 20 AASHTO Type I girders at the University of Tennessee by Deatherage et al. in 1989 suggested that the use of ACI

43

estimation of the transfer length (Equation 2.19) for ½, ½ special, 9/16, and 0.6-in. diameter Grade 270 prestressing strands should consider the stress in prestressing strand after transfer, f_{si}, instead of the stress in prestressing strand after losses, f_{se} (Equation 2.24). Also, an increase of 50% of the flexural bond length in AASHTO and ACI expression for development length was proposed to avoid bond failure, as shown in Equation 2.25.

$$l_t = \frac{f_{si} \cdot d_b}{3} \tag{2.24}$$

$$l_d = \frac{f_{si} \cdot d_b}{3} + 1.50 \left(f_{su} - f_{se} \right) \cdot d_b \tag{2.25}$$

f) Russell and Burns (1992).

A comprehensive study of the influence of the size and shape of prestressed concrete sections, number of strands, nominal diameter of strands, debonding, confining reinforcement, and strand spacing was developed at the University of Texas, Austin, in 1992 (Russell, 1992; Russell and Burns, 1993). They concluded that bond failure is a result of shear cracking through the transfer region. Thus, the prevention of these cracks will allow the strand to develop its prestressing force and the additional tension required by external loads. Proposed expressions for l_t and l_d consider a criterion to prevent cracking in the transfer region. However, variables analyzed by Russell and Burns did not include the strength of concrete.

Equations 2.26 and 2.27 were suggested for strands fully bonded to the ends of the members, where the following guidelines are met: $M_{cr} > l_t \cdot V_u$ and web shear cracks are prevented to occur in the transfer zone if $V_u > V_{cw}$.

$$l_t = \frac{f_{se} \cdot d_b}{2} \tag{2.26}$$

$$l_d = \frac{M_n}{M_{cr}} l_t \tag{2.27}$$

g) Mitchell, Cook, Khan, and Tham (1993).

Study developed by Mitchell et al. (1993) was focused on the impact of compressive strength of high-strength concrete on the bond performance of prestressing strand. Rectangular prestressed concrete beams were eccentrically prestressed with 3/8, ½, and 0.62-in. diameter strands (Reutlinger, 1999). Compressive strength of concrete varied from 3,000 to 7,310 psi (20.7 to 50.4 MPa) at transfer, and from 4,500 to 12,900 psi (31.0 to 88.9 MPa) at 28 days. Beams were tested under three and four-point bending and two types of failures were identified: flexural failure defined by crushing of concrete in the compressive zone, and bond failure, where a significant strand slip was measured, followed by premature shear or flexural failure. They concluded that the increase of concrete strength at release decreases the transfer length, while the increase of concrete strength at 28 days decreases the flexural bond length. In order to prevent bond failure, Equations 2.28 and 2.29 were proposed for the estimation of l_t and l_d, respectively.

$$l_t = 0.33 \ f_{si} \ d_b \sqrt{\dfrac{3}{f_{ci}'}} \tag{2.28}$$

$$l_d = 0.33 \ f_{si} \ d_b \sqrt{\dfrac{3}{f_{ci}'}} + \left(f_{ps} - f_{se} \right) \cdot d_b \sqrt{\dfrac{4.5}{f_c'}} \tag{2.29}$$

h) Buckner (1995).

In order to consider a broad range of recommendations found in the research, an extensive literature review was conducted by Buckner (1995). The analysis of test results determined that the use of Equation 2.30 was a reasonable estimation of the transfer length for seven-wire, low-relaxation, Grade 250 and 270 strands in normalweight concrete with design compressive strength higher than 3,500 psi (24.1 MPa).

$$l_t = \dfrac{f_{si} \ d_b}{3} \tag{2.30}$$

In the case of development length test results, a great discrepancy of test methods and determination of poor bond performance was found. Buckner (19952) suggested that, instead of considering the strand stress at ultimate for development length estimation, the ultimate strain affects more directly the flexural bond strength between strand and concrete. Thus, Equation 2.31 was proposed.

$$l_d = \dfrac{f_{si} \ d_b}{3} + \lambda \cdot \left(f_{su} - f_{se} \right) \cdot d_b \tag{2.31}$$

where the multiplying factor applied to flexural bond length, λ, is calculated using the strain in prestressing strand at nominal strength: $1.0 \leq \left[\lambda = 0.6 + 40 \cdot \varepsilon_{ps} \right] \leq 2.0$. ε_{ps} is the strain corresponding to f_{su}.

Additionally, Buckner developed Equation 2.32 for the best fit of transfer length results considering an apparent elastic modulus, calculated from previous studies based upon the midspan strains reported right after release.

$$l_t = \frac{1,250 \cdot f_{si} \, d_b}{E_{ci}} \qquad (2.32)$$

i) Lane (1998).

A FHWA study was performed on rectangular prestressed concrete elements, AASHTO Type II beams, and prestressed concrete sub-deck panels in order to evaluate the AASHTO equation for development length (Lane, 1998). Two primary types of failures were identified. A flexural failure due to crushing of concrete in the compression zone, and bond failure, where strand slip exceeded 0.01-in. (0.254 mm) and shear cracking was observed at the ends of the elements.

Analysis of results showed that the most influential parameters were the stress in the prestressing strand prior to transfer, f_{pt}, the nominal diameter of the strand, and the strength of concrete at 28 days.

Suggested expressions, given in Equations 2.33 and 2.34, provided a 95% confidence level for the experimental data.

$$l_t = \frac{4 \cdot f_{pt} \cdot d_b}{f'_{c,28}} - 5 \tag{2.33}$$

$$l_d = \left(\frac{4 \cdot f_{pt} \cdot d_b}{f'_{c,28}} - 5 \right) + \left(\frac{6.4 \cdot \left(f_{ps} - f_{se} \right) \cdot d_b}{f'_{c,28}} + 15 \right) \tag{2.34}$$

j) Meyer (2002).

Meyer (2002) studied the transfer and development length of 0.6-in. (15.24 mm), low-relaxation strands in high-strength lightweight concrete, with concrete strengths of 8,000 and 10,000 psi (55.2 and 68.9 MPa). This study was performed on pretensioned AASHTO Type II girders, and Equations 2.35 and 2.36 were proposed for estimation of l_t and l_d, respectively.

$$l_t = 50 \cdot d_b \sqrt{\frac{6{,}000}{f'_{ci}}} \tag{2.35}$$

$$l_d = \left(50 \sqrt{\frac{5{,}000}{f'_{ci}}} + f_{ps} - f_{se} \right) \cdot d_b \tag{2.36}$$

Additionally, the best fit of experimental results was determined by Equations 2.37 and 2.38.

$$l_t = 50 \cdot d_b \sqrt{\frac{4{,}000}{f'_{ci}}} \tag{2.37}$$

$$l_d = \left(50 \sqrt{\frac{2{,}500}{f'_{ci}}} + f_{ps} - f_{se} \right) \cdot d_b \tag{2.38}$$

k) Ramirez and Russell – NCHRP Report 603 (2008).

The specifications provided by Section 5: "Concrete Structures" of AASHTO LRFD Bridge Design Specifications are mostly developed for concrete compressive strengths between 4.0 and 10.0 ksi (27.6 to 68.9 MPa). In order to broaden the applicability of AASHTO LRFD, Ramirez and Russell (2008) developed expressions for transfer and development length for high-strength, normal weight concretes, with compressive strength up to 15 ksi (103.4 MPa).

Transfer and development lengths were measured on rectangular and I-shaped pretensioned concrete beams. Similar to previous research results, it was observed that the increase of concrete strength decreases the transfer and development length in high-strength concrete.

Equations 2.39 and 2.40 were proposed as modifications of current ACI and AASHTO equations, extending the applicability of the codes to design concrete strength of 14 ksi.

$$l_t = \min\left(\frac{120}{\sqrt{f_{ci}^{'}}} \cdot d_b, \quad 40 \cdot d_b \right) \tag{2.39}$$

$$l_d = \min\left(\left[\frac{120}{\sqrt{f_{ci}^{'}}} + \frac{225}{\sqrt{f_c^{'}}} \right] \cdot d_b, \quad 100 \cdot d_b \right) \tag{2.40}$$

CHAPTER 3

DESIGN AND CONSTRUCTION OF PRESTRESSED PILES

Three 70-ft. long (21.3 m), 16-in. (40.6 cm) square piles were built using duplex HSSS 2205 prestressing strands, while two of the same size piles were built using conventional (AISI 1080) prestressing strands as controls. All piles used the same concrete mix proportions with a design strength of 5,000 psi. These full scale piles were used to determine the driving performance, shear and flexural capacity of piles, transfer length and prestress losses. The design followed GDOT requirements, and the piles were built in the Savannah plant of Standard Concrete Products (Figure 3.1). Additionally, two 27-ft. (8.2 m) long, 16-in. square piles were constructed with each type of strand in order to test the development length, and four 20-in. (50.8 cm) long pile specimens were built using each type of strand for long-term durability assessments. The durability specimens were left underwater in the Savannah River. Periodic evaluations of corrosion of steel and concrete degradation were performed.

Figure 3.1 Standard Concrete Products plant, located in Savannah, GA.

3.1 Design of Prestressed Piles

The piles were designed according to GDOT requirements detailed on GDOT Standard 3215 for prestressed concrete piles. The dimensions of a 16×16-in. (40.6×40.6-cm) square pile cross section and reinforcement layout are shown in Figure 3.2. The conventional prestressing reinforcement is 7-wire low relaxation strands, with a nominal diameter of $^{7}/_{16}$ in. (11.1 mm), and minimum ultimate tensile strength (UTS) of 270 ksi (1,862 MPa). GDOT also requires the use of concrete conforming to Class AAA of the GDOT Standard Specification 500: Concrete Structures and wire spirals for shear reinforcement conforming to ASTM A82 or AASHTO M32.
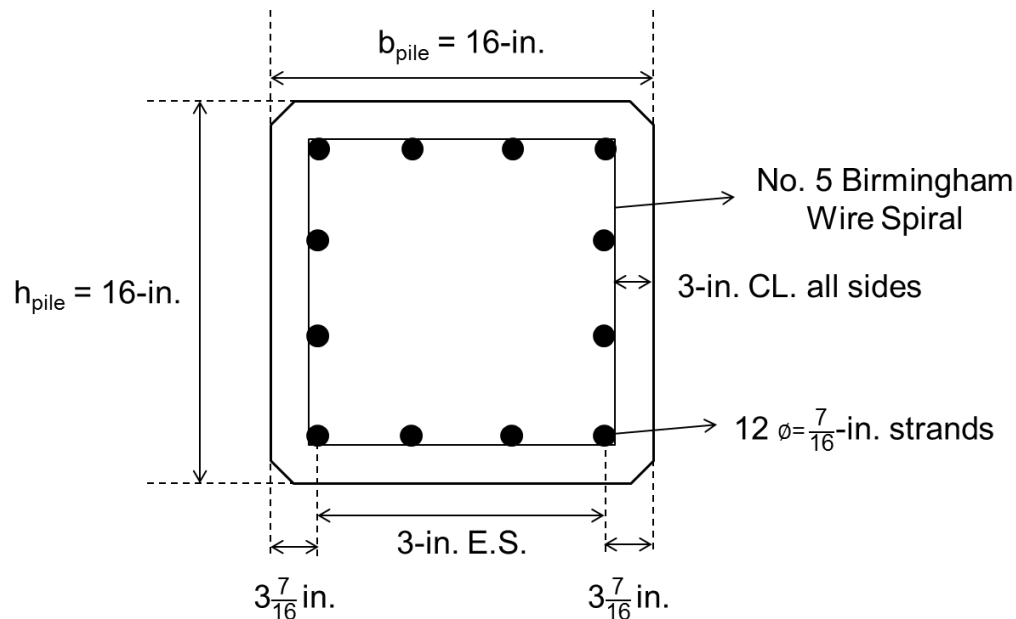
Figure 3.2 Cross section of a Grade 270 strand, 16-in. squared pile (GDOT Spec 3215). 1-in. = 2.54 cm.

In order to calculate the stresses developed at the depth of the strands, the actual dimensions of the transverse cross sections of the piles were measured and are given in Appendix A.

51

The transverse shear reinforcement is No. 5 Birmingham gauge wire (nominal W3.4 standard gauge) with a minimum yield stress of 70 ksi (482.6 MPa) (Figure 3.3). The wire spiral spacing along the pile is shown in Figure 3.3. At the pile ends, the 8 turns with 1-in. (2.54 cm) spacing prevent bursting due to stressing and due to pile driving; spacing is then increased to 16 turns with 3-in. (7.62 cm) spacing followed by 6-in. (15.24 cm) spacing throughout the middle length of each pile.
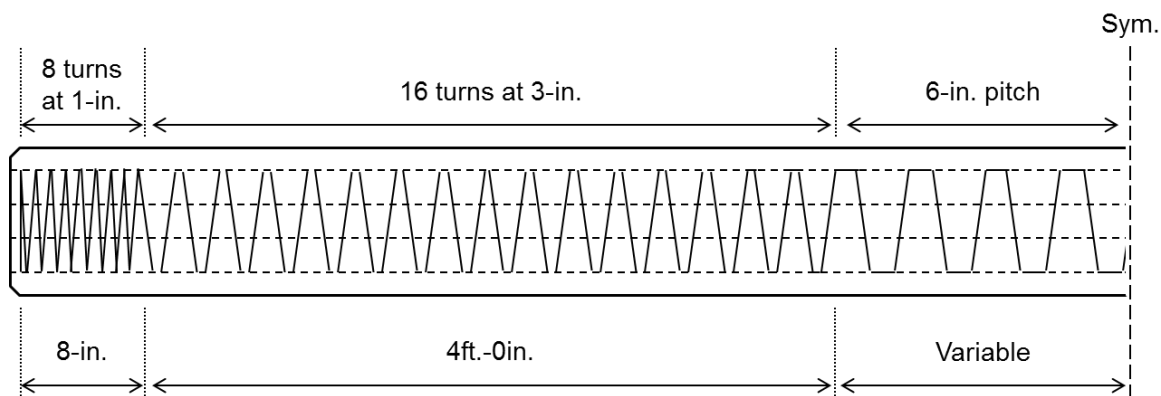
Figure 3.3 Cross section of a Grade 270 strand 16-in. squared pile cross section.
1-in. = 2.54 cm.

For the use of duplex HSSS 2205 strands, a higher area of strands was selected to account for the lower UTS compared to conventional steel as discussed further in Chapter 4. The diameter of these HSSS strands was increased from $7/16$-in. (11.1 mm) to $1/2$-in. (12.7 mm), which represents an increase of 30% of the nominal area of steel. Additionally, to avoid the galvanic corrosion of the spiral wire with the duplex HSSS 2205 strand, the No. 5 Birmingham wire was replaced by austenitic SS 304 wire, with the same diameter and the same spacing distribution shown in Figure 3.3. Austenitic SS 304 wire was selected due to its lower cost and good corrosion resistance, and because duplex HSSS 2205 wire reduced to the 0.226-in. (5.74 mm) diameter was brittle and could not be

52

bent to radii required for the spiral transverse reinforcement. Separate tests indicated no galvanic corrosion between the 304 and 2205 stainless steels.

3.2 Piles Fabrication and Instrumentation

The piles were built using two rigid parallel metallic beds or forms, one for prestressed concrete elements using duplex HSSS 2205 and the other one for AISI 1080 steel specimens. The same construction procedure was used for both types of steel.

The forms were cleaned and sprayed with lubricant to ease the removal of the piles, and metallic spacers were used to divide each element (Figure 3.4). The strands were anchored to one end of the forms (dead end) and jacked from the other one.

Figure 3.4 Prestressing forms and metallic spacers.

The durability specimens were positioned closest to the jacking end, followed by the 27-ft. piles. The 70-ft. piles were positioned closer to the dead end of the forms. The prestressing cables were fixed at the dead end using anchorage chucks, composed by restraining rings to secure the position of the strands (see Figure 3.5).

Figure 3.5 Anchorage chucks at the dead end of the strands.

The strands were individually loaded using a hydraulic jack (see Figure 3.6). An average jacking load of 22.5 kips (100 kN) was applied to each strand, which represents an initial prestressing stress (f_{si}) of 70% and 61% of the UTS for AISI 1080 conventional steel and duplex HSSS 2205 strands (281 [1,937 MPa] and 242 ksi [1,669 MPa]), respectively.

After strand prestressing, the spiral reinforcement was distributed along the specimens (see Figure 3.7). In the piles using stainless steel, plastic ties were used to attach the spiral wire to the strands and to fix the spacing in order to avoid the occurrence of galvanic corrosion.

Figure 3.6 Loading of strands.
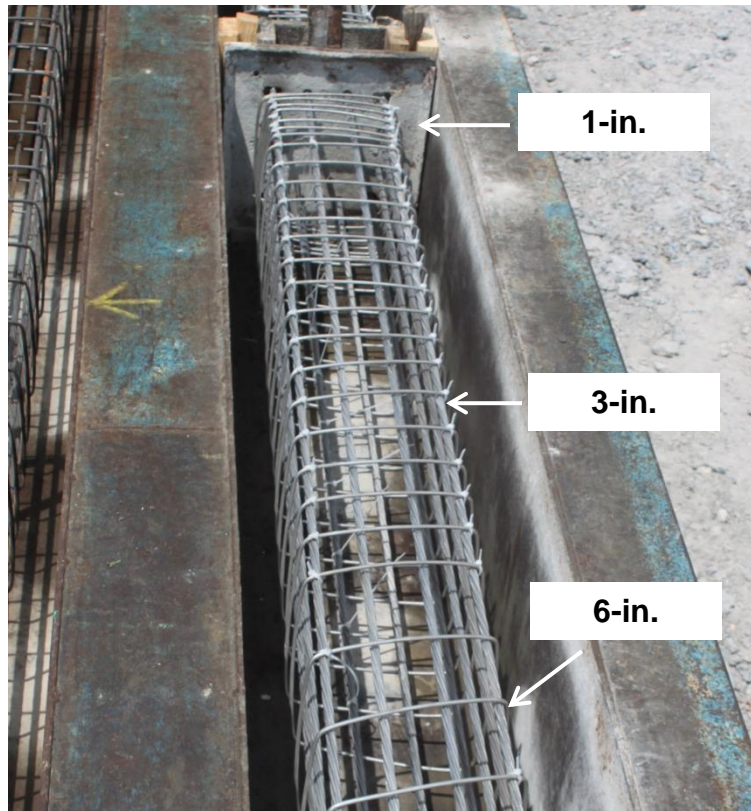
Figure 3.7 Spiral wire distribution. 1 in. = 2.54 cm.

Before concrete placement, four Geokon Model 4200 vibrating wire strain gauges (VWSG) were installed in each 70-ft. pile for the determination of prestress losses. The VWSGs were placed at the mid-height of the piles, at approximately 17.5 ft. (5.3 m) from each end and on both sides of the piles. The sensors in piles using stainless steel were tied to the middle strands using austenitic SS 304 wire pieces and plastic ties (Figure 3.8).

VWSG consists of a tensioned wire connected to end blocks and an electromagnetic coil that excites and helps to obtain the resonant frequency of the wire. Changes on the wire tension by relative movements of the blocks will produce changes on the resonant frequency of the wire that can be translated to strain units by the readout.

VWSGs used in the piles had a gauge length of 6-in. (15.24 cm), a nominal range of 3,000 με, a resolution of 1 με, an operational temperature range from -4 to 176 °F (-20 to 80 °C), and included a thermistor to control the internal temperature of concrete. The thermistor had an operational temperature range from -112 to 302 °F (-80 to 150 °C) and an accuracy of ± 0.9 °F (± 0.5 °C).

Figure 3.8 Vibrating wire strain gauge for prestress losses measurement.

The instrument cables of the VWSGs were run along the length of the prestressing strands to one end of the piles, where the cables were numbered and kept inside embedded terminal boxes for protection of the lead wires (Figure 3.9). Strain measurements were collected using a Geokon GK-404 manual readout. The zero measurement was taken the morning after concrete placement, before the release of the strands (Figure 3.10). The results for prestress losses are presented in Chapter 8.

Figure 3.9 Instrument cables for prestress losses measurement.
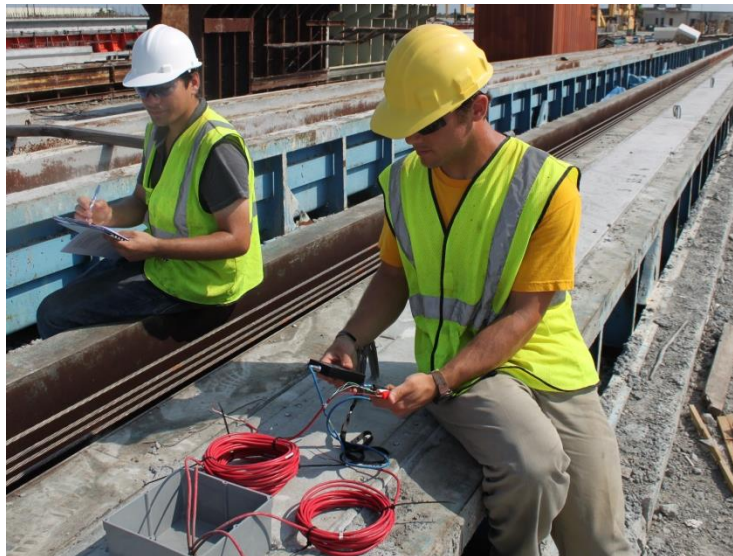
Figure 3.10 Prestress losses measurements.

Concrete was prepared in the plant using nine batches. Cylinder samples (dimensions 4×8-in. [10.2×20.3-cm] and 6×12-in. [15.2×30.5-cm]) were prepared with concrete from the first eight batches. Slump of 8 in. (20.3 cm) and air content of 5% were measured for the first batch which was used to place the material durability samples and the 20-ft long development length piles. The second through ninth batches were used to place the conventionally reinforced and stainless steel reinforced piles in that order.

The concrete was deposited in the forms by the transit truck using a chute, spread with shovels, and compacted with portable internal vibrators, while the surface was finished with manual darbies (Figure 3.11). Then, the concrete surface was covered with plastic sheets for curing. The ambient temperature during placing of concrete was 92 °F (33.3 °C), and the relative humidity was close to 100%.
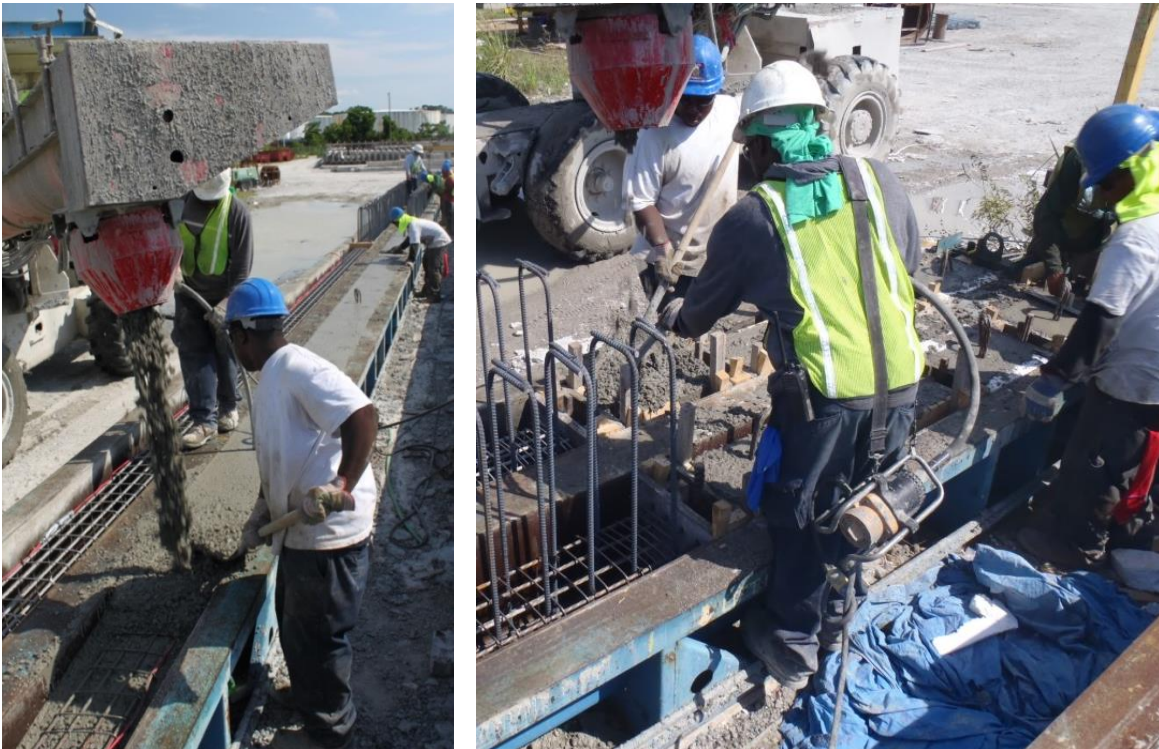
Figure 3.11 Concrete placing and compaction.

The properties of concrete are presented in Chapter 4.

For the determination of the transfer length, the concrete surface strain profile was measured using a detachable mechanical strain gauge (DEMEC gauge). DEMEC points were fixed on the concrete surface at the end of each pile using two embedded metal strips (Figures 3.12 and 3.13). DEMEC points were spaced at 2 in. (5.1 cm); a 10-in. (25.4 cm) gauge length reader with a precision of ±0.0001 in. (±0.00254 mm) was used for each reading.

Figure 3.12 Strips for embedment of DEMEC points for transfer length measurement.

Steel nuts and brass pieces were screwed to the metal strips to create the embedded DEMEC measurement points (Figure 3.13). The surface of the metal strips was sprayed with demolding oil. Transverse wood strips were used to fix the distance

between metal strips and to position the strips at the end of the piles, immediately after the finishing of the concrete surface.

After 15 hours, the metal strips were removed from the piles and the DEMEC points remained for the determination of the transfer length (Figure 3.13). The initial measurement (zero measurement) was taken before the release of the strands. The following measurements were taken after release and then before sunrise on the following days to avoid the influence of temperature changes between measurements. Transfer length results are presented in Chapter 9.
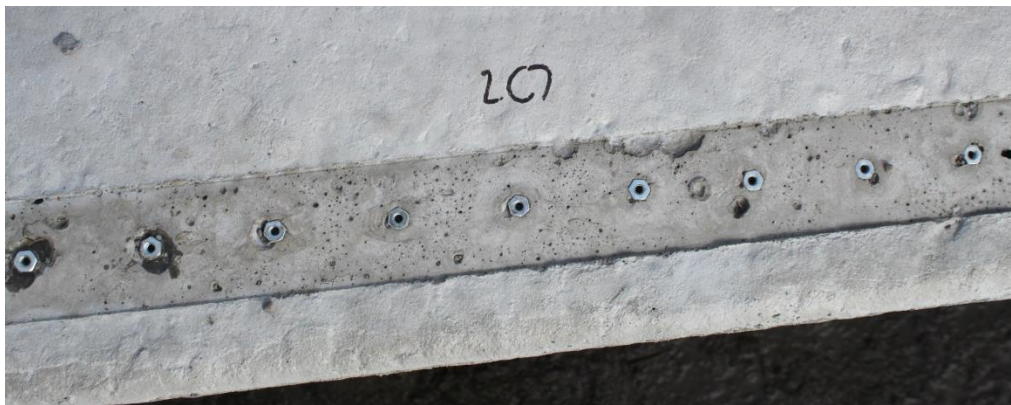
Figure 3.13 DEMEC points in pile concrete surface.

One day after concrete placement, the strands were released by cutting them using a gas torch (Figure 3.14). The required compressive strength of concrete before strand release was 4,000 psi (27.6 MPa), and an average value of 4,018 psi (27.7 MPa) was measured in cast cylinders.

After strand release, the piles and specimens were removed from the prestressing beds to an adjacent position (Figure 3.15).

Figure 3.14 Strand release.

Figure 3.15 Piles removal from the prestressing forms.

3.3 Composite Beam Construction

Two 27-ft. (8.23 m) piles per type of steel were built in order to evaluate the development length (l_d) of the strands. The l_d is the required length from the end of the pile over which the strand and concrete should be effectively bonded in order to develop the nominal strength of the prestressing steel.

An additional 27-in. (68.6 cm) top section was added to the piles to assure a strain in the prestressing strand greater than 2% to test the l_d. To provide an appropriate bond between the pile and the top section, the surface of the pile was roughed, and #5 bar stirrup reinforcement, spaced 6-in. along the pile, was embedded during pile construction (see Figure 3.16).

Figure 3.16 27-ft. (8.23 m) piles for development length evaluation.

These short piles were transported to the Georgia Tech Structures and Materials Lab, where the top section was placed. Details regarding the construction of the development length specimens are presented in Appendix B.

Concrete of the top section of the beams was ready-mixed concrete with design strength of 6,000 psi (41.4 MPa) at 28 days. Water addition was required to reach proper workability. Concrete was placed on different dates for piles containing stainless and conventional steel strands. Companion 4×8-in. (10.2×20.3 cm) cylinder samples were prepared and fogroom cured until compressive strength testing.

The compressive strengths of the top concrete sections are shown in Figure 3.17, where the final point in each curve corresponds to the strength of concrete at the time of flexural testing of beams for development length determination. Variable addition of water before placing can explain differences in compressive strength.

The results of development length testing are presented in Chapter 10, and the final condition of 27-ft. (8.23 m) piles after the addition of the top section is shown in Figure 3.18.
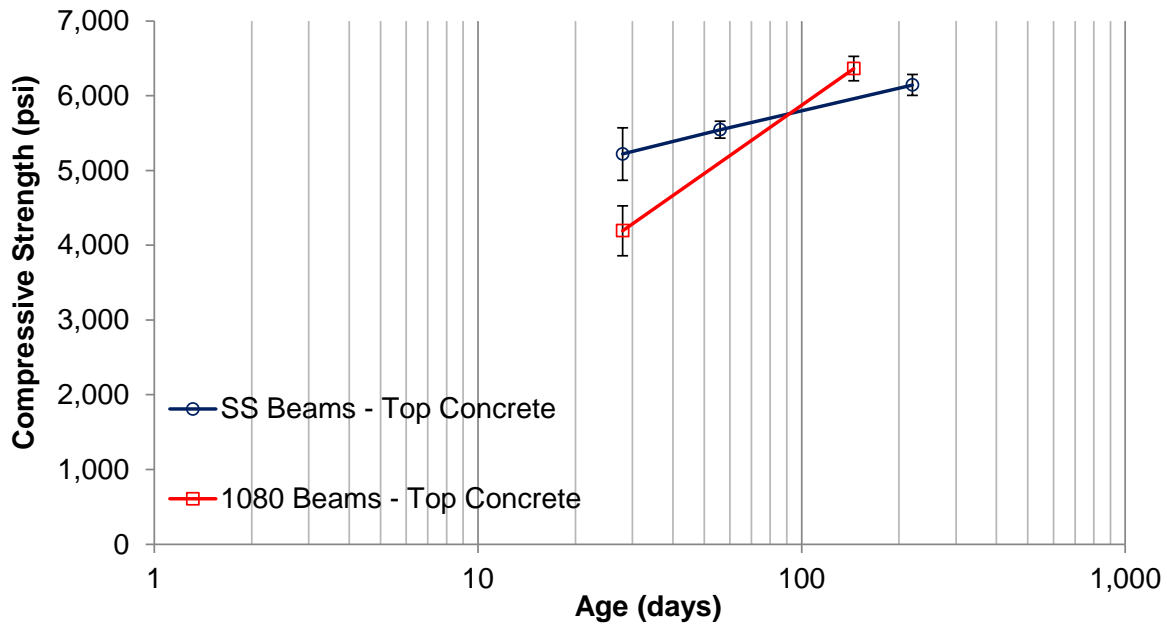
Figure 3.17 Compressive strength of concrete used in top section of beams.
1,000 psi = 6.9 MPa.

Figure 3.18 Development length testing specimen.

CHAPTER 4

MATERIAL PROPERTIES

The material property test results of concrete compressive strength, elastic modulus, splitting tensile strength, creep, and rapid chloride permeability, and of the steel reinforcement, duplex HSSS 2205, SS 304, and AISI 1080, are presented in this chapter.

4.1 Steel Properties

Moser et al. (2012) studied the corrosion resistance of AISI 1080 steel, duplex HSSS 2205, and austenitic SS 304, while Schuetz (2013) investigated the mechanical behavior of AISI 1080 and duplex HSSS 2205 strands. A summary of those findings is presented in this chapter.

Additionally, the mechanical properties of SS 304 wire and the galvanic corrosion evaluation between duplex HSSS 2205 strands and SS 304 wire are included.

4.1.1 Duplex high-strength stainless steel 2205

Duplex HSSS 2205 (ASTM A276 grade UNS S31803), ½ in. (12.7 mm) diameter 7-wire prestressing strands were produced at Sumiden Wire Products Corporation in Dickson, TN, using the same equipment and production techniques used for conventional AISI 1080, low relaxation prestressing strands (see Figure 4.1). More information about the production process of SS strands can be found in Chapter 7 of Moser et al. (2012).

Figure 4.1 Duplex HSSS 2205 strand and austenitic SS 304 wire samples.

The mechanical properties of the strands tested by Schuetz (2013) are given in Table 4.1 and in Figure 4.2. Duplex HSSS 2205 strands have a lower ultimate tensile strength (UTS), elastic modulus, and yield stress compared to conventional strands. To account for lower mechanical properties, the area of the strand was increased about 30% in the case of duplex HSSS 2205 (diameter of $^1/_2$-in. [12.7 mm] instead of the commonly used $^7/_{16}$-in. [11.1 mm]). Also, the ultimate strain of HSSS 2205 is only 27% of the value for conventional AISI 1080 steel, which indicates a lower ductility of duplex HSSS 2205 strands (Figure 4.2).

Table 4.1 Mechanical properties of duplex HSSS 2205 and conventional steel strands. 1 ksi = 6.9 MPa.

	Duplex HSSS 2205		AISI 1080 Steel	
	Average	Std Dev	**Average**	Std Dev
UTS (ksi)	**241.5**	1.6	**281.8**	2.0
Ultimate strain (in/in)	**1.60%**	0.07%	**5.89%**	0.59%
Elastic modulus (ksi)	**23,500**	190	**29,400**	130
Yield Stress (ksi, 0.2% offset criterion)	**228.7**	2.4	**254.7**	0.6
Stress-relaxation 70% UTS – 1,000 h	**2.49%**	0.24%	**2.40%**	---------

Schuetz (2013) observed a stress relaxation loss of 2.49% when testing duplex HSSS 2205 strands following standard ASTM E328 (1,000 hours of test duration, temperature controlled room, at 70% UTS), while Moser et al. (2012) estimated a stress loss of 2.40% in AISI 1080 wires from 200 hours results. The limit for low relaxation prestressing strand according to ASTM A416 is 2.5% for 1,000 h tests with strands loaded at 70% of UTS.
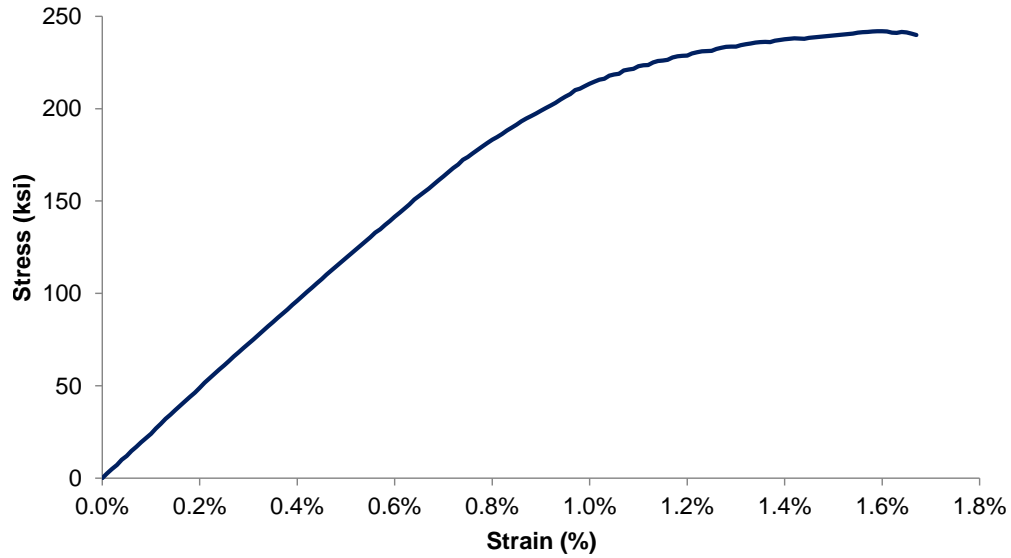
Figure 4.2 Stress-strain curve of duplex HSSS 2205 strand. 1 ksi = 6.9 MPa.

Moser et al. (2012) analyzed the corrosion behavior of the steels included in this report. Using electrochemical cyclic potentiodynamic polarization techniques in simulated concrete alkaline and carbonated environments contaminated by chloride ions, they found the results given in Table 4.2, where the higher corrosion resistance of duplex 2205 is evidenced.

Table 4.2 Corrosion behavior of different steel alloys (modified from Moser et al. (2012)).

	Alkaline (pH = 12.5)				**Carbonated** (pH = 9.5)			
Cl^- content (M)	0.00	0.25	0.50	1.00	0.00	0.25	0.50	1.00
Duplex 2205	NC	NC	NC	NC	NC	NC	NC	NC
Austenitic 304	NC	NC	MP	SP	NC	MP	SP	SP
AISI 1080	NC	SP	SP	SP	MP	SP	SP	SP

Note: **NC**: no corrosion initiated - **MP**: metastable pitting - **SP**: stable pitting

4.1.2 Austenitic stainless steel 304

Austenitic SS 304 wire (ASTM A276 grade UNS 30400), with a diameter of 0.226-in. (5.74 mm), was selected for the transverse confinement and shear spiral reinforcement of piles using duplex HSSS 2205 strands. Higher CTL and lower time to corrosion initiation were observed in wires compared with prestressing strands, due to the presence of crevices and surface imperfections that provide initiation sites for corrosion.

One of the main concerns in order to test the suitability of the wire is the potential formation of a galvanic couple when in contact with the strands. Two dissimilar metals electronically connected in a conductive environment can undergo galvanic corrosion. In this case, the anodic member of the couple will present local accelerated corrosion, while the other metal will be cathodically protected. This reaction is not necessarily related with the difference in standard half-cell potential from the electromotive force (emf) Series, and its occurrence and kinetics depend on the composition of every member of the galvanic couple, the exposed area of the cathode and the anode, and the environmental conditions (e.g., temperature, pH) under which both metals are in contact (Zhang, 2011).

To evaluate the occurrence of galvanic corrosion, samples of HSSS 2205 strand and SS 304 spiral wire were tested following the standard ASTM G71. The description and results of the test are detailed in Appendix C. In summary, in a seawater solution, the current measured between both metals did not indicate the formation of a galvanic couple. Thus, the combined use of both types of stainless steels will not compromise the durability of the prestressed concrete piles due to localized accelerated galvanic corrosion.

The tensile capacity of the wires was tested in an electromechanical universal testing machine. Three samples obtained from the spiral wire reinforcement, with gauge lengths of approximately 4.3-in. (10.9 cm), were tested individually under direct tension. A typical stress-strain curve of the SS 304 wire is shown in Figure 4.3, and a summary of the results of the tensile strength test is given in Table 4.3.
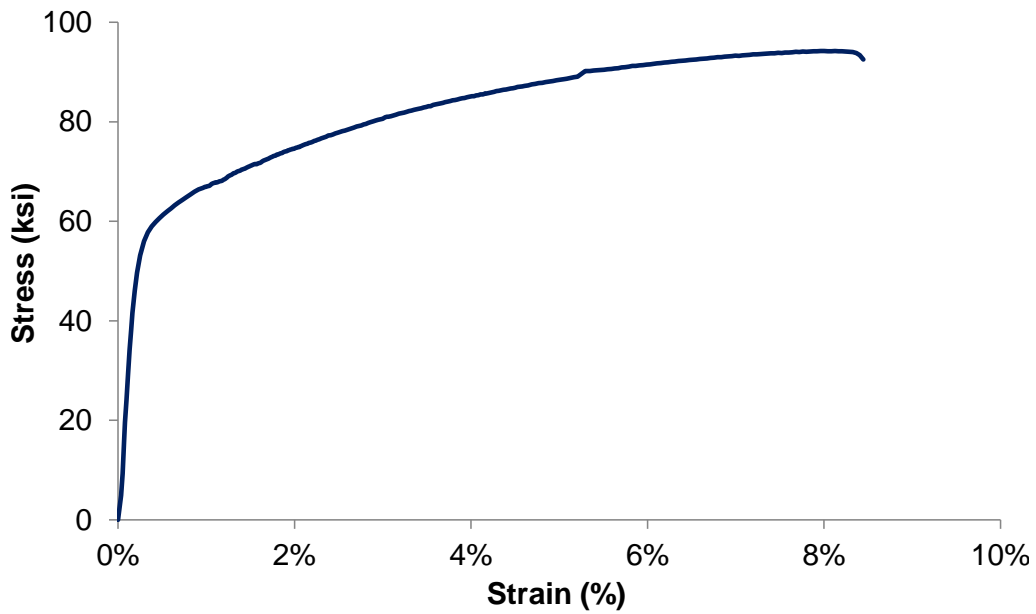
Figure 4.3 Stress-strain curve for austenitic SS 304 wire. 1 ksi = 6.9 MPa.

Table 4.3 Mechanical properties of austenitic SS 304 wire. 1 ksi = 6.9 MPa.

	Average	**Std Dev**
UTS (ksi)	**91.8**	3.5
Yield stress (ksi, 0.2% offset)	**61.9**	---------
Ultimate strain (in/in)	**7.8%**	0.2%
Elastic modulus (ksi)	**26,182**	394

For the determination of the yield point, a 2-in. (5.1 cm) SATEC extensometer was attached to the wire during the test and removed when an 80% of the UTS was reached. The calculation of the yield point according to the 0.2% offset and the 1% strain criteria is shown in Figure 4.4. For calculation of the shear capacity of the piles, the lower yield stress value was used in order to perform a conservative evaluation.

The chart shows a stress-strain curve with two yield criteria marked:
- 0.2% Offset Yield Criterion: $\sigma_Y = 61.9$ ksi, $\varepsilon_Y = 0.3\%$
- 1% Yield Criterion: $\sigma_Y = 69.0$ ksi, $\varepsilon_Y = 1.0\%$

X-axis: Strain (in/in), Y-axis: Stress (ksi)
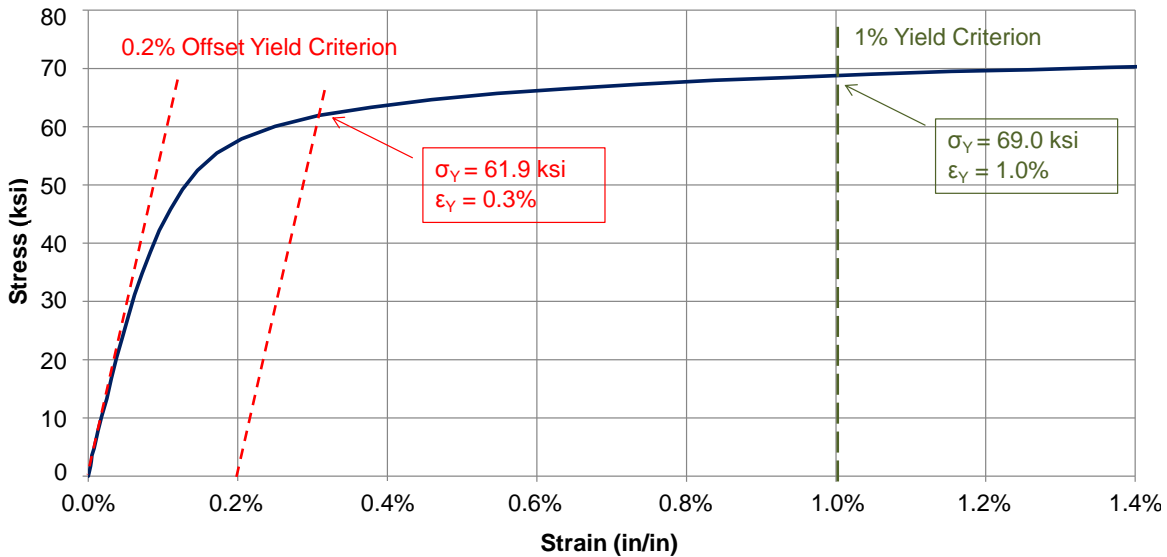
Figure 4.4 Yield point calculation for austenitic SS 304 wire. 1 ksi = 6.9 MPa.

4.2 Concrete Properties

Concrete was prepared in the plant, using nine consecutive batches to fill the forms. Cylinders of two different sizes (dimensions 4×8-in. [10.2×20.3 cm] and 6×12-in. [15.2×30.5 cm]) were prepared using the first eight batches of concrete in order to determine the mechanical properties, the chloride permeability and to assess the variability within the piles. Samples from the ninth batch accidentally were not taken. The excellent consistency in batches four through eight indicates that batch nine would be similar. Batch one was a little weaker than the others for reasons unknown.

4.2.1 Concrete mixture composition

GDOT Class AAA HPC mixture was used in the piles to assure a chloride ion permeability less than 2000 coulombs. The specified design compressive strength at 28 days (f_c') was 5,000 psi (34.5 MPa). The mixture proportions are given in Table 4.4.

A 14.8% mass substitution of cement by ASTM C618 Class F fly ash was used (replacement of 19.5% by volume). The water-to-cementitious material ratio (w/cm) was 0.23 and a coarse aggregate size #67 was used (maximum size of aggregate, MSA = ¾" [19.1 mm]). The aggregate volumetric fraction corresponded to 71.4%, and the design air content was 4.0%. The measured slump for the first batch was 8 inches (20.3 cm).

Table 4.4 Mixture design of concrete.

	Specific Gravity	**Mix Design (lbs/yd^3)**	**Mix Design (kg/m^3)**
Type I Cement	3.14	687	408
Water	1.00	188	112
Class F Fly Ash	2.26	119	71
Coarse Aggregate	2.65	1,870	1,109
Fine Aggregate	2.62	1,305	774
Design air content:	4.0%		
Retarder (Goulston Chupol N20):	2.36 fl. oz./cwt		479.5 ml
HRWR (Goulston Chupol N60):	6.45 fl. oz./cwt		1,310.5 ml
AEA (Goulston Chupol FA-10):	0.46 fl. oz./cwt		93.5 ml

The chemical composition of the cement (ASTM C150 Type I/II cement) is given in Table 4.5. The composition was obtained by quantitative X-ray diffraction (QXRD) refinement.

Table 4.5 QXRD analysis of cement type I/II used.

C_3S	C_2S	C_3A	C_4AF	Free CaO	Free MgO	Quartz	K_2SO_4
62.5%	16.1%	3.8%	11.1%	0.2%	0.2%	0.1%	0.2%

Gypsum	Hemihydrate	Anhydrate	$CaCO_3$	$Ca(OH)_2$
1.3%	0.6%	0.2%	1.1%	2.7%

4.2.2 Variability of concrete

Different batches of concrete were used for each pile and durability specimens. Considering that differences in concrete composition can produce differences during pile testing, Table 4.6 shows the variability of concrete strength measured at 28 and at 438 days. Chloride ion permeability results are discussed in Section 4.2.7.

Table 4.6 Variability of concrete strength of prestressed concrete elements at 28 and 438 days (time of flexure and shear testing). 1,000 psi = 6.9 MPa.

Prestressed Concrete Elements	Compressive Strength (psi)	Std Dev (psi)	Number of Cylinders
28 Days			
Durability Specimens	6,475	101	2
Pile 1080 #1	8,795	---------	1
Pile 1080 #2	6,761	500	3
Pile HSSS 2205 #1	7,801	500	2
Pile HSSS 2205 #2	7,905	398	3
Pile HSSS 2205 #3	8,139	33	2
438 Days			
Durability Specimens	8,819	94	2
Pile 1080 #1	12,064	318	5
Pile 1080 #2	9,678	814	5
Pile HSSS 2205 #1	10,611	328	6
Pile HSSS 2205 #2	10,686	292	9
Pile HSSS 2205 #3	10,931	179	5

The statistical similarity of piles and specimens was analyzed using the results of concrete strength at 438 days, given that they are a better representation of the long-term strength of concrete and that a larger number of cylinders were used for their determination (see Table 4.6).

Table 4.7 shows the results of the statistical analysis performed for the results summarized in Table 4.6. The hypotheses of similarity of means (H_0) for the whole set of cylinders and for concrete cylinders of piles using conventional steel are rejected for an α = 5% significance level. In the case of concrete cylinders representing the strength of piles using duplex HSSS 2205, there is no evidence to reject H_0. The p-value, the conditional probability of rejecting H_0 given that H_0 is true, is also included for every statistical hypothesis test; μ_i is the mean of the sampling distribution for each selected subset i.

Table 4.7 Statistical analysis of compressive strength results at 438 days.

Test	Decision (α = 5%)	p-value
H_0: $\mu_i = \mu$	Reject H_0	2.41×10^{-8}
H_0: $\mu_{2205\text{-}1} = \mu_{2205\text{-}2}$	Fail to Reject H_0	65.19%
H_0: $\mu_{2205} = \mu$	Fail to Reject H_0	17.63%
H_0: $\mu_{1080} = \mu$	Reject H_0	0.02%

Even when piles using duplex HSSS 2205 were built with different batches of concrete, their long-term strength can be considered statistically similar. In the case of piles using conventional steel, strength of concrete in pile 1080 #1 is higher than concrete in pile 1080 #2.

4.2.3 Strength of concrete

Strength of concrete was tested using 4×8-in. (10.2×20.3 cm) cylinders at 4, 7, 28, and 91 days from casting, following standard ASTM C39. Two cylinders were tested at the plant just before release to assure adequate release strength. This "one-day" strength was not included in Figure 4.5 because it is not representative of all the concrete piles. The strength was also tested at 243 days during the flexure test for development length evaluation, and at 438 days during the flexural and shear capacity testing. The results of strength vs. time are shown in Figure 4.5. Individual results per cylinder at every age of testing are included in Appendix D. The error bars indicate ± one standard deviation.
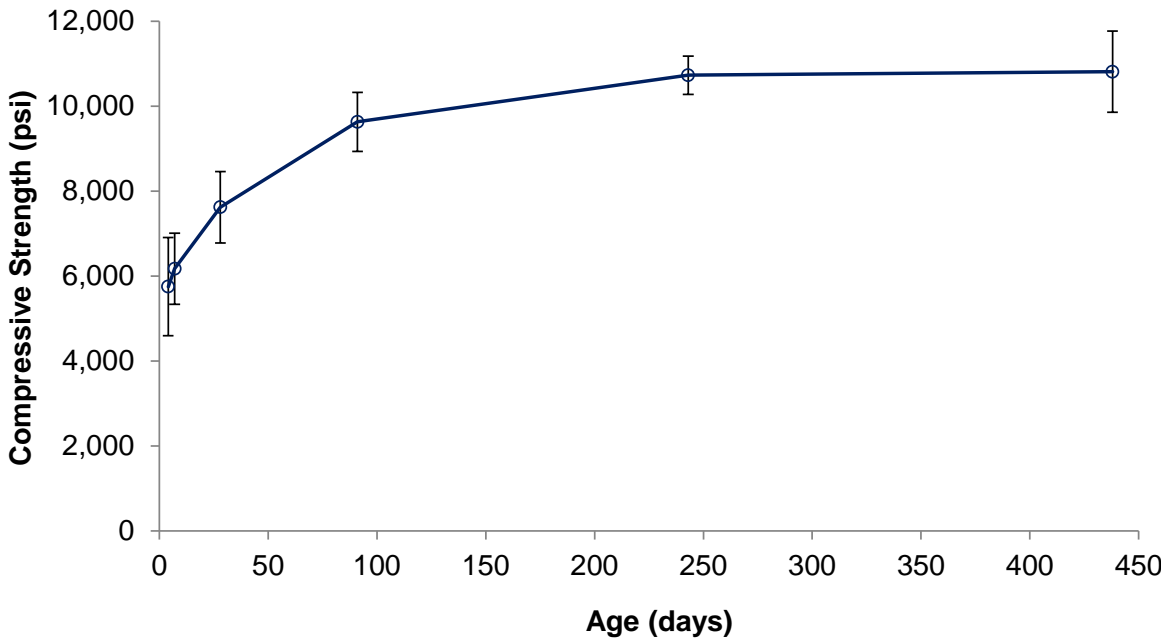
Figure 4.5 Compressive strength of concrete at 4, 7, 28, 91, 243, and 438 days from casting. 1,000 psi = 6.9 MPa. Vertical bars indicate ± one standard deviation.

GDOT requires a minimum compressive strength of 5,000 psi (34.5 MPa) at 28 days for the concrete piles. The measured average strength at 28 days was 7,619 psi (52.5

MPa), and the average strength for every pile or specimen was also higher than the requirement (see Table 4.6). Also, the strength of concrete was tested before strand release in the plant at 1 day from casting, and an average value of 4,018 psi (27.7 MPa) was measured (result not included in Figure 4.5). A minimum compressive strength of concrete of 4,000 psi (27.6 MPa) is required to release the strands. The relationship of strength-time of concrete can be represented by Equation 4.1 (*t* in days, R^2=98.4%).

$$f_c' = 1,174 \cdot 3 \cdot \ln(t) + 3,999 \qquad 1 \le t \le 438 \tag{4.1}$$

ACI 363R: Report on High Strength Concrete (2010) defines the term *high-strength concrete* as "concrete that has a specified compressive strength for design of 8000 psi (55.2 MPa) or greater". Even considering that the report recognizes that there is no definitive limit that determines a dramatic change on the mechanical properties of concrete and that the design strength is commonly considered at 28 days of age (in this case, lower than 8,000 psi [55.2 MPa]), the equations of reports ACI 363R and ACI 318 to predict the elastic modulus and splitting tensile strength are compared with the results obtained experimentally.

4.2.4 Stress-strain behavior of concrete

The modulus of elasticity and Poisson's modulus were obtained according to standard ASTM C469 at 4, 28, 91, and 445 days. Cylinders of dimensions 6×12-in. (15.2×30.5 cm) were selected from different batches. Three cylinders were tested at every age, and the deformations until 40% of the ultimate load were used for the calculation of

76

the elastic modulus. Individual results and individual stress-strain curves up to

approximately 60% of the maximum load are given in Appendix D. A summary of the

results is shown in Table 4.8, where they are compared with estimations suggested by

ACI reports 318 and 363R, and AASHTO LRFD.

Table 4.8 Elastic modulus and Poisson's ratio of concrete at 4, 28, 91, and 445 days.
1 ksi = 6.9 MPa.

Age (days)	Elastic Modulus (ksi) Average (Std Dev)	Poisson's Ratio Average (Std Dev)	Exp. Estimation (Eq. 4.5, ksi)	Estimation ACI-318 (Eq. 4.3, ksi)	Estimation ACI-363R (Eq. 4.2, ksi)	Estimation AASHTO (Eq. 4.4, ksi)
4	**6,138** (354)	**0.17** (0.01)	6,195	4,322	5,007	4,460
28	**6,683** (677)	**0.20** (0.02)	6,607	4,976	5,445	5,134
91	**6,892** (423)	**0.22** (0.02)	6,857	5,594	5,859	5,772
445	**7,138** (448)	**0.17** (0.01)	7,193	5,927	6,082	6,115

The ACI 363R proposed estimation of the elastic modulus for ASTM moist-cured

cylinders is shown in Equation 4.2 (compressive strength in psi).

$$E_c = 38,200 \cdot \left(f_c' \right)^{0.50} + 2,110,000 \qquad (4.2)$$

Equation 4.2 is an empirical relationship developed by Myers and Carrasquillo

(1998) that considers the use of fly ash in high-performance mixtures.

ACI 318 (2011) proposes an estimated elastic modulus of normal weight concrete,

shown in Equation 4.3 (compressive strength in psi).

$$E_c = 57,000 \sqrt{f_c'} \qquad (4.3)$$

Alternatively, AASHTO LRFD estimates the elastic modulus of concrete using the compressive strength of concrete f_c', in ksi, and the unit weight of concrete w_c, in kcf (Equation 4.4).

$$E_c = 33,000 \cdot w_c^{1.5} \cdot \sqrt{f_c'} \qquad (4.4)$$

Experimental results are given in Table 4.8. The relationship, elastic modulus-age of concrete, can be represented by Equation 4.5 (t in days, R^2=97.6%).

$$E_c = 211.9 \cdot \ln(t) + 5,900.8 \qquad 1 \le t \le 438 \qquad (4.5)$$

Table 4.8 shows that Equation 4.2 is a better estimation than the equation obtained from ACI 318 (Equation 4.3), but both equations fail to estimate the experimental value at every age of testing. AASHTO LRFD estimation (Equation 4.4) is also highly inaccurate compared to experimental results, although it is a better estimation than the ACI 318 equation. Estimations from the codes are compared with estimated values using the expression derived from experimental results (Equation 4.5).

4.2.5 Splitting tensile strength

The tensile strength of concrete was indirectly measured using the splitting tensile strength test described in ASTM C496. A summary of results is shown in Table 4.9. At every age, three 4×8-in. cylinders were tested and the development of a crack in the direction of the application of the load was checked in order to calculate the splitting tensile strength according to the standard.

Results obtained from this method are generally higher than the ones obtained
from direct tensile strength and lower than the modulus of rupture.

Table 4.9 Splitting tensile strength of concrete at 7, 28, and 445 days.
1,000 psi = 6.9 MPa.

Age (days)	Splitting Tensile Strength (f_{sp}, psi)			$\dfrac{f_{sp}}{f'_c}$	Estimation ACI-318 (psi)	Estimation ACI-363R (psi)
	Average	Std Dev				
7	**670**	41	$8.5\sqrt{f'_c}$	10.9%	526	581
28	**697**	20	$8.0\sqrt{f'_c}$	9.2%	585	646
445	**797**	48	$7.7\sqrt{f'_c}$	7.4%	697	769

Similar to the estimation of the elastic modulus, the equation from ACI 363R
($7.4\sqrt{f'_c}$) is closer to the experimental value than the estimation of ACI 318 ($6.7\sqrt{f'_c}$) at
every age. At 28 days, the splitting tensile strength of the pile concrete had a mean of 8.0
$\sqrt{f'_c}$. Also, it is observed that the ratio between splitting tensile strength and compressive
strength decreases with time. This behavior is related to the reduced extensibility and the
higher cracking potential of high-strength concrete. The rate of tensile strength evolution
over time is lower compared to compressive strength. At a given strain, stresses in
concrete will be proportional to the elastic modulus, considerably higher than the
predictions as seen in Table 4.8. The combination of these two factors produces a
concrete more prone to cracking.

4.2.6 Creep of concrete

Creep testing was performed according to ASTM C512, beginning at 28 days from casting. Three 6×12-in. cylinders, cured in fogroom until testing and obtained from different batches, were placed in the creep loading frame, while two additional cylinders were kept in the same temperature and humidity controlled room during the duration of the tests to evaluate drying shrinkage. The cylinder ends were ground smooth with a water grinder (Figure 4.6).
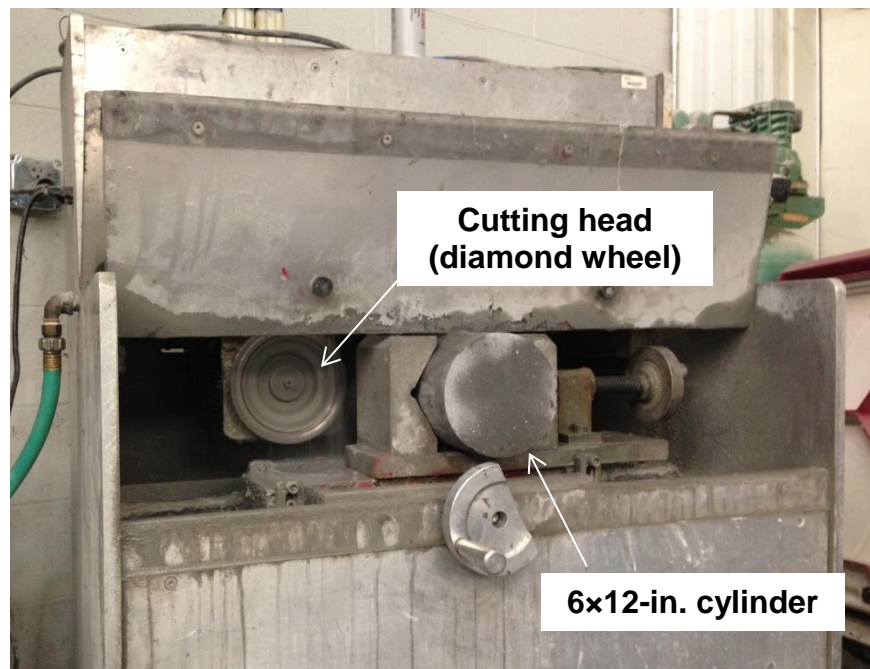
Figure 4.6 Cylinder end grinding machine.

DEMEC points were epoxied to the cylinders for creep and shrinkage evaluation at two opposite sides of the cylinders. The measurements were made by the same person, using the same DEMEC gauge equipment to minimize the variability of the test. The test

was performed inside a conditioned room, where the temperature and relative humidity were kept at constant values of 73 ± 1 °F (23 ± 0.6 °C) and $50 \pm 2\%$, respectively.

The test setup is shown in Figure 4.7. The load was applied using a hydraulic jack and controlled by a load cell. The top loading plate was fixed to the loading bars of the frame, while the bottom loading plate was allowed to move upwards. At 28 days from casting, the cylinders were loaded to 40% of their ultimate strength. Before every measurement, the applied load was adjusted to account for pressure losses. Losses not higher than 10 lbf (44 N) were observed during the testing period. The nuts fixing the position of the bottom loading plate were also adjusted before every measurement.

After 52 days from the start of the test, several cracks appeared at the top and bottom cylinders and dummy samples. The cracks extended to the mid-height of the cylinders after one day. The test was terminated.
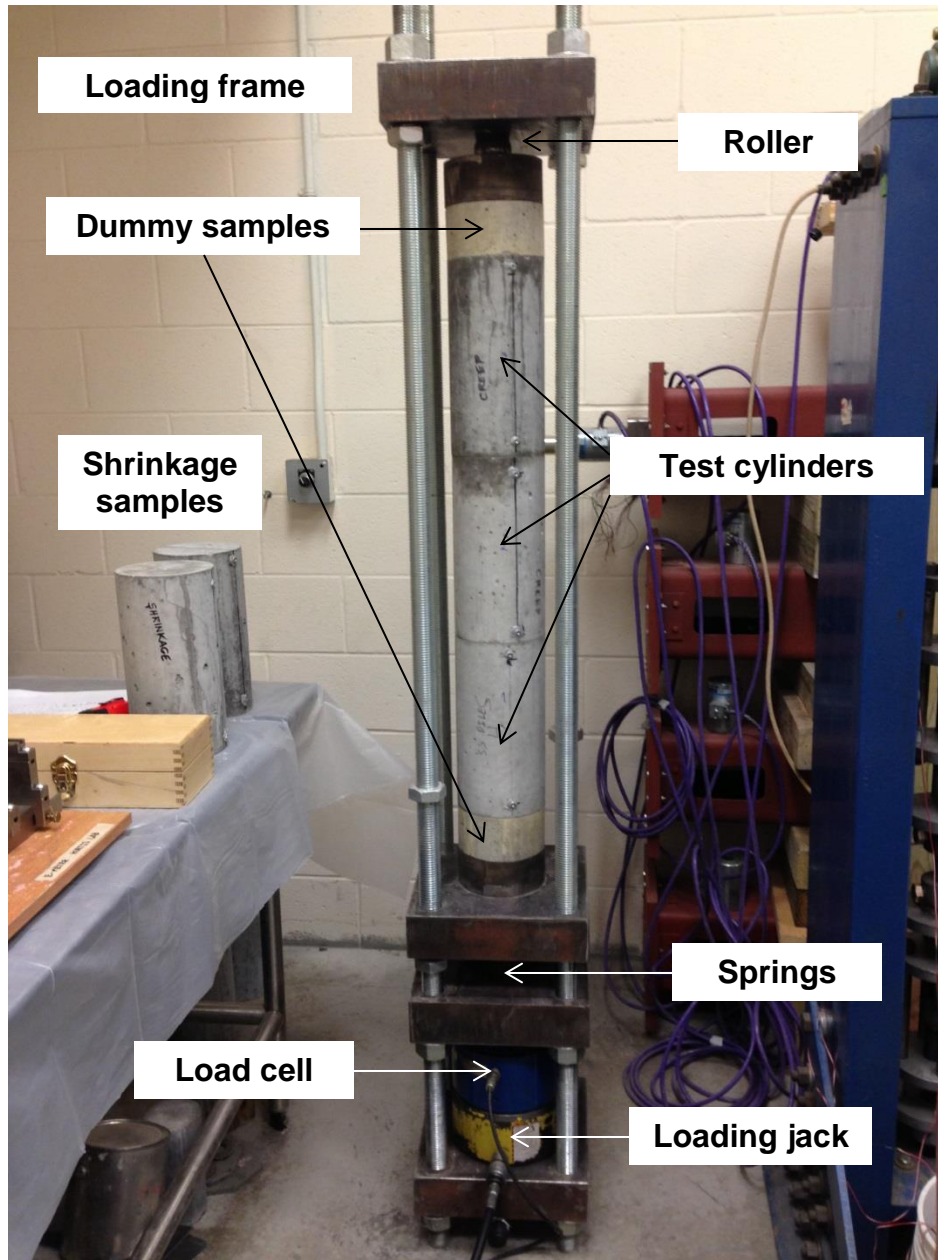
Figure 4.7 Creep test set up (ASTM C512).

The results of the creep test, including the deformations due to shrinkage, during the first 1,247 hours are shown in Figure 4.8. A logarithmic correlation of the results is shown in Equation 4.6 (t in hours, R^2=97.7%).

$$\varepsilon_{c,sh} = 59.68 \cdot \ln(t) + 116.78 \qquad 1 \leq t \leq 438 \tag{4.6}$$
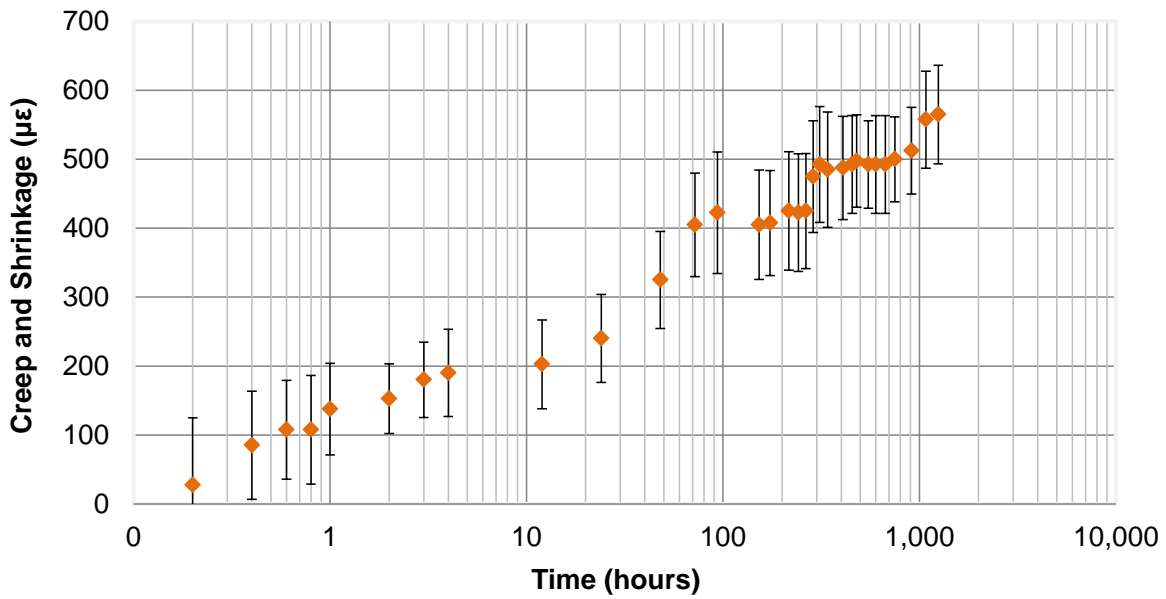
Figure 4.8 Creep and shrinkage measurements during the first 1,247 hours.

Using the measurements on the cylinder samples for shrinkage evaluation, the deformation due to creep was isolated from results shown in Figure 4.8. Creep deformations increased logarithmically for around 100 hours, and remained at an approximately constant value for later ages. The average creep strain after 100 hours was 341.7 με (Figure 4.9).
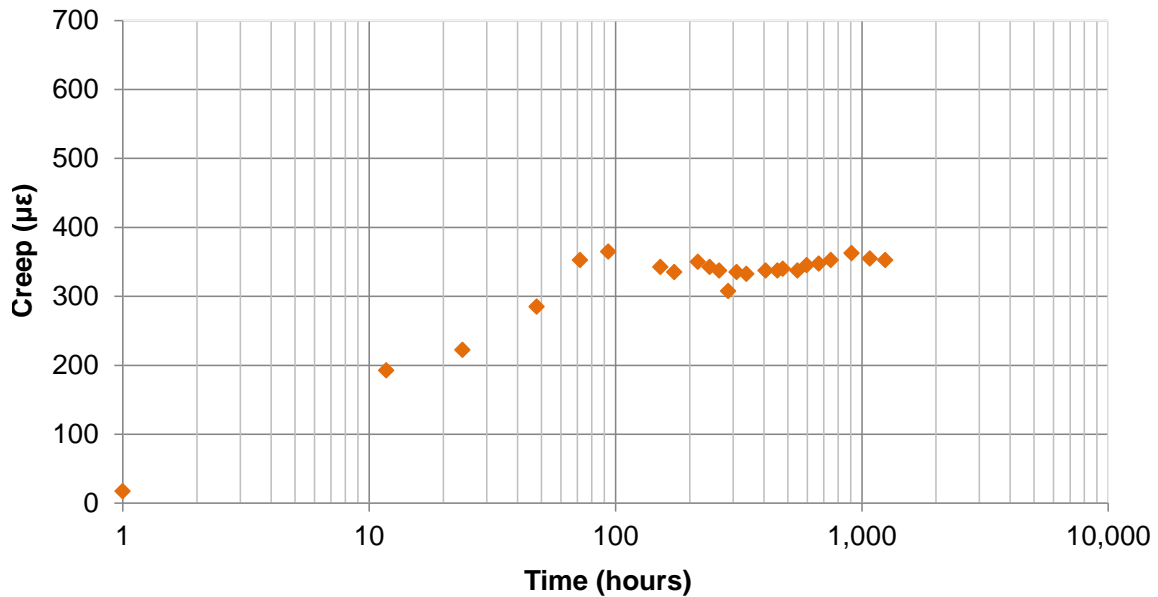
Figure 4.9 Creep calculation during the first 1,247 hours.

In order to compare the results with previous creep testing of high-strength and high-performance concrete (Kahn et al., 2005), the specific creep (strain relative to applied stress) and the creep coefficient (ratio of creep strain to initial elastic strain) were calculated. The previous 2005 study used a higher cementitious content (cement plus silica fume plus fly ash) than the concrete used for the piles. The concrete compressive strengths in the previous study ranged from 14.14 ksi (97.5 MPa) to 16.38 ksi (112.9 MPa) at 28 days; and the specimens were loaded when the concrete was 28 days old. Those specimens had creep coefficients of 0.752 and 0.690 measured at 376 days, respectively; the specific creep values were of 0.197 µε/psi (28.57 µε/MPa) for both strengths, and the values were measured at 376 days.

Calculated specific creep for the pile specimen concrete is shown in Figure 4.10. The regression for these results is given in Equation 4.6 (*t* in days, R^2=97.7%), which predicts a specific creep of 0.217 µε/psi (31.47 µε/MPa) at 376 days.

$$\varepsilon' = 0.0196 \cdot \ln(t) + 0.1005 \tag{4.6}$$
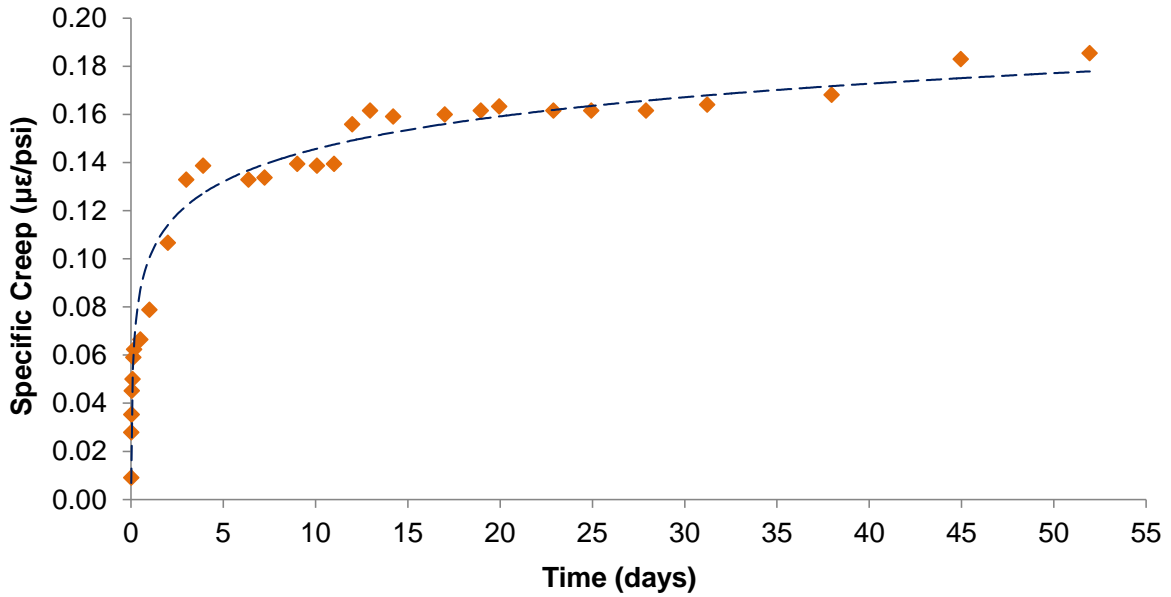
Figure 4.10 Specific creep calculation during the first 52 days. Blue dashed line shows correlation expressed in Equation 4.6. 1 με/psi = 145 με/MPa.

Calculated creep coefficient, ϕ, for the pile concrete is shown in Figure 4.11. The regression for these results is given in Equation 4.7 (t in days, R^2=97.8%), which predicts a creep coefficient of 1.56 at 376 days.

$$\phi = 0.1468 \cdot \ln(t) + 0.6862 \tag{4.7}$$
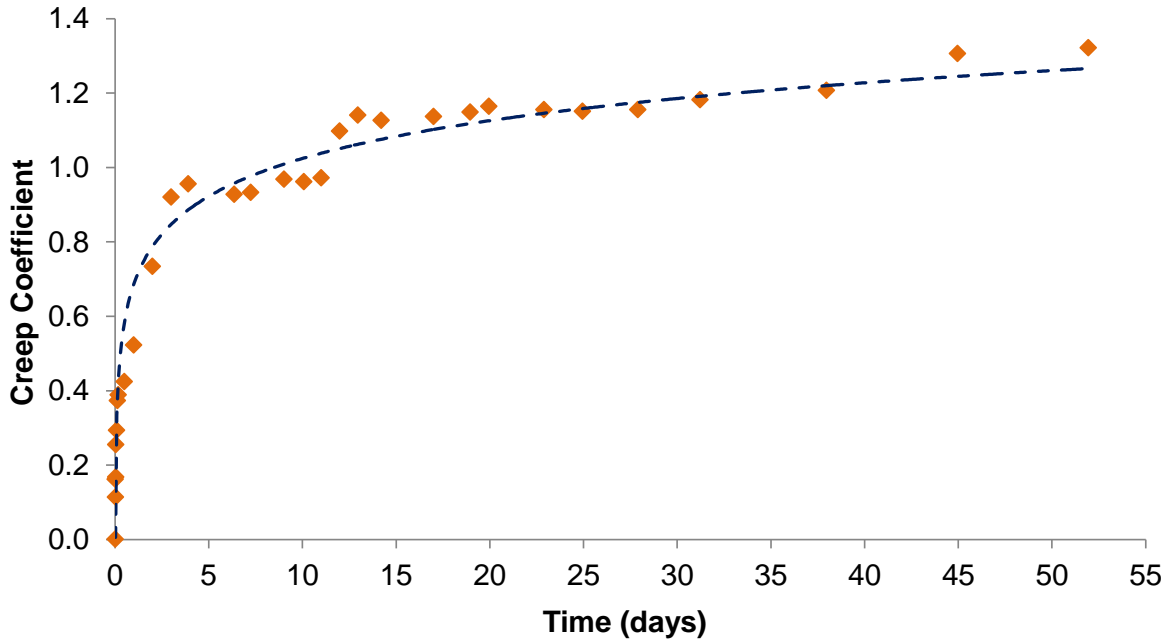
Figure 4.11 Creep coefficient calculation during the first 52 days. Blue dashed line shows correlation expressed in Equation 4.7.

ACI 209.R-92: Prediction of Creep, Shrinkage, and Temperature Effects in Concrete Structures (1992, reapproved in 1997) provides equations to predict creep and shrinkage deformations of concrete. Creep strains can be calculated from the prediction of the creep coefficient (Equation 4.8), while an expression for prediction of shrinkage strains is provided in the report (Equation 4.9).

$$\phi = \frac{t^{\psi}}{d + t^{\psi}} \cdot \phi_u \tag{4.8}$$

$$\varepsilon_{sh} = \frac{t^{\alpha}}{f + t^{\alpha}} \cdot \left(\varepsilon_{sh}\right)_u \tag{4.9}$$

where t is the time from loading for Equation 4.8 and the time from the beginning of drying for Equation 4.9, ϕ is the creep coefficient at time t, ϕ_u is the ultimate creep coefficient, ε_{sh} is the shrinkage strain at time t, and $(\varepsilon_{sh})_u$ is the ultimate shrinkage strain. ψ, d, α, and f are constants that depend on member shape and size.

The value of ϕ_u depends on the age of loading, the ambient relative humidity, the volume-to-surface area ratio, the slump, fine aggregate-to-total aggregate ratio, and air content. The value of $(\varepsilon_{sh})_u$ depends on the cementitious material content, the ambient relative humidity, the volume-to-surface area ratio, the slump, fine aggregate-to-total aggregate ratio, and air content. ACI 209 recommends expressions to calculate ϕ_u and $(\varepsilon_{sh})_u$, and values for ψ, d, α, and f. They are not included in this report.

Values obtained from Equations 4.8 and 4.9 overestimate experimental creep and shrinkage strains (Figure 4.12) for the concrete studied in this research.
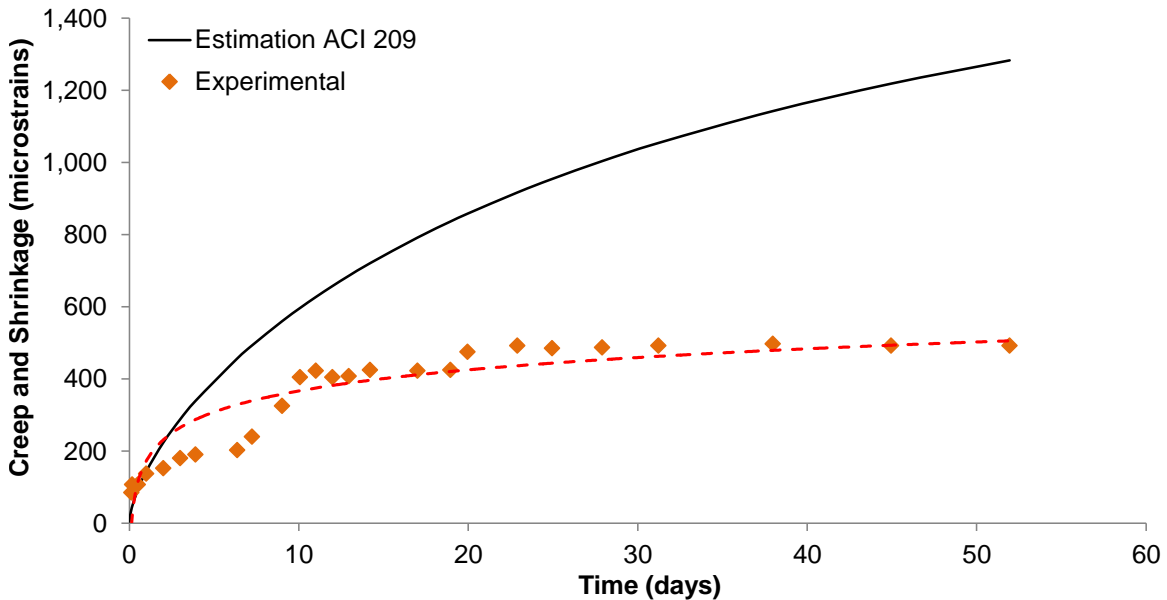
Figure 4.12 Creep plus shrinkage results compared to ACI 209 estimations. Red dashed line shows logarithmic correlation of experimental results.

87

Overall, the long-term creep response of the high-performance concrete used for the piles is much less than predicted using standard models and it is similar to the behavior of very high-performance concrete used for long-span bridge girders in Georgia. Such lower creep deformations are expected to lead to reduced prestress losses in marine piles.

4.2.7 Rapid chloride permeability test (RCPT)

To evaluate the permeability to chloride ions of concrete, the standard ASTM C1202 test was performed on 2-in. (5.1 cm) long sections of 4×8-in. (10.2×20.3 cm) cylinders at 56 days. Three cylinders cured in fogroom were sawed to obtain the testing specimens. An average charge of 2,850 C (standard deviation of 156 C) passed during the test period of 6 hours. According to the standard, the chloride penetrability of this concrete can be categorized as "moderate."

Special Provision for GDOT Standard Specification 500 specifies a maximum chloride permeability at 56 days of 2,000 C for HPC, but Holland et al. (2012) proposed a maximum charge of 1,000 C passed during the test for a concrete to be considered a high-performance mixture for prestressed concrete piles exposed to marine environments. The two recommended ternary concrete mixtures given by Holland et al. (2012) for marine piles showed a total charge passed of 354 and 273 C, at 56 days.

CHAPTER 5

DRIVING AND EXTRACTION OF PILES

The driving capacity of piles using duplex HSSS 2205 strands was tested six months after the pile construction, and the driving performance was compared to that of piles constructed with conventional steel strands. Overdriving and reflective cracking of piles may be a concern in coastal zones, and they can compromise the durability of the structure. Reflective cracking can be produced by impact stress wave reflection when piles are driven into soft soils underneath hard soils; thin transverse cracks can be generated by the tensile stresses produced after the reflective wave (Holland et al., 2012).

The three HSSS 2205 piles and two conventional 1080 piles were driven to refusal into the Savannah River, and then they were extracted by use of a water jet to erode the soil next to the pile. In order to evaluate the ability of the piles to resist the impact loading during driving, the piles were examined for damage and cracking after pile extraction.

As a result of the driving operation, piles using duplex HSSS 2205 showed no spalling, visible damage or cracks. Also, the bearing capacity of these piles averaged 27% more than the design requirement, and the HSSS 2205 piles performed similarly to those using conventional steel strands. It was concluded that piles built with duplex HSSS 2205 strands can withstand the applied impact loading and be successfully driven without damage.

This chapter details the driving operation and summarizes the driving capacity and behavior exhibited by the piles. As presented in Table 1.1 (page 3), the piles were driven at age 174 days. They were extracted the following day on the advice of the

89

geotechnical engineer and the pile driving contractor; those experts explained that the river bottom soil would adhere so tightly to the piles within two weeks that the piles could not be extracted. The flexural and shear testing of the piles were performed beginning 180 days after extraction.

5.1 Driving Operation and Procedures

Piles were driven into the Savannah River, in a space adjacent to an old dock at the Standard Concrete Products Company plant in Savannah, Georgia. The driving operation was performed by TIC Marine & Heavy Civil Corporation 174 days after the construction of the piles. They were extracted the following day. Figures 5.1 to 5.7 show the driving and extraction operations.

Piles were loaded onto a barge equipped with a crane and transported to a location about 50 ft. (15.2 m) from the river bank. A steel template was installed to place the piles and to assure vertical displacement during driving. A D-30 single-acting diesel hammer was used to drive the piles to refusal. A "refusal criterion", defined by the pile driving contractor as 10 blows of the hammer per ½-in. (12.7 mm), was selected to determine the end of the operation. Pile diving log, hammer specifications, and hammer bearing chart based on GDOT formula are given in Appendix E.

Figure 5.1 Piles being loaded onto a barge.

Figure 5.2 Barge, crane, and pile template in Savannah River, GA.

Figure 5.3 Lifting of pile HSSS #2 off the barge (left), and placing of pile HSSS #2 into the template (right).
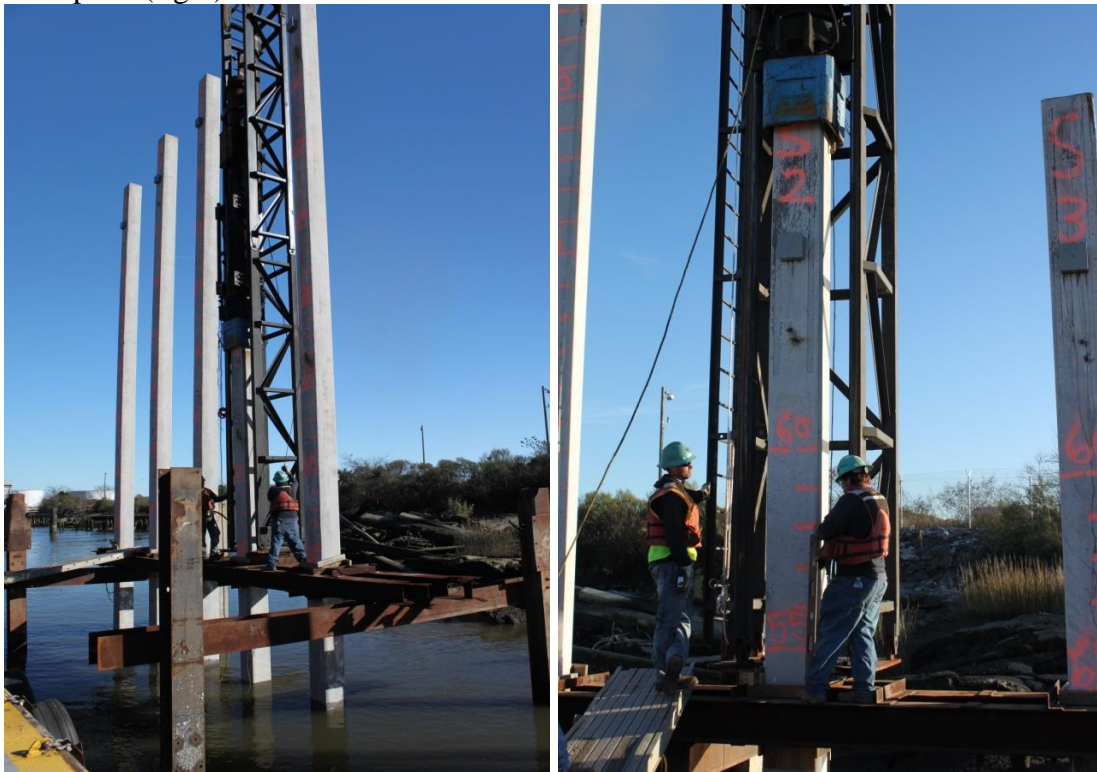
Figure 5.4 Driving of pile HSSS #2 (left), and blow counting of pile HSSS #2 (right).

Figure 5.5 Final condition of piles after driving operation.

Figure 5.6 Positioning of the water jet (left) and extraction of pile HSSS #1 (right).

93

Figure 5.7 Preparation to extract pile HSSS #1 (left), and extraction of pile HSSS #1 (right).

At the end of the driving operation, piles were extracted using a water jet system and carefully monitored to find reflective cracks, spalling, and other evidences of damage due to pile driving or extraction.

Then, piles were cut in halves in order to be transported to Georgia Tech Structures and Materials Lab for flexural and shear testing of piles (Figure 5.8). Description and results of these tests are presented in Chapters 6 and 7, respectively.

Figure 5.8 70-feet long piles were cut in halves and transported to Georgia Tech Structures and Materials Lab in Atlanta, GA.

5.2 Results and Conclusion of the Chapter

Pile driving was stopped by the contractor after the required capacity was greatly exceeded. The bearing capacity of the piles, estimated at the end of the driving operation, can be observed in Table 5.1. The capacity of the piles was 18% to 37% higher than the required design capacity (82 tons, 10 blows per ½-in. [12.7 mm]).

Table 5.1 Pile driving results for AISI 1080 steel and duplex HSSS 2205 strands. 1-in. = 2.54 cm.

	Penetration per 10 Blows (in.)	Bearing Capacity (ton)	Bearing to Design Capacity
Pile AISI 1080 #1	1.75	97	1.18
Pile AISI 1080 #2	1.25	112	1.37
Pile HSSS 2205 #1	1.50	104	1.27
Pile HSSS 2205 #2	1.50	104	1.27
Pile HSSS 2205 #3	1.50	104	1.27

Additionally, no damage, spalling or visible cracking was observed after driving in piles using duplex HSSS 2205 strands, while one of the piles including conventional steel exhibited a small hairline crack.

It can be concluded that piles using duplex HSSS 2205 strands can be successfully driven to refusal without visible damage.

CHAPTER 6

FLEXURAL CAPACITY OF PILES

Flexural behavior of piles was tested using the 70-ft. (21.3 m) long specimens, cut into two 35-ft. (10.7 m) long sections after the pile driving operation described in Chapter 5. The ten 35-ft. sections were transported to Georgia Tech Structures and Materials Lab.

Six piles using duplex HSSS 2205 strands and four piles using conventional AISI 1080 steel strands were tested in a four-point flexure setup (see Figure 6.1).
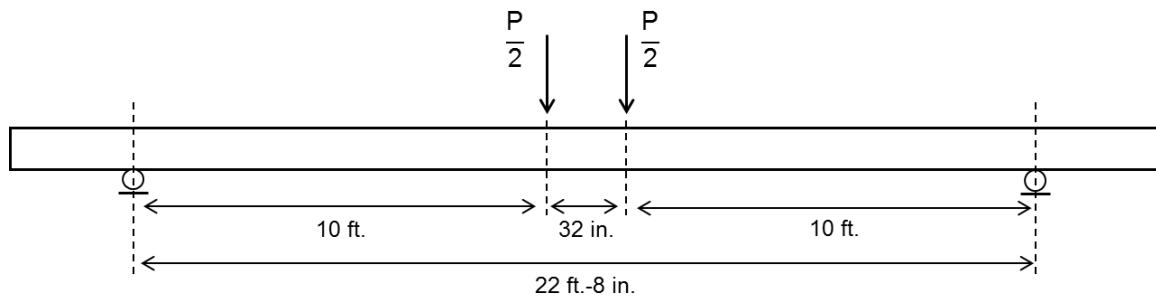
Figure 6.1 Diagram of flexure test. 1 in. = 2.54 cm, 1-ft. = 30.5 cm.

This chapter presents a description of the flexure test, a summary of the results, and a comparison with the behavior predicted by ACI 318 and AASHTO LRFD.

6.1 Flexure Test Setup

The piles were supported by rollers and loaded at their mid-length by a 2-point load system. The load was applied by a 500 ton hydraulic ram and recorded using a 200 kip (890 kN) load cell. A steel beam supported by rollers was used to transfer the load from the hydraulic ram to the piles as illustrated in Figure 6.2. The mid-length deflection

of the piles was measured using a string potentiometer. Three digital gauge dials were attached to one side of the piles, in order to estimate the strains in the prestressing strands at pile failure. Two dials were attached to the pile at 1-in. (2.54 cm) from the top and from the bottom, while a third was installed at the mid-height of the pile. Initially, a gauge length of 13-in. (33.0 cm) was used for the first four tests (pile 1080-1 Bottom, pile HSSS-1 Bottom and Top, and pile HSSS-3 Bottom); the gauge length was increased to 18-in. (45.7 cm) for the rest of the tests in order to cover the more extensive flexural cracking region. Strains were similar for both gauge lengths. The load was applied monotonically and was paused to mark crack patterns.

While the load-deflection data were recorded even after crushing of the concrete, the dial gauges were removed before the ultimate load to avoid damage. As a consequence, load-deflection curves show the behavior of the piles along the whole duration of the test, but some moment-curvature results calculated from strain and load measurements do not represent the complete behavior of the piles before failure. In these cases, the ultimate point was estimated from the load-deflection data, using a moment-area technique. The application of the moment-area method for the calculation of the ultimate curvatures is given and calculated ultimate curvatures are shown in Appendix F.

Average concrete compressive strength of individual piles (see Chapter 4) and the actual position of the strands (Appendix A) were used in the calculation of the flexural nominal strength. Also, a Todeschini stress block was assumed for the estimation of concrete compressive stresses (Wight and MacGregor, 2011) for ACI 318 method and a rectangular stress block was assumed for AASHTO calculations. ACI 318 and AASHTO calculations are given in Appendix G.

(a)
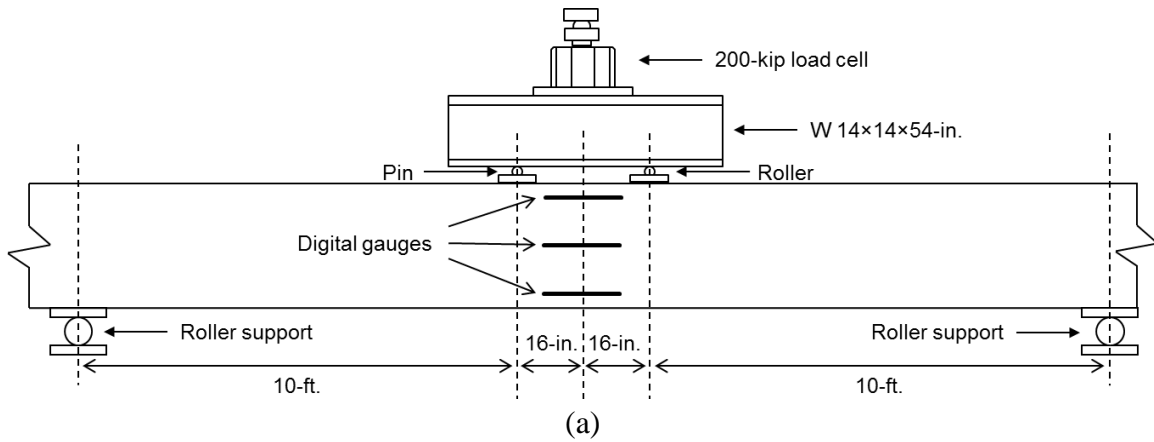
(b)

Figure 6.2 Flexure test setup. 1 in. = 2.54 cm, 1-ft. = 30.5 cm.

6.2 Results

Flexure tests of piles exhibited typical flexure, concrete crushing failures, with flexural cracks approximately evenly distributed every 10-in. (25.4 cm) and propagating from the bottom of the pile. The maximum crack widths were about 0.06-in. (1.52 mm). First crack was observed at an applied load between 15 (66.7 kN) to 20 kips (89.0 kN). Failure by concrete crushing at the top of the pile was observed in all the tests, as

predicted by calculations in Appendix G. The calculated moments and curvatures, the load-deflection and moment-curvature curves compared to predicted curves, the changes of the strain distribution along the depth of the pile during the test, and the crack pattern close to failure of each tested pile are detailed in Appendix H and they are summarized in Tables 6.1 and 6.2. Errors in the strain gauge measurements occurred in piles HSSS 2205 #1 – bottom half, HSSS 2205 #3 – bottom half, and AISI 1080 #2 – top half. Only the load-deflection curve and the crack pattern are presented in these cases.

       Experimental ultimate moments were calculated using the load and actual distances between supports and applied load. Ultimate curvatures were calculated using strain measurements and corrected, when possible, by the moment-area method. Differences in calculated ultimate moments were caused by differences in concrete strengths and small differences in measured locations of the prestressing strands through the length of the piles.

Table 6.1 Experimental and calculated ultimate moments. 1 kip·in = 113 N·m.

Pile	M_{exp} (kip·in)	$M_{u,ACI}$ (kip·in)	$M_{u,AASHTO}$ (kip·in)	$\dfrac{M_{u,exp}}{M_{u,ACI}}$	$\dfrac{M_{u,exp}}{M_{u,AASHTO}}$
1080 #1 – Top	2,585	2,436	2,406	1.06	1.07
1080 #1 – Bottom	2,507	2,436	2,419	1.03	1.04
1080 #2 – Top	2,654	2,530	2,313	1.05	1.15
1080 #2 – Bottom	2,686	2,530	2,321	1.06	1.16
HSSS 2205 #1 – Top	2,872	2,634	2,560	1.09	1.12
HSSS 2205 #1 – Bottom	2,835	2,634	2,564	1.08	1.11
HSSS 2205 #2 – Top	2,954	2,908	2,615	1.02	1.13
HSSS 2205 #2 – Bottom	3,044	2,877	2,560	1.06	1.19
HSSS 2205 #3 – Top	2,920	2,856	2,606	1.02	1.12
HSSS 2205 #3 – Bottom	2,868	2,866	2,606	1.00	1.10

Table 6.2 Experimental and calculated ultimate curvatures. 1 rad/in = 39.37 rad/m.

Pile	φ_{exp} (rad/in)	$\varphi_{u,ACI}$ (rad/in)	$\varphi_{u,AASHTO}$ (rad/in)	$\dfrac{\varphi_{exp}}{\varphi_{u,ACI}}$	$\dfrac{\varphi_{exp}}{\varphi_{u,AASHTO}}$
1080 #1 – Top*	1.073×10^{-3}	1.043×10^{-3}	8.819×10^{-4}	1.03	1.22
1080 #1 – Bottom	1.235×10^{-3}	1.043×10^{-3}	8.849×10^{-4}	1.18	1.40
1080 #2 – Top	--------	8.876×10^{-4}	7.190×10^{-4}	--------	--------
1080 #2 – Bottom*	1.013×10^{-3}	8.876×10^{-4}	7.190×10^{-4}	1.14	1.41
HSSS 2205 #1 – Top*	9.071×10^{-4}	9.146×10^{-4}	6.960×10^{-4}	0.99	1.30
HSSS 2205 #1 – Bottom	--------	9.146×10^{-4}	6.960×10^{-4}	--------	--------
HSSS 2205 #2 – Top	8.738×10^{-4}	8.873×10^{-4}	7.005×10^{-4}	0.98	1.25
HSSS 2205 #2 – Bottom	8.488×10^{-4}	8.921×10^{-4}	6.989×10^{-4}	0.95	1.21
HSSS 2205 #3 – Top	7.956×10^{-4}	9.042×10^{-4}	7.157×10^{-4}	0.88	1.11
HSSS 2205 #3 – Bottom	--------	9.018×10^{-4}	7.131×10^{-4}	--------	--------

* $\varphi_{u,exp}$ estimated using moment-area method.

Figure 6.3 shows the load-deflection curves of the flexure tests. At lower loads, close to the cracking point, greater deflections are observed in piles with the duplex HSSS 2205 strands compared to those with the conventional strand. This behavior can be attributed to the lower flexural stiffness as a result of the lower elastic modulus of stainless steel compared to conventional steel. Piles using stainless steel reinforcement exhibited higher ultimate loads, which were expected due to the greater area of prestressing strand used.

Figures 6.4 and 6.5 show moment-curvature results obtained from experimental data and the theoretical behavior, predicted by ACI 318. The moment at each point was calculated from the recorded applied load, while the curvature was calculated from the deformations measured by the dial gauges. When possible, the ultimate curvature was estimated using the moment-area method. In these cases, a dashed line shows the extended moment-curvature response after the strain gauges were removed.
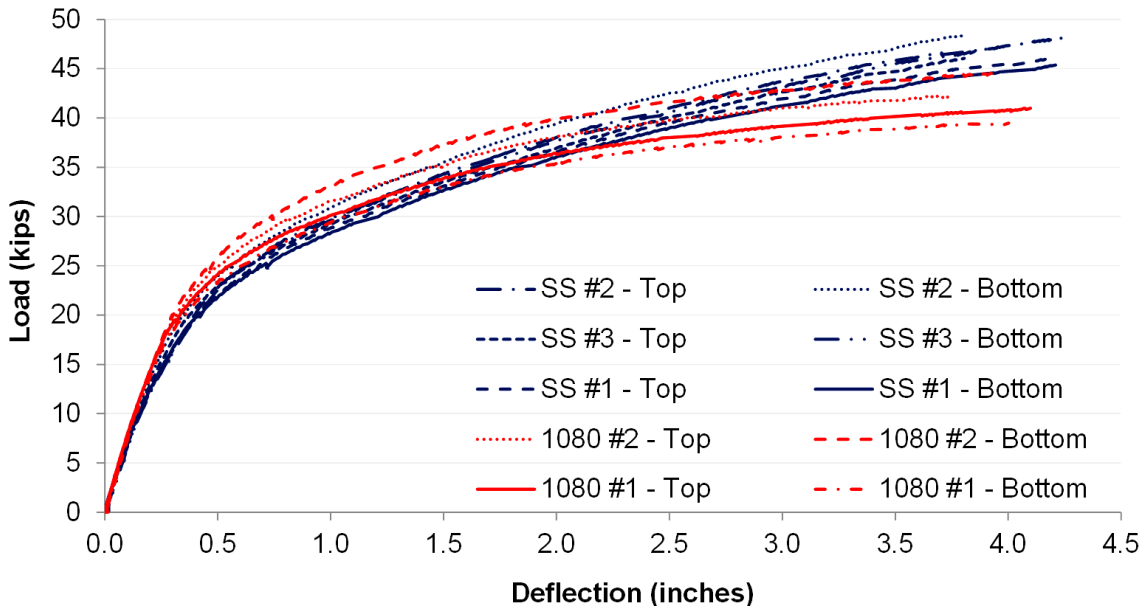
Figure 6.3 Summary of load-deflection (P-δ curves) for HSSS 2205 (blue) and AISI 1080 steel (red). 1 kip = 4.45 kN.
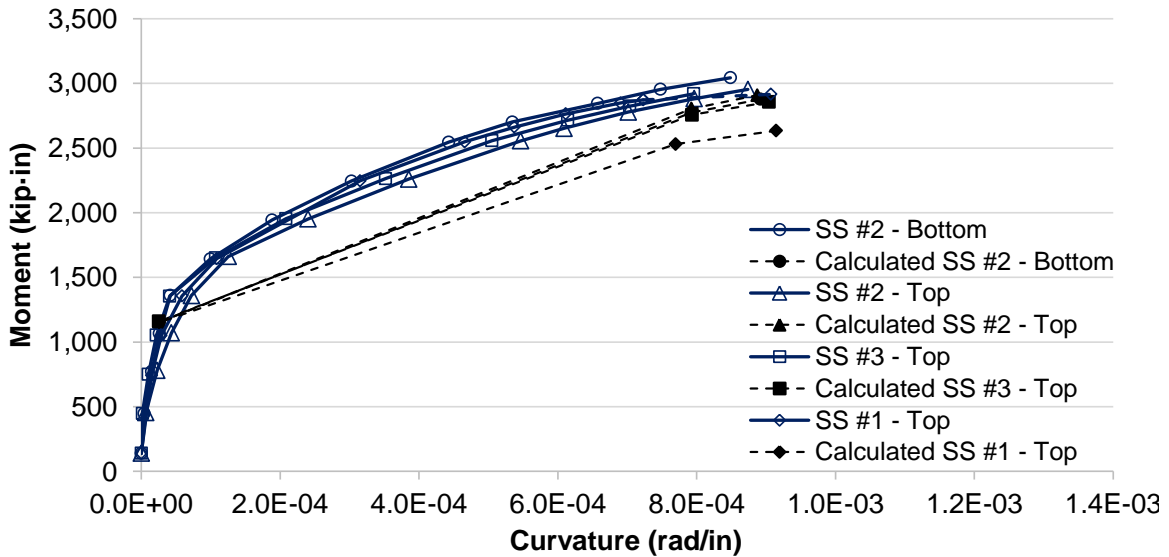
Figure 6.4 Summary of moment-curvature curves for piles using duplex HSSS 2205. Results are compared with calculated curves using ACI 318. 1 kip·in = 113 N·m.
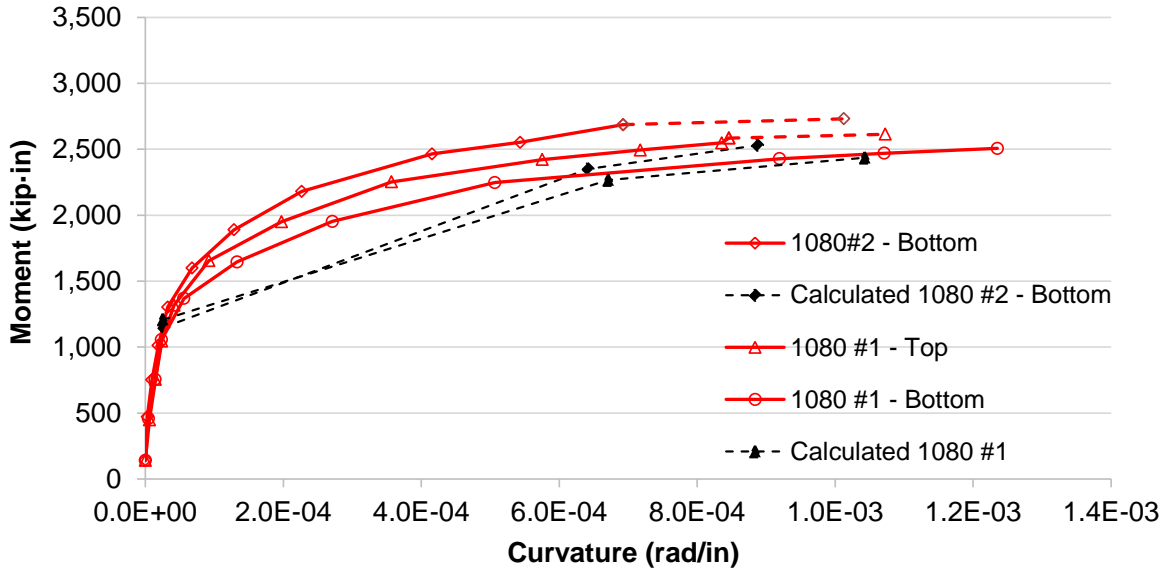
Figure 6.5 Summary of moment-curvature curves for piles using AISI 1080 steel. Results are compared with calculated curves using ACI 318. 1 kip·in = 113 N·m.

Figures 6.6 and 6.7 show the comparison of moment-curvature results with the predicted behavior by AASHTO LRFD.
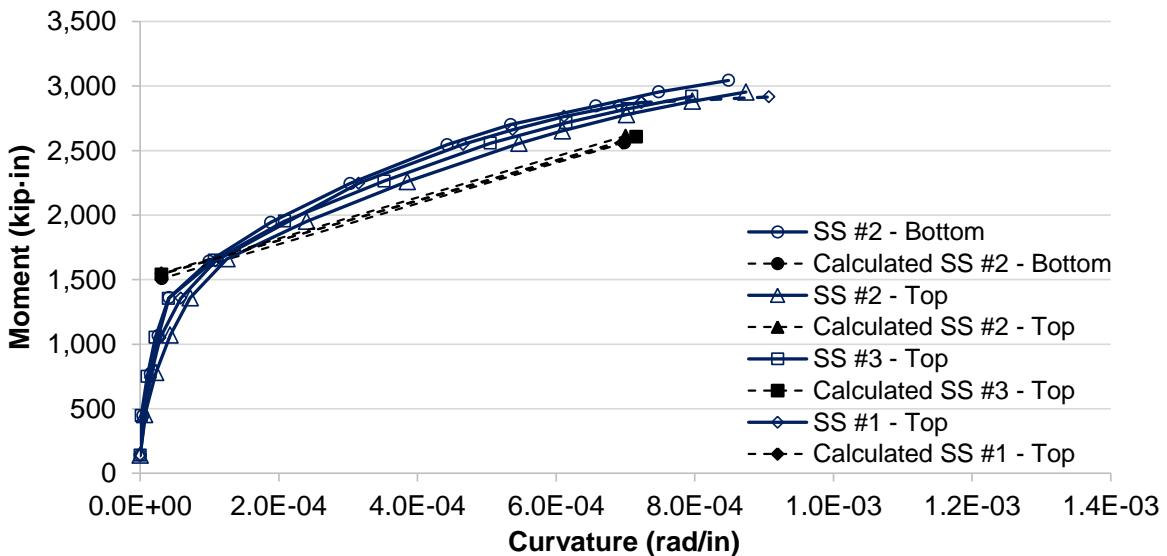
Figure 6.6 Summary of moment-curvature curves for piles using duplex HSSS 2205. Results are compared with calculated curves using AASHTO LRFD. 1 kip·in = 113 N·m.
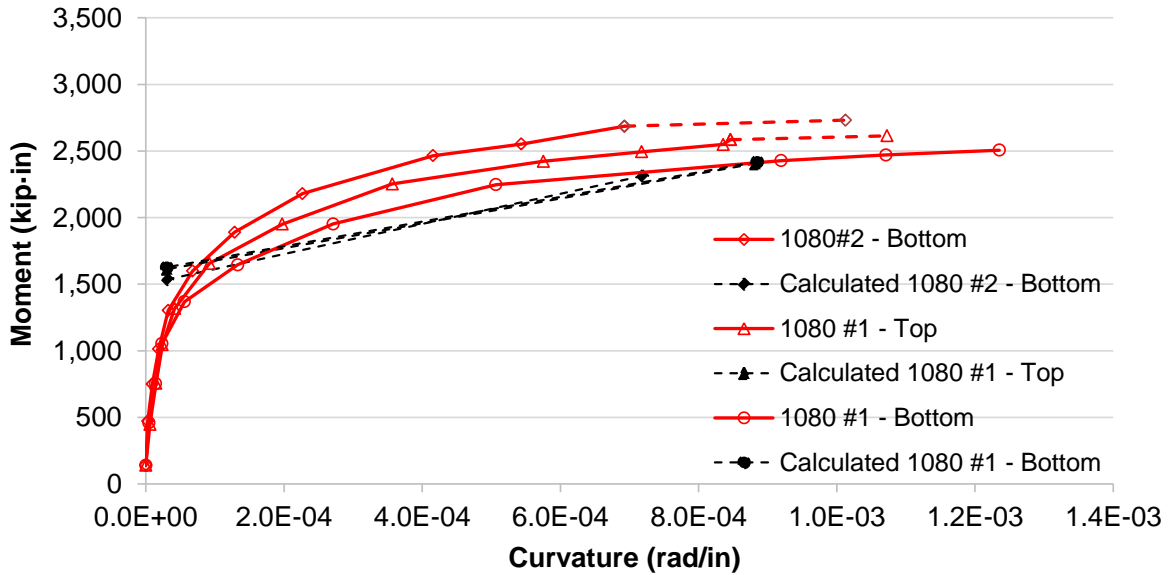
Figure 6.7 Summary of moment-curvature curves for piles using AISI 1080 steel. Results are compared with calculated curves using AASHTO LRFD. 1 kip·in = 113 N·m.

6.2.1 Comparison of results with ACI 318 and AASHTO LRFD

All the piles exhibited a higher ultimate moment than the predicted values using conventional analysis based on AASHTO LRFD and ACI 318.

Piles using duplex HSSS 2205 strands showed lower ultimate curvatures than the predicted values using ACI 318 and higher ultimate curvatures using AASHTO LRFD. This lower ductility is a consequence of the smaller plastic deformation range of duplex HSSS 2205 compared to AISI 1080 steel. The ultimate strains of duplex HSSS 2205 and conventional steel strands from direct tension tests were 1.60% and 5.89%, respectively.

6.2.2 Effect of type of steel

Piles using duplex HSSS 2205 strands showed a lower ultimate curvature and a higher ultimate moment compared to piles with conventional steel strands.

In the case of piles using conventional steel, the higher ultimate curvature of pile 1080 #1 compared to 1080 #2 can be attributed to the higher compressive strength of concrete used in pile 1080 #1 (see Chapter 4).

Additionally, at the moment of failure due to concrete crushing at the top of the pile, at least the bottom layer of stainless and conventional steel strands was yielding. Then, small increments of the load produced the breakage of duplex HSSS 2205 strands, while conventional strands were able to deform without failing for a considerably higher load increase.

6.2.3 Concrete at failure

The ultimate strain of concrete at the top section, calculated from the dial gauge measurements, ranged between 0.2% and 0.23%, lower than the assumed value of 0.3% used in ACI 318 and AASHTO LRFD. The lower extensibility of high-strength concrete, as mentioned in Section 4.2.5, is thought to be responsible for this difference.

6.3 Conclusions of the Chapter

From the results of the flexure tests, it was concluded that the flexural capacity of prestressed concrete piles using duplex HSSS 2205 strands may be conservatively predicted using AASHTO LRFD specifications and using provisions of ACI 318-11. However, the post-yield ductility of piles with HSSS 2205 strand is much less than that of piles with conventional prestressing strand. When a higher inelastic deformation energy dissipation capacity is required as needed for fender piles, the lower ductility of these piles should be considered. For stainless steel reinforced piles used as fender piles, a

lower strength reduction factor (ϕ) as used for compression-controlled members is

recommended.

CHAPTER 7

SHEAR CAPACITY OF PILES

The shear capacities of the piles were tested at each end of each 35-ft. (10.7 m) long pile segment; testing was conducted after the pile driving and extraction. Simply supported piles were loaded at a shear span approximately two times the pile height as illustrated in Figure 7.1. Through this configuration, two different spiral reinforcement spacings, 3-in. (7.6 cm) and 6-in. (15.2 cm), were tested per pile segment.
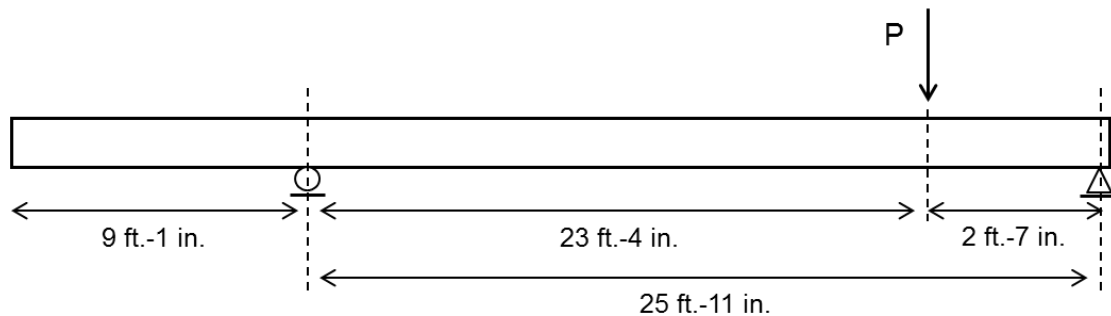
Figure 7.1 Diagram of shear test. 1 in. = 2.54 cm, 1-ft. = 30.5 cm.

Shear tests were performed on twelve pile segments reinforced with austenitic SS 304 transverse spiral reinforcement and eight pile segments reinforced with AISI 1080 transverse spiral reinforcement.

Shear failure of the piles was observed in every test, and no significant statistical difference was found in the ultimate shear and deflection of the piles, regardless of the spacing and type of transverse or longitudinal reinforcement tested. It was concluded that the replacement of conventional wire shear reinforcement with SS 304 wire spiral reinforcement in prestressed concrete piles produces equivalent shear capacity.

This chapter describes the shear tests and provides the analysis of the results.

107

7.1 Shear Test Setup

Figure 7.2 shows the detailed setup of the shear test. Piles 35-ft. (10.7 m) long were simply supported and a load was applied at 31-in. (78.7 cm) from the pin support. The load was applied using a 500 ton hydraulic ram and recorded every 0.5 seconds using a 200 kip (890 kN) load cell. The deflection was recorded using a wire potentiometer epoxied to the bottom of the pile at the same distance to the support from the applied load.
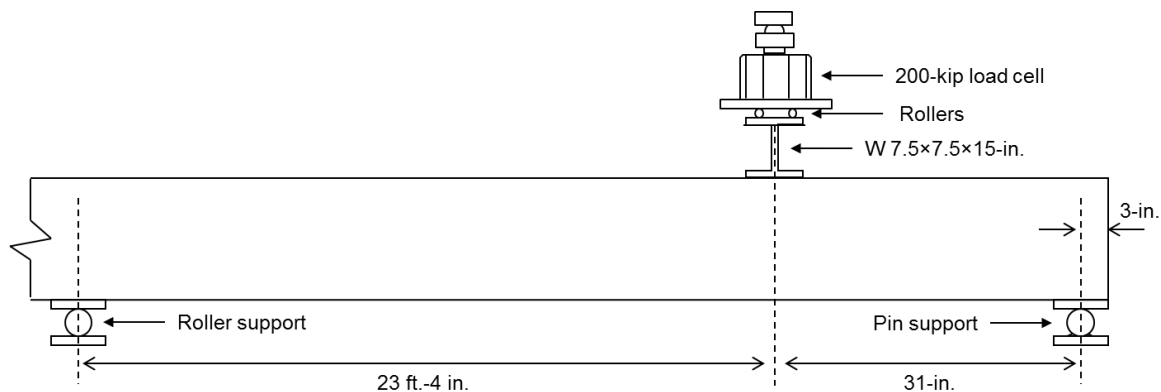
Figure 7.2 Shear test setup. 1 in. = 2.54 cm, 1-ft. = 30.5 cm.

In order to calculate the shear from the load measurements, the actual value of the nominal distances shown in Figure 7.2 were measured before every test. Actual shear span of 31.00-in. (78.74 cm) was measured in 65% of the tests and deviations no higher than 1 inch from this value were observed in the rest of the tests; the actual shear span was considered in the analysis of results. Rollers at the load application beam assured no longitudinal restraint of the pile (Figure 7.3).

Errors in test set-up and loading procedures occurred in tests of piles HSSS #2 and #3, top halves, and their results were not considered for the analysis of the results.

Figure 7.3 Load application system.

7.2 Results and Discussion

The first crack appeared when the shear at the loading point reached 45 (200 kN) to 50 kips (222.4 kN) and the deflection was close to 0.2-in. (5.08 mm). A shear crack propagated from the bottom of the pile, at a distance of 15-in. (38.1 cm) to 20-in. (50.8 cm) from the support, in the direction of the applied load with an angle close to 45°. Evidence of concrete crushing at the top of the beam and initiation of bond failure was observed at the end of the test (see Figure 7.4).

Examples of nominal shear strength calculations according to ACI 318 and AASHTO LRFD are given in Appendix I.

A summary of the experimental and calculated ultimate shear capacities of the piles is given in Table 7.1. A summary of the ultimate shear of every tested pile is given in Appendix J.
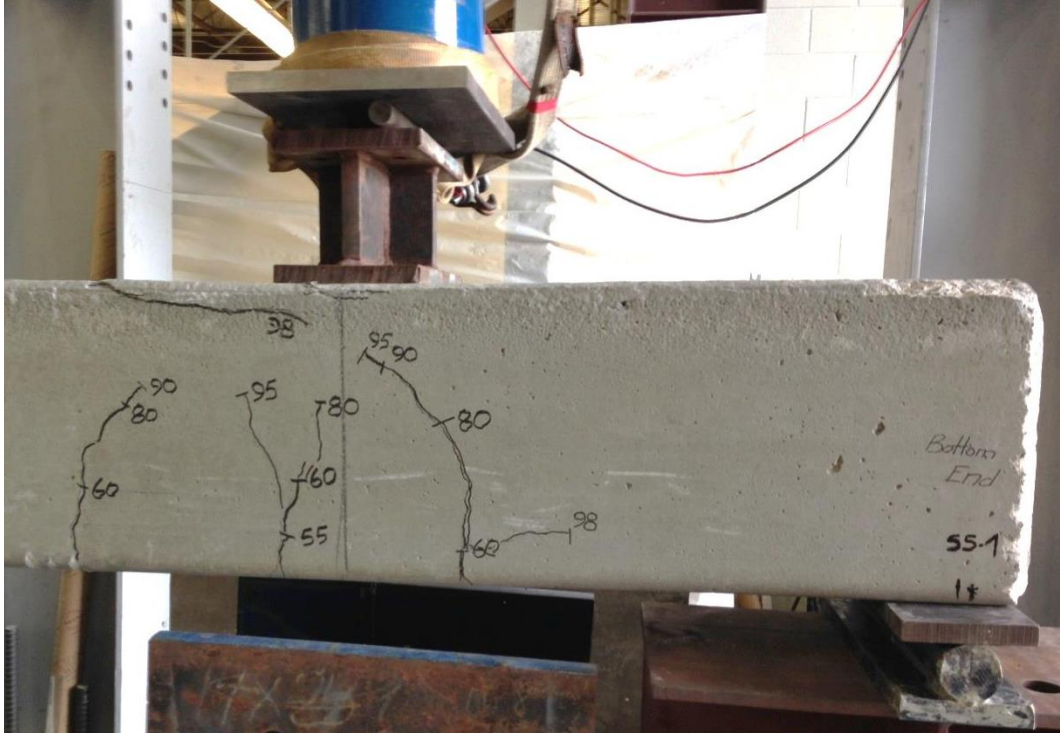
Figure 7.4 Typical crack pattern at failure. Numbers on the pile indicate the applied load when cracks appeared. 1 kip = 4.45 kN.

Table 7.1 Comparison of average ultimate shear with ACI 318 and AASHTO LRFD nominal shear strengths. 1 kip = 4.45 kN.

Pile – Spacing	$V_{u,exp}$ (kips)	$V_{u,ACI}$ (kips)	$V_{u,AASHTO}$ (kips)	$\dfrac{V_{u,exp}}{V_{u,ACI}}$	$\dfrac{V_{u,exp}}{V_{u,AASHTO}}$
HSSS 2205 – 3-in.	88.8	68.6	72.9	1.29	1.22
HSSS 2205 – 6-in.	93.4	58.2	62.4	1.61	1.50
AISI 1080 – 3-in.	87.1	70.9	75.3	1.23	1.16
AISI 1080 – 6-in.	88.9	59.6	63.9	1.49	1.39

It can be observed that the use of SS 304 spiral wire reinforcement is conservative with respect to ACI 318 and AASHTO LRFD provisions. In piles using stainless steel, ACI 318 predicts a nominal shear strength 23% and 38% lower than the average value obtained experimentally for spacings 3-in. (7.6 cm) and 6-in. (15.2 cm), respectively,

while AASHTO LRFD predicts a nominal shear strength 18% and 33% lower than the
average value obtained experimentally for spacings of 3-in. (7.6 cm) and 6-in. (15.2 cm),
respectively.

7.2.1 Shear-deflection curves

Figures 7.5 and 7.6 show the shear-deflection curves of the piles until failure. For
the HSSS 2205 piles, the black lines are used for the 3-in. (7.6 cm) spiral spacing and
blue lines for the 6-in. (15.2 cm) spiral wire spacing. For the AISI 1080 piles, the red
lines are used for the 3-in. (7.6 cm) spiral spacing and green lines for the 6-in. (15.2 cm)
spiral wire spacing.
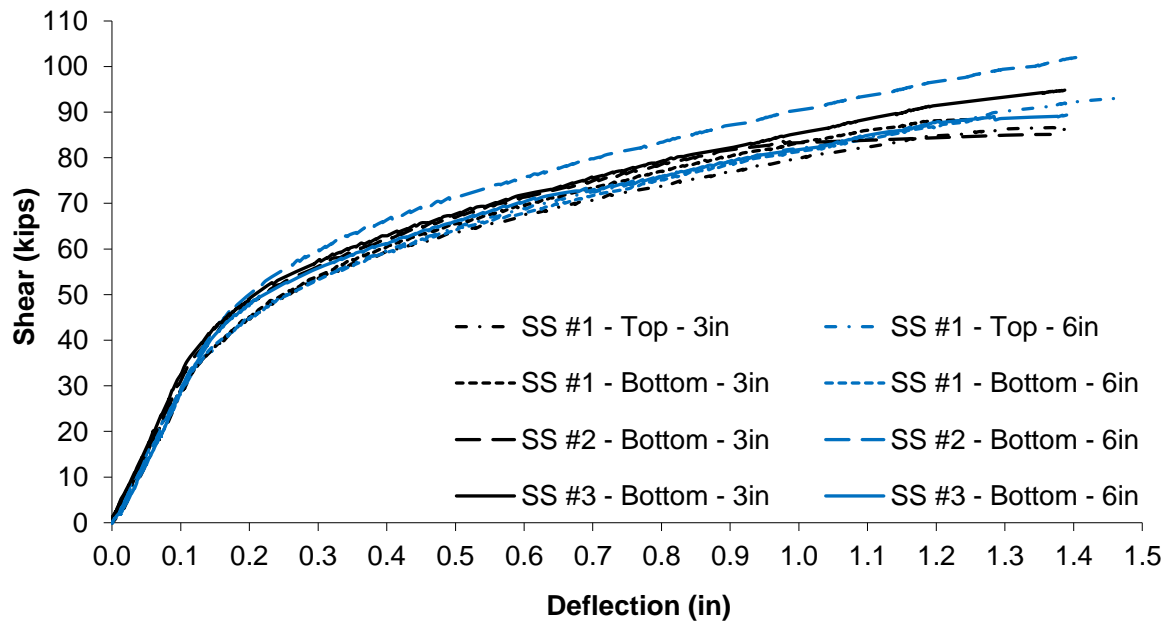
Figure 7.5 Shear-deflection curves for HSSS 2205 piles (spacings 3-in. and 6-in.).
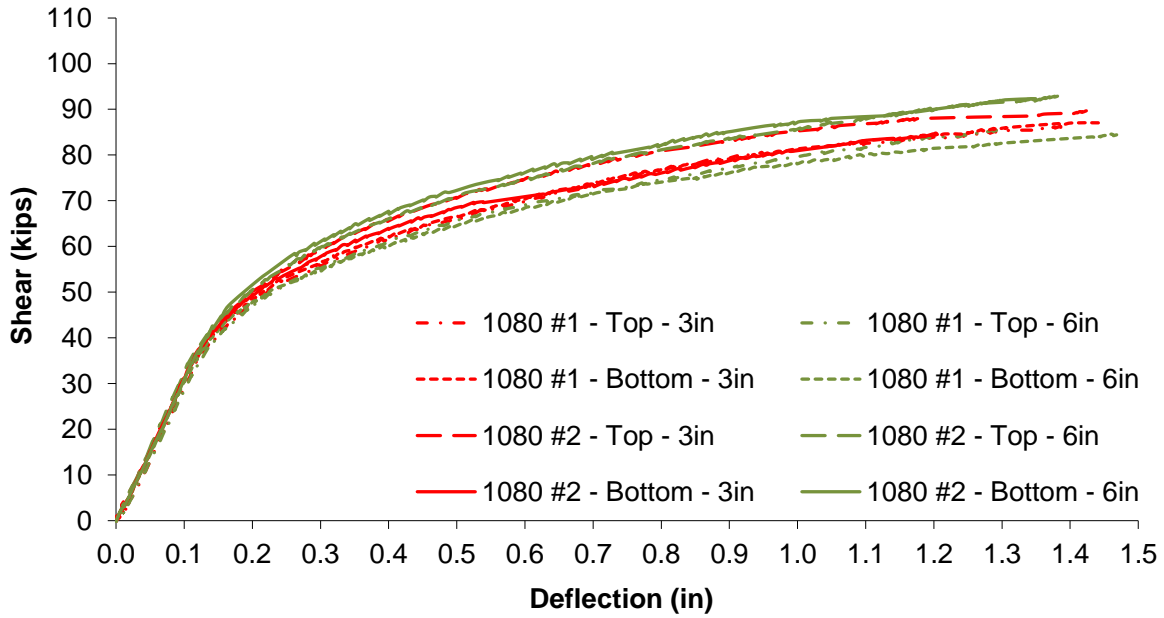
Figure 7.6 Shear-deflection curves for AISI 1080 piles (spacings 3-in. and 6-in.).

Figure 7.7 and 7.8 gives the shear force divided by $\sqrt{f'_c}$ for the HSSS 2205 piles and the AISI 1080 piles with 3-in. and with 6-in. spiral spacing, respectively.
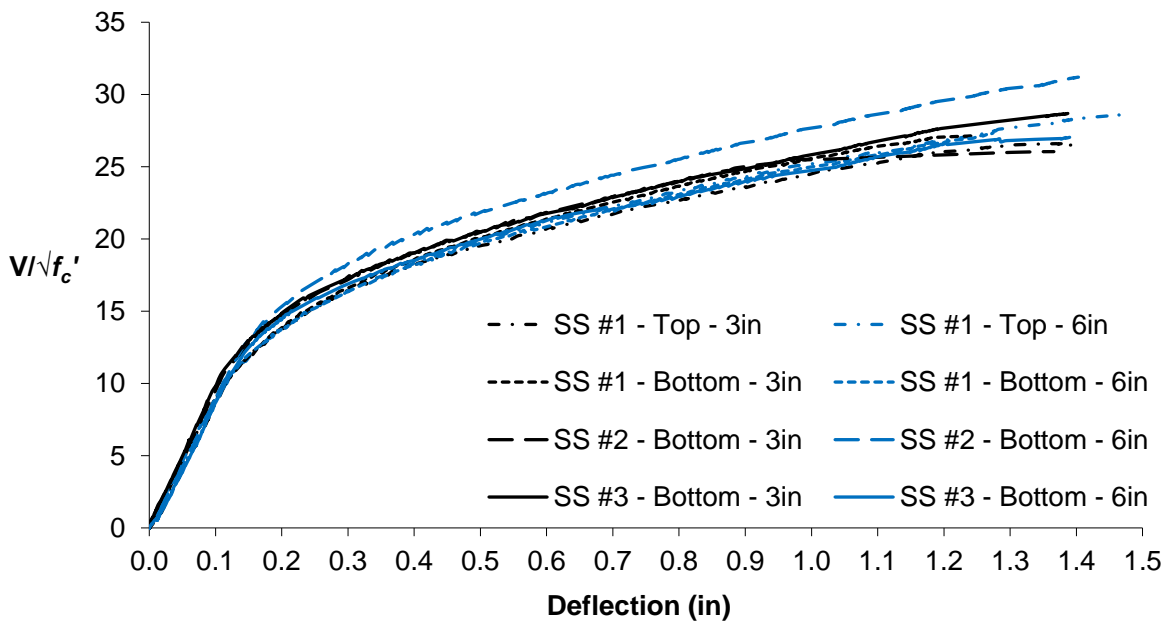
Figure 7.7 Shear divided by $\sqrt{f'_c}$ for HSSS 2205 piles (spacings 3-in. and 6-in.).

112
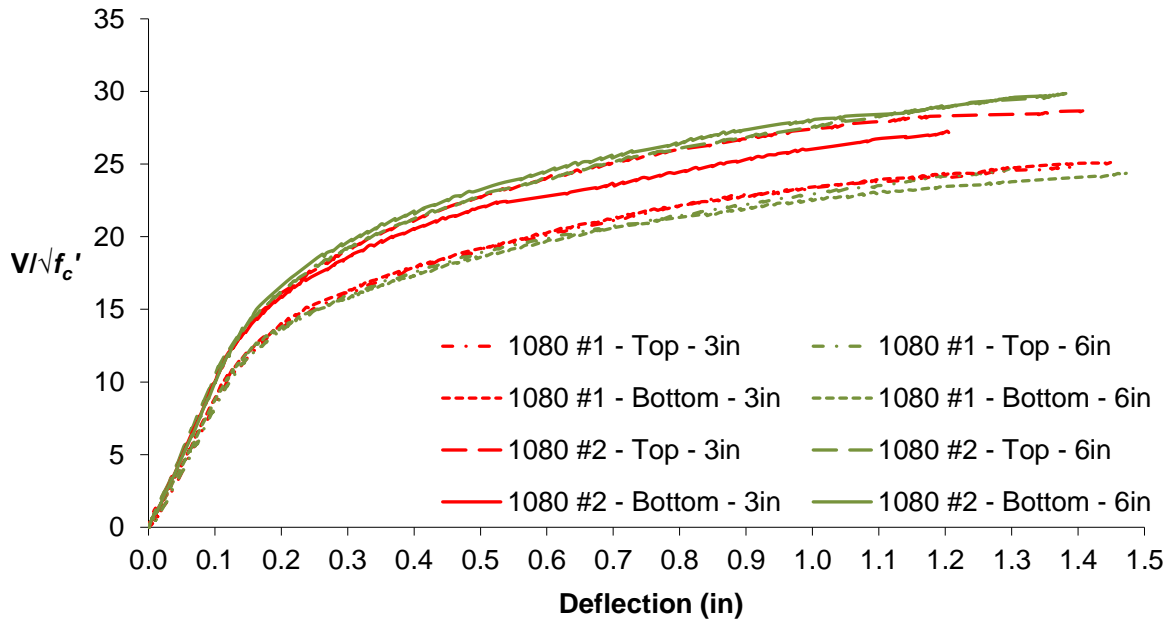
Figure 7.8 Shear divided by $\sqrt{f'_c}$ for AISI 1080 piles (spacings 3-in. and 6-in.).

Normalized shear by $\sqrt{f'_c}$ shows different trends depending on the type of prestressing steel. For piles using stainless steel, the strength of concrete shows no important effect on total shear, while the contribution of concrete to total shear on piles using conventional steel is different for both tested piles. The same observation is obtained for the calculated contribution of concrete by ACI 318 and AASHTO LRFD (Table 7.2).

Table 7.2 Shear strength provided by concrete, V_c, according to ACI 318 and AASHTO LRFD. 1 kip = 4.45 kN.

Pile	$V_{c,ACI}$ (kips)	$V_{c,AASHTO}$ (kips)
HSSS 2205 #1	47.65	51.94
HSSS 2205 #2	47.74	52.05
HSSS 2205 #3	48.04	52.40
AISI 1080 #1	49.75	54.33
AISI 1080 #2	46.65	50.94

7.2.2 Statistical analysis of results

In Figures 7.5 and 7.6, no clear difference is observed in the shear behavior of the piles using 3-in. (7.6 cm) and 6-in. (15.2 cm) spacing. Thus, statistical similarity of the ultimate shear and deflection was tested using ANOVA. The results of the statistical analysis are shown in Tables 7.3 and 7.4.

No significant difference is found between piles using conventional transverse reinforcement and piles reinforced with SS 304 spiral wire, for an $\alpha=5\%$ significance level. Also, similarity of means is observed between tests performed on different spiral wire spacing.

Table 7.3 Statistical analysis of ultimate shear results.

Test	Decision ($\alpha = 5\%$)	p-value
H_0: $\mu_{1080} = \mu$	Fail to Reject H_0	47.24%
H_0: $\mu_{2205} = \mu$	Fail to Reject H_0	25.20%
H_0: $\mu_i = \mu$	Fail to Reject H_0	25.64%
H_0: $\mu_{1080-1} = \mu_{1080-2}$	Fail to Reject H_0	8.89%

Table 7.4 Statistical analysis of ultimate deflection results.

Test	Decision ($\alpha = 5\%$)	p-value
H_0: $\mu_{1080} = \mu$	Fail to Reject H_0	91.15%
H_0: $\mu_{2205} = \mu$	Fail to Reject H_0	58.10%
H_0: $\mu_i = \mu$	Fail to Reject H_0	95.15%

7.3 Conclusions of the Chapter

The use of SS 304 wire spiral reinforcement provides shear strength equivalent to that of conventional wire spiral reinforcement.

Shear strength provided by SS 304 wire spiral reinforcement was 29% and 61% higher than predicted nominal shear strength by ACI 318 for spacings of 3-in. (7.6 cm) and 6-in. (15.2 cm), respectively, and 22% and 50% higher than the predicted nominal shear strength by AASHTO LRFD for spacings of 3-in. (7.6 cm) and 6-in. (15.2 cm), respectively.

CHAPTER 8

PRESTRESS LOSSES

As described in Chapter 3, prestress losses were measured using VWSGs embedded at 17.5 ft. (5.3 m) from each end of each pile. VWSGs were installed before concrete placement (Figure 8.1). The "zero," initial measurement was taken immediately before strand release, and subsequent measurements were taken right after strand release, before and after pile driving, and at intermediate times (Figure 8.1). The final measurement was performed before shear and flexural testing of the piles, 335 days after the initial measurement.

Figure 8.1 Strain gauge installation (left) and measurement of strains (right).

Experimental results were compared with the refined and lump-sum estimation methods described in AASHTO LRFD (2013) and as illustrated in Appendix K. The refined method calculates the total prestress loss in pretensioned elements as the sum of the losses due to elastic shortening at jacking, relaxation of steel, and shrinkage and creep of concrete. The lump-sum method estimates long-term losses (creep and shrinkage of concrete and relaxation of steel stress) using a single formula.

Losses predicted by the AASHTO LRFD refined method were 59% higher than the measured values. It was concluded that the use of AASHTO LRFD for the estimation of prestress losses of duplex HSSS 2205 strands is conservative.

Also, duplex HSSS 2205 strands exhibited similar early loss of the initial prestress and higher losses at later ages compared to conventional strands. GDOT Standard 3215 specifies a maximum loss of 22% of the initial pretension force. At 335 days, losses of the initial prestressing load of 7.84% and 9.39% were measured for AISI 1080 steel and duplex HSSS 2205 strands, respectively. The AASHTO refined method predicts that losses at 335 days are approximately 90% of the total losses considering a service life of 100 years for the analyzed prestressed concrete piles. Thus, it is very unlikely that prestress losses in prestressed concrete piles will surpass the GDOT Standard 3215 limit for loss of pretension force.

8.1 Results

Using vibrating wire strain gauges, the strains of the concrete over time and the internal temperature were obtained. Perfect bond between the strands and concrete was assumed so that the change in strain of the concrete equaled the change in strain of the

117

prestressing strands. Variations in concrete internal temperature were accounted for by calculating the relative thermal deformation of the steel vibrating wire with respect to concrete. The assumed coefficients of thermal expansion for steel and concrete were 12.2 $\mu\varepsilon/°C$ and 10.2 $\mu\varepsilon/°C$, respectively. Using the elastic modulus of the strands, obtained from tensile strength tests (Chapter 4), the prestress losses were calculated from the strain readings.

8.1.1 Experimental losses compared with the AASHTO refined method

Prestress losses during the first 335 days are shown in Figure 8.2 for conventional steel and duplex HSSS 2205 strands. Measured prestress losses are compared with AASHTO estimated values (black lines in the figure), calculated with the refined method (see calculations given in Appendix K).
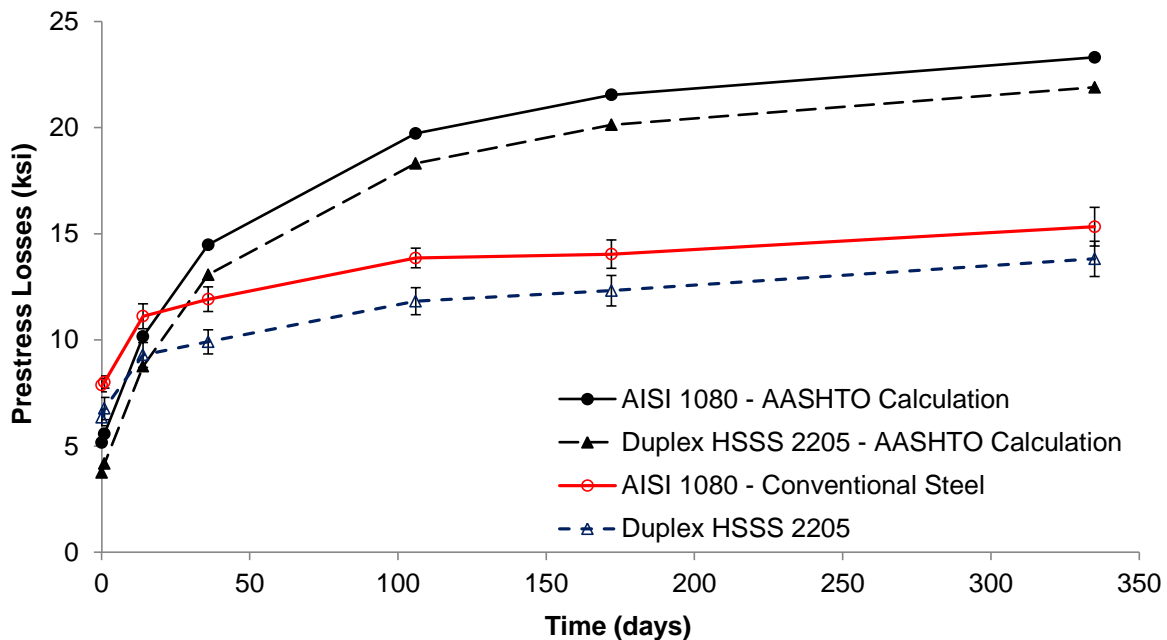
Figure 8.2 Prestress losses during the first 335 days.

118

The measured losses during the first 14 days were higher than the predicted

AASHTO values, while at later ages the values predicted by AASHTO were significantly

larger than the experimental results.

Table 8.1 Comparison between experimental and predicted prestress losses at 335 days.
1 ksi = 6.9 MPa.

	Duplex HSSS 2205		AISI 1080 Steel	
	Experimental (ksi)	AASHTO predictions (ksi)	Experimental (ksi)	AASHTO predictions (ksi)
Jacking Stress	144.9	144.9	196.8	196.8
Elastic Shortening (ES)	6.3	3.6	7.9	4.5
Stress Relaxation (RE)	4.2*	0.073	4.7*	0.567
Creep plus Shrinkage (ASTM C512)	15.5**	18.2	19.4**	18.2
Creep plus Shrinkage (Measured, CR + SH)	7.5	18.2	7.4	18.2
Total Losses (ES + CR + SH + RE)	18.0	21.9	20.1	23.3

 * Experimental stress relaxation calculated from experimental values obtained by Schuetz (2013) for initial stress of 70% UTS.
** Experimental creep and shrinkage losses estimated from results of ASTM C512 standard test.

In Table 8.1, the influence of each source of prestress loss in total experimental

losses is compared with the corresponding AASHTO predictions at 335 days. Relaxation

of steel stress was estimated from experimental results (Schuetz, 2013) and added to

losses measured using embedded strain gauges.

Experimental elastic shortening corresponds to the first measurement of prestress

losses on the piles, performed after strand release. The values are approximately 75%

higher than AASHTO predicted values, but it is expected that part of the stress relaxation

of the prestressing strands occurred at the time of the first reading. Schuetz (2013)

determined that as much as a 25% of the stress relaxation measured at 1,000 hours for HSSS 2205 strands can occur in one hour after the application of the prestressing force.

Time-dependent losses (creep, shrinkage, and stress relaxation losses) show a higher difference between experimental and predicted values. This difference corresponds mostly to creep and shrinkage losses estimation. Even though estimated creep and shrinkage losses from ASTM C512 test results (Chapter 4) are relatively closer to AASHTO predictions, experimental time-dependent losses measured in the piles, which correspond to the measurements after the first reading, are approximately 60% lower than predicted values. It is noted that the creep and shrinkage tests were performed under a relative humidity of 50% while the piles were at relative humidity between 70% (Savannah, Georgia) and 100% (Savannah River and exposed to rain). The higher humidity would reduce the combined creep and shrinkage strains.

At 335 days, predicted losses were approximately 22% higher than experimental results, including stress relaxation estimation, for duplex HSSS 2205. Additionally, if a service life of 100 years for the piles is considered, the AASHTO refined method predicts that losses at 335 days represent about 90% of total, 100-year losses for both types of strands (Table 8.2).

Table 8.2 Ratio of experimental to calculated losses at 335 days and estimated losses at 100 years.

Pile	Calc/Exp at 335 days	AASHTO Losses 100 years (ksi)	AASHTO Losses 100 years (MPa)	AASHTO Losses 100 years ($\mu\varepsilon$)
AISI 1080 Steel	1.16	25.61	176.57	871
Duplex HSSS 2205	1.22	24.20	166.85	1,030

8.1.2 Effect of pile driving and type of prestressing steel

The pile-driving operation was performed at day 174 from initial prestress application. As a result, no significant effect on prestress losses due to driving was observed.

Also, when prestress losses in each end of the piles are analyzed (see separated graphs in Appendix L), no clear differences are observed. Two piles using duplex HSSS 2205 strands and one pile using conventional steel exhibit similar prestress loss values at both ends. On the contrary, piles AISI 1080 #1 and HSSS 2205 #3 show higher prestress losses on the end closer to the jacking end of the prestressing form.

It was also observed in Table 8.1 that higher average values of prestress losses are obtained with the AISI 1080 steel strands. This difference is properly predicted by AASHTO. However, considering the lower elastic modulus of duplex HSSS 2205 strands, these prestress losses represent lower strains than in conventional steel.

Since duplex HSSS 2205 and conventional steel strands were prestressed at 60% and 70% of the UTS, respectively, a proper comparison should include the loss of the initial prestress of each type of strand. It is noted that the relaxation loss of prestressing force in each strand type was about 2.5% if loaded to 70% of UTS.

Figure 8.3 shows the loss of initial prestress with time. The initial elastic loss in the piles with HSSS 2205 and in piles with conventional strands was similar. The long-term loss in piles with duplex HSSS 2205 strands is slightly larger than the loss in piles with conventional strand. Considering the initial prestress of each strand (60% UTS vs. 70% UTS), the relaxation of duplex HSSS 2205 strands is slightly less than that of conventional steel strands. Given that the initial prestressing force is the same, a higher

121

force is applied by the duplex HSSS 2205 strands over time. This greater force would

lead to greater creep of the piles, and consequently to higher prestress losses.
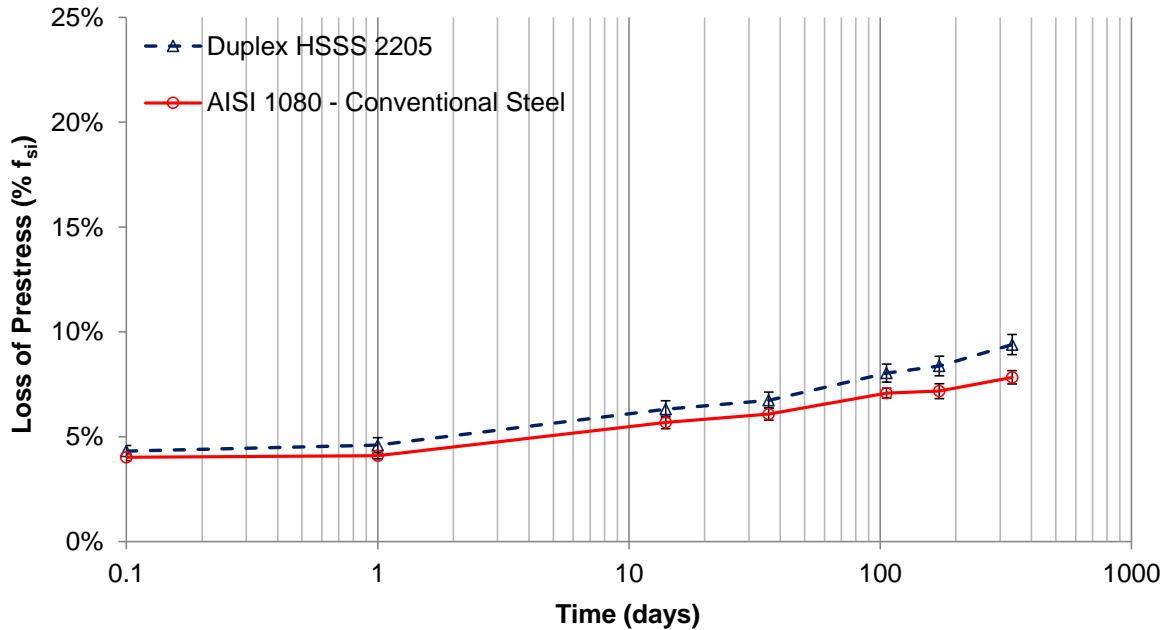
Figure 8.3 Loss of initial prestress for the first 335 days. Error bars correspond to standard deviation of losses.

A maximum loss of initial prestressing of 22% is required by GDOT Standard

3215. Regardless of the type of prestressing steel, losses at 335 days are predicted to be

90% of the total losses at the end of a service life of 100 years. Thus, it is unlikely that

the loss of prestress of the piles will exceed the specified limit.

8.1.3 Experimental losses compared with AASHTO lump-sum method

Table 8.3 shows the comparison between experimental losses, including strain

gauge measurements and stress relaxation estimation, and prestress losses calculated with

the AASHTO lump-sum method (see calculations given in Appendix K). The calculated

lump-sum losses at 335 days approximately equal the measured losses for piles with

HSSS 2205 strands, and they are 95% of those measured for piles with conventional

strand.

Table 8.3 Comparison of measured losses at 335 days and calculated losses with the
AASHTO lump-sum method.

Pile	Experimental Losses at 335 days (ksi)	Experimental Losses at 335 days (MPa)	AASHTO Lump-Sum Losses (ksi)	AASHTO Lump-Sum Losses (MPa)
AISI 1080 Steel	20.1	138.3	19.0	131.3
Duplex HSSS 2205	18.0	124.2	18.1	124.9

8.2 Conclusions of the Chapter

The use of AASHTO refined method for the estimation of prestress losses is

conservative for duplex HSSS 2205 strands. Experimental losses equaled 82.3% of those

predicted by the refined method, and 99% of those predicted by the lump-sum method.

Also, losses of prestressed concrete piles built using duplex HSSS 2205 strands comply

with current GDOT requirements.

CHAPTER 9

TRANSFER LENGTH

Transfer length (l_t) is defined by ACI 318 (2011) as the "length of embedded pretensioned strand required to transfer the effective prestress to the concrete," while AASHTO LRFD (2013) defines it as "the length over which the pretensioning force is transferred to the concrete by bond and friction in a pretensioned member." An idealized diagram of the steel stresses is illustrated in Figure 9.1 (Russell and Burns, 1993). It is assumed that, after strand release, the stresses transferred to the concrete increase linearly from zero at the end of the pile to a point where the prestress force is fully transferred. This distance is the transfer length.
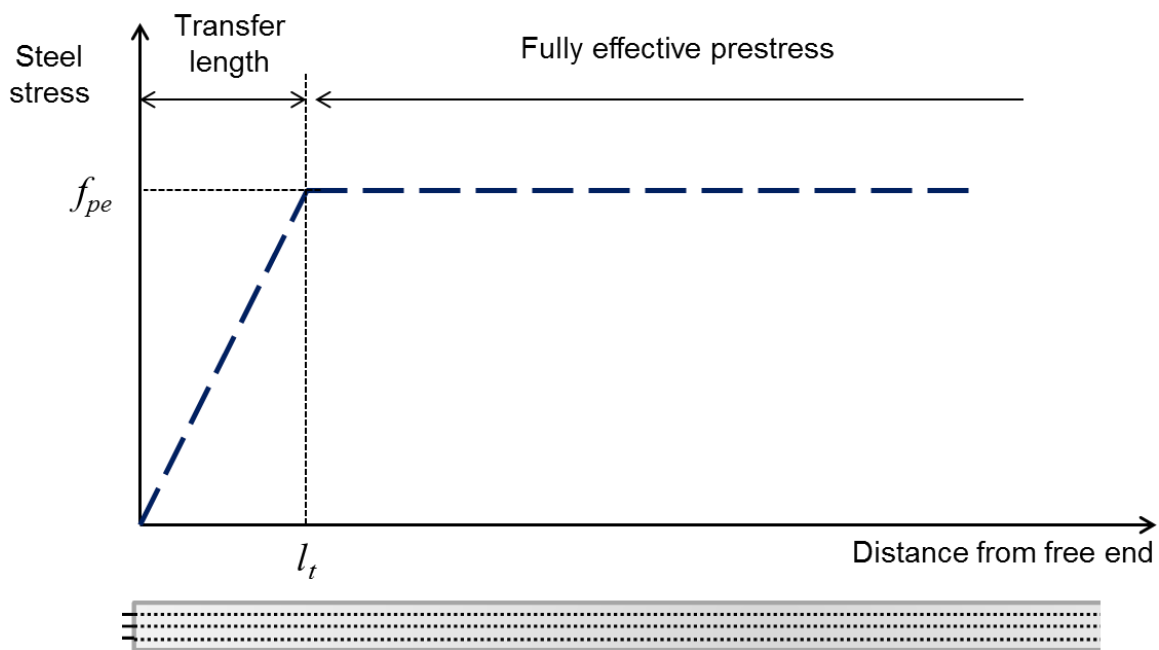
Figure 9.1 Idealization of strand stresses along the pile (modified from Russell and Burns (1993)).

Transfer length of the prestressed concrete piles was measured at each end of the piles, using the concrete surface strain (CSS) method (Russell and Burns, 1993). As a result of the prestressing force transferred from the steel strands to the concrete, strains and compressive stresses are induced. By equilibrium, these compressive stresses in the concrete balance the tensile stresses in the prestressing strands. Thus, the measurement of the concrete surface strains mirror the strain profile of the prestressing strands (Reutlinger, 1999; Kahn et al., 2002).

The average transfer lengths of the piles using duplex HSSS 2205 and conventional steel strands were shorter than the predicted values using AASHTO LRFD and ACI 318. After pile driving and extraction, the average transfer lengths of the piles remained the same or shorter than before driving and less than the AASHTO LRFD and ACI 318 predictions.

This chapter describes the determination of the transfer length of the piles by the CSS method. Also, results before and after driving are compared with estimated transfer lengths according to ACI 318, AASHTO LRFD, and expressions proposed in the literature and described in Chapter 2.

9.1 CSS Measurements

The CSS method was used by Russell (1992) to determine the transfer length of 0.6-in. (15.2 mm) diameter, 7-wire strands of prestressed concrete girders. This technique considers that 1) stress of prestressing strand varies linearly from zero at the end of the pretensioned element to a maximum value where full prestressing force is transferred to the concrete, 2) prestress transfer to the concrete depends on bond strength developed by

125

Hoyer's effect and, with a lower contribution, mechanical interlocking, and 3) equilibrium of compressive stresses in concrete and tensile stresses in the prestressing strands allows the determination of strand strains along the prestressed concrete element by the measurement of concrete surface strains.

As explained in Chapter 3, two rows of embedded DEMEC points were installed at the surface of each end of each pile. DEMEC points were placed along 8-ft. (2.44 m) at the ends of the piles; the points were spaced at 2-in. (5.1 cm) on centers, starting at 1-in. from the end. The measurements were performed using a DEMEC gauge with a gauge length of 8-in. (20.3 cm) and a precision of ±0.0001-in. (±0.00254 mm), which allowed 86 readings at each end (Figure 9.2). The same person performed the measurements along the piles, using the same DEMEC gauge. Before measurements were taken, the DEMEC tool was zeroed using an INVAR reference bar to account for temperature variations.

Figure 9.2 Concrete surface strain measurements. Note the two parallel rows of DEMEC gauge points on each side of the top surface of the pile

The first measurements were taken before the release of the strands. Then, an initial reading was performed after strand release, while the rest of the measurements were performed before sunrise beginning the following morning to avoid significant deformations in the concrete due to solar radiation and resulting temperature gradients.

In order to describe the CSS method in detail, results for pile 1080 #1, jacking end (i.e., the end of pile closer to the jacking end of the prestressing bed during construction) is presented. Figure 9.3 shows the raw concrete strain profile along pile 1080 #1, jacking end. Measurements of both rows of DEMEC points were averaged. It can be observed that at 14 days, less variable measurements were obtained compared to readings after release and at 1 day from release. Thus, measurements taken at 14 days were considered for the calculation of the transfer length before driving. The deformation of the pile at release was thought to be restrained by the prestressing bed.
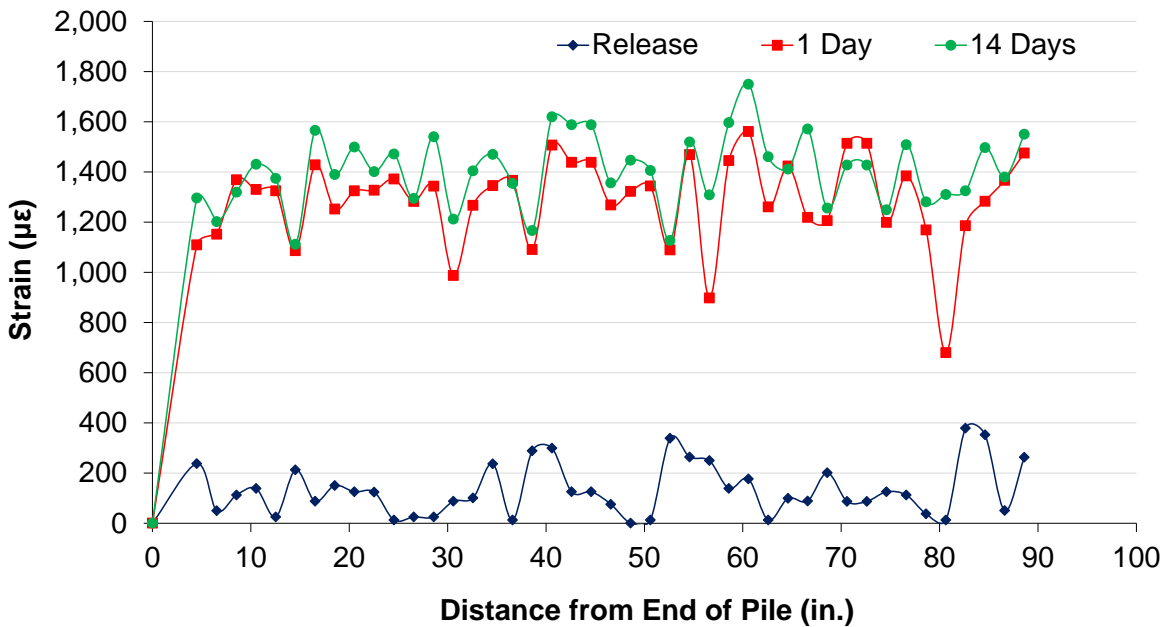
Figure 9.3 Raw concrete surface strain profile for Pile 1080 #1 – Jacking End.
1 in. = 2.54 cm

127

The CSS method smooths the raw strain profile shown in Figure 9.3 by averaging every three consecutive readings. The objective of the smoothening of the curve is to reduce anomalies and remove part of the noise associated with the measurement acquisition. Equation 9.1 was used for smoothening of raw data (Russell and Burns, 1993).

$$\varepsilon_i = \frac{\varepsilon_{i-1} + \varepsilon_i + \varepsilon_{i+1}}{3} \qquad (9.1)$$

where ε_i is the i-th strain for $i = 2,\ldots, 42$ in the case of the prestressed concrete piles.

As a result, the profile in Figure 9.4 was obtained by the smoothening of raw strain profiles. The smoothed strain profile was used to determine the transfer length of the prestressed concrete element. It should be noted that the distances of the reading points are also averaged in the smoothed profile. Thus, the initial strain of the raw profile (Figure 9.3) is located at 4.51-in. (11.46 cm) from the end of the pile, while the first averaged strain of the smoothed profile is positioned at 6.53-in (16.59 cm) from the end of the pile.
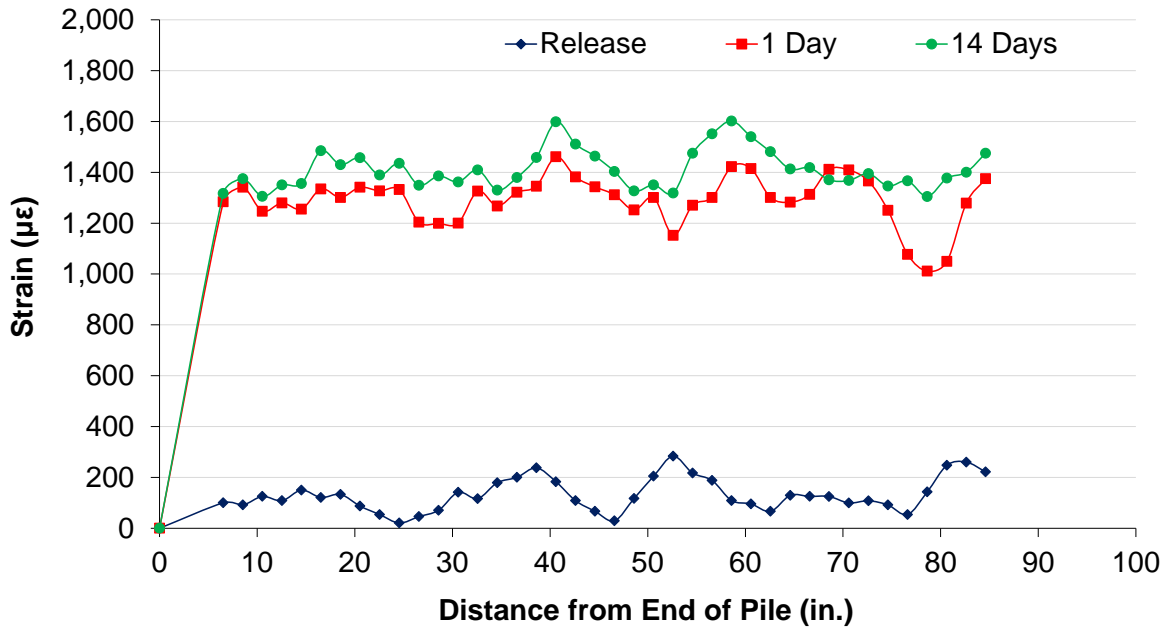
Figure 9.4 Smoothed concrete surface strain profile for Pile 1080 #1 – Jacking End.
1 in. = 2.54 cm

As mentioned by Russell and Burns (1993), DEMEC readings determine the average deformation of the concrete surface along the gauge length. In combination with the smoothening process, the averaged strain along the pile length shows a reduction of the slope around the position of the transfer length and the profile deviates from the assumed transferred strain profile (Figure 9.1), which usually artificially increases the calculated transfer length.

Following the smoothening of raw data, the calculation of the transfer length is performed by the 95% average maximum strain (AMS) method. In this method, the average maximum strain is calculated as the average of the strains in the constant strain plateau (section of the profile corresponding to the full transfer of the prestressing force). Then, a line corresponding to 95% of this value is intersected with the initial linear trend of the smoothed curve to obtain the transfer length of the element, as seen in Figure 9.5. The use of the 95% AMS method corrects part of the inaccuracies introduced by the

smoothening of the curve, and the obtained transfer length is still conservative compared with the one calculated if a bilinear strain profile is used.
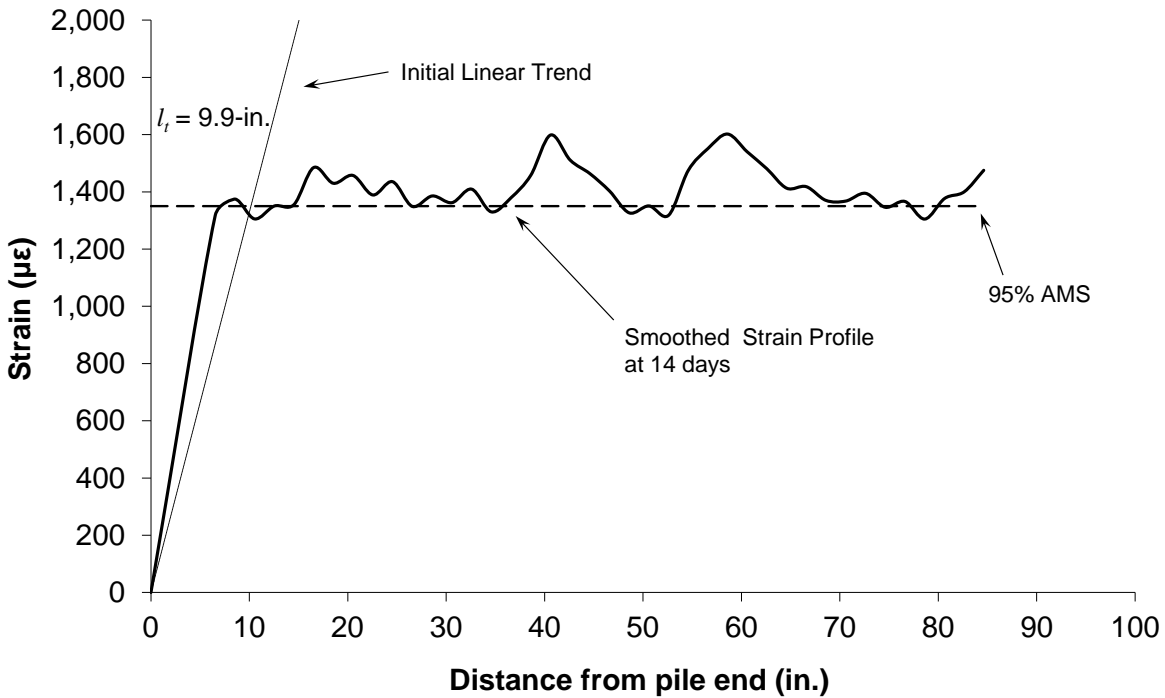
Figure 9.5 Determination of transfer length from the smoothed strain profile for Pile 1080 #1 – Jacking End at 14-days after release. 1 in. = 2.54 cm

Given that some of the piles showed strains before the constant strain plateau that are not clearly represented by a straight line and to avoid arbitrary interpretation of the data, the initial linear trend was calculated by the ordinary least squares method with a zero intercept.

To understand the effect of driving on the transfer length of prestressed concrete piles, the same procedure was repeated after the driving and extraction operation. Smoothed strain profiles and transfer length determination of the piles before and after driving can be observed in Appendix M.

130

9.2 Transfer Length Results

Table 9.1 shows the calculated transfer length before and after driving for each pile end using the CSS method. Experimental transfer lengths are compared with predicted values by AASHTO LRFD and ACI 318. In each case, the jacking end of the pile was the one which was hit by the pile driver hammer.

Table 9.1 Summary of transfer lengths of piles before and after driving. The percentage of the value given by AASHTO LRFD is shown in parenthesis. 1 in. = 2.54 cm.

Pile End	Day 14	Average Day 14	Day 273, after driving	Average Day 273	AASHTO LRFD (2013)	ACI 318 (2011)
1080 #1 Jacking End	9.9-in. (38%)		10.0-in. (38%)			
1080 #1 Dead End	22.2-in. (85%)	**17.8-in. (68%)**	22.0-in. (84%)	**15.2-in. (58%)**	26.3-in.	25.5-in.
1080 #2 Jacking End	13.4-in. (51%)		12.3-in. (47%)			
1080 #2 Dead End	25.5-in. (97%)		16.4-in. (62%)			
HSSS 2205 #1 Jacking End	9.8-in. (33%)		10.3-in. (34%)			
HSSS 2205 #1 Dead End	15.6-in. (52%)		11.5-in. (38%)			
HSSS 2205 #2 Jacking End	17.3-in. (58%)	**17.1-in. (57%)**	23.7-in. (79%)	**17.3-in. (58%)**	30.0-in.	21.2-in.
HSSS 2205 #2 Dead End	24.7-in. (82%)		24.0-in. (80%)			
HSSS 2205 #3 Jacking End	13.6-in. (45%)		13.3-in. (44%)			
HSSS 2205 #3 Dead End	21.7-in. (72%)		20.9-in. (70%)			

The average transfer length of HSSS 2205 ½-in. strands and AISI 1080 conventional 7/16-in. (11.1 mm) strands are lower than the respective AASHTO and ACI calculated values. At 14 days for the AISI 1080 strands, the average transfer lengths were

68% and 66% of the AASHTO and ACI 318 lengths, respectively. At 14 days for the duplex HSSS 2205 strands, the average transfer lengths were 57% and 74% of the AASHTO and ACI 318 lengths, respectively. Also, individual results at 14 and 273 days ranged between 33% and 97% of the AASHTO prediction. Conversely, the transfer lengths of conventional steel strands were less than the ACI equation, but not all of the duplex HSSS 2205 strand lengths were.

In the case of pile HSSS 2205 #2, one end showed a transfer length higher than the ACI 318 prediction before driving, while both ends showed a higher transfer length after driving. Pile HSSS 2205 #2 was not easily removed from the form bed during fabrication and additional mechanical hammering was required. This early disturbance and vibration of the pile may have contributed to the relatively higher transfer length values.

Transfer length results present an important variability, with values ranging from 9.8-in. (24.9 cm) to 25.5-in. (64.8 cm). Transfer length of pretensioned elements may be influenced by strand diameter, specimen cover, concrete strength at strand release, and is usually higher at the cut end (Oh and Kim, 2000; Oh et al., 2006). As mentioned in Chapter 4, the use of concrete mixtures from different batches introduced variability in the strength of concrete for different specimens. Even when concrete strength measured in cylinders before strand release was 4,018 psi (27.7 MPa), it is expected that concrete strength varied among the piles. Additionally, results show that the tested end of the pile has a high influence on the obtained transfer length. Calculated transfer length at the jacking end was lower than the dead end (anchorage end) in all cases. The anchorage end

had approximately 100 ft. (30.5 m) of free strand compared to about 10 ft. (3 m) at the jacking end.

Pile driving had little effect on calculated transfer length. While Figures M.1 to M.10 in Appendix M show an increase of the overall compressive strain after driving, the transfer lengths remained the same.

9.3 Comparison of Results with Proposed Expressions

Expressions for transfer length reported by previous studies and detailed in Chapter 2 are compared with experimental results in Table 9.2. Calculation of transfer lengths considers prestress losses obtained by the AASHTO refined estimation method. Percentage difference was calculated using Equation 9.2. Thus, a positive difference between experimental l_t and a proposed equation indicated that the equation is a conservative prediction.

$$Difference = \frac{l_{t,proposed} - l_{t,\exp erimental}}{l_{t,\exp erimental}} \tag{9.2}$$

Experimental results are conservative compared to most of the expressions. The equation described by Buckner (1995) for the best fit for transfer length results, calculated using the 95% AMS method from data originated in many research programs, is the only non-conservative expression for both types of steel.

Equations based only on the diameter of the prestressing strand (AASHTO LRFD (2013) and Martin and Scott (1976)) are overly conservative for duplex HSSS 2205

133

strand. These equations consider the increase of the transfer length when strands with higher diameter are used. In this case, the same jacking force was applied to the piles, therefore a lower initial prestress was applied to duplex HSSS 2205 strands.

Table 9.2 Comparison of experimental transfer length with code values and research proposed expressions. 1 in. = 2.54 cm.

	Duplex HSSS 2205		AISI 1080 Steel	
	l_t (in)	Difference	l_t (in)	Difference
Experimental	**17.1**	---------	**17.8**	---------
AASHTO LRFD	**30.0**	+ 75.2%	**26.3**	+ 47.9%
ACI 318	**21.2**	+ 24.1%	**25.5**	+ 43.5%
Zia and Mostafa	**22.3**	+ 30.2%	**26.8**	+ 50.7%
Martin and Scott	**40.0**	+ 133.6%	**35.0**	+ 97.2%
Russell and Burns	**31.9**	+ 86.1%	**38.2**	+ 115.2%
Deatherage et al.	**23.9**	+ 39.6%	**27.9**	+ 57.0%
Mitchell et al.	**20.5**	+ 19.7%	**23.9**	+ 34.6%
Buckner – Design	**23.9**	+ 39.6%	**27.9**	+ 57.0%
Buckner – Best Fit	**14.6**	− 14.7%	**17.0**	− 4.1%
Lane	**32.0**	+ 87.2%	**42.1**	+ 137.2%
Meyer – Design	**30.6**	+ 78.8%	**26.8**	+ 50.9%
Meyer – Best Fit	**25.0**	+ 46.0%	**21.9**	+ 23.2%
Ramirez and Russell	**20.0**	+ 16.8%	**17.5**	− 1.4%

Expressions using stress in prestressing strand after release, f_{si}, (i.e., stress after losses due to elastic shortening) and concrete strength at release, f_{ci}', provide better agreement with experimental transfer lengths than the predictions using the effective stress at the prestressing strand after all losses, f_{se}. It has been observed previously that transfer length of pretensioned members is directly related to the stress of prestressing strand right after or at release and inversely related to the strength of concrete at release (Oh and Kim, 2000; Barnes et al., 2003). The use of these parameters can account for the use of non-conventional strands.

9.4 Conclusions of the Chapter

Transfer length of prestressed concrete piles using duplex HSSS 2205 strands can be conservatively estimated using predicted values by AASHTO LRFD and ACI 318. Additionally, pile driving does not affect the transfer length of prestressed concrete piles.

CHAPTER 10

DEVELOPMENT LENGTH

The development length of the ½-in. (12.7 mm) diameter HSSS 2205 prestressing strand was determined experimentally by testing the 27-ft. (8.23 m) long composite pile specimens. Development length is the length of prestressing strand required to develop the design strength of the prestressing strand, f_{ps}. When the tension in the strand increases by the action of external forces, the bond stress also increases to maintain the equilibrium and to anchor the strand (Russell and Burns, 1993). Thus, the development length can be defined as the minimum embedment required to avoid strand slip when the design stress of the strand is reached (Buckner, 1995). Figure 10.1 shows an idealized model of the steel stress buildup, starting from the free end of the pile, until the design stress f_{ps} is reached at l_d.
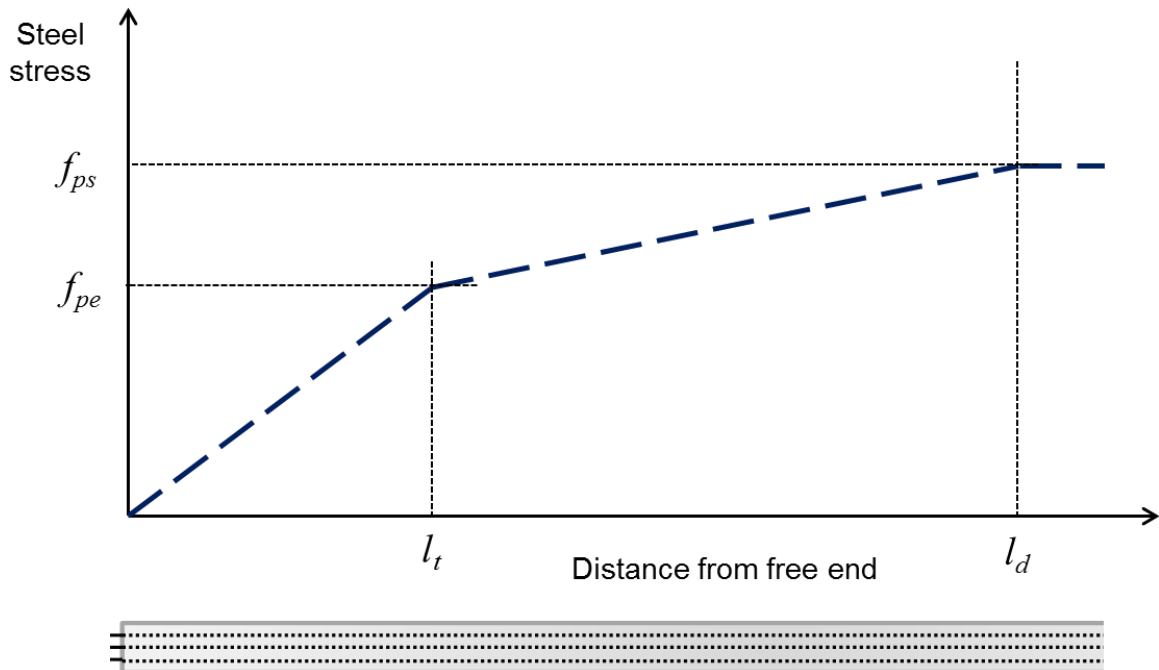
Figure 10.1 Idealized steel stress along the pile.

ACI 318 (2011) and AASHTO LRFD (2013) define the development length required for bonded prestressing strands in pretensioned members using the expressions given in Equations 10.1 and 10.2, respectively. For pretensioned members with a depth greater than 24-in. (61.0 cm), the AASHTO equation increases the calculated l_d by 60% using the 1.6 factor shown in Equation 10.2.

ACI:
$$l_d \geq \left(\frac{f_{se}}{3,000} \right) \cdot d_b + \left(\frac{f_{ps} - f_{se}}{1,000} \right) \cdot d_b \qquad (10.1)$$

AASHTO:
$$l_d \geq 1.6 \cdot \left(f_{ps} - \frac{2}{3} f_{pe} \right) \cdot d_b \qquad (10.2)$$

where d_b is the nominal diameter of strands, f_{ps} is the stress in the prestressing steel at the time of the nominal resistance (experimental failure) of the pile, and f_{pe} (f_{se} in ACI 318) is the effective stress in the prestressing strand after losses.

The development length of duplex HSSS 2205 strands was evaluated by loading the composite 27-ft. (8.23 m) piles in flexure. Embedment length (distance between pile end and applied load) at which strand slip was greater than 0.01-in. (0.254 mm) was considered lower than l_d. Experimental results of piles constructed using duplex HSSS 2205 and conventional steel strands showed development lengths 85% to 88% of the value predicted by ACI 318, and 53% to 55% of the value predicted by AASHTO LRFD.

It was concluded that the use of ACI 318 and AASHTO LRFD to predict the development length of duplex HSSS 2205 strands is conservative.

The setup of the flexural test used for development length determination is discussed below. The results of the tests are compared with the predicted values from the codes and expressions proposed in the literature.

10.1 Test Description

A flexural test for the determination of the development length was performed on 27-ft. (8.23 m) long piles, after the addition of a top concrete section that increased the depth of the section to 43-in. (109.2 cm). During testing, the average compressive strength of concrete in the piles was 10,728 psi (74.0 MPa), while the compressive strength of the top, composite concrete section of the piles using duplex HSSS 2205 and conventional steel strands was 5,925 and 6,251 psi (40.9 and 43.1 MPa), respectively. Details of the construction of the specimens are given in section 3.3 and in Appendix B.

The 27-ft. composite pile sections were simply supported and loaded at a variable embedment length with two point loads spaced 4-in. (10.16 cm) apart. The load was applied by a 500 ton hydraulic ram, equipped with a 1,000 kip (4.45 MN) load cell. A W10×77×24-in. (25.4×195.6×61 cm) long steel beam with stiffeners was placed under the load cell, supported by two 1-in. diameter rollers. The displacement of the pile at the position of load was recorded using a string potentiometer. The diagram in Figure 10.2 shows the test setup.

Three dial gauges were attached at each side of the piles to estimate the strains in the prestressing strands and at the top section. Gauge lengths of 35-in. (89 cm) and 17.5-in. (44.5 cm) were used for the measurement of the strains in the strands and at 1-in. below the top of the composite section, respectively, as shown in Figure 10.3.

138

At the end of the pile closer to the applied load, four dial gauges were epoxied to the bottom row of strands and two additional dial gauges were attached to the pile in order to determine strand slip (Figure 10.4). A strand slip higher than 0.01-in. indicated slip and that the bond stress capacity was not able to counteract the increasing stress in the prestressing steel, meaning that the embedment length was lower than the development length.

Load was applied monotonically and was intermittently paused to mark crack patterns and to record dial gauge measurements.
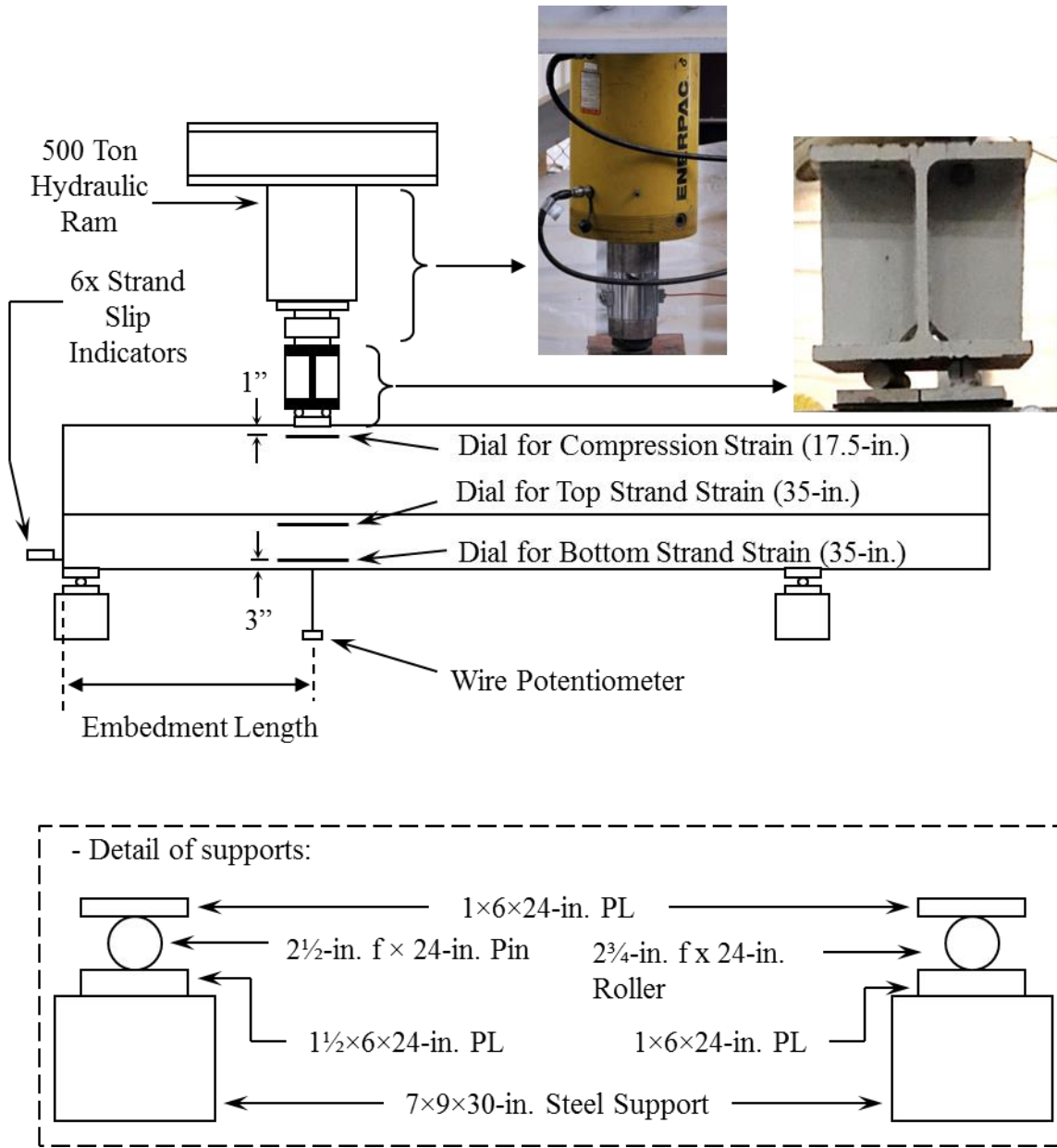
Figure 10.2 Setup for development length test. 1 in. = 2.54 cm.

Figure 10.3 Development length test. Opposite side of the pile was equipped with analog dial strain gauges, in the same way as shown in the picture.

Figure 10.4 Analog dial gauges were epoxied to bottom strands for slip determination.

In order to identify the minimum embedment length that provided development of the strands, the initial test was performed using the value predicted by the ACI Equation 10.1, where f_{ps} was defined as the ultimate stress of the strand. Then, the embedment length was progressively reduced until shear failure or strand slip occurred (74% of the predicted development length); Table 10.1 shows the embedment length tested for every pile and their ratio with respect to the predicted development length. Eight development length tests were performed, four for each type of prestressing steel.

Table 10.1 Embedment lengths used for development length determination. 1 in. = 2.54 cm.

Pile	Embedment Length (in.)	% l_d ACI Eq. 10.1	% l_d AASHTO Eq. 10.2	Failure Mode
AISI 1080 Steel	53.5	74%	46%	shear/bond
	57	79%	49%	shear/bond
	61	85%	53%	flexure
	72	100%	62%	flexure
Duplex HSSS 2205	57	73%	46%	shear/bond
	61.75	79%	49%	shear/bond
	69	88%	55%	flexure
	79.75	102%	64%	flexure

10.2 Development Length Results

In all the tests, the first flexural crack appeared when the load was about 60% of the ultimate load and the tests were stopped when the beam failed in either a flexural mode or shear/bond mode.

Load-deflection curve, strain distribution of the section during the test, moment-curvature curve, and shear-strand slip curve for each individual development length test are given in Appendix N.

10.2.1 Strand slip results

Displacements measured by the dials epoxied to the strands were subtracted from that measured by the dials epoxied to the end of the pile. The relative displacement of the strand with respect to the pile was the strand slip. Figure 10.5 shows the results of shear vs. average slip for each test, and Figure 10.6 shows the slip at failure for each embedment length.
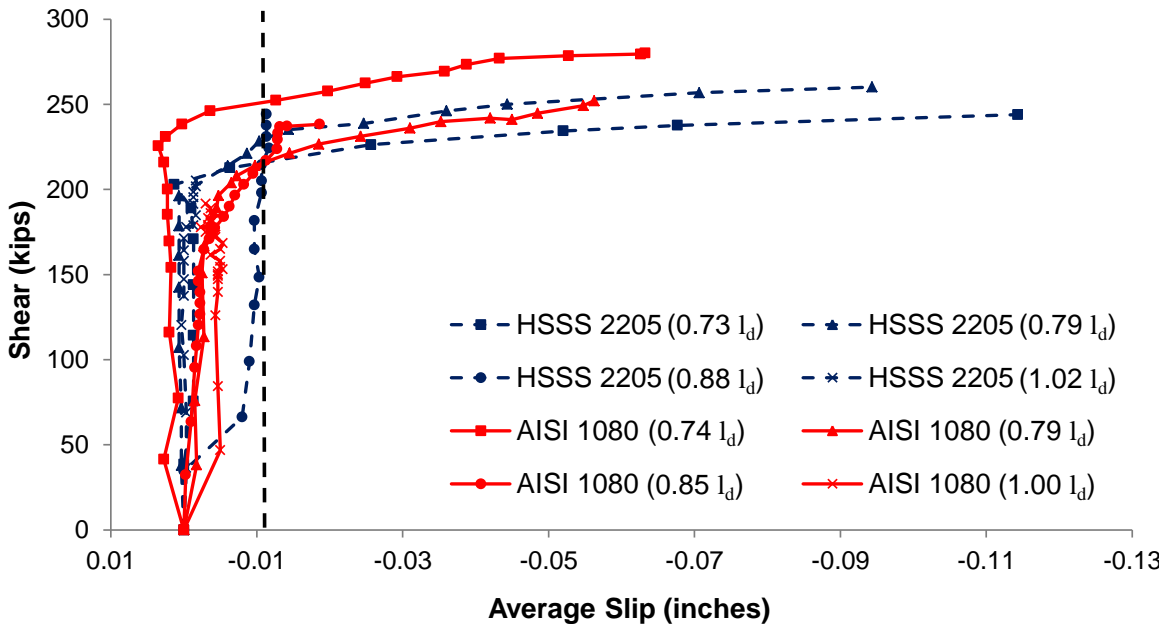
Figure 10.5 Average strand slip with shear increase during testing. Dashed, vertical line shows limit of 0.01-in. (0.254 mm) for strand slip at failure. 1-in. = 2.54 cm.

When the theoretical l_d calculated using Equation 10.1 was used as embedment length, negligible strand slips were observed (0.002-in. [0.0508 mm] and 0.003-in. [0.0762 mm] for duplex HSSS 2205 and conventional steel strands, respectively).

143

Embedment lengths corresponding to a 79% and 74% of the predicted l_d by Equation 10.1 exhibited strand slip that exceeded the 0.01-in. (0.254 mm) limit. Embedment length of 85% l_d for conventional steel strands and 88% l_d for duplex HSSS 2205 strands corresponded to strand slip at failure closest to 0.01-in. (0.254 mm).
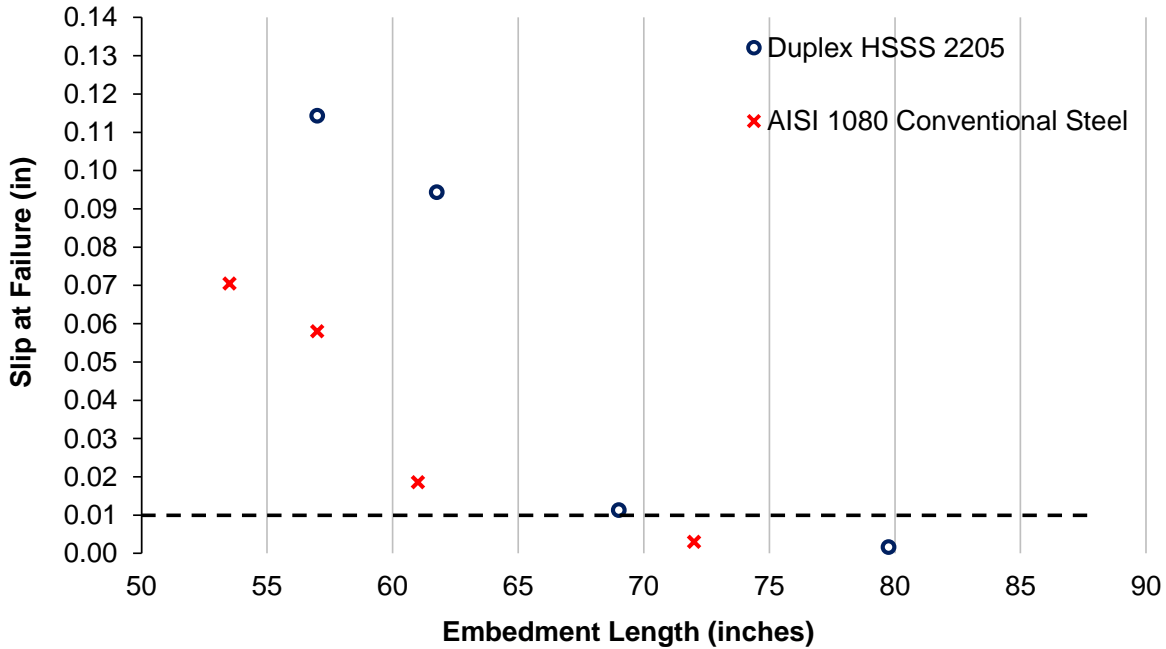
Figure 10.6 Slip at failure. Dashed line shows the assumed slip failure limit and defined flexure and shear failure of piles. The calculated l_d by Equation 10.1 for duplex HSSS 2205 and conventional steel are 78.3 and 72.0-in., respectively. Using Equation 10.2, these values are 125.2 and 115.3-in., respectively. 1 in. = 2.54 cm.

Figure 10.7 shows the strain and stress at the bottom layer of strands during the test. The initial stress corresponds to the effective stress of the prestressing strands (f_{se} or f_{pe}) at start of testing. This value was calculated by subtracting the experimental losses measured with internal vibrating wire strain gauges from the initial jacking stress. Increasing strains in the strands during the test were measured using the external strain gauges located at the depth of the bottom layer. The measured stress-strain curves of the

144

prestressing strands were used to determine the strand stress based on the measured strand strains.

Figure 10.8 shows the stress at the bottom layer of strands vs. average slip. It is observed that the use of an embedment length of 73% l_d for duplex HSSS 2205 strands was the only test where the ultimate estimated stress was lower than 97% of the UTS.
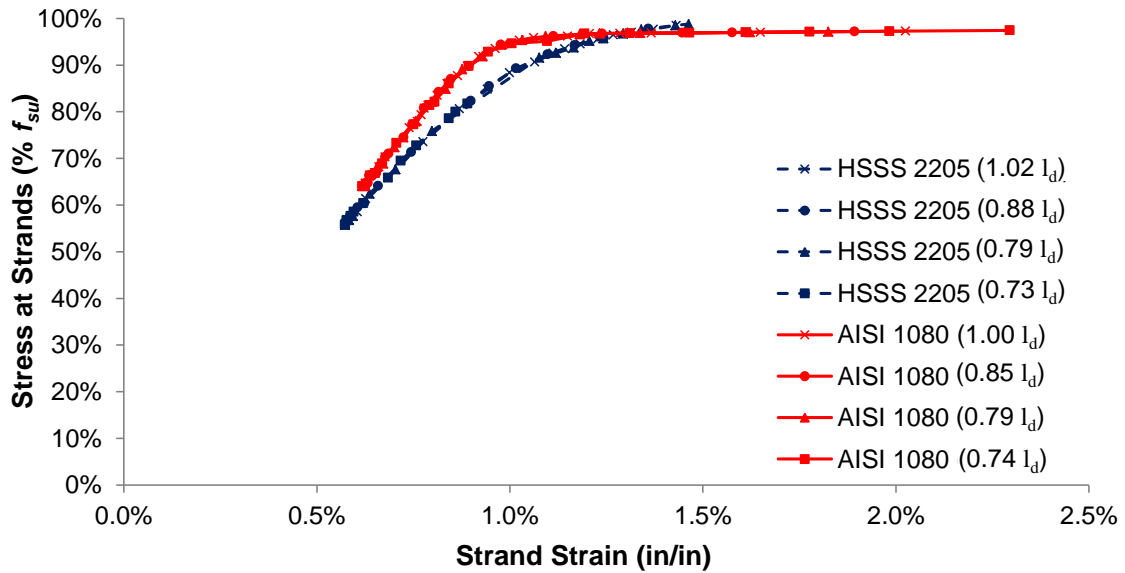
Figure 10.7 Stress and strain of bottom layer of strands during testing. Stress is shown as percentage of the UTS of the strand.
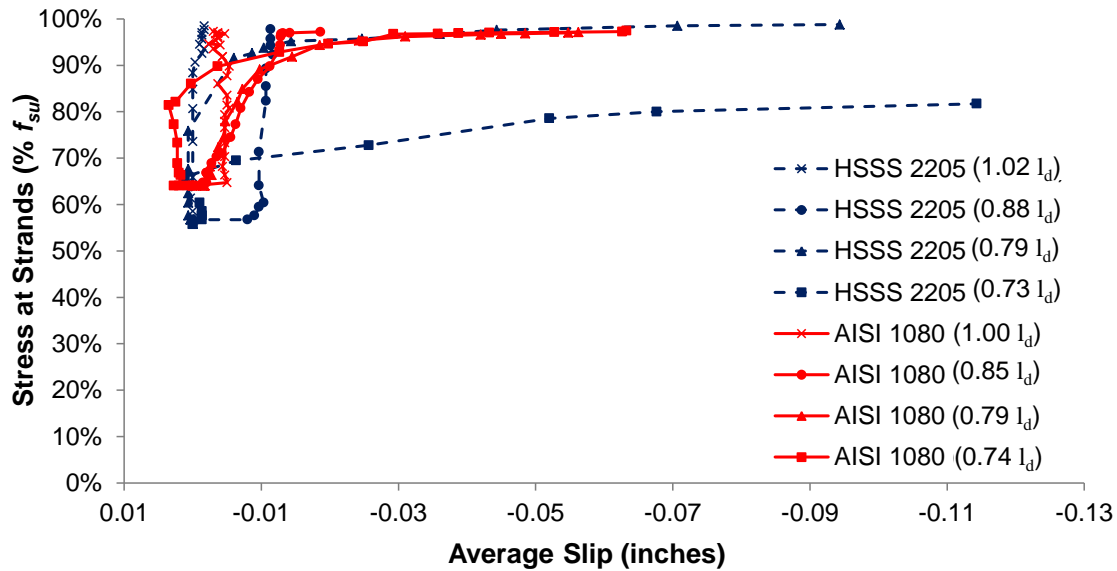
Figure 10.8 Average strand slip with stress increase in the bottom layer of strands. Stress is shown as percentage of the UTS of the strand. 1-in. = 2.54 cm.

For conventional steel strands, ultimate stress estimated in all the tests ranged

between 97.2% and 97.4% of f_{su}. Ultimate strains ranged between 1.83% and 2.29%; the

test with shortest embedment length (0.74 l_d) was the one with the highest strand strains.

In the case of duplex HSSS 2205 strands, ultimate stresses and strains of the

bottom strands for embedment lengths 102%, 88%, and 79% l_d ranged between 97.8%

and 98.8% of the UTS, and between 1.36% and 1.46%, respectively. However, for the

test with the shorter embedment length (73% l_d) the ultimate stress was only 81.7% of the

UTS at strand slip.

The differences between both types of steel can be explained by the higher

ductility of conventional steel strands compared to duplex HSSS 2205 strands given in

Table 4.1 (ε_u of 5.89% vs. 1.60%).

The experimental development length was selected as the lowest embedment

length for which the strand slip was less than 0.01-in and in which the member failed in a

flexural rather than shear/bond mode. From Table 10.1, the shortest embedment length

which led to a flexural failure with no strand slip was 61 in. for piles made with

conventional 1080 strand and was 69 in. for piles made with HSSS 2205 strand. This

meant that the experimental development length of conventional 1080 strand was 85% of

the predicted value by ACI 318 and 53% of the predicted value by AASHTO LRFD. The

experimental development length of duplex HSSS 2205 strand was 88% of the predicted

value by ACI 318 and 55% of the predicted value by AASHTO LRFD. Thus, the use of

ACI 318 Equation 10.1 and AASHTO LRFD Equation 10.2 to estimate the development

length of duplex HSSS 2205 strands gave values which were greater than the

experimental values; therefore, use of those standard equations is conservative.

10.2.2 Failure type

Crack pattern observed in both types of failure is shown in Figure 10.9, where the

number next to the crack corresponds to the recorded load at the time that the crack was

at the cross-mark position. Loads in Figure 10.9 are different than the shears given in

Figure 10.5.

(a)
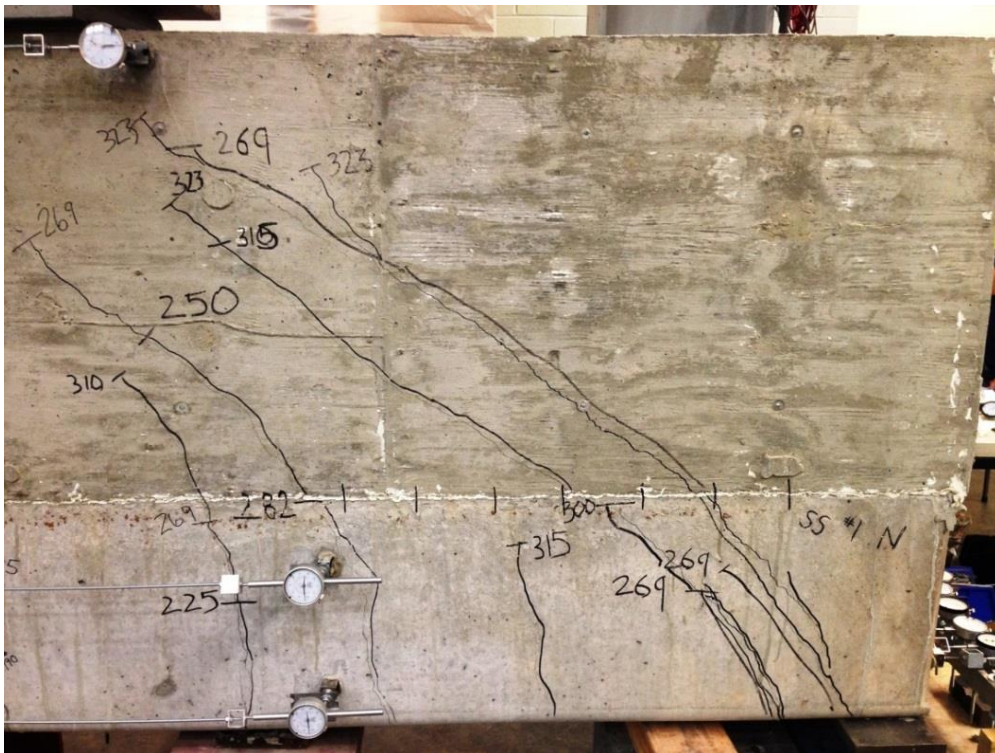
(b)

Figure 10.9 Typical crack pattern exhibited after (a) flexural failure when the strands ruptured, and (b) shear/bond failure of piles. 1 kip = 4.45 kN.

Good composite behavior was evidenced by the continuity of the cracks between the precast pile and poured-in-place top section.

Piles loaded at an embedment length around 102% and 88% of l_d predicted by ACI 318 exhibited a typical flexural failure (Figure 10.9a) with the HSSS 2205 strand breaking at the end of the test and with strand slips lower or similar to the 0.01-in. (0.254 mm) limit. After strand breaking, the rupture of the whole section was observed at the location of the applied load.

Piles loaded at embedment lengths of 79% and 73% of l_d predicted by ACI 318 showed shear failure (Figure 10.9b). Shear cracks initiated at 2 to 8-in. (5 to 23 cm) from the pin support at a moment that coincided with the onset of slip of the strands (see Figure 10.5). Large increases of strand slip after initiation of shear cracks in the transfer length zone have also been reported by Meyer (2002) and Russell (1992).

The first shear crack extended from the bottom of the pile to the mid-height of the original pile, passing through at least two rows of strands at an angle approximately 45° from the horizontal. Tests that exhibited shear failures were stopped after a sudden drop of the recorded load was observed, which corresponded to strand slip and before a general rupture of the section.

10.2.3 Moment-curvature behavior

The experimental curvature was estimated using the strain distributions included in Appendix N, which were determined from the strain gauges attached to the sides of the composite pile specimens; the experimental moment was estimated using the applied load and the actual position of the load with respect to the supports.

Figure 10.10 shows the experimental moment curvature for duplex HSSS 2205 (blue lines) and conventional steel (red lines) piles. Black lines show the predicted, theoretical behavior using a Todeschini concrete stress block (Wight and MacGregor, 2011).
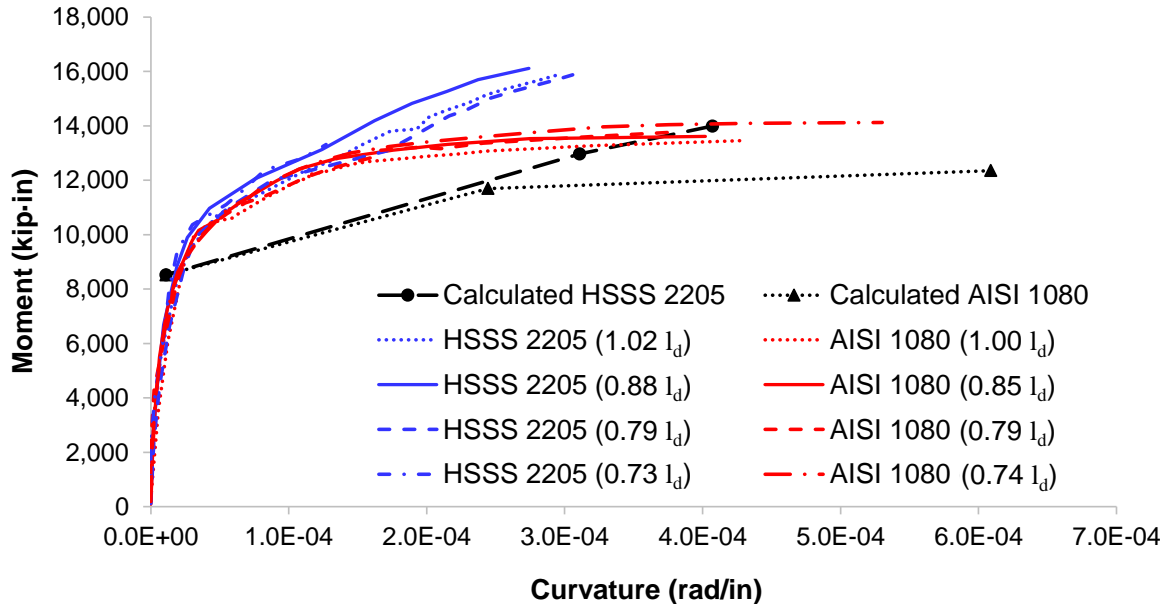
Figure 10.10 Experimental and predicted moment-curvature results. The ratio of the actual embedment length to predicted development lengths from Equation 10.1 are given in parentheses. 1 kip·in = 113 N·m, 1 rad/in = 39.37 rad/m.

Piles using both types of steel showed higher ultimate moments than predicted values. It is noted that the comparison of the nominal capacity of the piles should be made with experimental results that showed no strand slip, given that this assumption is made on the theoretical calculation.

In the case of conventional steel strand, the ultimate moment is similar for every test. However, the test that showed highest strand slip (0.071-in. [1.8 mm]) also exhibited an ultimate curvature 32% higher than the average of the rest of the tests. The difference

in ultimate curvature can be attributed to a higher deformation of the horizontal strain

gauges due to the combined effect of the applied load and the slip of the strands.

However, using the measurement of the deformations of the pile, an estimated ultimate

stress in the bottom strands of about 273.5 ksi was calculated in each case.

For the piles using duplex HSSS 2205 strands, similar behavior was observed on

tests with the three higher embedment lengths, but the test with the lowest embedment

length and highest strand slip (0.114-in. [2.9 mm]) present an ultimate moment and

curvature 17% and 57% lower than the average of the rest of the tests, respectively. Also,

the estimated ultimate stress in the bottom strands dropped from 237.9 ksi ($l_e = 1.02\ l_d$,

[1,640 MPa]) to 197.4 ksi ($l_e = 0.73\ l_d$, [1,361 MPa]).

10.2.4 Evaluation of development length using experimental prestress losses

The calculation of f_{pe} and f_{se} in Equations 10.1 and 10.2 was performed by the

estimation of prestress losses at testing time using the AASHTO refined method (Chapter

8 and Appendix K). However, the measured losses were lower than the predicted ones.

Thus, the use of experimental losses leads to lower calculated development lengths for

the piles.

Estimated prestress losses during testing were 21.0 and 19.6 ksi (145 MPa and

135 MPa) for piles using conventional steel and duplex HSSS 2205 strands, respectively;

measured prestress losses closest to testing time were 14.0 and 12.3 ksi (96.5 MPa and

84.8 MPa). Using the latter values for the estimation of the development length in

Equation 10.1, l_d changes from 72.0-in. to 70.0-in. (182.9 to 177.8 cm) for piles using

conventional steel, and from 78.3-in. to 75.8-in. (198.9 to 192.5 cm) for piles using duplex HSSS 2205.

Considering this change, embedment lengths that exhibited strand slips close to 0.01-in. correspond to 87% and 91% of l_d based on Equation 10.1 for piles using conventional steel and duplex HSSS 2205 strands, respectively. Thus, the experimental estimations of development length remain conservative when actual losses are considered in the calculation of l_d.

10.3 Comparison of Results with Proposed Expressions

Table 10.2 shows the experimental estimation of the development length compared to expressions proposed in the literature. The difference was calculated with respect to the experimental estimation, according to Equation 10.3.

$$Difference = \frac{l_{d,proposed} - l_{d,\exp erimental}}{l_{d,\exp erimental}} \tag{10.3}$$

Expressions with positive difference were considered conservative. Thus, equations proposed by Russell and Burns (1993), Mitchell et al. (1993), and Ramirez and Russell (2008) are non-conservative expressions for the estimation of l_d.

Good approximations of development length consider the nominal diameter of strand, d_b, the stress in the strand after transfer, f_{si}, the effective stress after prestress losses, f_{pe} or f_{se}, and the stress in the strand at nominal strength of member, f_{ps}. Concrete strength at strand release is also considered by some of the theoretical relations.

Table 10.2 Comparison of experimental l_d with codes values and research proposed expressions for development length. 1 in. = 2.54 cm.

	Duplex HSSS 2205		AISI 1080 Steel	
	l_d (in)	Difference	l_d (in)	Difference
Experimental	69.0	---------	61.0	---------
ACI 318	78.3	+ 13.4%	72.0	+ 18.1%
AASHTO LRFD	125.2	+ 81.4%	115.3	+ 89.0%
Zia and Mostafa	93.5	+ 35.6%	85.0	+ 39.3%
Martin and Scott	115.3	+ 67.1%	141.5	+ 132.0%
Russell and Burns	52.3	− 24.2%	55.4	− 9.2%
Deatherage et al.	109.4	+ 58.6%	97.7	+ 60.2%
Mitchell et al.	59.5	− 13.8%	55.7	− 8.6%
Buckner	94.6	+ 37.1%	165.5	+ 171.4%
Lane	93.0	+ 34.8%	88.5	+ 44.3%
Meyer – Design	84.9	+ 23.1%	71.0	+ 16.4%
Meyer – Best Fit	76.7	+ 11.2%	63.9	+ 4.7%
Ramirez and Russell	50.0	− 27.5%	43.8	− 28.3%

Equations included in ACI 318 (2011) and AASHTO LRFD (2013) provided conservative estimations for transfer and development length. Additionally, Table 10.3 shows the expressions proposed in the literature that gave closer approximations of experimental transfer and development length for piles using duplex HSSS 2205 and conventional steel strands. The selection of the best proposed equations other than ACI

and AASHTO are those which gave a ratio of experimental-to-predicted development

length and a ratio of experimental-to-predicted transfer length less than 1.0.

Table 10.3 Expressions closer to experimental values.

Zia and Mostafa (1977)	l_t	$l_t = 1.5 \dfrac{f_{si}}{f'_{ci}} d_b - 4.6$
	l_d	$l_d = \left(1.5 \dfrac{f_{si}}{f'_{ci}} d_b - 4.6 \right) + 1.25 \left(f_{su} - f_{se} \right) \cdot d_b$
Deatherage et al. (1994)	l_t	$l_t = \dfrac{f_{si} \cdot d_b}{3}$
	l_d	$l_d = \dfrac{f_{si} \cdot d_b}{3} + 1.50 \left(f_{su} - f_{se} \right) \cdot d_b$
Meyer (2002)	l_t	$l_t = 50 \cdot d_b \sqrt{\dfrac{6{,}000}{f'_{ci}}}$
	l_d	$l_d = \left(50 \sqrt{\dfrac{5{,}000}{f'_{ci}}} + f_{ps} - f_{se} \right) \cdot d_b$

10.4 Conclusions of the Chapter

Experimental development length of duplex HSSS 2205 strands were found to be

88% of the specified value computed by ACI 318, and 55% of the specified value

computed by AASHTO LRFD. Thus, development length of prestressed concrete piles

using duplex HSSS 2205 strands can be conservatively estimated using equations given

by AASHTO LRFD and ACI 318.

CHAPTER 11

LONG-TERM DURABILITY ASSESSMENT

Eight 20-in. (50.8 cm) long specimens were placed in the tidal zone of the Savannah River to evaluate the long-term performance of prestressed concrete piles, using duplex HSSS 2205 and conventional steel, exposed to marine environments. Periodic extraction of cores and evaluation of the specimens were used to determine the rate of chloride ingress as well as the extent of steel corrosion and concrete degradation due to sulfate attack, abrasion, or carbonation. Such damage to existing concrete substructure elements in coastal Georgia bridges has been described in a previous report presented to GDOT (Moser et al., 2011a).

11.1 Durability Samples

The durability specimens were prestressed in the same conditions as the piles and kept in a location adjacent to the prestressing forms for about one month (Figure 11.1). No cover was provided on two sides of each specimen in order to accelerate corrosion of the strands on those two sides. The selected location for durability assessment is the old dock at Standard Concrete Products plant in Savannah, GA, latitude 32.07876° N, longitude 81.05012° W (see Figure 11.2). Average high and low annual temperatures were 77.4° F (25.2°) and 56.1° F (13.4° C), respectively, and average monthly humidity ranged between 69% and 79% during the year. The Savannah River exhibits a combination of fresh and seawater and has two tidal cycles per day according to the Center for Operational Oceanographic Products and Services, NOAA (2014). The presence of algae and mollusks were observed at the dock, a pH of 6.78 was measured

using a Thermo Scientific Orion 3-Star Plus pH Portable Meter, and a chloride ion

concentration of 4,552 mg/L was measured on water samples obtained at high tide,

following ASTM D4458.

Figure 11.1 Construction of small specimens for long term evaluation of concrete and steel.

Figure 11.2 Placement of specimens in the Savannah River.

11.2 Results

Before placing the samples in the river, five cores were drilled from different specimens at 42 days from piles construction, following the guidance of ASTM C42. A drilling head with a nominal diameter of 3-in. (76.2 mm) was used, and samples of prestressing strands and spiral wire were included on the drilled cores. The cores were transported to Georgia Tech Structures and Materials Lab in closed plastic bags, where three samples were sawed from the cores for determination of the compressive strength and were kept under fogroom conditions (73.5±3.5 °F [23.0±2.0 °C], RH > 98%) for five days before testing. These compressive strength samples were obtained from core regions without steel strands or wires (Figure 11.3).

Figure 11.3 Core drilling operation.

After 20 months (620 days) from pile construction, one specimen made with conventional reinforcement and one made with stainless steel reinforcement were retrieved from the river, cleaned to remove the river mud, and transported to Georgia Tech Structures and Materials Lab (Figure 11.4). At high tide, specimens were completely submerged; while at low tide (6 to 7-ft. lower), part of the specimens was exposed. Also, due to the difficulty to lift the specimens from the bottom of the river and the surface condition before cleaning, it is believed that the bottom section of the specimens was partially buried in the soft soil present in the dock.

In each specimen, one core was taken in the top-to-bottom direction, at the position of one of the middle strands of the top layer, and another core was taken transversally. These cores were kept in closed plastic bags at constant temperature (73.5±3.5 °F [23.0±2.0 °C]). Two compressive strength samples were cut from the cores taken from 620-day old samples.

(a)   (b)
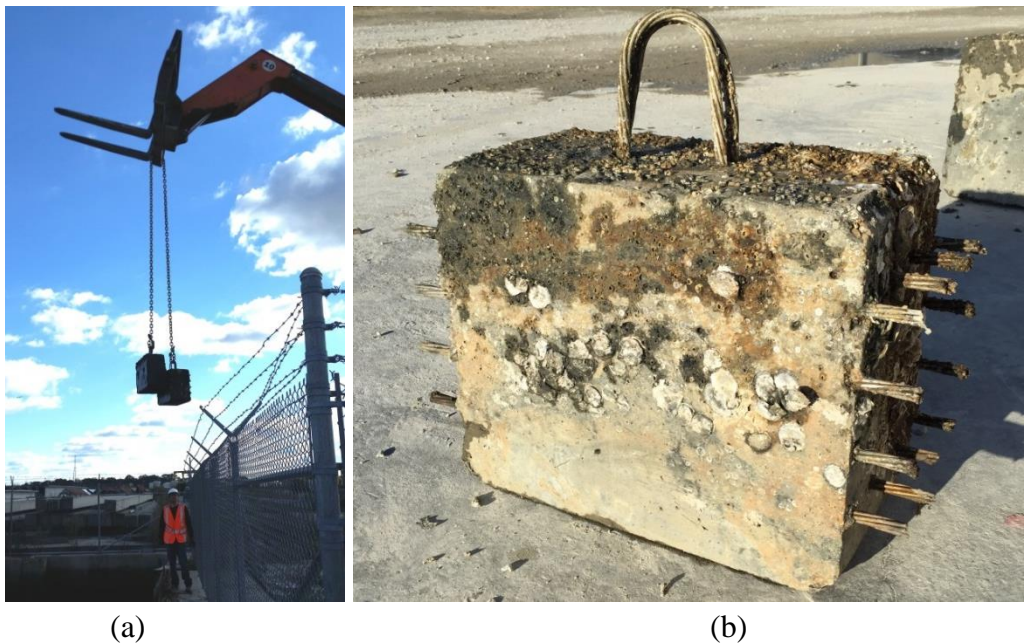
Figure 11.4 (a) Removal of specimens from the river and (b) stainless steel specimen after cleaning.

11.2.1 Compressive strength of cores

The compressive strengths of cores were compared with the strength obtained from cylinder samples corresponding to the first batch, given that this first batch was used for the small durability specimens. All of the 4x8 in. cylinder samples were kept in the fogroom until the time of testing. The ends of the core cut compression samples were smoothed with a manual rubbing stone, and unbonded rubber pad caps were used during testing. The average length-to-diameter ratio (l/d) of the 42-day old samples was 2.19, and the apparent density of the saturated cores was 147 pcf (2,355 kg/m^3). The average l/d of the 620-day old samples was 2.02, and the apparent density of the saturated cores was 144 pcf (2,307 kg/m^3). Table 11.1 shows the results obtained for both sets of samples at 42 and 620 days from casting. Following procedures from ACI 214.4R (2010), the average strength of the cores was compared to 85% of the average strength $\left(\overline{f}_c\right)$ of 6×12-in. (15.2×30.5 cm) control cylinders, and individual strength of cores was compared with the 75% of the average strength of cylinders (Table 11.1).

Table 11.1 Compressive strength of cores and cylinders of batch #1 at 42 days.
1,000 psi = 6.9 MPa, $\overline{f}_c$ = average strength of cylinders.

Age of Testing	Sample	Compressive Strength (psi)		Average of cores (psi) $> 85\% \, \overline{f}_c$	Individual cores (psi) $> 75\% \, \overline{f}_c$
		Average	Std Dev		
42 days	Cores	**6,696**	542	OK	OK
	Cylinders	**6,886**	72	5,853	5,164
620 days	Cores	**11,908**	1,154	OK	OK
	Cylinders	**9,186**	867	7,808	6,889

The higher strength observed in cylinders at 42 days is attributed to the use of fogroom curing conditions (Gonnerman and Shuman, 1928) or to the use of an l/d of the cores which was slightly higher than the specified maximum value in ASTM C42 ($l/d = 2.1$). Cylinders were demolded at the Georgia Tech Structures and Materials Lab three days after casting and kept inside the fogroom until testing, while the 42-day old cores were exposed to air curing in a coastal environment after removal from the prestressing beds. However, the objective of the determination of the compressive strength of cores was not the estimation of the strength of concrete in the piles, but to establish a baseline for future evaluations. Decrease of compressive strength typically indicates deterioration of concrete due to environmental exposure.

At 620 days, the average compressive strength of the cores was about 30% higher than the strength of the companion test cylinders.

11.2.2 Chloride content

Powder samples were obtained by drilling the cores at three different depth intervals, 0 to 1-in. (0 to 2.54 cm), 1-in. to 2-in. (2.54 cm to 5.08 cm), and 2-in. to 3-in. (5.08 to 7.62 cm) from the top surface (Figure 11.5).

Collection of pulverized concrete in 620-days cores was performed on cores obtained in the top-bottom direction, in order to determine the chloride content at the top strand position. Four measurements were made at each depth range.

Powder samples were kept in separate sealed containers, and only the fraction passing sieve No. 20 (< 850 μm) was conserved for testing. Then, the acid-soluble

content of chloride was determined by potentiometric titration (Figure 11.6), following

the procedure in ASTM C1152.

Figure 11.5 Drilled core at different depths for chloride content determination.

Concrete powder was dissolved in (1:1) nitric acid, boiled for 10 seconds, and

filtered using a Buchner funnel and filtration flask with suction through a Grade 41 coarse-

textured filter paper. Then, the sample was stirred in the presence of an indicator

silver/silver chloride standard electrode on a Metrohm 798 MPT Titrino autotitrator. The

electrode was used to measure the change of potential during the addition of a titrant

(silver nitrate solution, 0.1 N AgNO$_3$) to the sample. The equipment determines and

graphs the relationship between the potential of Ag$^+$ (calculated from the change of

potential) and the added amount of titrate. The amount of silver nitrate needed to stabilize

the reaction, identified from the inflection point of the curve, is used to calculate the

chloride content of the sample. The results are compared with a blank measurement

performed with deionized (DI) water (electrical resistivity $\rho = 18.2$ MΩ·cm).
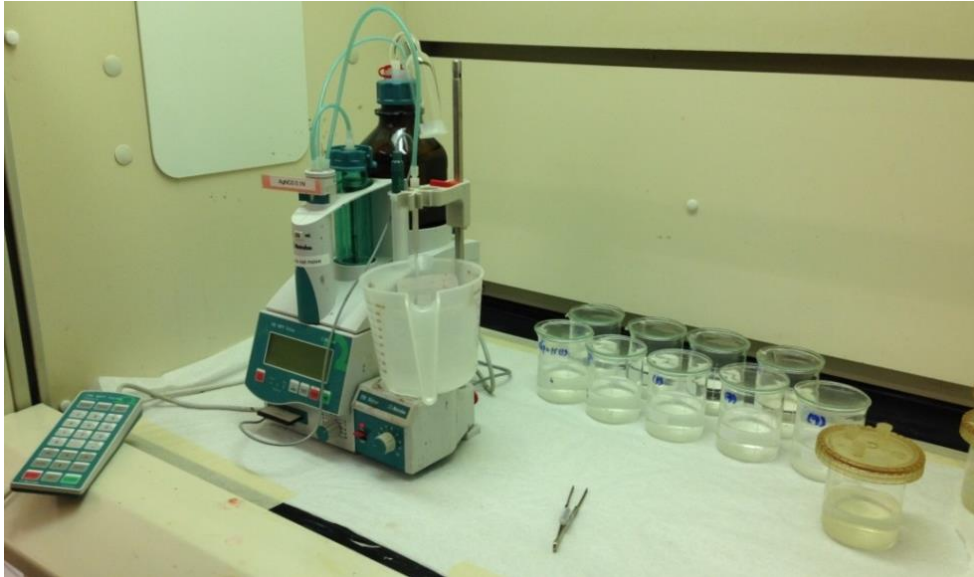
Figure 11.6 Autotitrator for chloride content determination.

The determination of the percentage of chloride that initiates steel corrosion

(chloride threshold limit, CTL) is of interest, but various CTL values have been reported

in the literature and various values are found in standards. For prestressed concrete using

conventional steel, the British standard BS 8110 set the maximum chloride content of

0.10% by mass of cement, while ACI 357 and ACI 222 use 0.06% and 0.08% for the

same CTL estimation, respectively (Ann and Song, 2007). In a previous report (Holland

et al., 2012), a value of 0.05% of chloride content by mass of concrete was chosen as a

reference for corrosion initiation. This number is the default chloride threshold for

corrosion initiation used in Life-365 software (Bentz, 2003), and the 0.05% value was

selected as a representative value of the suggested range of chloride threshold levels to initiate corrosion by Glass and Buenfeld (1997). Chloride content of 0.05% by mass of concrete is used as the CTL for durability assessment in this project.

The results of the test at 42 and 620 days are given in Table 11.2.

Table 11.2 Acid-soluble chloride content of cores, obtained by titration (ASTM C1152). 1 in. = 2.54 cm

Age of Testing	Distance from Surface	%Cl by Mass of Concrete
42 days	0 - 1 inches	0.000
	1 - 2 inches	0.000
	2 - 3 inches	0.000
620 days	0 - 1 inches	0.008
	1 - 2 inches	0.006
	2 - 3 inches	0.019

A negligible amount of acid-soluble chloride was found in the 42-days cores. In the case of 620-days samples results, the chloride content at every depth was lower than the CTL. The higher concentration in the sample obtained at 2 to 3-in. from the top surface can be explained by the chloride ingress from the side of the specimen. Top middle prestressing strands of durability specimens are at a similar distance from top and side surfaces.

11.2.3 Corrosion of prestressing strands

After the compressive strength samples were sawed from the cores, the rest of the samples were kept in an air-dried condition inside closed plastic bags. The condition of the prestressing strands was inspected using a stereo microscope.

Since corrosion of prestressing strands is typically initiated at impingement sites between prestressing wires by the influence of surface imperfections (Moser et al., 2011b), two or three wires of the strands were removed, and the crevice regions were exposed (Figure 11.7). Assessment of strand corrosion included the cores obtained from the top surface and from the side of the specimen, for both types of steel – the side samples had about 0.2-in. (5 mm) cover while the top and bottom had about 3.2-in. (81 mm) cover.

Figure 11.7 Presence of corrosion products at AISI 1080 prestressing steel (top surface core), after 620 days from casting.

(a) AISI 1080 Steel.

The condition of the conventional steel strands was compared with an AISI 1080 prestressing strand exposed to room conditions for several years. In this control sample, mild chemical action is evidenced by uniform discoloration of the impingement sites (Figure 11.8). In contrast, both AISI 1080 strand samples (top and side surface cores) show indications that suggest the initiation of localized active corrosion. Micrographs of of strand taken from the top of the top surface core are shown in Figures 11.9 to 11.11; the presence of corrosion products is observed next to regions where loss of material is appreciable, and growth of tubular corrosion products from the steel surface are noted.
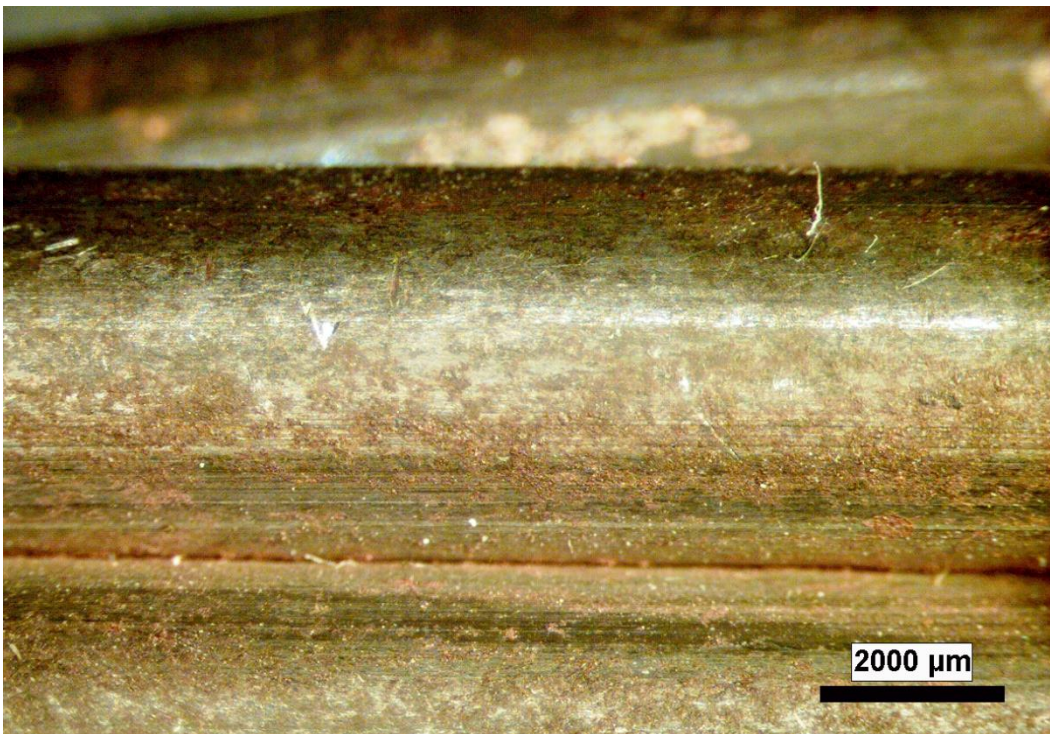
Figure 11.8 Surface of control AISI 1080 prestressing strand, exposed to room conditions (X6.5).
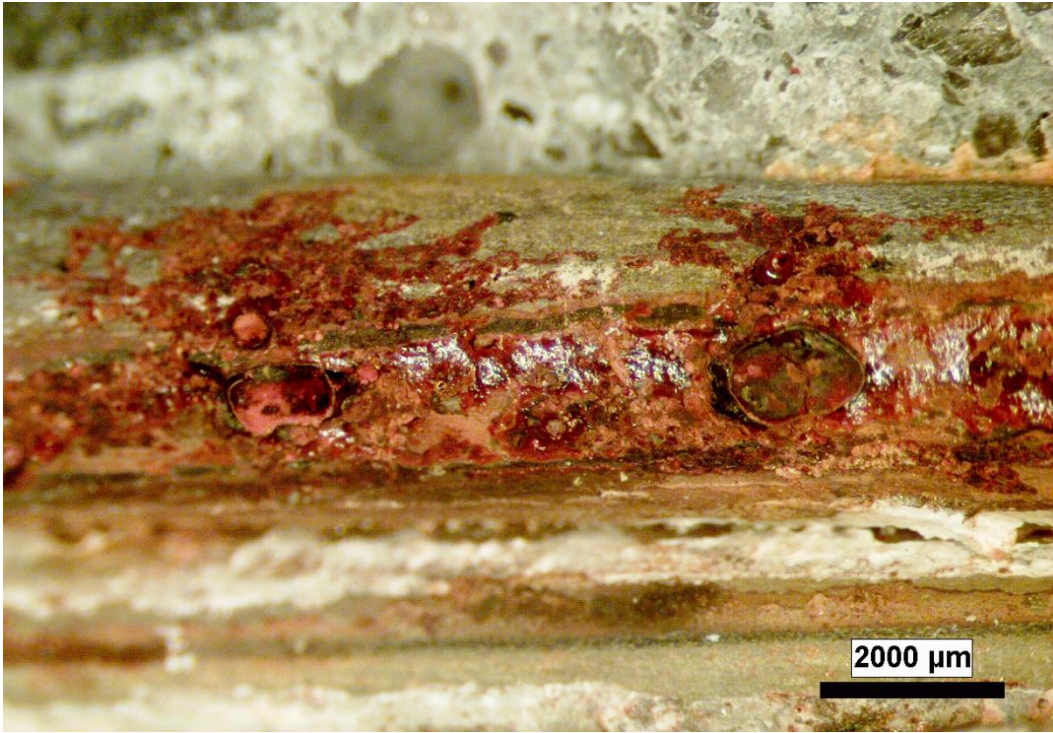
Figure 11.9 Surface of AISI 1080 prestressing strand from top surface core (X6.5).

Figure 11.10 Corrosion products in AISI 1080 prestressing strand surface (top surface core, X6.5).

Figure 11.11 Surface of AISI 1080 prestressing strand from top surface core (X10).

Core samples also were taken from the side surface of the durability specimens where there was about ¼-in. of cover. AISI 1080 strand samples from the side surface core show similar, though more extensive, deterioration as the top surface strand (Figure 11.12). The presence of localized corrosion activity in prestressing strands at chloride concentrations lower than the CTL of 0.05 suggests that this parameter should be lower than the conventional 0.05 limit when used for conventional prestressing strand.

Figure 11.12 Surface of AISI 1080 prestressing strand from side surface core (X10).

(b) Duplex HSSS 2205.

Similar to the AISI 1080 case, the condition of duplex HSSS 2205 strands was compared with a strand sample obtained from the pile construction. The samples were kept at Georgia Tech Structures and Materials Lab. Figure 11.13 shows an excellent condition of the surface of the control strand, no evidence of corrosion initiation, or chemical activity at the impingement sites.

Figure 11.13 Surface of control duplex HSSS 2205 prestressing strand (X6.5).

Micrographs of top surface duplex HSSS 2205 strand show a general good condition (Figures 11.14 and 11.15), but uniform discoloration at some of the contact regions between adjacent strands evidencing chemical activity occurring at these sites. A similar condition is observed in strand samples obtained from the core drilled at the specimen side (Figures 11.16 and 11.17). Overall, the condition of the stainless steel strand was considered excellent.
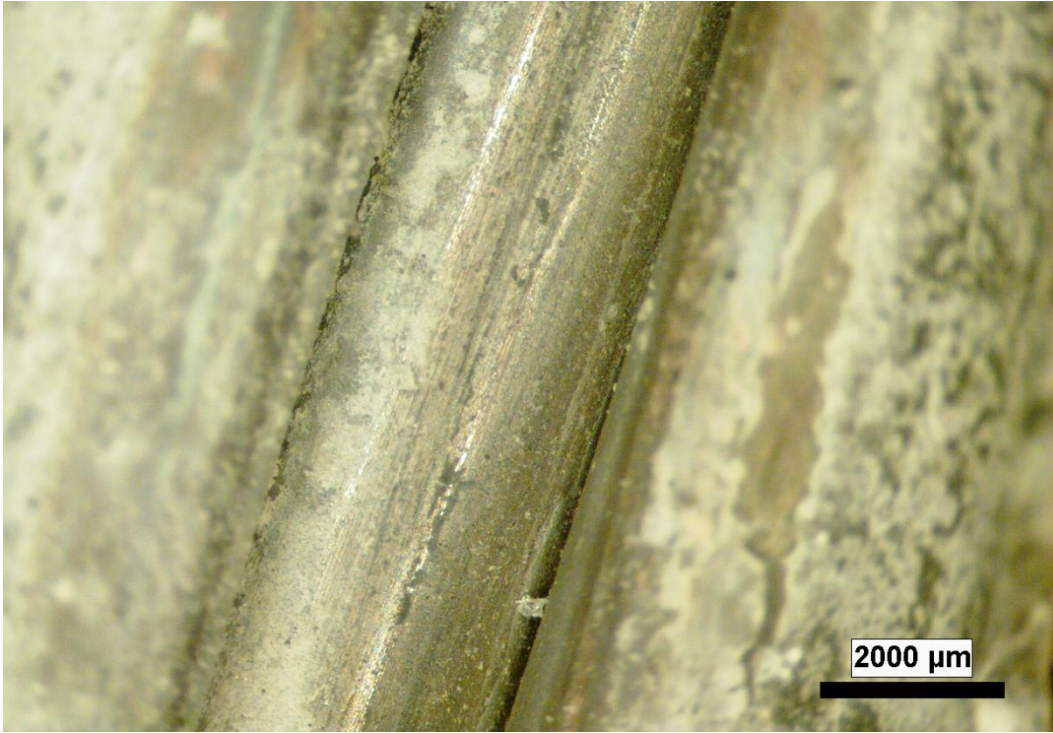
Figure 11.14 Surface of duplex HSSS 2205 prestressing strand (top surface core, X6.5).

Figure 11.15 Surface of duplex HSSS 2205 prestressing strand (top surface core, X6.5).

Figure 11.16 Surface of duplex HSSS 2205 prestressing strand (side surface core, X6.5).

Figure 11.17 Surface of duplex HSSS 2205 prestressing strand (side surface core, X6.5).

171

CHAPTER 12

CONCLUSIONS AND RECOMMENDATIONS

The use of duplex HSSS 2205 (ASTM A276 grade UNS S31803) to replace conventional AISI 1080 steel prestressing strands is proposed to increase the durability and provide a 100+ year service life of precast, prestressed concrete bridge piles exposed to marine environments. Further, special wire made using an austenitic stainless steel grade 304 (ASTM A276, UNS 30400) was investigated as a replacement for conventional wire spiral (AASHTO M32) and proved satisfactory.

The research reported in this report evaluated the transfer and development lengths, driving performance, prestress losses, flexural and shear behavior of prestressed concrete piles built with duplex HSSS 2205 and AISI 1080 steel strands, and with stainless steel and conventional spiral wire reinforcement. The performance of the piles is compared with the behavior predicted according to building codes ACI 318 and AASHTO LRFD.

This chapter summarizes the conclusions of the project, provides recommendations for the use of duplex HSSS 2205 in prestressing strands, and identifies further studies and research needs.

12.1 Conclusions

- Prestressed concrete piles reinforced with duplex HSSS 2205 strands can be built using the conventional precast concrete plant construction procedures.

- Duplex HSSS 2205 strand does not form a galvanic couple with austenitic SS 304 wire samples under alkaline, carbonated, and seawater conditions. Thus, these two

172

different stainless steel alloys may be used together to reinforce prestressed concrete piles.

- Total prestress loss in piles with duplex HSSS 2205 was 18.0 ksi which represented a 12.4% loss from the initial jacking stress at 335 days. Total prestress loss in piles with conventional 1080 strand was 20.1 ksi which represented a 10.2% loss from the initial jacking stress at 335 days. The lower relaxation of duplex HSSS 2205 strands resulted in higher compressive stresses in the piles with the HSSS 2205 strand which caused higher creep strains and increased total loss. A loss of prestressing force lower than the GDOT specified limit is expected at the end of the service life.

- Prestress losses of duplex HSSS 2205 are 82.3% and 99.4% of the value predicted by AASHTO LRFD refined and lump-sum methods at 335 days, respectively. It is concluded than the use of AASHTO LRFD refined method for the calculation of prestress losses of duplex HSSS 2205 strands is conservative.

- Prestress losses of duplex HSSS 2205 and conventional steel strands were not affected by pile driving and extraction.

- The transfer lengths (l_t) of duplex HSSS 2205 and conventional steel obtained by concrete surface strain measurements at 14 days were shorter than the l_t predicted using AASHTO LRFD and ACI 318. Compared to calculations of transfer length following AASHTO LRFD, AISI 1080 steel and duplex HSSS 2205 presented average experimental values that were 68% and 57% of the predicted value, respectively.

- Prestressed concrete piles using duplex HSSS 2205 can be driven until refusal following GDOT requirements, without appreciable damage or visible cracking. The

bearing capacity of piles using duplex HSSS 2205 was 27% higher than the design capacity.

- The transfer lengths of duplex HSSS 2205 and conventional steel strands were not significantly affected by pile driving and extraction. After driving, the l_t of AISI 1080 steel and duplex HSSS 2205 strands were 58% and 58% of the predicted value by AASHTO LRFD, respectively.

- The shortest embedment length which led to a flexural failure with no strand slip was 61 in. for piles made with conventional 1080 strand. Based on this experimental development length (l_d), the l_d of conventional AISI 1080 strands was found to be 53% of the value computed by AASHTO LRFD and 85% of the value computed by ACI 318.

- The shortest embedment length which led to a flexural failure with no strand slip was 69 in. for piles made with HSSS 2205 strand. Based on this experimental development length (l_d), the l_d of duplex HSSS 2205 strands was found to be 55% of the value computed by AASHTO LRFD and 88% of the value computed by ACI 318..

- Development and transfer length results demonstrated that duplex HSSS 2205 strands may be designed using current AASHTO LRFD and ACI 318 standards.

- For piles made with duplex HSSS 2205 strands, ultimate moment strengths obtained experimentally were 10 to 19% higher than those calculated using AASHTO LRFD provisions, and they were 0 to 9% higher than those calculated using ACI 318 provisions. For piles made with conventional AISI 1080 strands, ultimate moment strengths obtained experimentally were 4 to 16% higher than those calculated using AASHTO LRFD provisions, and they were 3 to 6% higher than those calculated using ACI 318 provisions.

- Piles using duplex HSSS 2205 and with spiral, transverse reinforcement made using SS 304 showed statistically similar ultimate shear strengths as the piles made with conventional steel. There was no significant difference in pile strengths with spiral reinforcement spaced between 3 in. and 6 in.

Considering the conclusions stated above, duplex HSSS 2205 can be used in prestressing strands in combination with austenitic SS 304 for the transverse confinement and shear reinforcement for prestressed concrete piles, using the same design requirements and construction procedures used for conventional AISI 1080 steel.

12.2 Recommendations and Research Needs

It is recommended that duplex HSSS 2205 prestressing strand be used to reinforce precast prestressed concrete piles in marine environments and that austenitic SS 304 be used as transverse, spiral reinforcement in these same piles.

Until further studies are completed, it is recommended that the HSSS 2205 be initially stressed to not greater than 70% of the ultimate tensile strength.

Further research is recommended in order to develop a heat treatment for the 2205 alloy or to develop a new alloy which has greater ductility than the current 2205 strand studied herein.

REFERENCES

AASHTO LRFD (2013). "AASHTO LRFD Bridge Design Specifications (6th Edition) with 2012 and 2013 Interim Revisions," American Association of State Highway and Transportation Officials, Washington, DC, USA.

ACI Committee 209 (1992). "Prediction of Creep, Shrinkage, and Temperature Effects in Concrete Structures (ACI 209.R-92)," American Concrete Institute, Farmington Hills, MI, USA.

ACI Committee 214 (2010). "Guide for Obtaining Cores and Interpreting Compressive Strength Results (ACI 214.4R-10)," American Concrete Institute, Farmington Hills, MI, USA.

ACI Committee 222 (2001). "Corrosion of Prestressing Steels (ACI 222.2R-01)," American Concrete Institute, Farmington Hills, MI, USA.

ACI Committee 318 (2011). "Building Code Requirements for Structural Concrete (ACI 318-11) and Commentary," American Concrete Institute, Farmington Hills, MI, USA.

ACI Committee 363 (2010). "Report on High-Strength Concrete (ACI 363R-10)," American Concrete Institute, Farmington Hills, MI, USA.

Alvarez-Armas, I. (2008), Duplex Stainless Steels: Brief History and Some Recent Alloys, *Recent Patents on Mechanical Engineering* 1 (1), 51-57.

Ann, K.Y., and Song, H.-W. (2007), Chloride Threshold Level for Corrosion of Steel in Concrete, *Corrosion Science* 49 (11), 4113-4133.

ASTM A82 (2002). "Standard Specification for Steel Wire, Plain, for Concrete Reinforcement," American Society for Testing and Materials West Conshohocken, PA, USA.

ASTM A276 (2013). "Standard Specification for Stainless Steel Bars and Shapes," American Society for Testing and Materials West Conshohocken, PA, USA.

ASTM A416/A416M (2012). "Standard Specification for Steel Strand, Uncoated Seven-Wire for Prestressed Concrete," American Society for Testing and Materials West Conshohocken, PA, USA.

ASTM A580/A580M (2014). "Standard Specification for Stainless Steel Wire," American Society for Testing and Materials West Conshohocken, PA, USA.

ASTM C39/C39M (2014). "Standard Test Method for Compressive Strength of Cylindrical Concrete Specimens," American Society for Testing and Materials West Conshohocken, PA, USA.

ASTM C42/C42M (2013). "Standard Test Method for Obtaining and Testing Drilled Cores and Sawed Beams of Concrete," American Society for Testing and Materials West Conshohocken, PA, USA.

ASTM C150/C150M (2012). "Standard Specification for Portland Cement," American Society for Testing and Materials West Conshohocken, PA, USA.

ASTM C469/C469M (2014). "Standard Test Method for Static Modulus of Elasticity and Poisson's Ratio of Concrete in Compression," American Society for Testing and Materials West Conshohocken, PA, USA.

ASTM C496/C496M (2011). "Standard Test Method for Splitting Tensile Strength of Cylindrical Concrete Specimens," American Society for Testing and Materials West Conshohocken, PA, USA.

ASTM C512/C512M (2010). "Standard Test Method for Creep of Concrete in Compression," American Society for Testing and Materials West Conshohocken, PA, USA.

ASTM C618 (2012). "Standard Specification for Coal Fly Ash and Raw or Calcined Natural Pozzolan for Use in Concrete," American Society for Testing and Materials West Conshohocken, PA, USA.

ASTM C1152/C1152M (2012). "Standard Test Method for Acid-Soluble Chloride in Mortar and Concrete," American Society for Testing and Materials West Conshohocken, PA, USA.

ASTM C1202 (2012). "Standard Test Method for Electrical Indication of Concrete's Ability to Resist Chloride Ion Penetration," American Society for Testing and Materials West Conshohocken, PA, USA.

ASTM D4458 (2009). "Standard Test Method for Chloride Ions in Brackish Water, Seawater, and Brines," American Society for Testing and Materials West Conshohocken, PA, USA.

ASTM E328 (2013). "Standard Test Methods for Stress Relaxation for Materials and Structures," American Society for Testing and Materials West Conshohocken, PA, USA.

ASTM G71 (2014). "Standard Guide for Conducting and Evaluating Galvanic Corrosion Tests in Electrolytes," American Society for Testing and Materials West Conshohocken, PA, USA.

Azizinamini, A., Ozyildirim, H.C., Power, E.H., Kline, E.S., Mertz, D.R., Myers, G.F., and Whitmore, D.W. (2013). "Design Guide for Bridges for Service Life," Prepublication Draft Report No. SHRP 2 Renewal Project R19A, Transportation Research Board, National Academy of Sciences, 744 pp.

Bandyopadhyay, T.K. and Sengupta, B. (1986), Determining Time Dependent Losses of Prestress with due Consideration of Aging Coefficient and Percentage of Steel, *ACI Journal Proceedings* 83 (2), 236-243.

Barnes, R.W., Grove, J.W., and Burns, N.H. (2003), Experimental Assessment of Factors Affecting Transfer Length, *ACI Structural Journal* 100 (6), 740-748.

Bautista, A., and Gonzalez, J.A. (1996), Analysis of the Protective Efficiency of Galvanizing Against Corrosion of Reinforcements Embedded In Chloride Contaminated Concrete, *Cement and Concrete Research* 26 (2), 215-224.

Bentz, E.C. (2003), Probabilistic Modeling of Service Life for Structures Subjected to Chlorides, *ACI Materials Journal* 100 (5), 391-397.

Bertolini, L., Elsener, B., Pedeferri, P. and Polder, R (2004), *Corrosion of Steel in Concrete: Prevention, Diagnosis, Repair*, Wiley-VCH, Heppenheim, Germany.

Bohni, H. (2005), *Corrosion in Reinforced Concrete Structures*, Woodhead Publishing Limited, Cambridge, England.

Buckner, C.D. (1995), A Review of Strand Development Length for Pretensioned Concrete Members, *PCI Journal* 40 (2), 84-105.

Cannon, E., Lewinger, C., Abi, C., and Hamilton, H.R. (2006). "St. George Island Bridge Pile Testing," Final Report, UF Project No. 00051711, Florida Department of Transportation, 113 pp.

Center for Operational Oceanographic Products and Services, National Oceanic and Atmospheric Administration (NOAA), November 6th, 2014 (website update date: October 15th, 2013), from http://tidesandcurrents.noaa.gov/

Chaix, O., Hartt, W.H., Kessler, R., and Powers, R. (1995), Localized Cathodic Protection of Simulated Prestressed Concrete Pilings in Seawater, *Corrosion Science* 51 (5), 386-398.

Darmawan, M.S. and Stewart, M.G. (2007), Effect of Pitting Corrosion on Capacity of Prestressing Wires, *Magazine of Concrete Research* 59 (2), 131-139.

Deatherage, J.H., Burdette, E.G., and Chew, C.K. (1994), Development Length and Lateral Spacing Requirements of Prestressing Strand for Prestressed Concrete Bridge Girders, *PCI Journal* 39 (1), 70-83.

Ehlen, M.A., Thomas, M.D.A, and Bentz, E.C. (2009), Life-365 Service Life Prediction Model[TM] Version 2.0, *Concrete International*, 31 (5), 41-46.

Erdogdu, S., Bremner, T.W., and Kindratova, I.L. (2001), Accelerated Testing of Plain and Epoxy-coated Reinforcement in Simulated Seawater and Chloride Solutions, *Cement and Concrete Research* 31 (6), 861-867.

Fontana, M. (1986), *Corrosion Engineering, 3rd Edition*, McGraw-Hill, New York, USA.

Frankel, G.S. (1998), Pitting Corrosion of Metals, A Review of the Critical Factors, *Journal of The Electrochemical Society* 145 (6), 2186-2198.

Gardner, L. (2005), The Use of Stainless Steel in Structures, *Progress in Structural Engineering and Materials* 7 (2), 45-55.

Geng, J., Easterbrook D., Li, L-Y, and Mo, L-W (2015), The Stability of Bound Chlorides in Cement Paste with Sulfate Attack, *Cement and Concrete Research* 68, 211-222.

Glass, G.K., and Buenfeld, N.R. (1997), Chloride Threshold Levels for Corrosion Induced Deterioration of Steel in Concrete, in: L.O. Nilsson and J. Ollivier (Eds.), *Chloride Penetration into Concrete*, Proceedings of the RILEM International Workshop on Chloride Penetration into Concrete, RILEM Paris, 429–452.

Gonnerman, H.F., and Shuman, E.C. (1928), Flexure and Tension Tests of Plain Concrete, *Major Series* 171 (209), 149.

Griess, J.C., and Naus, D.J. (1980), Corrosion of Steel Tendons Used in Prestressed Concrete Pressure Vessels, in: D.E. Tonini and J.M. Gaidis (Eds.), *Corrosion of Reinforcing Steel in Concrete, ASTM STP 713*, American Society for Testing and Materals, 32–50.

Hanson, N.W. and Kaar, P.H (1959), Flexural Bond Tests of Pretensioned Prestressed Beams, *ACI Journal* 55 (1), 783-802.

Hart, W.H. and Rosenberg, A.M. (1980), Influence of $Ca(NO_2)_2$ on Sea Water Corrosion of Reinforcing Steel in Concrete, *ACI Special Publication 65*, 609-622.

Hart, W.H., Powers, R.G., Lysogorski, D.K., Paredes, M., and Virmani, Y.P. (2006). "Job Site Evaluation of Corrosion-Resistant Alloys for Use as Reinforcement in Concrete," Final Report, No. FHWA-HRT-06-078, Federal Highway Administration, 92 pp.

Holland, B., Moser, R., Kahn, L.F., Singh, P., and Kurtis, K.E. (2012). "Durability of Precast Prestressed Concrete Piles in Marine Environment, Part 2 Volume 1: Concrete," Georgia Institute of Technology, Atlanta, GA.

Hoyer, E. and Friedrich, E. (1939), Beitrag zur Frage der Haftspannung in Eisenbetonbauteilen, *Beton und Eisen* 50 (9), 717-736.

Hurley, M.F. and Scully, J.R. (2006), Threshold Chloride Concentrations of Selected Corrosion-Resistant Rebar Materials Compared to Carbon Steel, *Corrosion* 62 (10), 892-904.

Jenkins, J.F. (1987). "Validation of Nitronic 33 in Reinforced and Prestressed Concrete," Final Report, No. TN-1764, Naval Civil Engineering Laboratory, 63 pp.

Johannesson, B. and Utgenannt, P. (2001), Microstructural Changes Caused by Carbonation of Cement Mortar, *Cement and Concrete Research* 31 (6), 925-931.

Jones, D. (1996), *Principles and Prevention of Corrosion: 2nd Edition*, Princeton-Hall, Upper Saddle River, NJ.

Kaar, P.H., LaFraugh, R.W., and Mass, M.A. (1963), Influence of Concrete Strength on Transfer Length, *PCI Journal* 8 (5), 47-67.

Kahn, L.F., Dill, J.C, Reutlinger, C.G. (2002), Transfer and Development Length of 15-mm Strand in High Performance Concrete Girders, *Journal of Structural Engineering* 128 (7), 913-921.

Kahn, L.F., Lai, J.S., Kurtis, K., Saber, A., Shams, M., Reutlinger, C., Dill, J., Slapkus, A., Canfield, S., Lopez, M., and Haines, B. (2005). "High Strength/High Performance Concrete for Precast Prestressed Bridge Girders in Georgia," Georgia Institute of Technology, Atlanta, GA.

Kurtis, K.E. and Mehta, K. (1997), A Critical Review of Deterioration of Concrete Due to Corrosion of Reinforcing Steel, *ACI Special Publication 170*, 535-554.

Kurtis, K.E., Kahn, L.F., and Nadelman, E. (2013). "Viability of Concrete Performance-Based Specification for Georgia DOT Projects," Georgia Institute of Technology, Atlanta, GA.

Lane, S.N. (1998). "A New Development Length Equation for Pretensioned Strands in Bridge Beams and Piles," Final Report, No. FHWA-RD-98-116, Federal Highway Administration, 131 pp.

Lo K.H., Shek, C.H., and Lai, J.K.L. (2009), Recent Developments in Stainless Steels, *Materials Science and Engineering: R: Reports* 65 (4), 39-104.
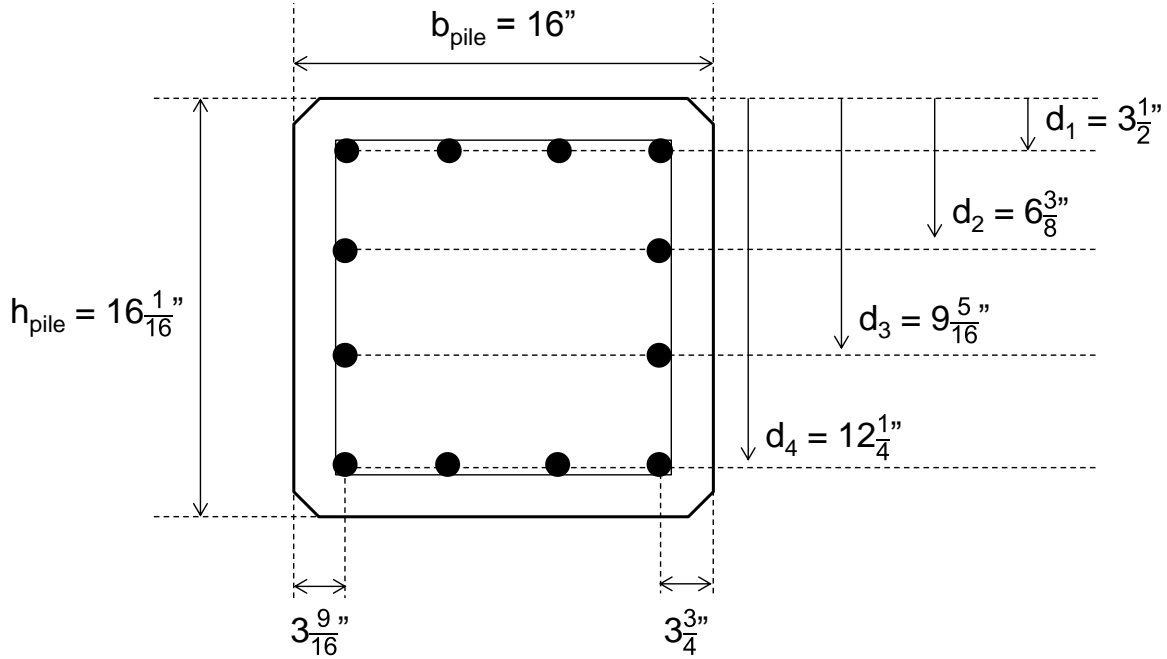
Martin, L.D., and Scott, N.L. (1976), Development of Prestressing Strand in Pretensioned Members, *ACI Journal* 73 (8), 453-456.

Meyer K.F. (2002). Transfer and Development Length of 0.6-inch Diameter Prestressing Strand in High Strength Lightweight Concrete. Doctoral Thesis, Georgia Institute of Technology, pp. 643.

Milad, M., Zreiba, V., Elhalouani, F., and Baradai, C. (2008), The Effect of Cold Work on Structure and Properties of AISI 304 Stainless Steel, *Journal of Materials Processing Technology* 203 (1-3), 80-85.

Mitchell, D., Cook, W.D., Khan, A.A., and Tham, T. (1993), Influence of High Strength Concrete on Transfer and Development Length of Pretensioning Strand, *PCI Journal* 38 (3), 52-66.

Moser, R.D., Holland, B., Kahn, L.F., Singh, P., and Kurtis, K.E. (2011). "Durability of Precast Prestressed Concrete Piles in Marine Environment: Reinforcement Corrosion and Mitigation – Part 1," Georgia Institute of Technology, Atlanta, GA.

Moser, R.D., Singh, P.M., Kahn, L.F., Kurtis, K.E. (2011), Chloride-Induced Corrosion of Prestressing Steels Considering Crevice Effects and Surface Imperfections, *Corrosion* 67 (6), 065001-1–065001-14.

Moser, R.D., Singh, P., Kahn, L.F., and Kurtis, K.E. (2012). "Durability of Precast Prestressed Concrete Piles in Marine Environment, Part 2 Volume 2: Stainless Steel Prestressing Strand and Wire," Georgia Institute of Technology, Atlanta, GA.

Myers, J.J., and Carrasquillo, R. L. (1998). "The Production and Quality Control of High Performance Concrete in Texas Bridge Structures," The University of Texas at Austin, Austin, TX.

Nawy, E.G. (2009), *Prestressed Concrete: A Fundamental Approach, 5th Edition*, Princeton-Hall, Upper Saddle River, NJ, USA.

Neville, A.M. (1995), *Properties of Concrete, Fourth Edition*, Pearson Education Limited, Essex, England.

Novokshchenov, V. (1994), Brittle Fractures of Prestressed Bridge Steel Exposed to Chloride-Bearing Environments Caused by Corrosion-Generated Hydrogen, *Corrosion*, 50 (6), 477-485.

Nurnberger, U. (2002), Corrosion Induced Failure Mechanisms of Prestressing Steel, *Materials and Corrosion*, 53 (8), 591-601.

Oh, B.H., and Kim, E.S. (2000), Realistic Evaluation of Transfer Lengths in Pretensioned, Prestressed Concrete Members, *ACI Materials Journal* 97 (6), 821-830.

Oh, B.H., Kim, E.S., and Choi, Y.C. (2006), Theoretical Analysis of Transfer Lengths in Pretensioned Prestressed Concrete Members, *Journal of Engineering Mechanics* 132 (10), 1057-1066.

Papadakis, V.G, Vayenas, C.G., and Fardis, M.N. (1991), Experimental Investigation and Mathematical Modeling of the Concrete Carbonation Problem, *Chemical Engineering Science* 46 (5-6), 1333-1338.

Ramberg, W. and Osgood W.R. (1941), Determination of Stress–Strain Curves by Three Parameters, *NACA Technical Note* 503.

Ramirez, J.A. and Russell, B.W. (2008). "Transfer, Development, and Splice Length for Strand/Reinforcement in High-Strength Concrete," NCHRP Report No. 603, National Cooperative Highway Research Program, Transportation Research Board, National Research Council.

Rasheeduzzafar, Dakhil, F.H., Bader, M.A., and Khan, M.M. (1992), Performance of Corrosion-Resisting Steels in Chloride-Bearing Concrete, *ACI Materials Journal* 89 (5), 439-448.

Rasmussen, K.J.R (2003), Full-Range Stress–Strain Curves for Stainless Steel Alloys, *Journal of Constructional Steel Research* 59 (1), 47-61.

Recio, F.J., Wu, Y., Alonso, M.C., and Nurnberger, U. (2013), Hydrogen Embrittlement Risk in Cold-Drawn Stainless Steels, *Materials Science and Engineering: A* 564, 57-64.

Reutlinger, C.G. (1999). Direct Pull-Out Capacity and Transfer Length of 0.6-inch Diameter Prestressing Strand in High-Performance Concrete. Master's Thesis, Georgia Institute of Technology, pp. 371.

Rosenberg, A., Hansson, C.M. and Andrade, C. (1989), Mechanisms of Corrosion of Steel in Concrete, *Materials Science of Concrete* 1, 285-314.

Russell, B.W. (1992). Design Guidelines for Transfer, Development and Debonding of Large Diameter Seven Wire Strands in Pretensioned Concrete Girders. Doctoral Thesis, The University of Texas at Austin.

Russell, B.W., and Burns, N.H. (1993). "Design Guidelines for Transfer, Development and Debonding of Large Diameter Seven Wire Strands in Pretensioned Concrete Girders," The University of Texas at Austin, Austin, TX.

Schmitt, R.J., and Mullen, C.X. (1969), Influence of Chromium on the Atmospheric-Corrosion Behavior of Steel, in: *Stainless Steel for Architectural Use, ASTM STP 454*, American Society for Testing and Materials, 124–136.
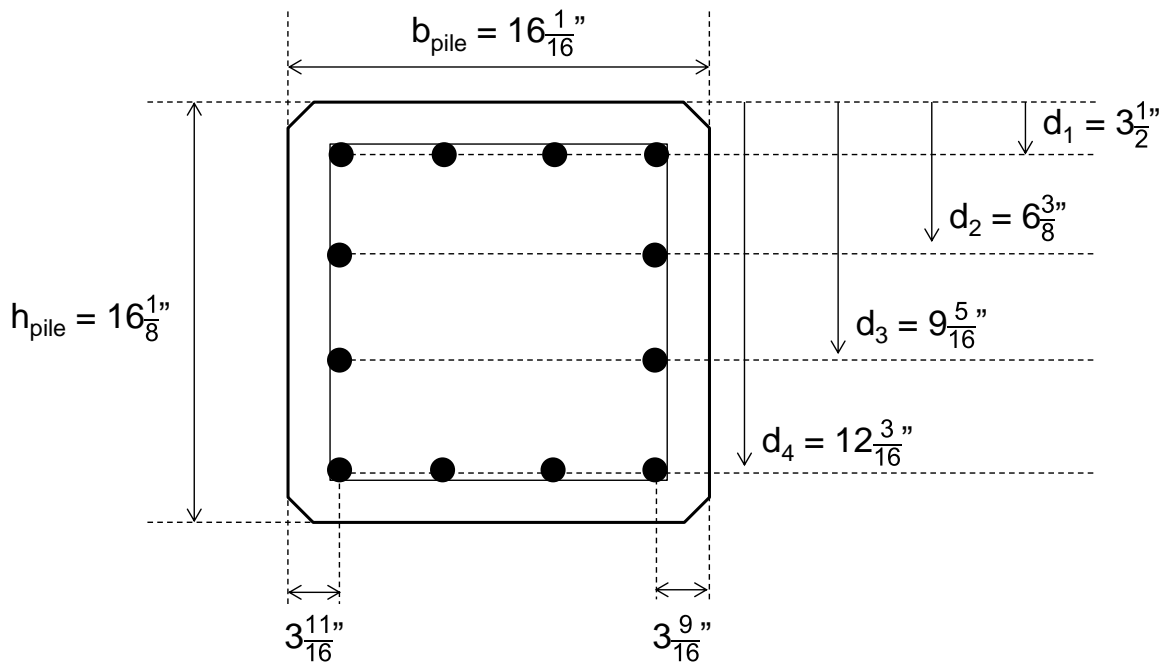
Schuetz, D.P. (2013). Investigation of High Strength Stainless Steel Prestressing Strands. Master's Thesis, Georgia Institute of Technology, pp. 173.

Shirahama, S., Fang, S., Kobayashi, T., and Miyagawa, T. (1999), Basic Properties of Duplex Stainless Prestressing Steel and Flexural Behaviors of Prestressed Concrete Beams Using the Tendon, *Journal of the Society of Material Science Japan* 48 (10), 1199-1206.

Tadros, M.K., Al-Omaishi, N., Seguirant, S.J., and Gallt, J.G. (2003). "Prestress Losses in Pretensioned High-Strength Concrete Bridge Girders," NCHRP Report No. 496, National Cooperative Highway Research Program, Transportation Research Board, National Research Council.

Toribio, J. and Ovejero, E. (2005), Failure Analysis of Cold Dawn Prestressing Steel Wires Subjected to Stress Corrosion Cracking, *Engineering Failure Analysis* 12 (5), 654-661.

Wallinder, I.O., Lu, J., Bertling, S., and Leygraf, C. (2002), Release Rates of Chromium and Nickel from 304 and 316 Stainless Steel During Urban Atmospheric Exposure—A Combined Field and Laboratory Study, *Corrosion Science* 44 (10), 2303-2319.

Weyers, R.E., Sprinkel, M.M., and Brown, M.C. (2006). "Summary Report on the Performance of Epoxy-Coated Reinforcing Steel in Virginia," Final Report No. FHWA/VTRC 06-R29, Federal Highway Administration and Virginia Department of Transportation, 37 pp.

Wight, J.K., and MacGregor, J.G. (2011), *Reinforced Concrete: Mechanics and Design (6th Ed.)*, Prentice Hall, Upper Saddle River, NJ.

Wu, Y. and Nurnberger, U. (2009), Corrosion-Technical Properties of High-Strength Stainless Steels for the Application in Prestressed Concrete Structures, *Materials and Corrosion* 60 (10), 771-780.

Zhang, X.G. (2011), Galvanic Corrosion, in: R.W. Revie (Ed.), *Uhlig's Corrosion Handbook, Third Edition*, John Wiley & Sons, Inc., 123–143.

Zia, P. and Mostafa, T. (1977), Development Length of Prestressing Strands, *PCI Journal* 22 (5), 54-65.

APPENDIX A: ACTUAL DIMENSIONS OF PILE SECTIONS

- Pile AISI 1080 #1 – Top Half:

- Pile AISI 1080 #1 – Bottom Half:

- Pile AISI 1080 #2 – Top Half:
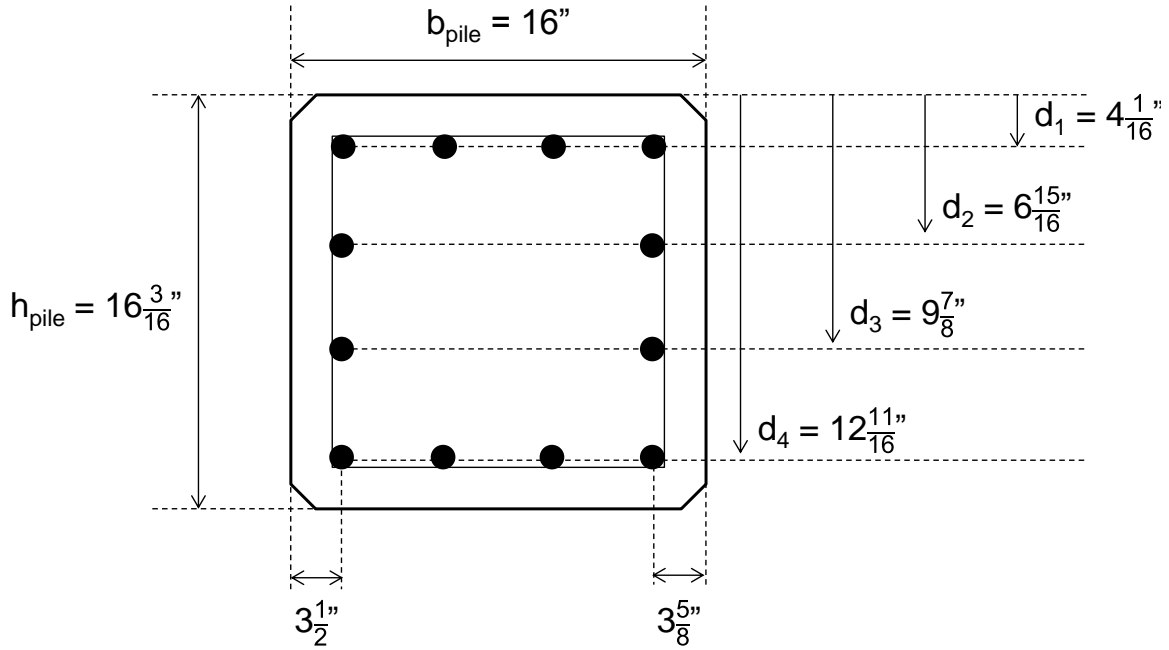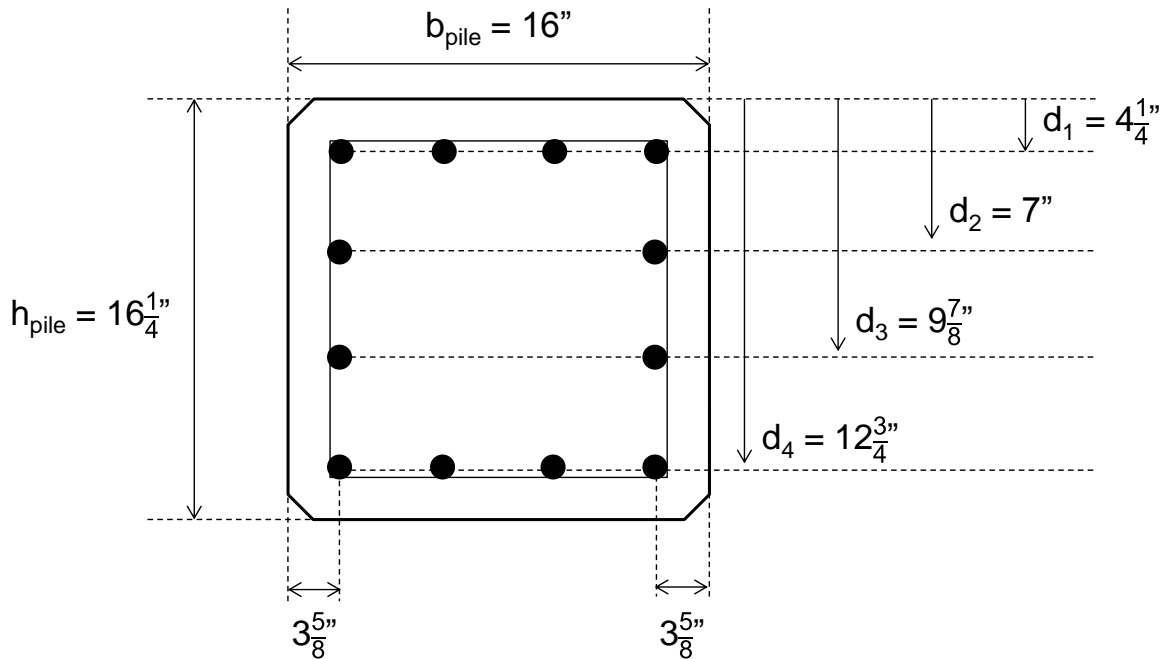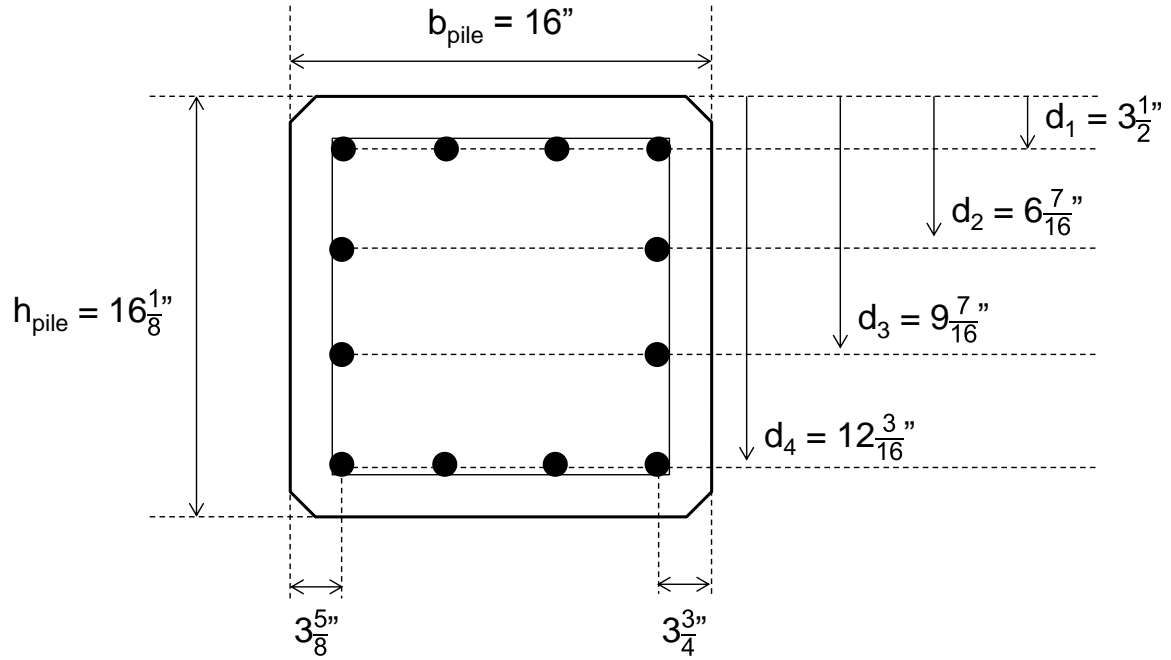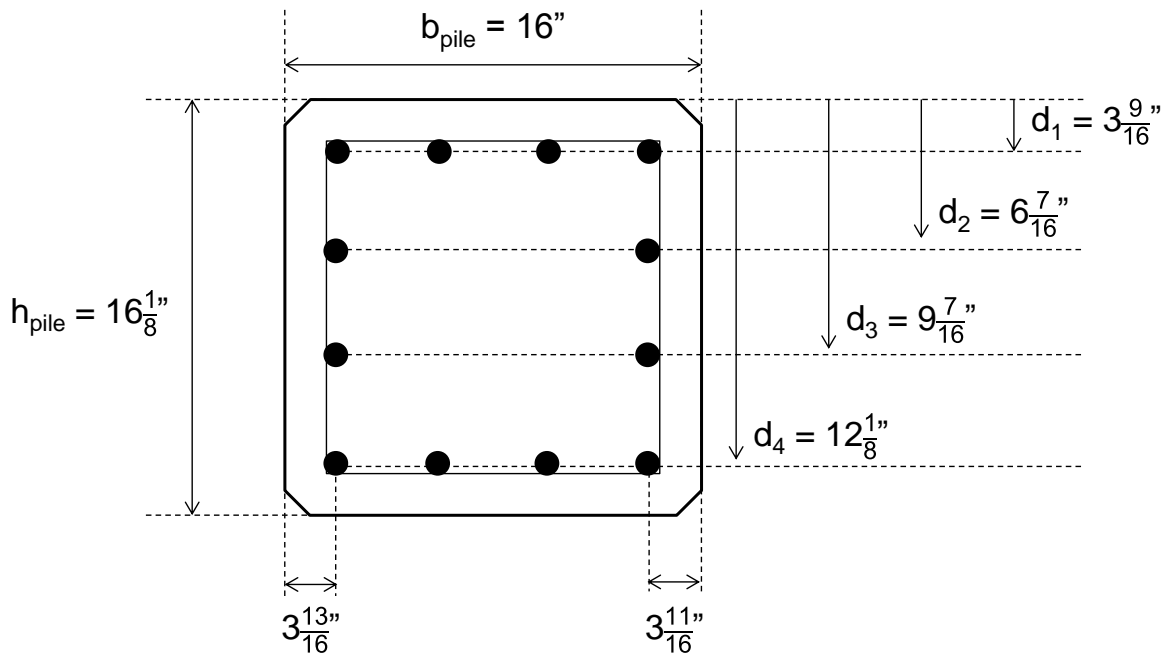
$b_{pile} = 16"$

$h_{pile} = 16\frac{3}{16}"$

$d_1 = 4\frac{1}{16}"$

$d_2 = 6\frac{15}{16}"$

$d_3 = 9\frac{7}{8}"$

$d_4 = 12\frac{11}{16}"$

$3\frac{1}{2}"$

$3\frac{5}{8}"$

- Pile AISI 1080 #2 – Bottom Half:

$b_{pile} = 16"$

$h_{pile} = 16\frac{1}{4}"$

$d_1 = 4\frac{1}{4}"$

$d_2 = 7"$

$d_3 = 9\frac{7}{8}"$

$d_4 = 12\frac{3}{4}"$

$3\frac{5}{8}"$

$3\frac{5}{8}"$

185

- Pile HSSS 2205 #1 – Top Half:

b_{pile} = 16"

h_{pile} = $16\frac{1}{8}$"

$d_1 = 3\frac{1}{2}$"

$d_2 = 6\frac{7}{16}$"

$d_3 = 9\frac{7}{16}$"

$d_4 = 12\frac{3}{16}$"

$3\frac{5}{8}$"

$3\frac{3}{4}$"

- Pile HSSS 2205 #1 – Bottom Half:

b_{pile} = 16"

h_{pile} = $16\frac{1}{8}$"

$d_1 = 3\frac{9}{16}$"

$d_2 = 6\frac{7}{16}$"

$d_3 = 9\frac{7}{16}$"

$d_4 = 12\frac{1}{8}$"

$3\frac{13}{16}$"

$3\frac{11}{16}$"

186

- Pile HSSS 2205 #2 – Top Half:

$b_{pile} = 16"$

$d_1 = 4\frac{3}{16}"$

$d_2 = 7\frac{1}{8}"$

$d_3 = 10\frac{1}{8}"$

$d_4 = 12\frac{7}{8}"$

$h_{pile} = 15\frac{15}{16}"$

$3\frac{9}{16}"$

$3\frac{1}{4}"$

- Pile HSSS 2205 #2 – Bottom Half:

$b_{pile} = 16"$

$d_1 = 4\frac{1}{8}"$

$d_2 = 7\frac{1}{16}"$

$d_3 = 10"$

$d_4 = 12\frac{13}{16}"$

$h_{pile} = 15\frac{7}{8}"$

$3\frac{3}{4}"$

$3\frac{9}{16}"$

- Pile HSSS 2205 #3 – Top Half:

$b_{pile} = 16\frac{1}{16}"$

$h_{pile} = 16"$

$d_1 = 4\frac{3}{16}"$

$d_2 = 6\frac{7}{8}"$

$d_3 = 9\frac{15}{16}"$

$d_4 = 12\frac{11}{16}"$

$3\frac{3}{4}"$

$3\frac{1}{2}"$

- Pile HSSS 2205 #3 – Bottom Half:

$b_{pile} = 16"$

$h_{pile} = 16"$

$d_1 = 4\frac{1}{4}"$

$d_2 = 6\frac{7}{8}"$

$d_3 = 9\frac{7}{8}"$

$d_4 = 12\frac{3}{4}"$

$3\frac{5}{8}"$

$3\frac{5}{8}"$

188
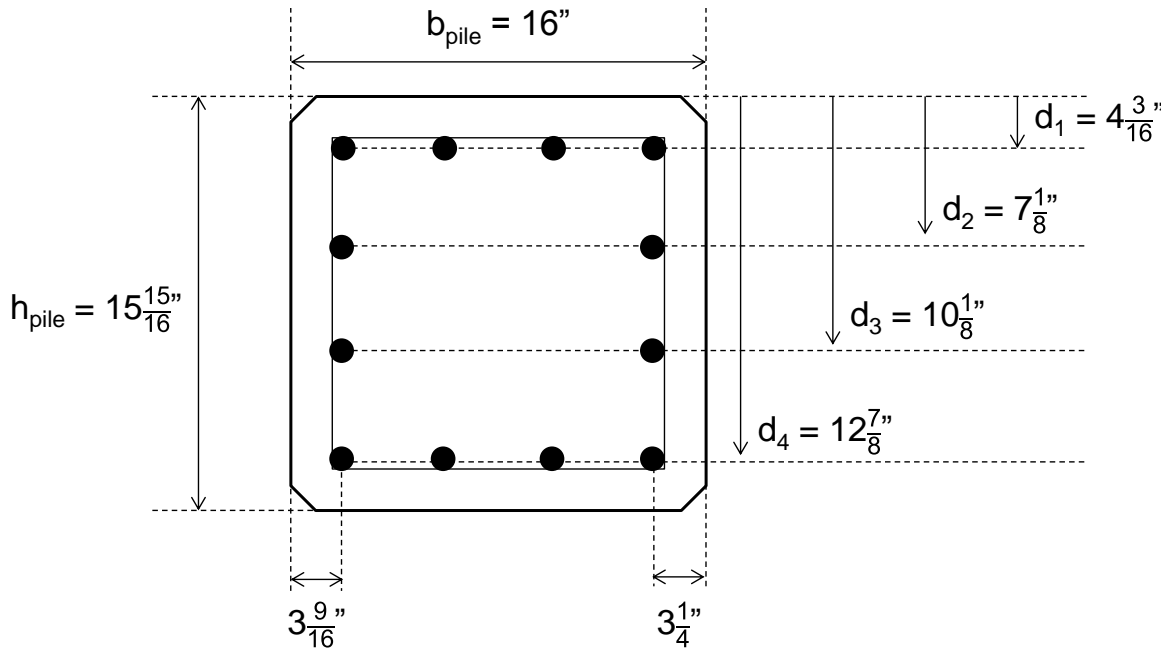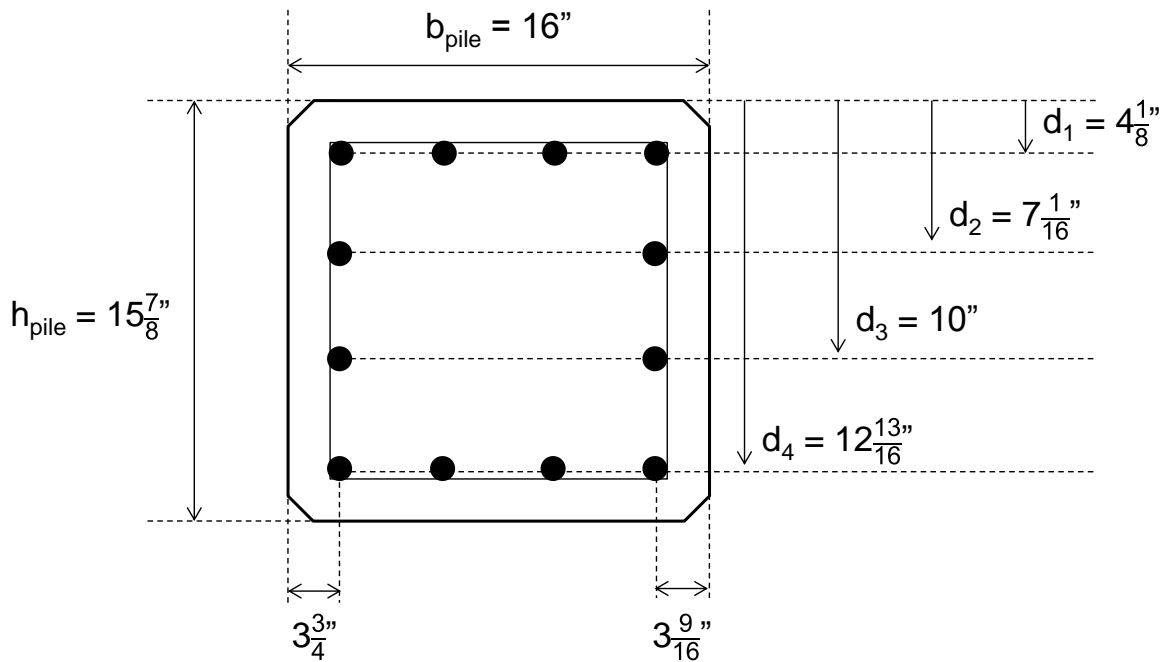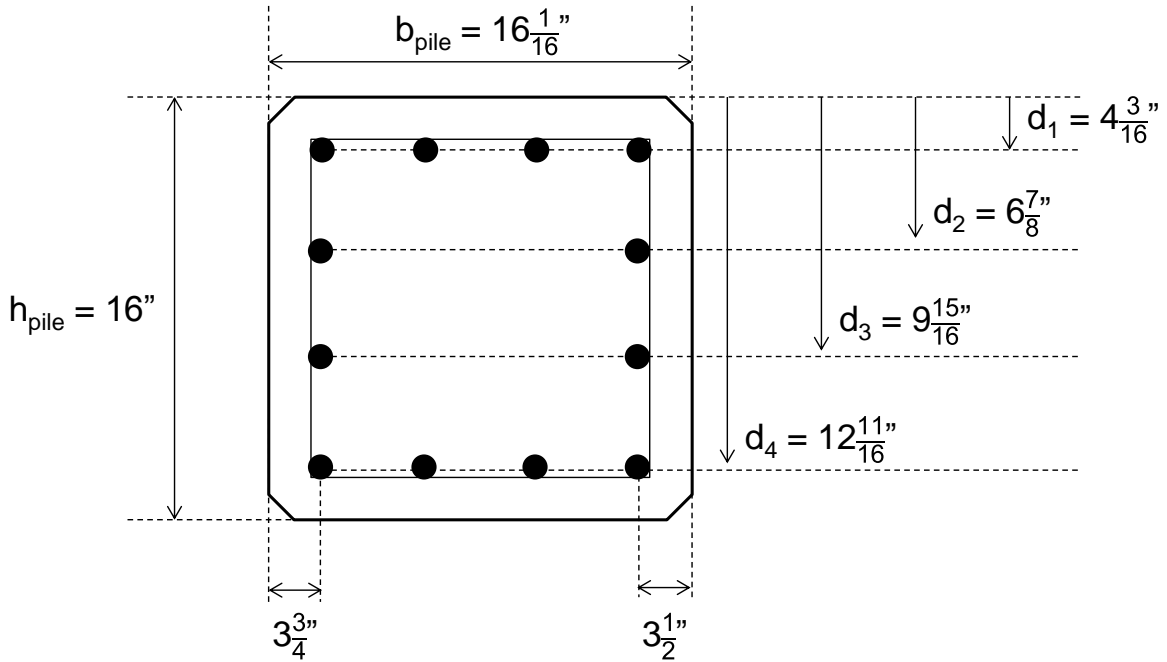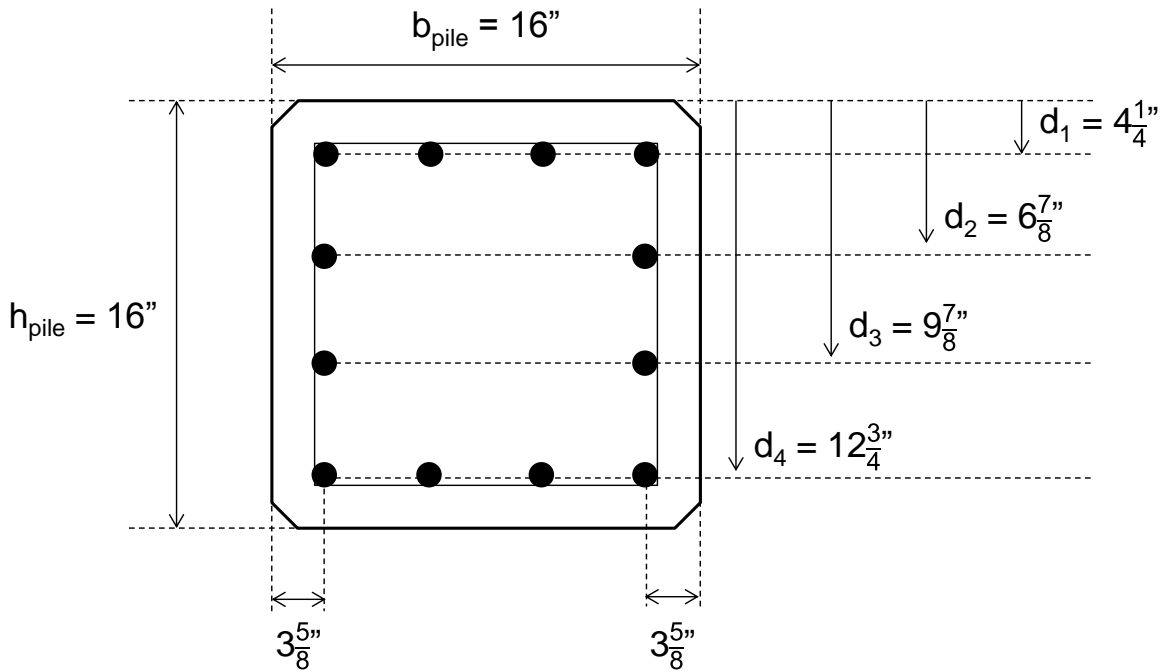
APPENDIX B: FORMWORK DESIGN AND CONSTRUCTION

The determination of the development length of the piles was performed by flexural testing of the 27-ft. long piles. In order to produce pile failure by having a strain in the strands greater than 2% or the breaking of the strands themselves, the depth of the specimens was increased by the addition of a top section of concrete to get a final 16×43-in. rectangular section. The top surface of the piles was roughened after screeding the surface; #5 U-shaped stirrups were embedded to provide good bonding between the hardened concrete of the pile and the fresh concrete from added section and to assure development failure of the strands rather than shear failure of the specimens.

The 27-ft. long piles were transported to the Georgia Tech Structures and Materials Lab, where the placement of the top section took place. The formwork designed for the construction of the top section consisted of plywood ¾-in. sheathing, supported by horizontal 2x4-in. studs. The forms were drilled at the positions shown in Figure B.1 to position tie rods to hold the formwork panels at the 16.5-in. width of the top of the piles.
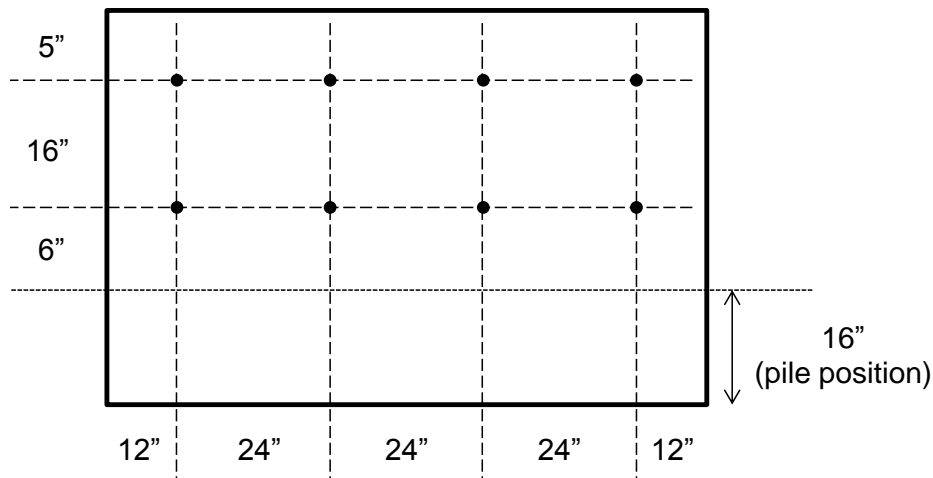
Figure B.1 Diagram of a plywood panel and position of the drilled holes.

Two layers of acrylic latex paint were applied at the side of the panels facing concrete, to seal the surface of plywood in order to avoid moisture absorption from fresh concrete (see Figure B.2). Then, a wax release agent was sprayed on the same surface.

Vertical 2×4-in. wood studs were nailed to plywood in order to provide stiffness and strength to formwork during concrete placement (see Figure B.3).

Figure B.2 Surface coating application.
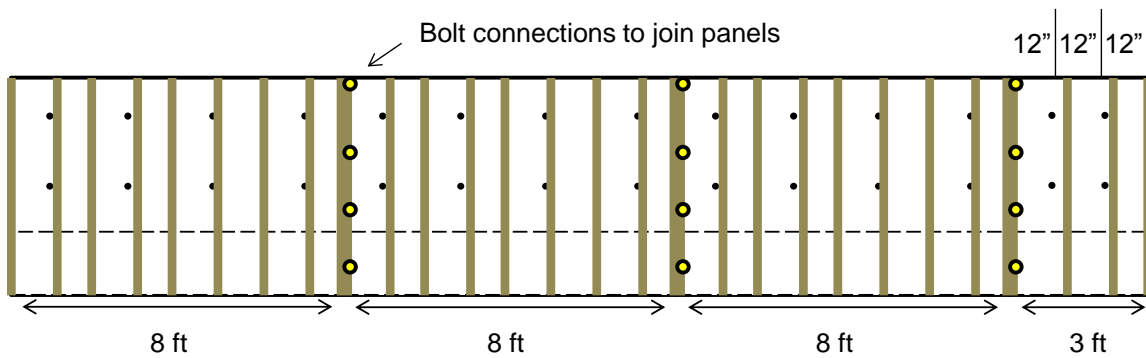
Figure B.3 Distribution of studs on the formwork sheathing.

Horizontal 8-ft. long 2×4-in. double wales were nailed to the studs at the position of the drilled holes (Figure B.4). The end panels were joined to the side panels using 1/4-in. bolts. The ¼-in. diameter threaded rods were attached to the wales by nuts and washers, and a constant distance between opposing panels of 16.5-in. was fixed along the pile. After positioning of the panels (see Figure B.5), the joints were caulked with silicone.

Concrete was placed directly from the ready-mix truck, and then consolidated with an internal spud vibrator (Figure B.6). The surface was screeded and floated with wood boards, and the surface was covered with plastic sheets (Figure B.7).

Formwork panels were removed after one week from casting (Figure B.8).

Figure B.4 Formwork panel before positioning on the piles.

Figure B.5 Formwork sheathing before concrete placing.

Figure B.6 Placing (left) and vibration (right) of the top section of concrete.

Figure B.7 Curing and protection of concrete after placing.

Figure B.8 27-ft piles with top concrete section.

APPENDIX C: GALVANIC CORROSION EVALUATION: SS 304 and HSSS 2205

The use of dissimilar metals for prestressing strands and transverse shear reinforcement in the piles can create the conditions under which a galvanic couple and accelerated corrosion of the more active metal (anode) could happen. To evaluate the occurrence of galvanic corrosion between the couple duplex HSSS 2205 (strands) – austenitic SS 304 (shear reinforcement), the standard test ASTM G71 was performed under three exposures representing potential environments for the metallic couple during service life: seawater, alkaline and carbonated conditions.

C.1 Test Procedure

To represent each condition, the following solutions were used:

a) Seawater: 0.5M Cl⁻ solution (pH=6.5).

b) Carbonated: 0.3M $NaHCO_3$ + 0.1M Na_2CO_3 (pH=9.5).

c) Alkaline: 4 g/l $Ca(OH)_2$ (pH=12.5).

Standard ASTM G71 suggests the use of 40 cm^3 of solution for every 1 cm^2 of exposed surface area of the couple. Thus, 2-cm (0.787-in.) long samples for duplex 2205 strands and austenitic 304 wires were cut using a precision water saw (Figures C.1 and C.2). Strand and shear reinforcement samples had approximately 22.87 cm^2 (3.545 in^2) and 4.12 cm^2 (0.639 in^2) of exposed area, respectively. Following the suggestion of the standard, a volume of 1 liter (33.814 oz.) was used for every condition. Additionally, the anode-to-cathode area ratio was kept constant at 0.18 and the surfaces were used as-received.
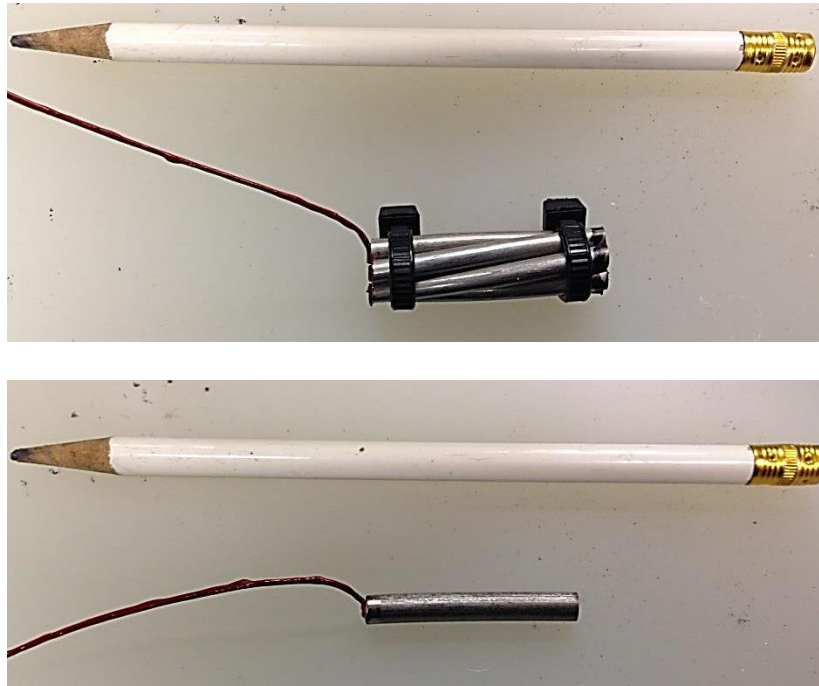
194

Figure C.1 Sample preparation

Figure C.2 Duplex HSSS 2205 (top) and austenitic SS 304 (bottom) samples.

Then, the samples were welded to a stainless steel austenitic 316 wire to apply the

required potential during the test. To avoid the electrochemical reaction of the SS 316

wire with any of the metals in the couple, an insulating epoxy coating was applied at the

connection between the samples and the SS 316 wire, which was also covered with the

epoxy coating (see Figure C.3). The area covered by the epoxy coating was not

considered in the calculation of the exposed area.

Figure C.3 Epoxy coating application.

Every cell included of a couple composed by samples of HSSS 2205 strand and

SS 304 wire, and a reference electrode calibrated before the test. They were connected to

a potentiostat to keep the potential of the working electrode (anode, in this case the SS

304 wire) at a constant value. Every cell was submerged in 1 liter of solution and the

system was connected to an 8-channel electrochemical multiplexer that provided the

current between both stainless steel alloys (Figures C.4 and C.5). Two replicates were prepared per solution. One measurement was obtained every minute for 60 hours.
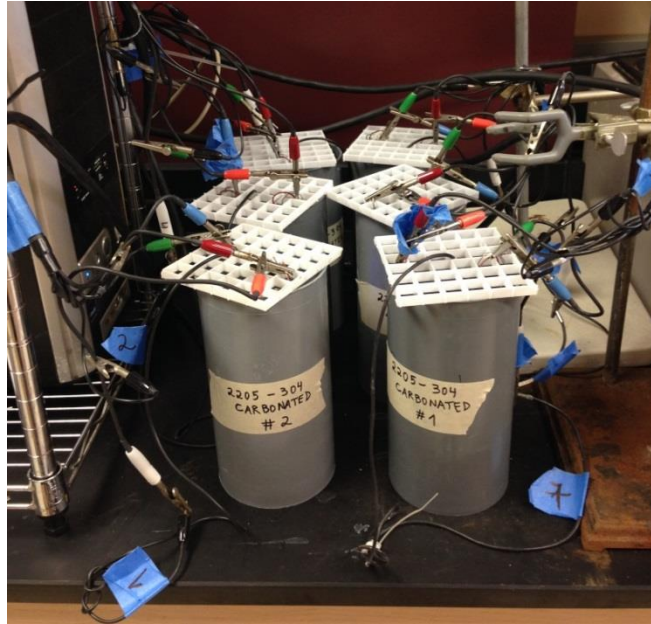
Figure C.4 System of 6 cells (three solutions, two replicates per solution).
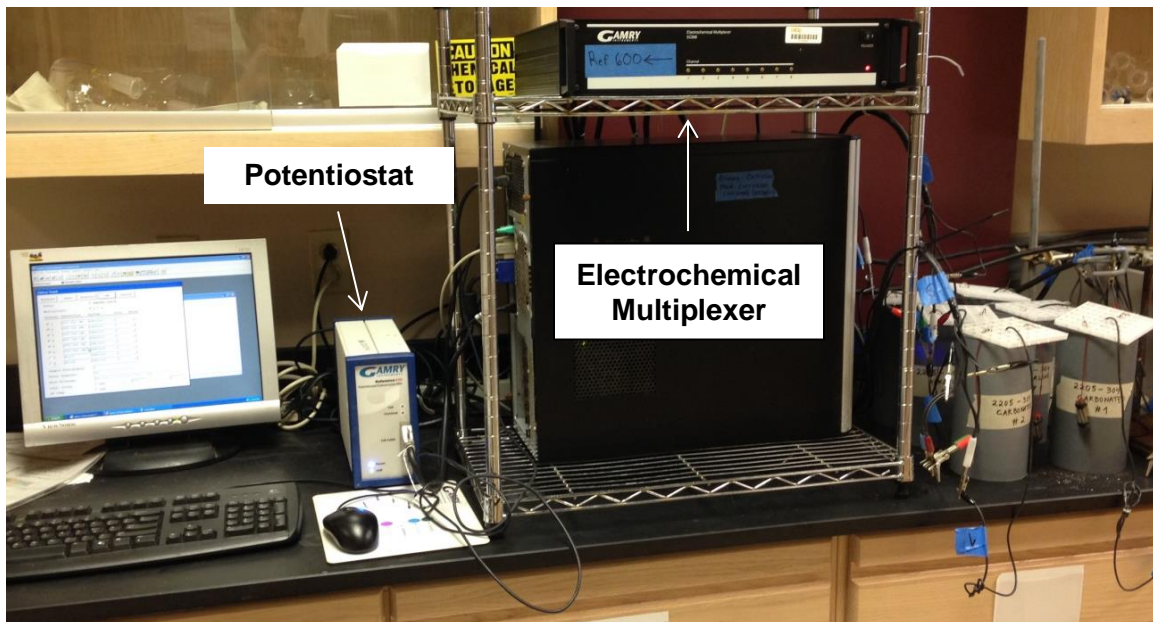
Figure C.5 Galvanic corrosion test set up.

C.2 Results

       The average current developed between the two stainless steels during the galvanic corrosion test is given in Figures C.6 and C.7. For every cell, the current between both samples (HSSS 2205 vs. SS 304) goes to values close to zero before 2 hours from the start of the test. The most extreme case, seawater condition, started with an average current of ~300 µA, but this value decreased quickly to 34.6 µA after 1 hour and 1.1 µA after 2 hours from the start of the test.
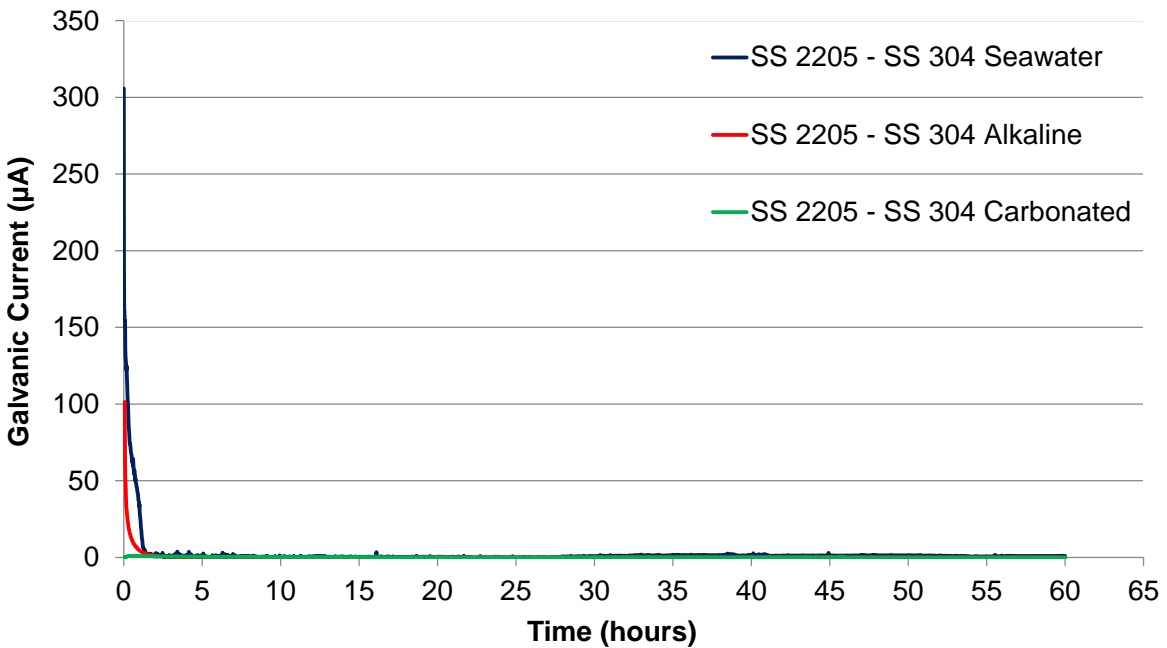
Figure C.6 Current evolution during galvanic corrosion test.
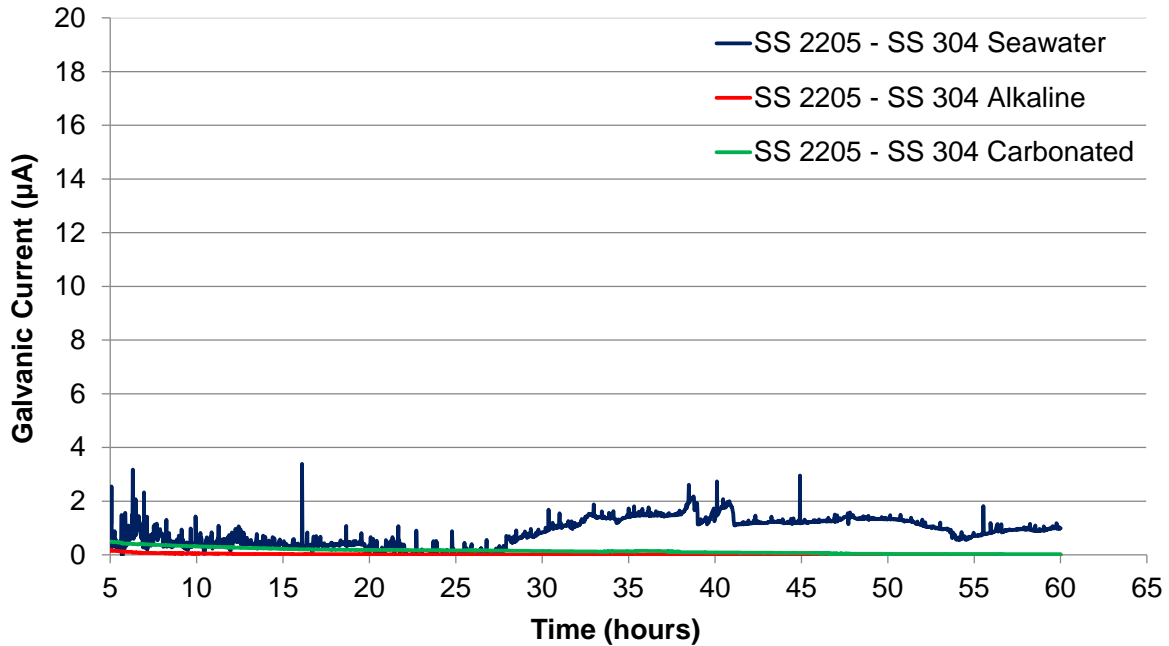
Figure C.7 Current evolution from 5 to 60 hours.

The occurrence of a galvanic couple produces a current flowing between the anode and the cathode, an accelerated corrosion of the anode, and an electrochemical protection for the cathodic member.

The measured current can be converted to corrosion rate using Faraday's law (Equation C.1).

$$r = 0.129 \; \frac{ia}{nF} \tag{C.1}$$

where r is the corrosion rate in mpy (mils per year), i is the current density, a is the atomic weight, F is Faraday's constant (96,500 C/equivalents), and n is the number of equivalents (electrons) exchanged. In the case of alloys, the number of equivalents can be calculated using Equation C.2.

$$N_{eq} = \sum \left(\frac{f_i \cdot n_i}{a_i} \right) \tag{C.2}$$

where f_i is the mass fraction, a_i is the atomic weight, and n_i is the numbers of electrons exchanged, for every i element in the alloy.

For austenitic SS 304 (anode), $N_{eq} = 0.03981$. The rate of corrosion for the anode was calculated using the average current of the last 10 hours of the test (Figure C.6) and Equation C.1. The rate of corrosion calculated for each condition can be observed in Table C.1. Commonly, rates of corrosion below 1 mpy are considered negligible and are indication of an excellent corrosion resistance (Jones, 1996).

Table C.1 Rate of galvanic corrosion under tested conditions.

Testing Condition	Rate of Corrosion (mpy)
Seawater	0.095775
Alkaline	0.000230
Carbonated	0.002832

Results observed in Figure C.6 and Table C.1 indicate that, in the case of a couple formed by HSSS duplex 2205 and austenitic SS 304 under tested conditions, both samples will passivate and the development of galvanic corrosion is highly unlikely.

APPENDIX D: PROPERTIES OF CONCRETE

- Compressive strength of concrete:

Age of Testing (days)	Batch*	Maximum Load (lbs)	Compressive Strength (psi)	Average (psi)	Std Dev (psi)
4	2	83,960	6,681.3	5,750	1,155
	1	51,160	4,071.2		
	6	75,260	5,989.0		
	7	78,660	6,259.6		
7	8	77,880	6,197.5	6,173	836
	2	87,910	6,995.7		
	1	66,909	5,324.4		
28	2	110,520	8,794.9	7,619	841
	4	92,140	7,332.3		
	7	102,470	8,154.3		
	6	101,980	8,115.3		
	1	82,260	6,546.0		
	8	93,580	7,446.9		
	5	102,570	8,162.3		
	1	80,470	6,403.6		
91	2	124,810	9,932.1	9,630	696
	3	127,220	10,123.8		
	4	111,000	8,833.1		
243	3	140,600	11,188.6	10,728	450
	2	134,550	10,707.1		
	5	129,290	10,288.6		
438	1	109,990	8,752.7	10,811	956
	1	111,660	8,885.6		
	2	147,980	11,775.9		
	2	149,100	11,865.0		
	2	156,220	12,431.6		
	3	149,030	11,859.4		
	3	155,660	12,387.0		
	4	124,580	9,913.8		
	4	129,900	10,337.1		
	4	131,940	10,499.5		
	5	138,150	10,993.6		
	5	140,230	11,159.1		
	6	134,010	10,664.2		
	6	137,100	10,910.1		
	6	137,340	10,929.2		
	7	131,590	10,471.6		
	7	136,580	10,868.7		
	7	137,720	10,959.4		
	8	127,110	10,115.1		
	8	130,970	10,422.3		
	8	136,090	10,829.7		

- Additional compressive strength test results of batch #1 cylinders and compressive strength of cores obtained from durability specimens:

Age of Testing (days)	Sample	Maximum Load (lbs)	Diameter (in)	Length (in)	L/d	Compressive Strength (psi)
42	Cores	41,820	2.73	6.01	2.2	7,145
		35,670	2.73	6.02	2.2	6,094
		40,090	2.73	5.90	2.2	6,849
42	Cylinders	85,850	4.00	8.00	2.0	6,832
		86,170	4.00	8.00	2.0	6,857
		87,560	4.00	8.00	2.0	6,968
624	Cores	74,480	2.73	5.51	2.0	12,724
		64,740	2.73	5.50	2.0	11,093
620	Cylinders	104,460	4.00	8.00	2.0	8,313
		115,600	4.00	8.00	2.0	9,199
		126,240	4.00	8.00	2.0	10,046

- Elastic modulus and Poisson's ratio of concrete:

Age of Testing (days)	Batch*	Poisson's Ratio	Average ν	Std Dev ν	Modulus of Elasticity (ksi)	Average E_c (ksi)	Std Dev E_c (ksi)
4	7	0.19			6,428.4		
	6	0.19	**0.19**	0.05	5,920.6	**6,138**	354
	7	0.21			6,065.8		
28	3	0.20			6,655.3		
	6	0.21	**0.20**	0.02	7,136.1	**6,683**	677
	8	0.20			6,256.9		
91	3	0.21			6,831.8		
	5	0.23	**0.22**	0.02	6,676.9	**6,892**	423
	8	0.24			7,235.1		
445	7	0.18			7,428.8		
	8	0.16	**0.17**	0.01	7,228.7	**7,138**	448
	5	0.17			6,733.7		

*Note: Batch #1 was used for the material evaluation blocks and 27-feet long piles used for development length tests.
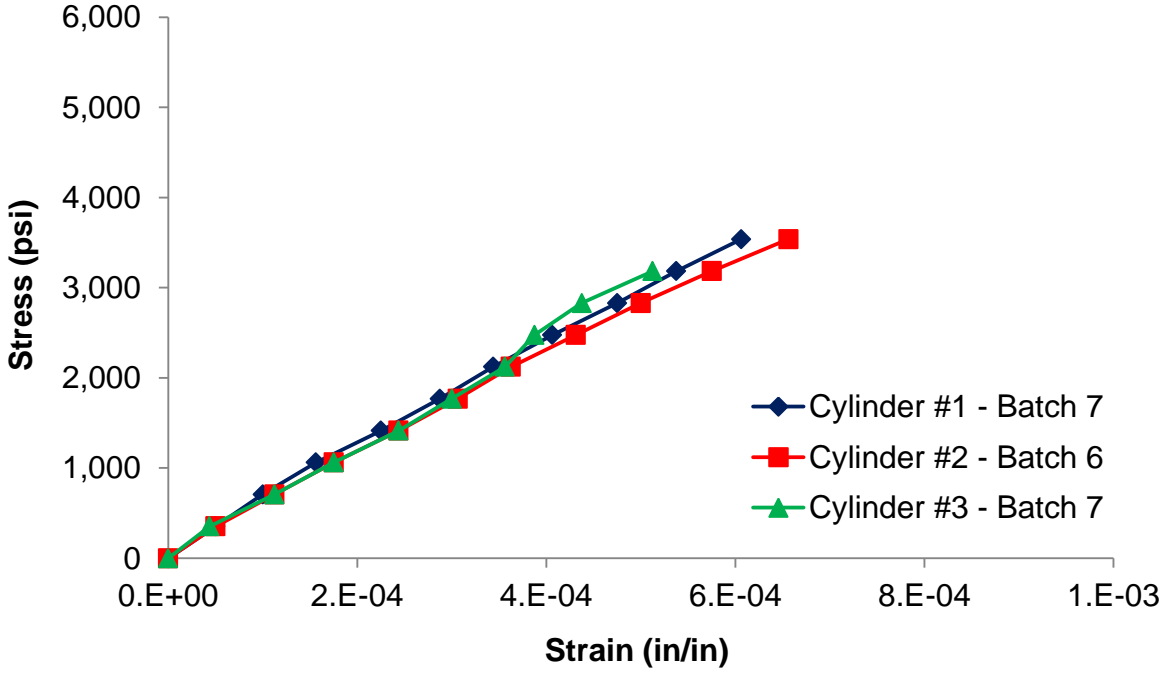
- Stress-strain curves (ASTM C469):

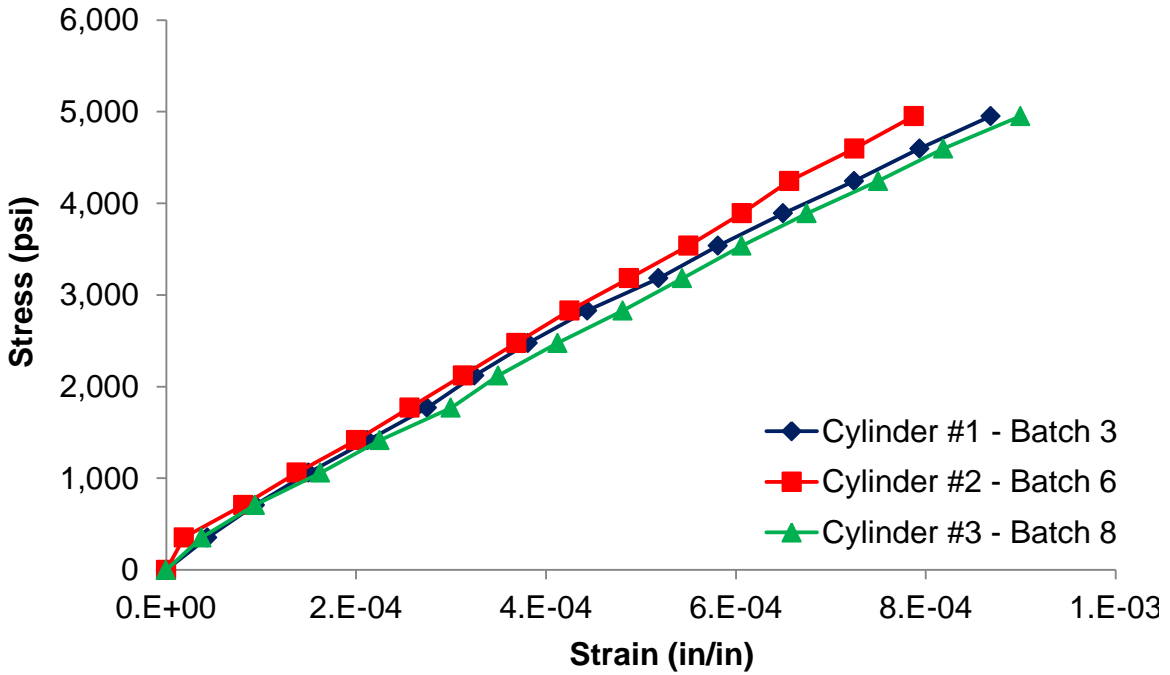**Figure D.1** Stress-strain curve of concrete at 4 days (ASTM C469).

Figure D.2 Stress-strain curve of concrete at 28 days (ASTM C469).
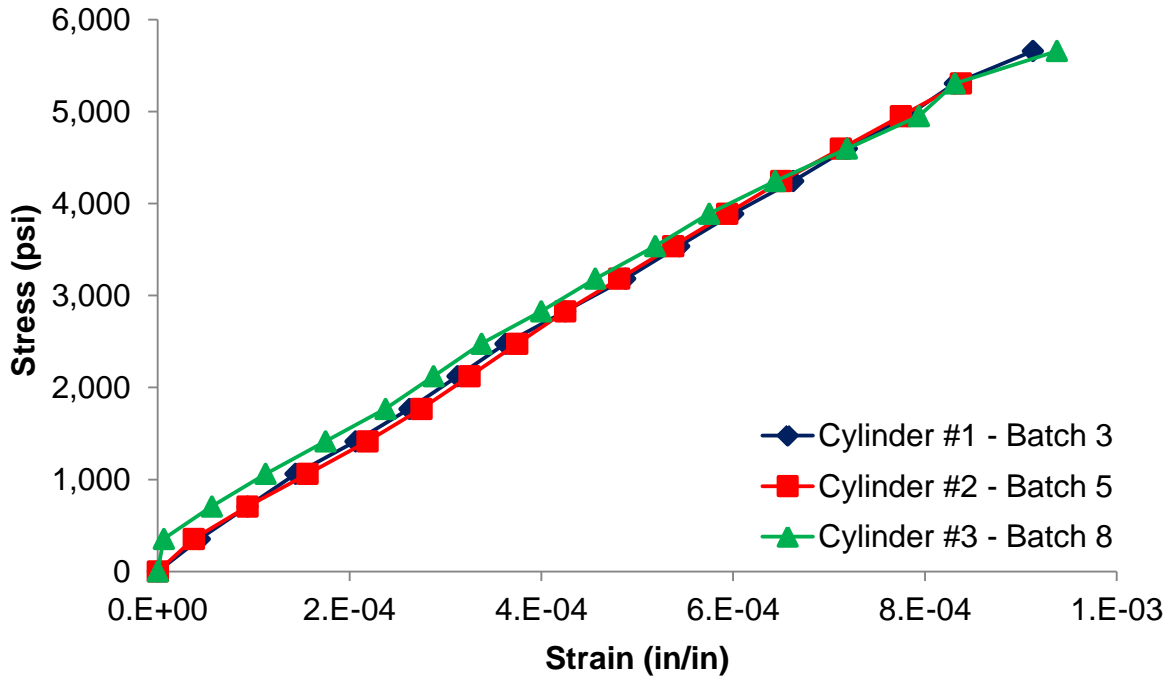
203

Figure D.3 Stress-strain curve of concrete at 91 days (ASTM C469).
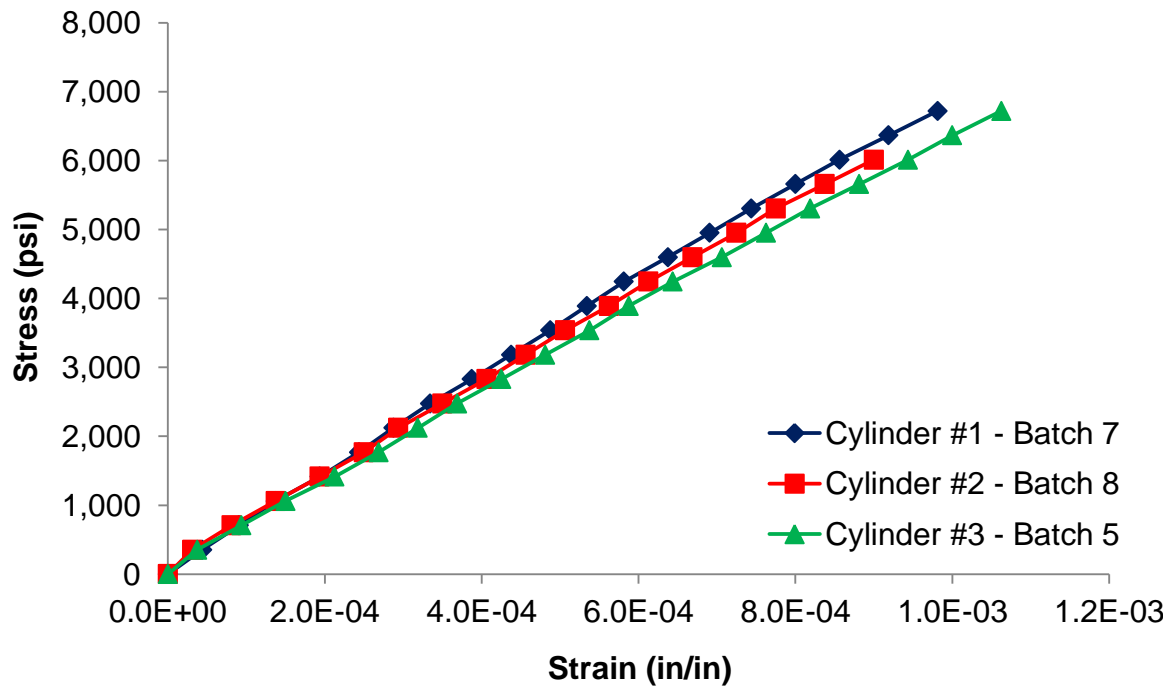

Figure D.4 Stress-strain curve of concrete at 445 days (ASTM C469).

APPENDIX E: PILE DRIVING INFORMATION

- Hammer specification provided by American Piledriving Equipment, Inc. [https://www.apevibro.com/]:

APE Model D30-32 Diesel Hammer

Batter Pile Energy Reduction Chart   Batter Pile Angle Chart   Bearing Chart: D30-32

Maximum rated energy	91,088 ft-lbs
Maximum obtainable stroke	165 inches
Pump setting 1: (minimum)	35,381 ft-lbs
Pump setting 2:	51,662 ft-lbs
Pump setting 3:	62,950 ft-lbs
Pump setting 4: (maximum)	69,458 ft-lbs
**Optional variable throttle gives infinte stroke control.	
Stroke at rated energy	126 inches
Energy at rated stroke	76,000 ft-lbs
Speed (blows per minute)	36-52
Ram	6,615 lbs
Avil	1,360 lbs
Hammer weight (includes trip device)	14,991 lbs
Typical operating (weight with drive cap)	17,076 lbs
Weight	675 lbs
Diameter	22.5 inches
Thickness (the 6 in above equation is thickness of plate)	6 inches
Type	Aluminum/Micarta
Diameter	22.5 inches
Thickness	2 inches
Elastic-Modulus	285 kips per square inch
Coeff. of Restitution	0.8
Weight (fits 8 by 26 leads)	1,166 lbs
Weight (fits 8 by 26 inch leads)	1,350 lbs
Square box inserts size 10 through 20 inch:	1,400 lbs
Pipe inserts for pipe size 12 to 24 diameter:	2,545 lbs

205
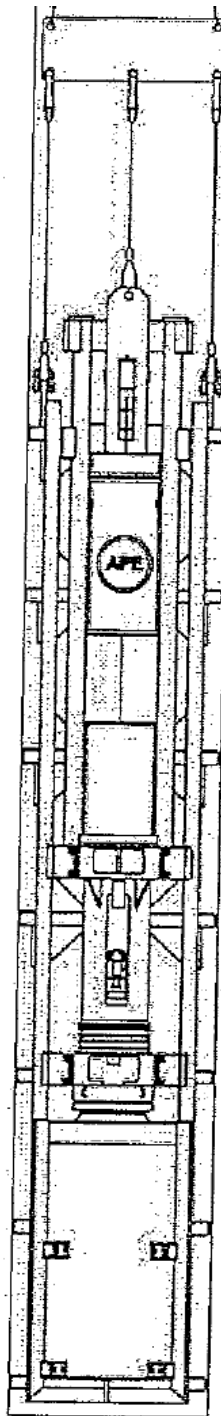
Fuel tank (runs on diesel or bio-diesel)	17.70 gal
Oil tank	2.4 gal
Diesel or Bio-diesel fuel	2.64 gal/hr
Lubrication oil	0.26 gal/hr
**Grease twice per day or after 45 minutes of continous driving	
Length overall	207.1 inches
Length over cylinder extension	246.4 inches
Impact block diameter	22.0 inches
Hammer width overall	28.3 inches
Minimum clearance for leads	19.7 inches
Note: if using 32 inch leads the drive cap will weigh:	1,550 lbs

Specifications may vary due to site conditions or hammer conditions or set up. Specifications may change without notice. Consult the factory for details on any specific hammer.

- APE diesel pile hammer bearing chart (based on GDOT formula) provided by The

Industrial Company (TIC), Savannah, Georgia:

Ram Weight (#) 6615 Penetration for 10 blows (In)	Bearing in tons when H, in feet, equals												
	4.0	4.5	5.0	5.5	6.0	6.5	7.0	7.5	8.0	8.5	9.0	9.5	10.0
0.5	106	119	132	146	159	172	185	198	212	225	238	251	265
0.625	101	113	126	139	151	164	176	189	202	214	227	239	252
0.75	96	108	120	132	144	156	168	180	192	204	216	229	241
0.875	92	104	115	127	138	150	161	173	184	196	207	219	230
1	88	99	110	121	132	143	154	165	176	187	198	209	221
1.125	85	95	106	116	127	138	148	159	169	180	191	201	212
1.25	81	92	102	112	122	132	142	153	163	173	183	193	204
1.375	78	88	98	108	118	127	137	147	157	167	176	186	196
1.5	76	85	95	104	113	123	132	142	151	161	170	180	189
1.625	73	82	91	100	109	119	128	137	146	155	164	173	182
1.75	71	79	88	97	106	115	123	132	141	150	159	168	176
1.875	68	77	85	94	102	111	119	128	137	145	154	162	171
2	66	74	83	91	99	107	116	124	132	141	149	157	165
2.125	64	72	80	88	96	104	112	120	128	136	144	152	160
2.25	62	70	78	86	93	101	109	117	125	132	140	148	156
2.375	60	68	76	83	91	98	106	113	121	129	136	144	151
2.5	59	66	74	81	88	96	103	110	118	125	132	140	147
2.625	57	64	72	79	86	93	100	107	114	122	129	136	143
2.75	56	63	70	77	84	91	97	104	111	118	125	132	139
2.875	54	61	68	75	81	88	95	102	109	115	122	129	136
3	53	60	66	73	79	86	93	99	106	112	119	126	132
3.125	52	58	65	71	77	84	90	97	103	110	116	123	129
3.25	50	57	63	69	76	82	88	95	101	107	113	120	126
3.375	49	55	62	68	74	80	86	92	98	105	111	117	123
3.5	48	54	60	66	72	78	84	90	96	102	108	114	120
3.625	47	53	59	65	71	76	82	88	94	100	106	112	118
3.75	46	52	58	63	69	75	81	86	92	98	104	109	115
3.875	45	51	56	62	68	73	79	84	90	96	101	107	113
4	44	50	55	61	66	72	77	83	88	94	99	105	110
4.125	43	49	54	59	65	70	76	81	86	92	97	103	108
4.25	42	48	53	58	64	69	74	79	85	90	95	101	106
4.375	42	47	52	57	62	67	73	78	83	88	93	99	104
4.5	41	46	51	56	61	66	71	76	81	87	92	97	102
4.625	40	45	50	55	60	65	70	75	80	85	90	95	100
4.75	39	44	49	54	59	64	69	74	78	83	88	93	98
4.875	38	43	48	53	58	63	67	72	77	82	87	91	96
5	38	43	47	52	57	61	66	71	76	80	85	90	95
5.125	37	42	46	51	56	60	65	70	74	79	84	88	93
5.25	36	41	46	50	55	59	64	68	73	78	82	87	91
5.375	36	40	45	49	54	58	63	67	72	76	81	85	90
5.5	35	40	44	49	53	57	62	66	71	75	79	84	88
5.625	35	39	43	48	52	56	61	65	69	74	78	82	87
5.75	34	38	43	47	51	55	60	64	68	73	77	81	85
5.875	34	38	42	46	50	55	59	63	67	71	76	80	84
6	33	37	41	45	50	54	58	62	66	70	74	79	83
6.125	33	37	41	45	49	53	57	61	65	69	73	77	81
6.25	32	36	40	44	48	52	56	60	64	68	72	76	80
6.375	32	36	39	43	47	51	55	59	63	67	71	75	79
6.5	31	35	39	43	47	51	54	58	62	66	70	74	78

Pile Bearing (TN) = 2WH / (S + 0.2)   WH = Hammer Energy (ft-lbs)   S = Pile Pentration per blow

- Pile driving log provided by The Industrial Company (TIC), Savannah, Georgia:

TIC PILE LOG

Hammer	D-30	Datum	Top of Template	Pile size	16"	Date	18-Dec-13
Fuel setting	#3	Elevation	~ +8 MHW	Type	PSC	By	WBJ
Cushion	6" plywood	Run of the pile		Pile length	70'		
		Weight of the hammer		Design Capacity	82 Tons		

Georgia Tech SS Test Pile Program

Pile 2 (cold hammer)			Pile 1 (PDA)			Pile S3 (PDA)			Pile S2			Pile S1		
Elev. (ft)	Depth (ft)	Blows	Elev. (ft)	Depth (ft)	Blows	Elev. (ft)	Depth (ft)	Blows	Elev. (ft)	Depth (ft)	Blows	Elev. (ft)	Depth (ft)	Blows
	1			1			1			1			1	
	2			2			2			2			2	
	3			3			3			3			3	
	4			4			4			4			4	
	5			5			5			5			5	
	6			6			6			6			6	
	7			7			7			7			7	
	8			8			8			8			8	
	9			9			9			9			9	
	10			10			10			10			10	
	11			11			11			11			11	
	12			12			12			12			12	
	13			13			13			13			13	
	14			14			14			14			14	
	15			15			15			15			15	
	16			16			16			16			16	
	17			17			17			17			17	
	18			18			18			18			18	
	19			19			19			19			19	
	20			20			20			20			20	
	21			21			21			21			21	
	22			22			22			22			22	
	23			23			23			23			23	
	24			24			24			24			24	
	25			25			25			25			25	
	26			26			26			26			26	
	27			27			27			27			27	
	28			28			28			28			28	
	29			29			29			29			29	
	30			30			30			30			30	
	31			31			31			31			31	
	32			32			32			32			32	
	33			33			33			33			33	
	34			34			34			34			34	
	35			35			35			35			35	
	36			36			36			36			36	
	37			37			37			37			37	
	38			38			38			38			38	
	39			39			39			39			39	
	40			40			40			40			40	
	41			41			41			41			41	
	42			42			42			42			42	
	43			43			43			43			43	
	44			44	8		44			44	3		44	
	45	1		45	22		45	8		45	7		45	
	46	3		46	32		46	18		46	17		46	8
	47	18		47	37		47	36		47	26		47	24
	48	27		48	36		48	46		48	28		48	26
	49	33		49	43		49	53		49	34		49	28
	50	35		50	44		50	50		50	40		50	33
	51	36		51	49		51	50		51	44		51	38
	52	41		52	53		52	52		52	54		52	41
	53	51		53	56		53	52		53	59		53	48
	54	51		54	56	-46	54	56	-46	54	stop		54	50
	55	52	-47	55	stop	-47	55	stop		55			55	61
	56	63		56			56			56		-48	56	stop
-49	57	stop		57			57			57			57	
	58			58			58			58			58	
	59	1 1/4"-5.5'		59	1 3/4"-5.5'		59	1 1/2"-5.5'		59	1 1/2"-5.5'		59	1 1/2"-5.5'
	60	112T		60	97T		60	104T		60	104T		60	104T

Note: Top of the marl was indicated at ~ EL -50 with the jet stopping penetration during extraction

Piles 1 and 2 were construction with conventional 270 ksi 7/16 strand and 5-gauge spiral
Piles S1, S2 and S3 were constructed with 2205 stainless steel 250 ksi 1/2 in. strand and stainless steel 5-gauge spiral

APPENDIX F: CALCULATION OF ULTIMATE CURVATURE BY MOMENT-AREA METHOD

The dial gauges, used for strain measurements during the flexure test, were removed before failure of the piles. However, the applied load and deflection at the mid-length were recorded during the complete duration of the test. Based on the ultimate load and deflection, the moment-area method was used for the estimation of the ultimate curvature.

Figure F.1 shows the applied symmetric curvature diagram, from a roller support to the mid-length of the pile. The length of the plastic hinge was assumed equal to the depth of the pile, 16-in. (40.6 cm), and Equation F.1 was used for the estimation of the ultimate curvature.

$$\Delta_u = \sum_{i=1}^{6} \left(A_i \times \bar{x}_i \right) \tag{F.1}$$

where A_i is the area of the region of the curvature diagram shown in Figure F.1, and $\bar{x}_i$ is the distance from the centroid of A_i to the roller support.

The ultimate moment was determined using the recorded ultimate load, while the moments and curvatures at cracking and yield points were obtained from calculated values using the actual position of strands and compressive strength of concrete of the piles. Cracking and yield moments were used to calculate the position of φ_{cr} and φ_y in the curvature diagram where φ is the curvature at the maximum moment section in radians/inch.

Given that the ultimate deflection was known from the flexure test data, Equation F.1 was solved for φ_u. The values of φ_u per each pile can be observed in Table F.1.
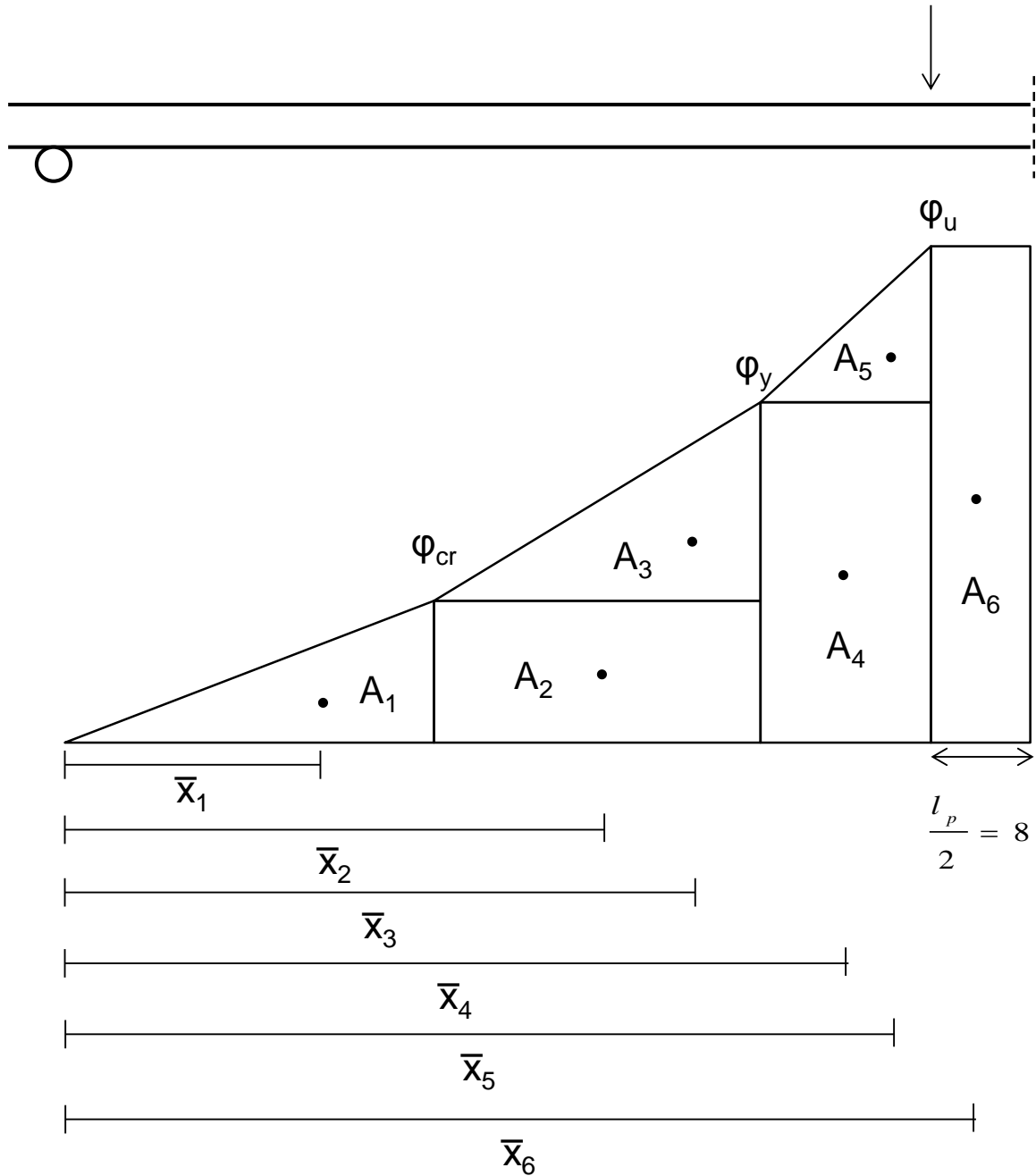
Figure F.1 Curvature diagram for ultimate curvature calculation where l_p is the plastic hinge length assumed as the distance between load points.

Table F.1 Ultimate curvature calculated by moment-area method. 1 rad/in = 39.37 rad/m.

	Ultimate curvature (rad/in)
Pile 1080 #1 - Top Half	1.073×10^{-3}
Pile 1080 #2 - Bottom Half	1.013×10^{-3}
Pile HSSS 2205 #1 - Top Half	9.071×10^{-4}

For piles 1080 #1 (bottom half), HSSS 2205 #2 (top half), HSSS 2205 #2 (bottom half), and HSSS 2205 #3 (top half) the calculated ultimate curvature was lower than the one obtained from test measurements. This can be attributed to a removal of the dial strain gauges close to the failure point in the case of pile 1080 #1 (bottom half), and to a brittle behavior that did not develop the assumed curvature diagram in Figure F.1, in the case of piles using duplex HSSS 2205 strands.

For piles 1080 #2 (top half), HSSS 2205 #1 (bottom half), and HSSS 2205 #3 (bottom half), the strain measurements were inappropriate for curvature calculations, due to failure of the dials during the test or mistakes in readings. Thus, the moment-curvature diagrams were not able to be calculated for these piles.

APPENDIX G: CALCULATION OF FLEXURAL CAPACITY OF PILES

G.1 ACI 318 Moment-Curvature Calculation for Pile SS #2 – Top Half.

Pile Properties:

$$L := 35ft \qquad \gamma := 150pcf \qquad \phi := 1.0$$

$$f_c := 10686psi \qquad f_{ci} := 4100psi$$

$$E_i := 57000 \cdot \sqrt{f_{ci} \cdot psi} = 3649.781 \cdot ksi$$

$$E := 57000 \cdot \sqrt{f_c \cdot psi} \qquad E = 5892.267 \cdot ksi$$

$$\beta_1 := \begin{vmatrix} 0.85 & \text{if } 2500psi \le f_c \le 4000psi & = 0.65 \\ 0.65 & \text{if } f_c \ge 8000psi \\ 1.05 - 0.05 \cdot \dfrac{f_c}{1000psi} & \text{otherwise} \end{vmatrix}$$

$$f_r := 7.5 \cdot \sqrt{f_c \cdot psi} = 0.775 \cdot ksi$$

$$b := 16.063in \qquad h := 16.125in \qquad A := b \cdot h = 259.016 \cdot in^2 \qquad I := \frac{1}{12} \cdot b \cdot h^3 = 5612.348 \cdot in^4$$

$$y_t := \frac{h}{2} = 8.063 \cdot in \quad y_b := -y_t \qquad k_t := \frac{I}{A \cdot y_b} = -2.687 \cdot in \qquad k_b := \frac{-I}{A \cdot y_t} = -2.687 \cdot in$$

Stainless Steel 2205 Strand Properties:

$$A_{strand} := 0.153in^2 \qquad f_{pu} := 241.5ksi \qquad \varepsilon_{us} := 0.016 \qquad d_b := \frac{1}{2}in = 0.5 \cdot in \qquad E_{ps} := 23500ksi$$

$$f_{py} := 228.7ksi \qquad \varepsilon_{ys} := 0.012 \qquad cover := 3.5in + \frac{d_b}{2} = 3.75 \cdot in \qquad P_{strand} := 22.5kip$$

$$f_{si} := \frac{P_{strand}}{A_{strand}} = 147.059 \cdot ksi \qquad e_{mid} := \frac{h - 2 \cdot cover}{6} = 1.438 \cdot in \qquad n := 12$$

$$num := \begin{pmatrix} 4 \\ 2 \\ 2 \\ 4 \end{pmatrix} \qquad e_p := \begin{pmatrix} \dfrac{h}{2} - cover \\ e_{mid} \\ -e_{mid} \\ cover - \dfrac{h}{2} \end{pmatrix} = \begin{pmatrix} 4.313 \\ 1.438 \\ -1.438 \\ -4.313 \end{pmatrix} \cdot in \qquad d_p := \begin{pmatrix} 4.188 \\ 7.125 \\ 10.125 \\ 12.875 \end{pmatrix} in$$

$$P_i := f_{si} \cdot num \cdot A_{strand} \qquad P_{tot} := \sum P_i = 270 \cdot kip \qquad \frac{f_{si}}{f_{pu}} = 60.894 \cdot \%$$

Calculated Prestress Losses (AASHTO): from mathcad spreadsheet.

$$Losses := -22.686ksi \qquad \Delta f_{ps} := Losses = -22.686 \cdot ksi \qquad f_{se} := f_{si} + \Delta f_{ps} = 124.373 \cdot ksi$$

$$\varepsilon_{calc} := \frac{\Delta f_{ps}}{E_{ps}} = -965.362 \cdot 10^{-6} \qquad F_i := f_{se} \cdot num \cdot A_{strand} \qquad F_{se} := \sum F_i = 228.349 \cdot kip$$

Cracking condition:

$$M_{cr} := -\left(\frac{F_{se}}{A} + f_r\right)\cdot\frac{I}{y_b} \qquad f_b := f_r \qquad f_t := \frac{-M_{cr}\cdot y_t}{I} = -1.657\cdot ksi$$

$$\varepsilon_b := \frac{f_b}{E} = 1.316 \times 10^{-4} \qquad \varepsilon_t := \frac{f_t}{E} = -2.812 \times 10^{-4} \qquad \phi_{cr} := \frac{\varepsilon_b - \varepsilon_t}{h}$$

$$\boxed{M_{cr} = 1153.376\cdot kip\cdot in} \qquad \boxed{\phi_{cr} = 2.56 \times 10^{-5}\cdot\frac{rad}{in}}$$

Yield condition:

$$\varepsilon_{tf} := 0.00241 \qquad\qquad \varepsilon_0 := 1.71\cdot\frac{f_c}{E} = 0.003$$

$$\beta_{1y} := \frac{\ln\left[1 + \left(\frac{\varepsilon_{tf}}{\varepsilon_0}\right)^2\right]}{\frac{\varepsilon_{tf}}{\varepsilon_0}} = 0.608 \qquad k_2 := 1 - 2\cdot\frac{\left(\frac{\varepsilon_{tf}}{\varepsilon_0} - atan\left(\frac{\varepsilon_{tf}}{\varepsilon_0}\right)\right)}{\left(\frac{\varepsilon_{tf}}{\varepsilon_0}\right)^2\cdot\beta_{1y}} = 0.365$$

$$\varepsilon_{se} := \frac{f_{se}}{E_{ps}} = 0.005292 \qquad f_{cgs} := \frac{-F_{se}}{A} = -0.882\cdot ksi \qquad \varepsilon_{ce} := \frac{f_{cgs}}{E} = -0.0001496$$

$$\boxed{c := 3.313in} \qquad \text{Manually adjust so T=C} \qquad C := \beta_{1y}\cdot f_c\cdot c\cdot b = 345.724\cdot kip$$

$$\varepsilon_c := \frac{\varepsilon_{tf}}{c}\cdot(d_p - c) = \begin{pmatrix} 0.00064 \\ 0.00277 \\ 0.00496 \\ 0.00696 \end{pmatrix} \qquad \varepsilon_s := \varepsilon_c + \varepsilon_{se} + \varepsilon_{ce} = \begin{pmatrix} 0.0058 \\ 0.0079 \\ 0.0101 \\ 0.0121 \end{pmatrix} \qquad \begin{array}{l}\text{Note:}\\ \text{Strand yields at 0.012}\\ \text{and ruptures at 0.016}\end{array}$$

$$f_s := \begin{pmatrix} 137.014ksi \\ 181.356ksi \\ 214.660ksi \\ 229.896ksi \end{pmatrix} \qquad \begin{array}{l}\text{Data from}\\ \text{stress-strain test}\end{array} \qquad \begin{array}{l} i := 0..3 \\ \\ P_i := f_{s_i}\cdot num_i\cdot A_{strand} \end{array} \qquad P = \begin{pmatrix} 83.853 \\ 55.495 \\ 65.686 \\ 140.696 \end{pmatrix}\cdot kip$$

$$T := f_s\cdot num\cdot A_{strand} = 345.73\cdot kip \qquad C = 345.72\cdot kip \qquad M_y := -C\cdot k_2\cdot c + P\cdot d_p$$

$$f_t := \frac{-M_y\cdot y_t}{I} = -4.029\cdot ksi \qquad \varepsilon_t := \frac{f_t}{E} = -6.838 \times 10^{-4} \qquad \varepsilon_b := \varepsilon_{s_3} = 0.0121$$

$$\phi_y := \frac{\varepsilon_b - \varepsilon_t}{h} \qquad\qquad \boxed{M_y = 2804.53\cdot kip\cdot in} \qquad \boxed{\phi_y = 7.927 \times 10^{-4}\cdot\frac{rad}{in}}$$

213

Ultimate capacity:

$$f''_c := 0.9 \cdot f_c = 9.617 \cdot ksi \qquad \varepsilon_u := 0.003$$

$$\beta_1 := \frac{\ln\left[1 + \left(\frac{\varepsilon_u}{\varepsilon_0}\right)^2\right]}{\frac{\varepsilon_u}{\varepsilon_0}} = 0.683 \qquad k_2 := 1 - 2 \cdot \frac{\left(\frac{\varepsilon_u}{\varepsilon_0} - atan\left(\frac{\varepsilon_u}{\varepsilon_0}\right)\right)}{\left(\frac{\varepsilon_u}{\varepsilon_0}\right)^2 \cdot \beta_1} = 0.347$$

$$\varepsilon_{se} := \frac{f_{se}}{E_{ps}} = 0.005292 \qquad f_{cgs} := \frac{-F_{se}}{A} = -0.882 \cdot ksi \qquad \varepsilon_{ce} := \frac{f_{cgs}}{E} = -0.0001496$$

$c := 3.381in$ Manually adjust so T=C $\qquad$ $C := \beta_1 \cdot f''_c \cdot c \cdot b = 356.636 \cdot kip$

$$\varepsilon_c := \frac{\varepsilon_u}{c} \cdot (d_p - c) = \begin{pmatrix} 0.00072 \\ 0.00332 \\ 0.00598 \\ 0.00842 \end{pmatrix} \qquad \varepsilon_s := \varepsilon_c + \varepsilon_{se} + \varepsilon_{ce} = \begin{pmatrix} 0.0059 \\ 0.0085 \\ 0.0111 \\ 0.0136 \end{pmatrix} \qquad \begin{array}{c} \text{Note:} \\ \text{Strand yields at 0.012} \\ \text{and ruptures at 0.016} \end{array}$$

$$f_s := \begin{pmatrix} 139.155ksi \\ 191.415ksi \\ 223.511ksi \\ 236.097ksi \end{pmatrix} \quad \begin{array}{c}\text{Data from} \\ \text{stress-strain test}\end{array} \qquad i := 0..3 \qquad P_i := f_{s_i} \cdot num_i \cdot A_{strand} \qquad P = \begin{pmatrix} 85.163 \\ 58.573 \\ 68.394 \\ 144.491 \end{pmatrix} \cdot kip$$

$$T := f_s \cdot num \cdot A_{strand} = 356.622 \cdot kip \qquad C = 356.636 \cdot kip$$

$$M_u := -C \cdot k_2 \cdot c + P \cdot d_p \qquad \phi_u := \frac{\varepsilon_u}{c} \qquad M_u = 2908.23 \cdot kip \cdot in \qquad \phi_u = 8.873 \times 10^{-4} \cdot \frac{rad}{in}$$

214

G.2 ACI 318 Moment-Curvature Calculation for Pile 1080 #1 – Bottom Half.

Pile Properties:

$$L := 35ft \qquad \gamma := 150pcf \qquad \phi := 1.0$$

$$f_c := 12064psi \qquad f_{ci} := 4100psi$$

$$E_i := 57000 \cdot \sqrt{f_{ci} \cdot psi} = 3649.781 \cdot ksi$$

$$E := 57000 \cdot \sqrt{f_c \cdot psi} \qquad E = 6260.666 \cdot ksi$$

$$f_r := 7.5 \cdot \sqrt{f_c \cdot psi} = 0.824 \cdot ksi$$

$$\beta_1 := \begin{vmatrix} 0.85 & \text{if } 2500psi \le f_c \le 4000psi & = 0.65 \\ 0.65 & \text{if } f_c \ge 8000psi \\ 1.05 - 0.05 \cdot \dfrac{f_c}{1000psi} & \text{otherwise} \end{vmatrix}$$

$$b := 16.063in \qquad h := 16.125in \qquad A := b \cdot h = 259.016 \cdot in^2 \qquad I := \frac{1}{12} \cdot b \cdot h^3 = 5612.348 \cdot in^4$$

$$y_t := \frac{h}{2} = 8.063 \cdot in \quad y_b := -y_t \qquad k_t := \frac{I}{A \cdot y_b} = -2.687 \cdot in \qquad k_b := \frac{-I}{A \cdot y_t} = -2.687 \cdot in$$

High Strength Steel AISI 1080 Strand Properties:

$$A_{strand} := 0.1155in^2 \quad f_{pu} := 281.1ksi \quad \varepsilon_{us} := 0.0547 \quad d_b := \frac{7}{16}in = 0.438 \cdot in \quad E_{ps} := 29400ksi$$

$$f_{py} := 265.47ksi \quad \varepsilon_{ys} := 0.01 \qquad cover := 3.5in + \frac{d_b}{2} = 3.719 \cdot in \qquad P_{strand} := 22.5kip$$

$$f_{si} := \frac{P_{strand}}{A_{strand}} = 194.805 \cdot ksi \qquad e_{mid} := \frac{h - 2 \cdot cover}{6} = 1.448 \cdot in \qquad n := 12$$

$$num := \begin{pmatrix} 4 \\ 2 \\ 2 \\ 4 \end{pmatrix} \qquad e_p := \begin{pmatrix} \dfrac{h}{2} - cover \\ e_{mid} \\ -e_{mid} \\ cover - \dfrac{h}{2} \end{pmatrix} = \begin{pmatrix} 4.344 \\ 1.448 \\ -1.448 \\ -4.344 \end{pmatrix} \cdot in \qquad d_p := \begin{pmatrix} 3.5 \\ 6.375 \\ 9.313 \\ 12.188 \end{pmatrix} in$$

$$P_i := f_{si} \cdot num \cdot A_{strand} \qquad P_{tot} := \sum P_i = 270 \cdot kip \qquad \frac{f_{si}}{f_{pu}} = 69.301 \cdot \%$$

Calculated Prestress Losses (AASHTO): from mathcad spreadsheet.

$$Losses := -24.42ksi \qquad \Delta f_{ps} := Losses = -24.42 \cdot ksi \qquad f_{se} := f_{si} + \Delta f_{ps} = 170.385 \cdot ksi$$

$$\varepsilon_{calc} := \frac{\Delta f_{ps}}{E_{ps}} = -830.612 \cdot 10^{-6} \qquad F_i := f_{se} \cdot num \cdot A_{strand} \qquad F_{se} := \sum F_i = 236.154 \cdot kip$$

Cracking condition:

$$M_{cr} := -\left(\frac{F_{se}}{A} + f_r\right) \cdot \frac{I}{y_b}$$

$$f_b := f_r \qquad f_t := \frac{-M_{cr} \cdot y_t}{I} = -1.736 \cdot ksi$$

$$\varepsilon_b := \frac{f_b}{E} = 1.316 \times 10^{-4} \qquad \varepsilon_t := \frac{f_t}{E} = -2.772 \times 10^{-4} \qquad \phi_{cr} := \frac{\varepsilon_b - \varepsilon_t}{h}$$

$$M_{cr} = 1208.095 \cdot kip \cdot in \qquad \phi_{cr} = 2.535 \times 10^{-5} \cdot \frac{rad}{in}$$

Yield condition:

$$\varepsilon_{tf} := 0.00177 \qquad \varepsilon_0 := 1.71 \cdot \frac{f_c}{E} = 0.003$$

$$\beta_{1y} := \frac{\ln\left[1 + \left(\frac{\varepsilon_{tf}}{\varepsilon_0}\right)^2\right]}{\frac{\varepsilon_{tf}}{\varepsilon_0}} = 0.472 \qquad k_2 := 1 - 2 \cdot \frac{\left(\frac{\varepsilon_{tf}}{\varepsilon_0} - atan\left(\frac{\varepsilon_{tf}}{\varepsilon_0}\right)\right)}{\left(\frac{\varepsilon_{tf}}{\varepsilon_0}\right)^2 \cdot \beta_{1y}} = 0.35$$

$$\varepsilon_{se} := \frac{f_{se}}{E_{ps}} = 0.005795 \qquad f_{cgs} := \frac{-F_{se}}{A} = -0.912 \cdot ksi \qquad \varepsilon_{ce} := \frac{f_{cgs}}{E} = -0.0001456$$

$$c := 3.359in \qquad \text{Manually adjust so T=C} \qquad C := \beta_{1y} \cdot f_c \cdot c \cdot b = 307.201 \cdot kip$$

$$\varepsilon_c := \frac{\varepsilon_{tf}}{c} \cdot (d_p - c) = \begin{pmatrix} 0.00007 \\ 0.00159 \\ 0.00314 \\ 0.00465 \end{pmatrix} \qquad \varepsilon_s := \varepsilon_c + \varepsilon_{se} + \varepsilon_{ce} = \begin{pmatrix} 0.0057 \\ 0.0072 \\ 0.0088 \\ 0.0103 \end{pmatrix} \qquad \begin{array}{l} \text{Note:} \\ \text{Strand yields at 0.010} \\ \text{and ruptures at 0.0547} \end{array}$$

$$f_s := \begin{pmatrix} 166.304ksi \\ 209.348ksi \\ 251.726ksi \\ 268.009ksi \end{pmatrix} \qquad \begin{array}{l} \text{Data from} \\ \text{stress-strain test} \end{array} \qquad \begin{array}{l} i := 0 .. 3 \\ P_i := f_{s_i} \cdot num_i \cdot A_{strand} \end{array} \qquad P = \begin{pmatrix} 76.832 \\ 48.359 \\ 58.149 \\ 123.82 \end{pmatrix} \cdot kip$$

$$T := f_s \cdot num \cdot A_{strand} = 307.16 \cdot kip \qquad C = 307.2 \cdot kip \qquad M_y := -C \cdot k_2 \cdot c + P \cdot d_p$$

$$f_t := \frac{-M_y \cdot y_t}{I} = -3.256 \cdot ksi \qquad \varepsilon_t := \frac{f_t}{E} = -5.2 \times 10^{-4} \qquad \varepsilon_b := \varepsilon_{s_3} = 0.0103$$

$$\phi_y := \frac{\varepsilon_b - \varepsilon_t}{h} \qquad M_y = 2266.26 \cdot kip \cdot in \qquad \phi_y = 6.711 \times 10^{-4} \cdot \frac{rad}{in}$$

216

Ultimate capacity:

$$f''_c := 0.9 \cdot f_c = 10.858 \cdot ksi \qquad \varepsilon_u := 0.003$$

$$\beta_{1u} := \frac{\ln\left[1 + \left(\dfrac{\varepsilon_u}{\varepsilon_0}\right)^2\right]}{\dfrac{\varepsilon_u}{\varepsilon_0}} = 0.663 \qquad\qquad k_2 := 1 - 2 \cdot \frac{\left(\dfrac{\varepsilon_u}{\varepsilon_0} - atan\left(\dfrac{\varepsilon_u}{\varepsilon_0}\right)\right)}{\left(\dfrac{\varepsilon_u}{\varepsilon_0}\right)^2 \cdot \beta_{1u}} = 0.375$$

$$\varepsilon_{se} := \frac{f_{se}}{E_{ps}} = 0.005795 \qquad f_{cgs} := \frac{-F_{se}}{A} = -0.912 \cdot ksi \qquad \varepsilon_{ce} := \frac{f_{cgs}}{E} = -0.0001456$$

$c := 2.876in$ Manually adjust so T=C $C := \beta_{1u} \cdot f''_c \cdot c \cdot b = 332.607 \cdot kip$

$$\varepsilon_c := \frac{\varepsilon_u}{c} \cdot (d_p - c) = \begin{pmatrix} 0.00065 \\ 0.00365 \\ 0.00671 \\ 0.00971 \end{pmatrix} \qquad \varepsilon_s := \varepsilon_c + \varepsilon_{se} + \varepsilon_{ce} = \begin{pmatrix} 0.0063 \\ 0.0093 \\ 0.0124 \\ 0.0154 \end{pmatrix}$$

Note:
Strand yields at 0.010
and ruptures at 0.0547

$$f_s := \begin{pmatrix} 181.957ksi \\ 260.217ksi \\ 271.957ksi \\ 271.957ksi \end{pmatrix}$$ Data from stress-strain test $i := 0..3$ $P_i := f_{s_i} \cdot num_i \cdot A_{strand}$ $$P = \begin{pmatrix} 84.064 \\ 60.11 \\ 62.822 \\ 125.644 \end{pmatrix} \cdot kip$$

$$T := f_s \cdot num \cdot A_{strand} = 332.64 \cdot kip \qquad C = 332.61 \cdot kip$$

$$M_u := -C \cdot k_2 \cdot c + P \cdot d_p \qquad \phi_u := \frac{\varepsilon_u}{c} \qquad M_u = 2435.55 \cdot kip \cdot in \qquad \phi_u = 1.043 \times 10^{-3} \cdot \frac{rad}{in}$$

217

G.3 AASHTO Moment-Curvature Calculation for Pile SS #2 – Top Half.

Pile Properties:

$$L := 35ft \qquad \phi := 1.0$$

$$f_c := 10686psi \qquad f_{ci} := 4100psi$$

$$\beta_1 := \begin{cases} 0.85 & \text{if } 2500psi \le f_c \le 4000psi & = 0.65 \\ 0.65 & \text{if } f_c \ge 8000psi \\ 1.05 - 0.05 \cdot \dfrac{f_c}{1000psi} & \text{otherwise} \end{cases}$$

$$E_i := 33000 \cdot (0.147)^{1.5} \cdot \sqrt{f_{ci} \cdot ksi} = 3766 \cdot ksi$$

$$E := 33000 \cdot (0.147)^{1.5} \cdot \sqrt{f_c \cdot ksi} = 6080 \cdot ksi$$

$$f_r := 0.24 \cdot \sqrt{f_c \cdot ksi} = 0.785 \cdot ksi$$

$$b := 16.063in \qquad h := 16.125in \qquad A := b \cdot h = 259.016 \cdot in^2 \qquad I := \frac{1}{12} \cdot b \cdot h^3 = 5612.348 \cdot in^4$$

$$y_t := \frac{h}{2} = 8.063 \cdot in \quad y_b := -y_t \qquad k_t := \frac{I}{A \cdot y_b} = -2.687 \cdot in \qquad k_b := \frac{-I}{A \cdot y_t} = -2.687 \cdot in$$

Stainless Steel 2205 Strand Properties:

$$A_{strand} := 0.153in^2 \qquad f_{pu} := 241.5ksi \qquad \varepsilon_{us} := 0.016 \qquad d_b := \frac{1}{2}in = 0.5 \cdot in \qquad E_{ps} := 23500ksi$$

$$f_{py} := 228.7ksi \qquad \varepsilon_{ys} := 0.012 \qquad cover := 3.5in + \frac{d_b}{2} = 3.75 \cdot in \qquad P_{strand} := 22.5kip$$

$$f_{si} := \frac{P_{strand}}{A_{strand}} = 147.059 \cdot ksi \qquad e_{mid} := \frac{h - 2 \cdot cover}{6} = 1.438 \cdot in \qquad n := 12$$

$$num := \begin{pmatrix} 4 \\ 2 \\ 2 \\ 4 \end{pmatrix} \qquad e_p := \begin{pmatrix} \dfrac{h}{2} - cover \\ e_{mid} \\ -e_{mid} \\ cover - \dfrac{h}{2} \end{pmatrix} = \begin{pmatrix} 4.313 \\ 1.438 \\ -1.438 \\ -4.313 \end{pmatrix} \cdot in \qquad d_p := \begin{pmatrix} 4.188 \\ 7.125 \\ 10.125 \\ 12.875 \end{pmatrix} in$$

$$P_i := f_{si} \cdot num \cdot A_{strand} \qquad P_{tot} := \sum P_i = 270 \cdot kip \qquad \frac{f_{si}}{f_{pu}} = 60.894 \cdot \%$$

Calculated Prestress Losses (AASHTO): from mathcad spreadsheet.

$$Losses := -22.686ksi \qquad \Delta f_{ps} := Losses = -22.686 \cdot ksi \qquad f_{se} := f_{si} + \Delta f_{ps} = 124.373 \cdot ksi$$

$$\varepsilon_{calc} := \frac{\Delta f_{ps}}{E_{ps}} = -965.362 \cdot 10^{-6} \qquad F_i := f_{se} \cdot num \cdot A_{strand} \qquad F_{se} := \sum F_i = 228.349 \cdot kip$$

Cracking condition:

$$\gamma_1 := 1.6 \qquad \gamma_2 := 1.1 \qquad \gamma_3 := 1.0 \qquad S_c := \frac{b \cdot h^2}{6}$$

$$M_{cr} := \gamma_3 \cdot \left[\left(\gamma_1 \cdot f_r + \gamma_2 \cdot \frac{F_{se}}{A} \right) \cdot S_c \right]$$

$$f_b := f_r \qquad f_t := \frac{-M_{cr} \cdot y_t}{I} = -2.225 \cdot ksi$$

$$\varepsilon_b := \frac{f_b}{E} = 1.29 \times 10^{-4} \qquad \varepsilon_t := \frac{f_t}{E} = -3.66 \times 10^{-4} \qquad \phi_{cr} := \frac{\varepsilon_b - \varepsilon_t}{h}$$

$$\boxed{M_{cr} = 1548.859 \cdot kip \cdot in} \qquad \boxed{\phi_{cr} = 3.07 \times 10^{-5} \cdot \frac{rad}{in}}$$

Ultimate capacity:

$$\varepsilon_u := 0.003 \qquad k := 2 \cdot \left(1.04 - \frac{f_{py}}{f_{pu}} \right) \qquad A_{ps} := n \cdot A_{strand} \qquad d := \frac{h}{2}$$

$$c := \frac{A_{ps} \cdot f_{pu}}{0.85 \cdot \left(f_c \cdot \beta_1 \cdot b + k \cdot A_{ps} \cdot \frac{f_{pu}}{d} \right)} = 4.283 \cdot in \qquad a := \beta_1 \cdot c$$

$$f_{ps} := f_{pu} \cdot \left(1 - k \cdot \frac{c}{d_p} \right) = \begin{pmatrix} 195.564 \\ 214.499 \\ 222.5 \\ 226.558 \end{pmatrix} \cdot ksi$$

$$M_u := \sum_{i=0}^{3} \left(f_{ps_i} \cdot num_i \cdot A_{strand} \right) \cdot \left(d - \frac{a}{2} \right) \qquad \phi_u := \frac{\varepsilon_u}{c}$$

$$\boxed{M_u = 2615.284 \cdot kip \cdot in} \qquad \boxed{\phi_u = 7.005 \times 10^{-4} \cdot \frac{rad}{in}}$$

G.4 AASHTO Moment-Curvature Calculation for Pile 1080 #1 – Bottom Half.

Pile Properties:

$$L := 35\text{ft} \qquad\qquad \phi := 1.0$$

$$f_c := 12064\text{psi} \qquad f_{ci} := 4100\text{psi}$$

$$\beta_1 := \begin{vmatrix} 0.85 & \text{if } 2500\text{psi} \le f_c \le 4000\text{psi} & = 0.65 \\ 0.65 & \text{if } f_c \ge 8000\text{psi} \\ 1.05 - 0.05\cdot\dfrac{f_c}{1000\text{psi}} & \text{otherwise} \end{vmatrix}$$

$$E_i := 33000\cdot(0.147)^{1.5}\cdot\sqrt{f_{ci}\cdot\text{ksi}} = 3766\cdot\text{ksi}$$

$$E := 33000\cdot(0.147)^{1.5}\cdot\sqrt{f_c\cdot\text{ksi}} = 6460\cdot\text{ksi}$$

$$f_r := 0.24\cdot\sqrt{f_c\cdot\text{ksi}} = 0.834\cdot\text{ksi}$$

$$b := 16.063\text{in} \qquad h := 16.125\text{in} \qquad A := b\cdot h = 259.016\cdot\text{in}^2 \qquad I := \frac{1}{12}\cdot b\cdot h^3 = 5612.348\cdot\text{in}^4$$

$$y_t := \frac{h}{2} = 8.063\cdot\text{in} \quad y_b := -y_t \qquad k_t := \frac{I}{A\cdot y_b} = -2.687\cdot\text{in} \qquad k_b := \frac{-I}{A\cdot y_t} = -2.687\cdot\text{in}$$

High Strength Steel AISI 1080 Strand Properties:

$$A_{strand} := 0.1155\text{in}^2 \quad f_{pu} := 281.1\text{ksi} \quad \varepsilon_{us} := 0.0547 \quad d_b := \frac{7}{16}\text{in} = 0.438\cdot\text{in} \quad E_{ps} := 29400\text{ksi}$$

$$f_{py} := 265.47\text{ksi} \quad \varepsilon_{ys} := 0.01 \qquad \text{cover} := 3.5\text{in} + \frac{d_b}{2} = 3.719\cdot\text{in} \quad P_{strand} := 22.5\text{kip}$$

$$f_{si} := \frac{P_{strand}}{A_{strand}} = 194.805\cdot\text{ksi} \qquad e_{mid} := \frac{h - 2\cdot\text{cover}}{6} = 1.448\cdot\text{in} \qquad n := 12$$

$$\text{num} := \begin{pmatrix} 4 \\ 2 \\ 2 \\ 4 \end{pmatrix} \qquad e_p := \begin{pmatrix} \dfrac{h}{2} - \text{cover} \\ e_{mid} \\ -e_{mid} \\ \text{cover} - \dfrac{h}{2} \end{pmatrix} = \begin{pmatrix} 4.344 \\ 1.448 \\ -1.448 \\ -4.344 \end{pmatrix}\cdot\text{in} \qquad d_p := \begin{pmatrix} 3.5 \\ 6.375 \\ 9.313 \\ 12.188 \end{pmatrix}\text{in}$$

$$P_i := f_{si}\cdot\text{num}\cdot A_{strand} \qquad P_{tot} := \sum P_i = 270\cdot\text{kip} \qquad \frac{f_{si}}{f_{pu}} = 69.301\cdot\%$$

Calculated Prestress Losses (AASHTO): from mathcad spreadsheet.

$$\text{Losses} := -24.42\text{ksi} \qquad \Delta f_{ps} := \text{Losses} = -24.42\cdot\text{ksi} \qquad f_{se} := f_{si} + \Delta f_{ps} = 170.385\cdot\text{ksi}$$

$$\varepsilon_{calc} := \frac{\Delta f_{ps}}{E_{ps}} = -830.612\cdot10^{-6} \qquad F_i := f_{se}\cdot\text{num}\cdot A_{strand} \qquad F_{se} := \sum F_i = 236.154\cdot\text{kip}$$

Cracking condition:

$$\gamma_1 := 1.6 \qquad \gamma_2 := 1.1 \qquad \gamma_3 := 1.0 \qquad S_c := \frac{b \cdot h^2}{6}$$

$$M_{cr} := \gamma_3 \cdot \left[\left(\gamma_1 \cdot f_r + \gamma_2 \cdot \frac{F_{se}}{A} \right) \cdot S_c \right]$$

$$f_b := f_r \qquad f_t := \frac{-M_{cr} \cdot y_t}{I} = -2.337 \cdot ksi$$

$$\varepsilon_b := \frac{f_b}{E} = 1.29 \times 10^{-4} \qquad \varepsilon_t := \frac{f_t}{E} = -3.617 \times 10^{-4} \qquad \phi_{cr} := \frac{\varepsilon_b - \varepsilon_t}{h}$$

$$\boxed{M_{cr} = 1626.565 \cdot kip \cdot in} \qquad \boxed{\phi_{cr} = 3.043 \times 10^{-5} \cdot \frac{rad}{in}}$$

Ultimate capacity:

$$\varepsilon_u := 0.003 \qquad k := 2 \cdot \left(1.04 - \frac{f_{py}}{f_{pu}} \right) \qquad A_{ps} := n \cdot A_{strand} \qquad d := \frac{h}{2}$$

$$c := \frac{A_{ps} \cdot f_{pu}}{0.85 \cdot \left(f_c \cdot \beta_1 \cdot b + k \cdot A_{ps} \cdot \frac{f_{pu}}{d} \right)} = 3.39 \cdot in \qquad a := \beta_1 \cdot c$$

$$f_{ps} := f_{pu} \cdot \left(1 - k \cdot \frac{c}{d_p} \right) = \begin{pmatrix} 229.037 \\ 252.517 \\ 261.534 \\ 266.149 \end{pmatrix} \cdot ksi$$

$$M_u := \sum_{i=0}^{3} \left(f_{ps_i} \cdot num_i \cdot A_{strand} \right) \cdot \left(d - \frac{a}{2} \right) \qquad \phi_u := \frac{\varepsilon_u}{c}$$

$$\boxed{M_u = 2418.986 \cdot kip \cdot in} \qquad \boxed{\phi_u = 8.849 \times 10^{-4} \cdot \frac{rad}{in}}$$

221

APPENDIX H: INDIVIDUAL RESULTS OF FLEXURE TEST

Table H.1 Calculated moments and curvatures at cracking, yield, and ultimate condition for piles using AISI 1080 steel strands (ACI 318).

	$M_{crack,calc}$ (kip·in)	$\varphi_{crack,calc}$ (rad/in)	$M_{yield,calc}$ (kip·in)	$\varphi_{yield,calc}$ (rad/in)	$M_{ult,calc}$ (kip·in)	$\varphi_{ult,calc}$ (rad/in)
Pile 1080 #1 Top Half	1,208	2.54×10^{-5}	2,266	6.71×10^{-4}	2,436	1.04×10^{-3}
Pile 1080 #1 Bottom Half	1,208	2.54×10^{-5}	2,266	6.71×10^{-4}	2,436	1.04×10^{-3}
Pile 1080 #2 Top Half	1,148	2.64×10^{-5}	2,351	6.42×10^{-4}	2,531	8.88×10^{-4}
Pile 1080 #2 Bottom Half	1,148	2.64×10^{-5}	2,351	6.42×10^{-4}	2,531	8.88×10^{-4}

Table H.2 Calculated moments and curvatures at cracking, yield, and ultimate condition for piles using duplex HSSS 2205 strands (ACI 318).

	$M_{crack,calc}$ (kip·in)	$\varphi_{crack,calc}$ (rad/in)	$M_{yield,calc}$ (kip·in)	$\varphi_{yield,calc}$ (rad/in)	$M_{ult,calc}$ (kip·in)	$\varphi_{ult,calc}$ (rad/in)
Pile 2205 #1 Top Half	1,151	2.56×10^{-5}	2,530	7.70×10^{-4}	2,633	9.15×10^{-4}
Pile 2205 #1 Bottom Half	1,151	2.56×10^{-5}	2,530	7.70×10^{-4}	2,633	9.15×10^{-4}
Pile 2205 #2 Top Half	1,153	2.56×10^{-5}	2,805	7.93×10^{-4}	2,908	8.87×10^{-4}
Pile 2205 #2 Bottom Half	1,153	2.56×10^{-5}	2,774	7.92×10^{-4}	2,877	8.92×10^{-4}
Pile 2205 #3 Top Half	1,160	2.55×10^{-5}	2,757	7.93×10^{-4}	2,856	9.04×10^{-4}
Pile 2205 #3 Bottom Half	1,160	2.55×10^{-5}	2,773	7.96×10^{-4}	2,866	9.02×10^{-4}

Table H.3 Calculated moments and curvatures at cracking and ultimate condition for piles using AISI 1080 steel strands (AASHTO LRFD).

	$M_{crack,calc}$ (kip·in)	$\varphi_{crack,calc}$ (rad/in)	$M_{ult,calc}$ (kip·in)	$\varphi_{ult,calc}$ (rad/in)
Pile 1080 #1 Top Half	1,613	3.06×10^{-5}	2,406	8.82×10^{-4}
Pile 1080 #1 Bottom Half	1,627	3.04×10^{-5}	2,419	8.85×10^{-4}
Pile 1080 #2 Top Half	1,536	3.14×10^{-5}	2,313	7.19×10^{-4}
Pile 1080 #2 Bottom Half	1,536	3.14×10^{-5}	2,321	7.19×10^{-4}

Table H.4 Calculated moments and curvatures at cracking and ultimate condition for piles using duplex HSSS 2205 strands (AASHTO LRFD).

	$M_{crack,calc}$ (kip·in)	$\varphi_{crack,calc}$ (rad/in)	$M_{ult,calc}$ (kip·in)	$\varphi_{ult,calc}$ (rad/in)
Pile 2205 #1 Top Half	1,546	3.07×10^{-5}	2,560	6.96×10^{-4}
Pile 2205 #1 Bottom Half	1,546	3.07×10^{-5}	2,564	6.96×10^{-4}
Pile 2205 #2 Top Half	1,549	3.07×10^{-5}	2,615	7.01×10^{-4}
Pile 2205 #2 Bottom Half	1,508	3.14×10^{-5}	2,560	6.99×10^{-4}
Pile 2205 #3 Top Half	1,540	3.09×10^{-5}	2,606	7.16×10^{-4}
Pile 2205 #3 Bottom Half	1,537	3.09×10^{-5}	2,606	7.13×10^{-4}

- Pile AISI 1080 #1 – Top Half:
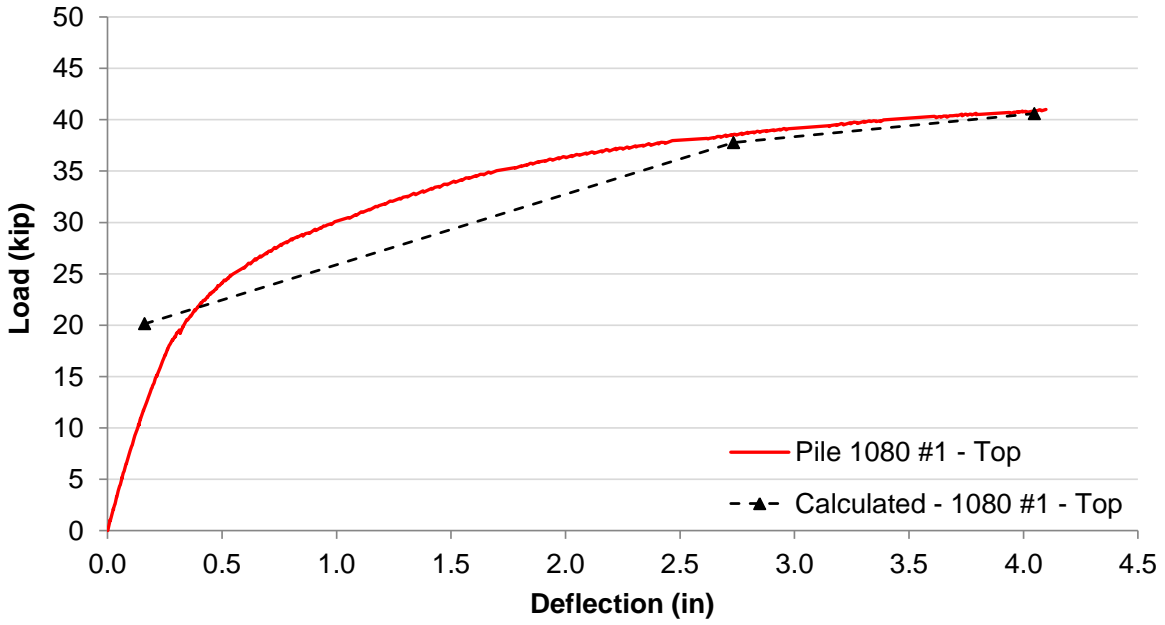
Figure H.1 Load-deflection curve for top half of pile 1080 #1, from flexure test. Dashed line shows calculations following ACI 318 requirements.
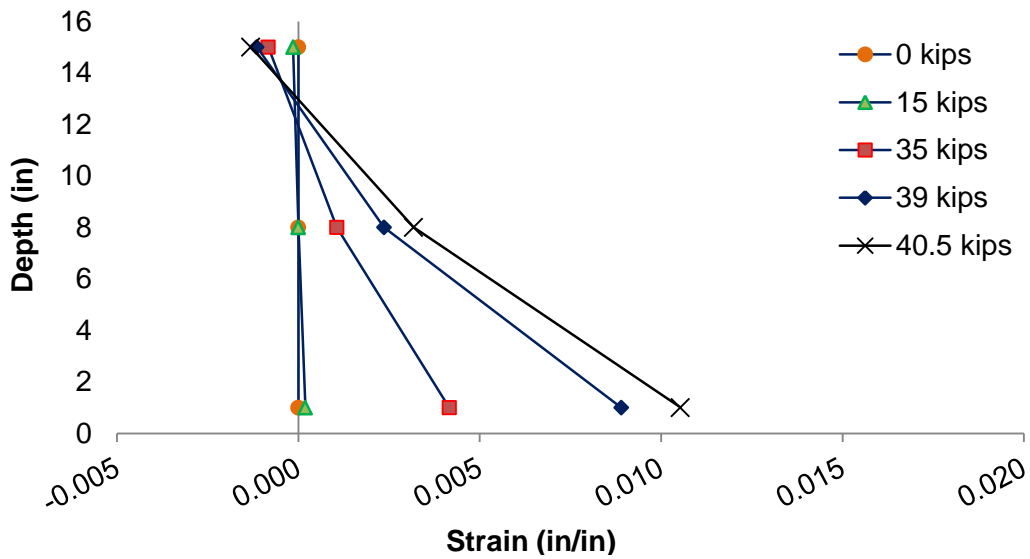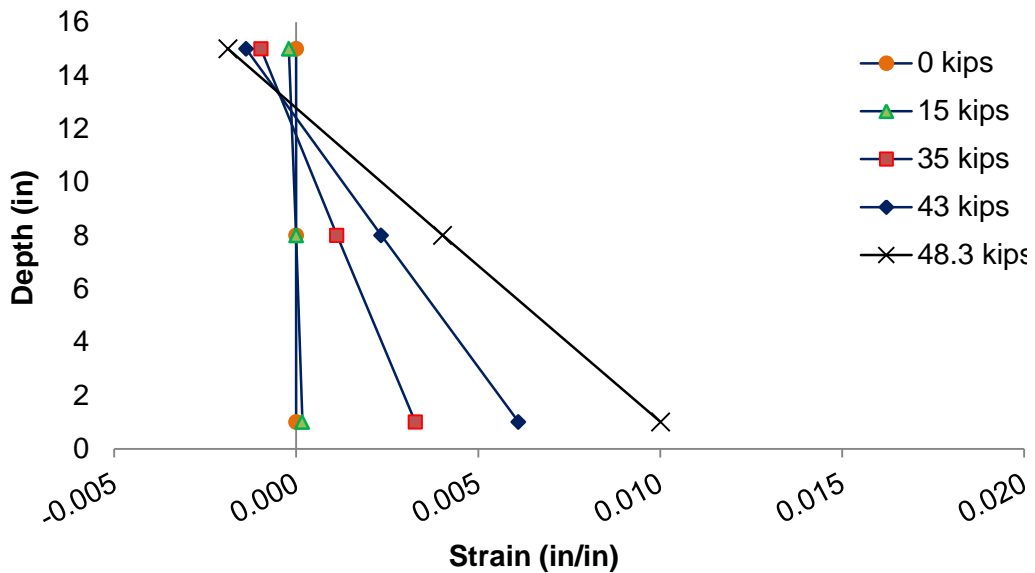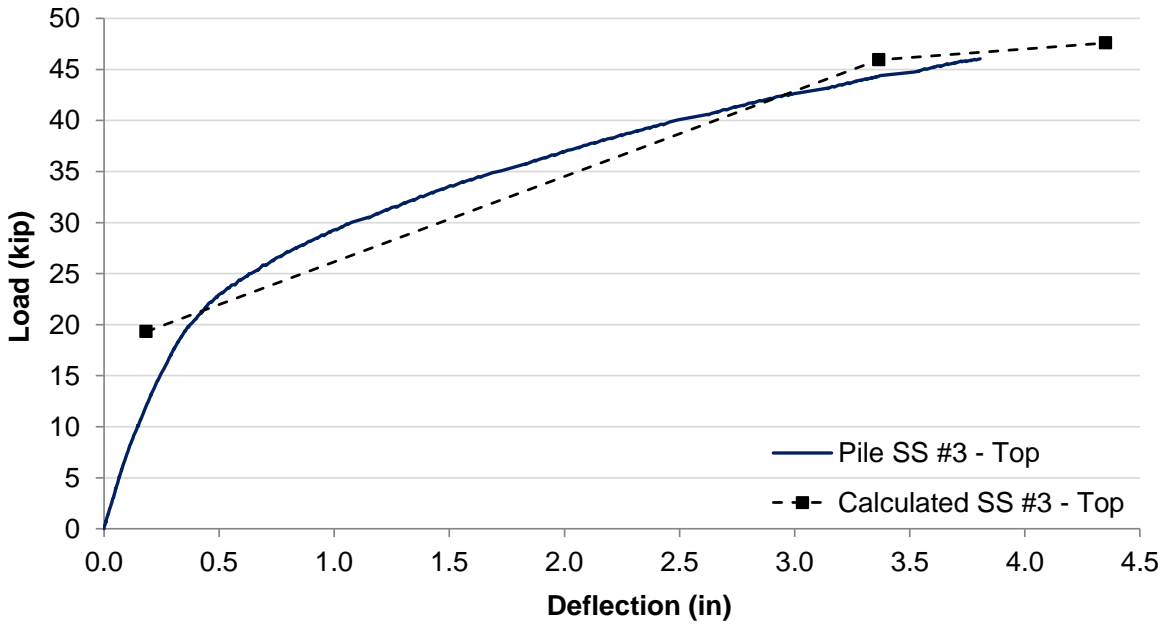

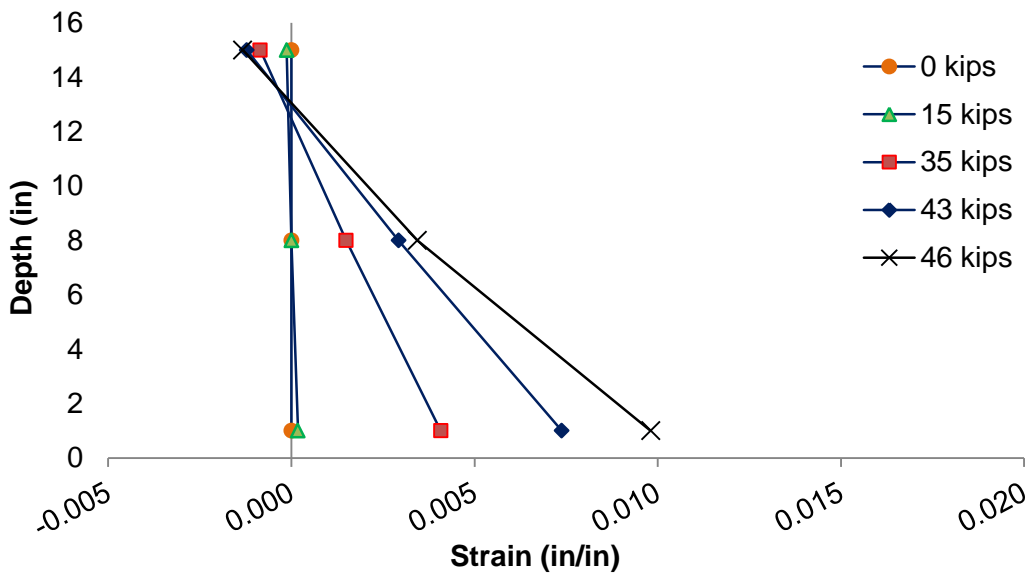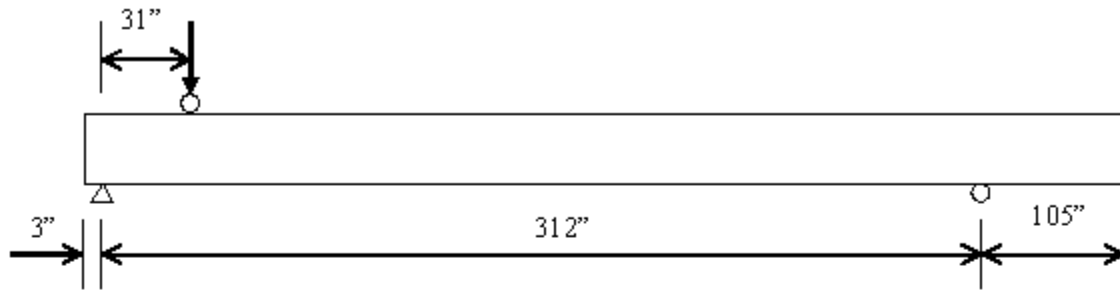**Figure H.2** Strain distributions of top half of pile 1080 #1.
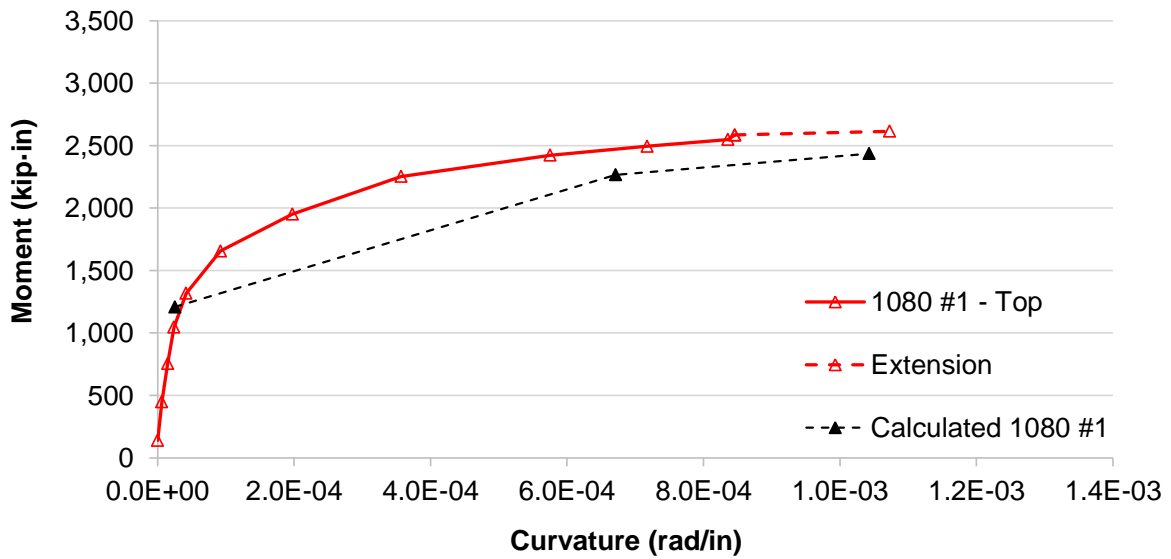
Figure H.3 Moment-curvature curve for top half of pile 1080 #1. Extension (dashed line) includes estimated ultimate curvature and moment. Dashed line shows calculations following ACI 318 requirements.

Figure H.4 Cracking pattern of top half of pile 1080 #1 before failure.

- Pile AISI 1080 #1 – Bottom Half:
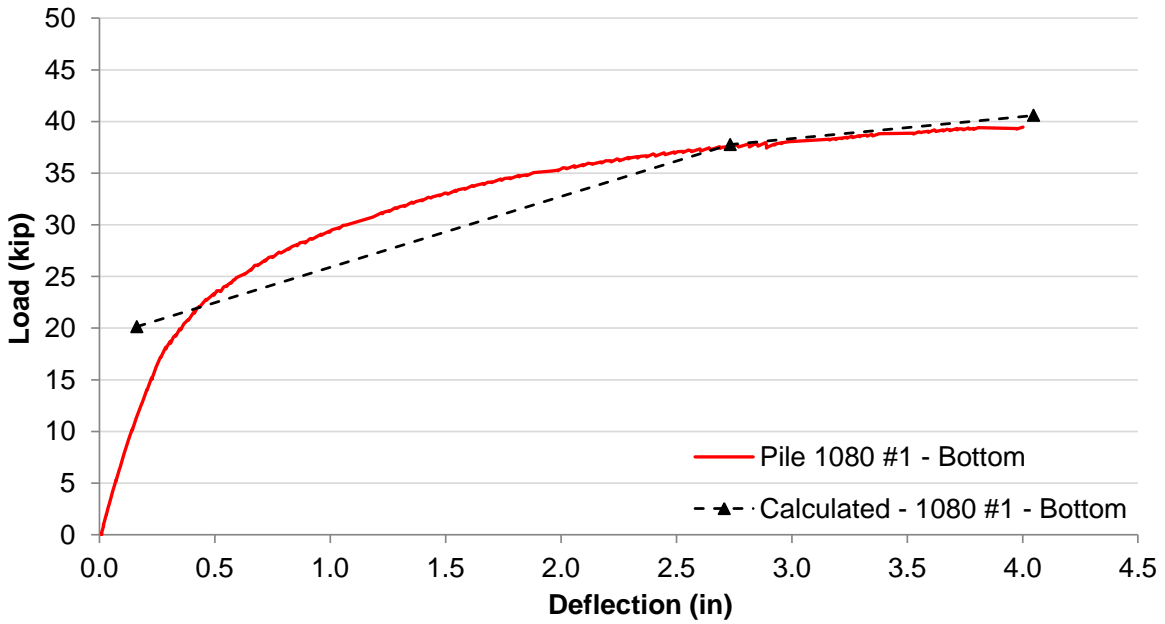
Figure H.5 Load-deflection curve for bottom half of pile 1080 #1, from flexure test. Dashed line shows calculations following ACI 318 requirements.
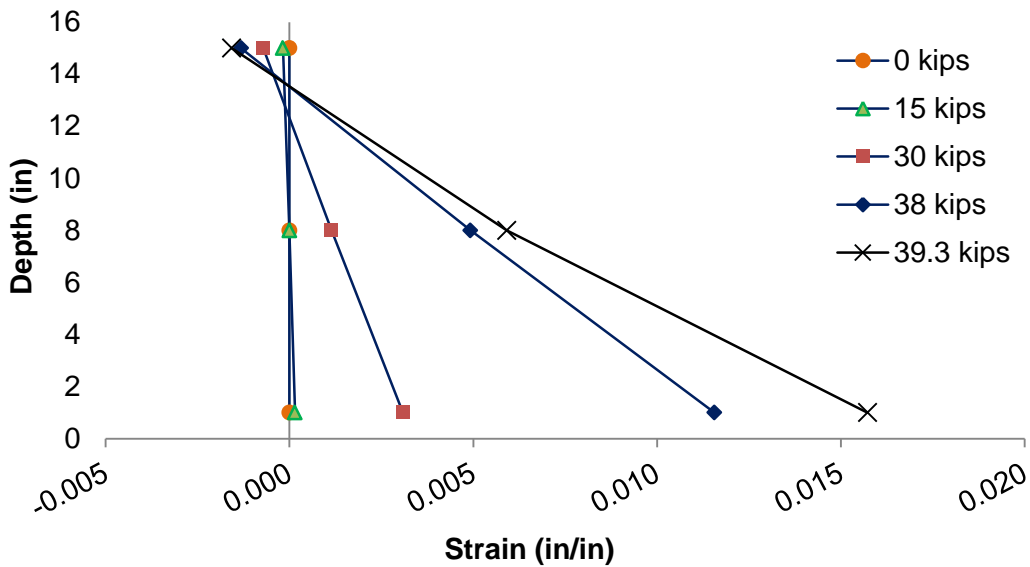
Figure H.6 Strain distributions of bottom half of pile 1080 #1.
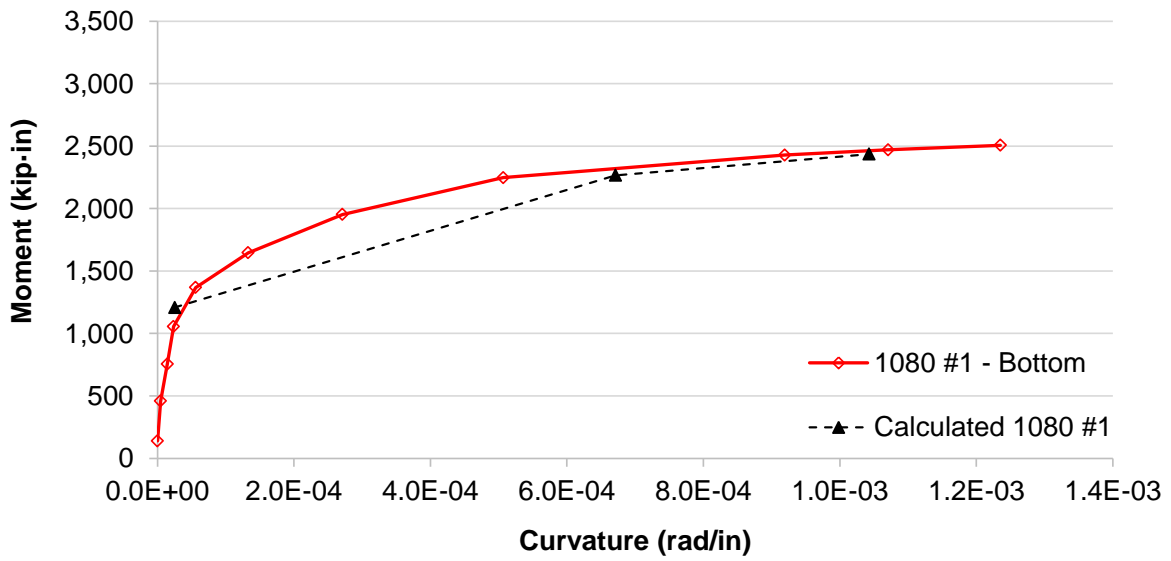
Figure H.7 Moment-curvature curve for bottom half of pile 1080 #1. Dashed line shows calculations following ACI 318 requirements.

Figure H.8 Cracking pattern of bottom half of pile 1080 #1 before failure.

- Pile AISI 1080 #2 – Top Half:
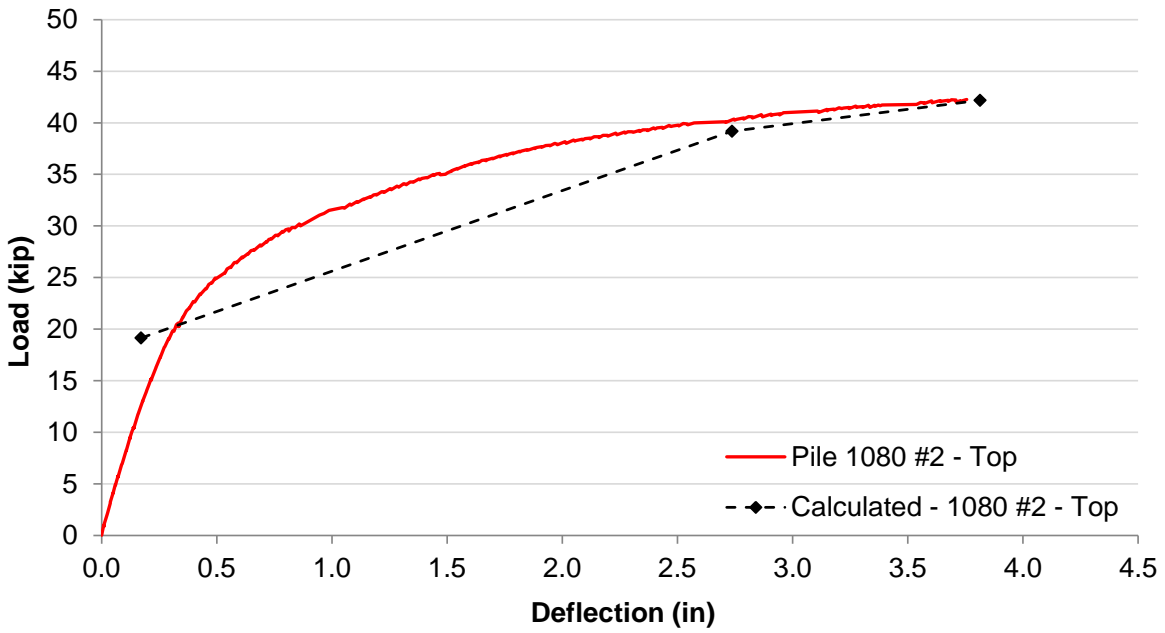
Figure H.9 Load-deflection curve for top half of pile 1080 #2, obtained from flexure test. Dashed line shows calculations following ACI 318 requirements.
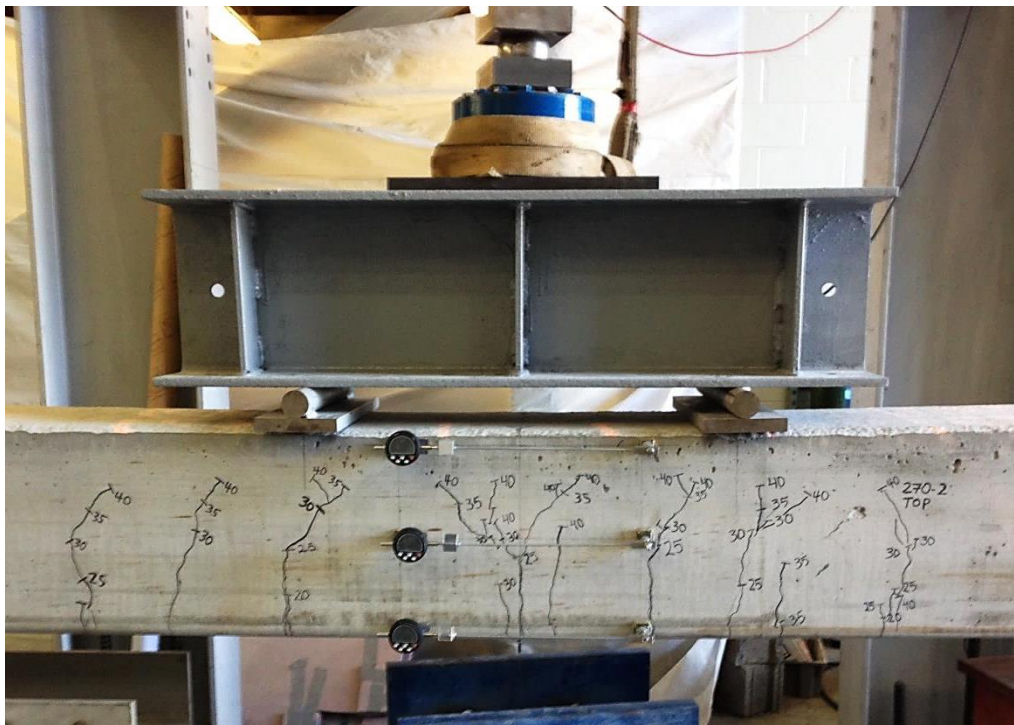
Figure H.10 Cracking pattern of top half of pile 1080 #2 before failure.

- Pile AISI 1080 #2 – Bottom Half:
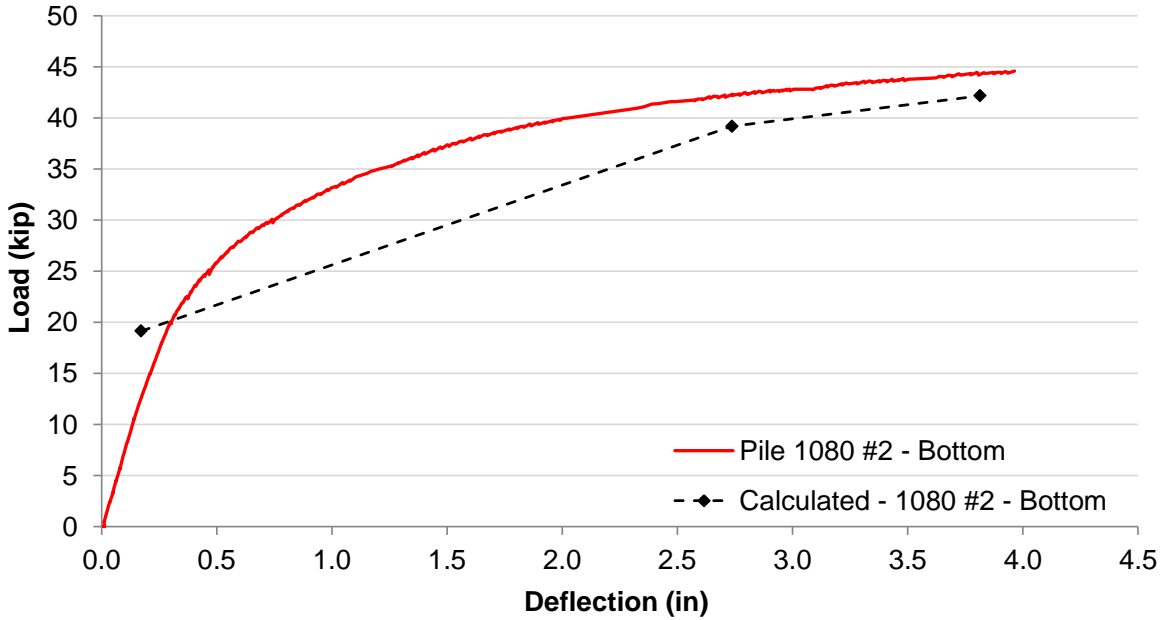
Figure H.11 Load-deflection curve for bottom half of pile 1080 #2, from flexure test. Dashed line shows calculations following ACI 318 requirements.
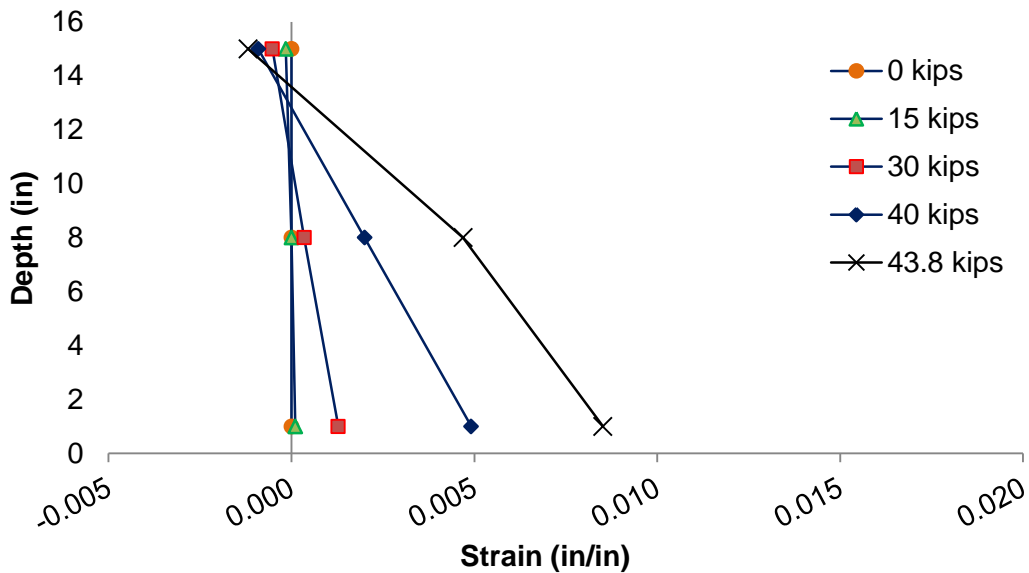
Figure H.12 Strain distributions of bottom half of pile 1080 #2.
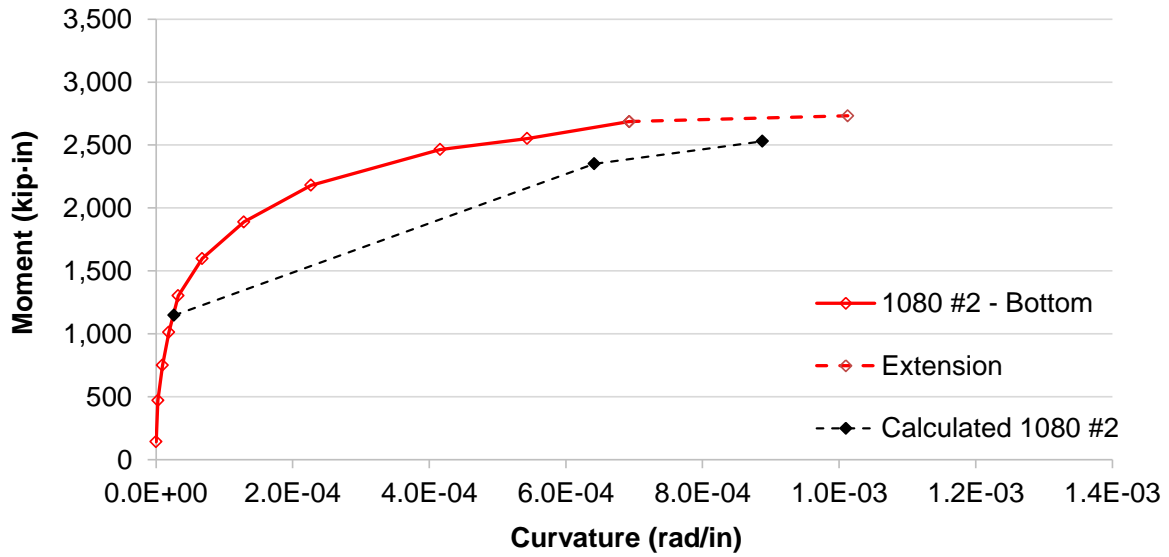
Figure H.13 Moment-curvature curve for bottom half of pile 1080 #2. Dashed line shows calculations following ACI 318 requirements.

Figure H.14 Cracking pattern of bottom half of pile 1080 #2 after failure.

- Pile HSSS 2205 #1 – Top Half:
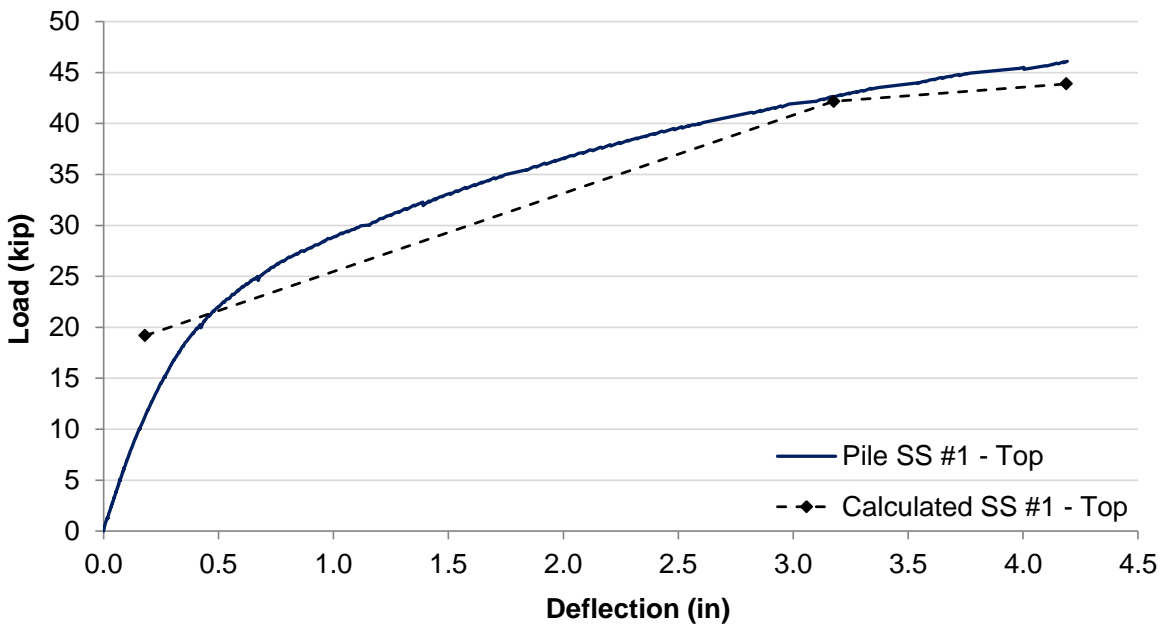
Figure H.15 Load-deflection curve for top half of pile HSSS 2205 #1, from flexure test. Dashed line shows calculations following ACI 318 requirements.
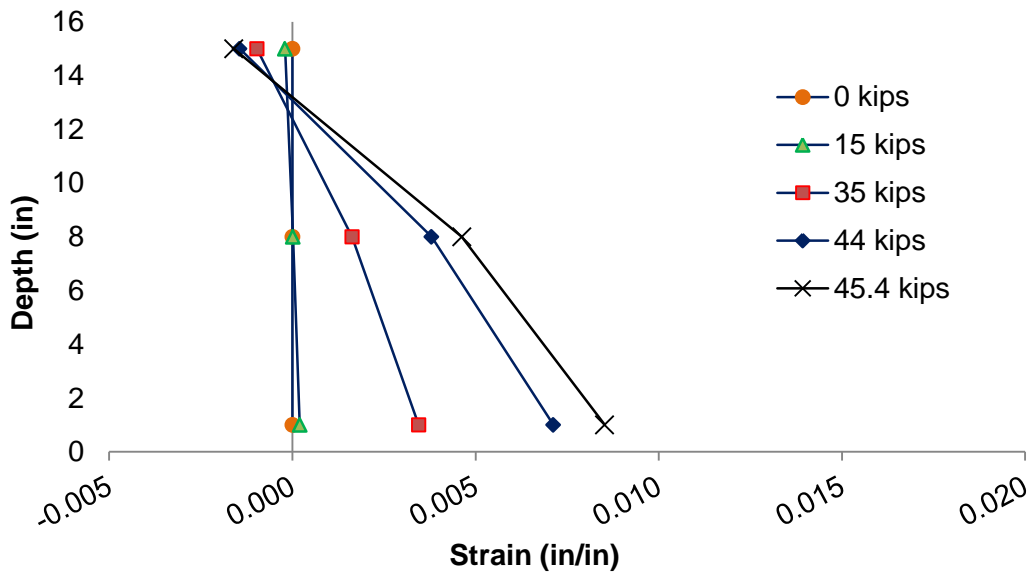
Figure H.16 Strain distributions of top half of pile HSSS 2205 #1.
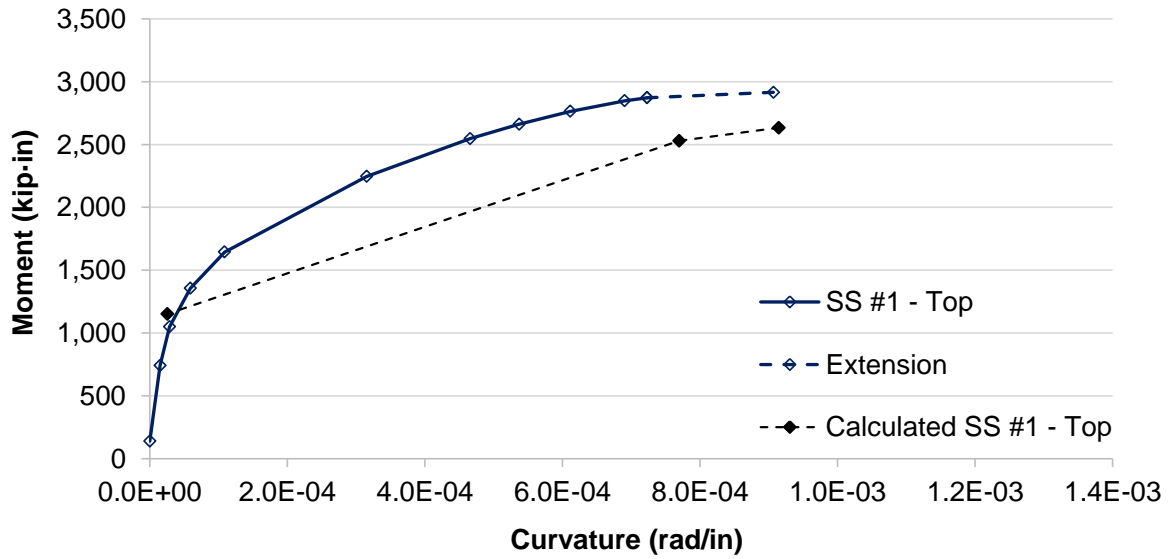
Figure H.17 Moment-curvature curve for top half of pile HSSS 2205 #1. Dashed line shows calculations following ACI 318 requirements.
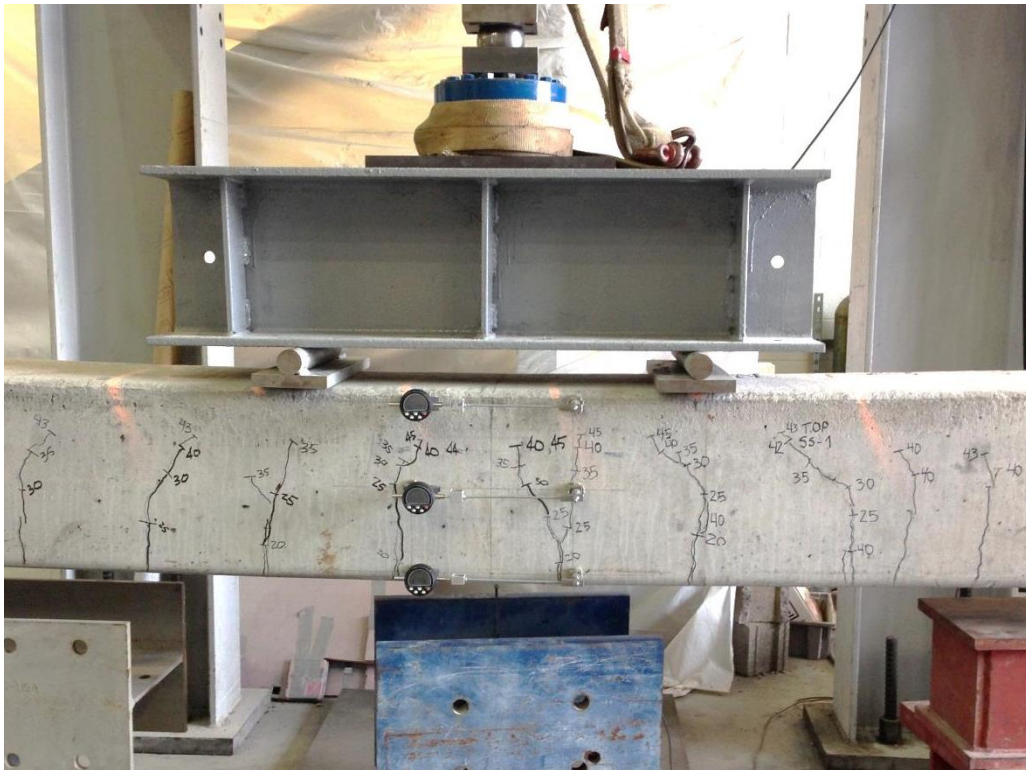
Figure H.18 Cracking pattern of top half of pile HSSS 2205 #1 before failure.

- Pile HSSS 2205 #1 – Bottom Half:
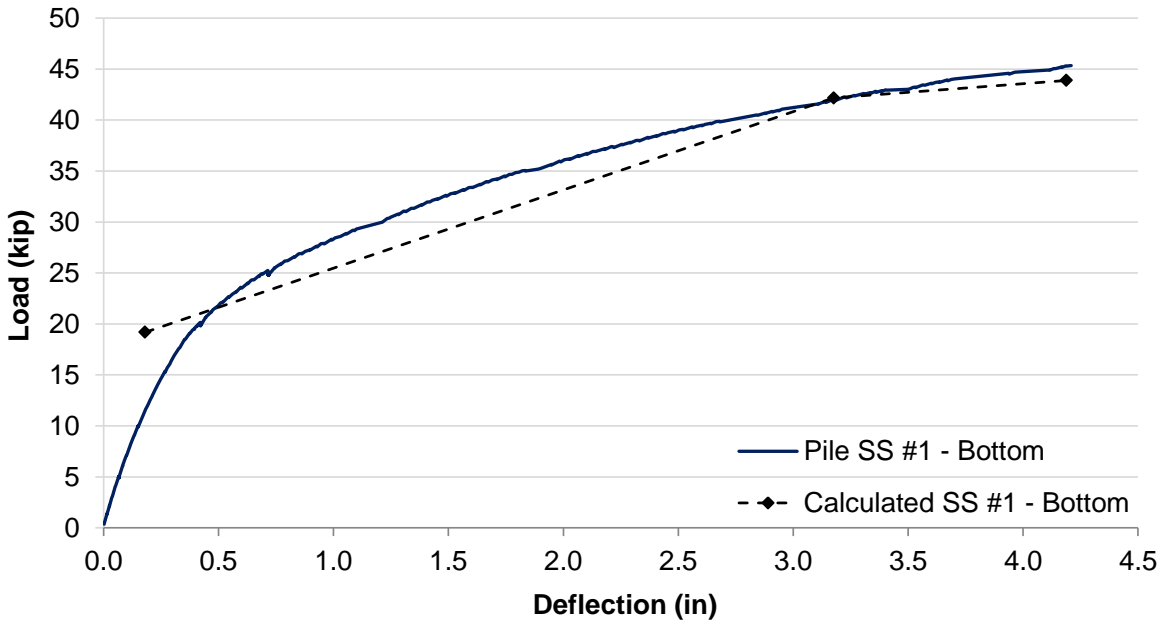
Figure H.19 Load-deflection curve for bottom half of pile HSSS 2205 #1, from flexure test. Dashed line shows calculations following ACI 318 requirements.

Figure H.20 Cracking pattern of bottom half of pile HSSS 2205 #1 after failure.

- Pile HSSS 2205 #2 – Top Half:
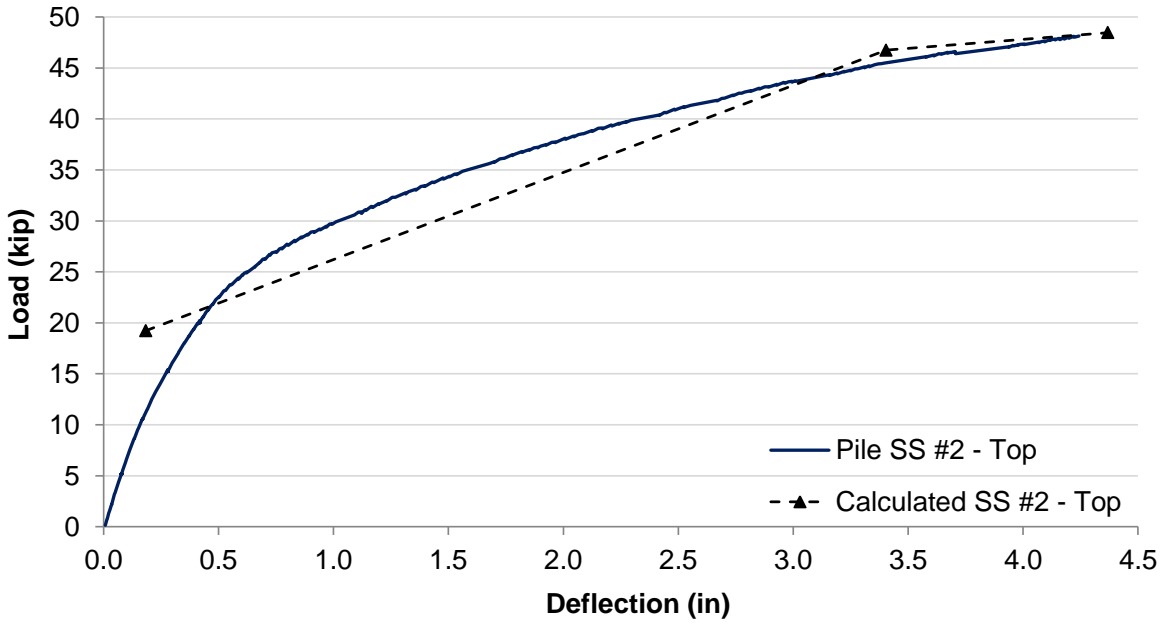
Figure H.21 Load-deflection curve for top half of pile HSSS 2205 #2, from flexure test. Dashed line shows calculations following ACI 318 requirements.
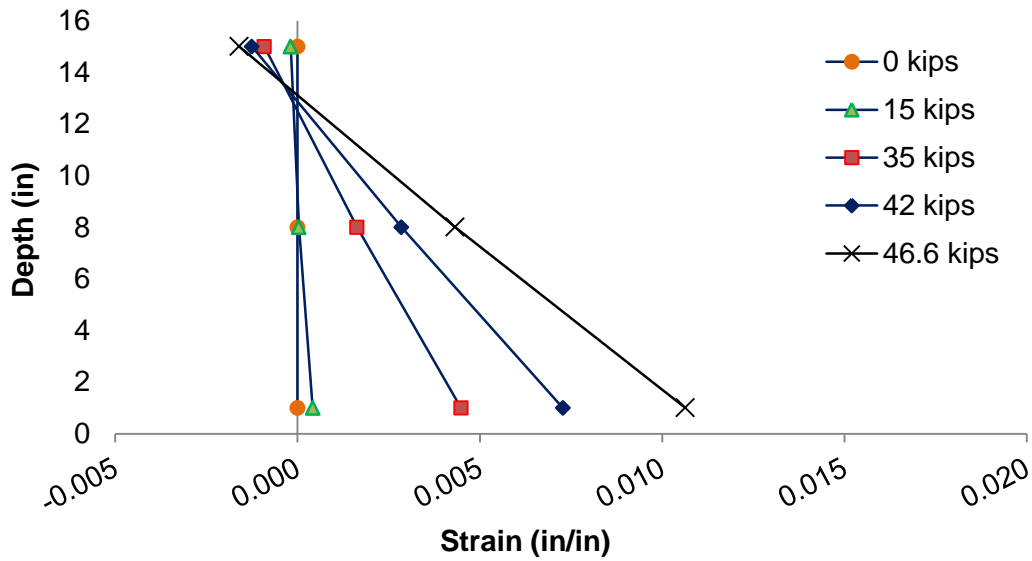
Figure H.22 Strain distributions of top half of pile HSSS 2205 #2.
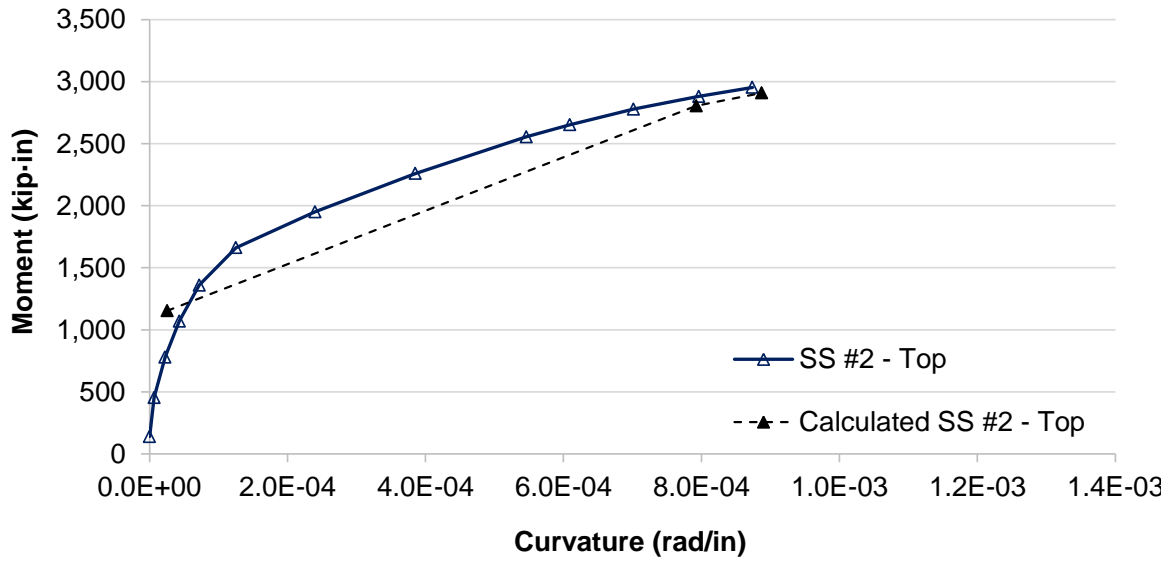
Figure H.23 Moment-curvature curve for top half of pile HSSS 2205 #2. Dashed line shows calculations following ACI 318 requirements.
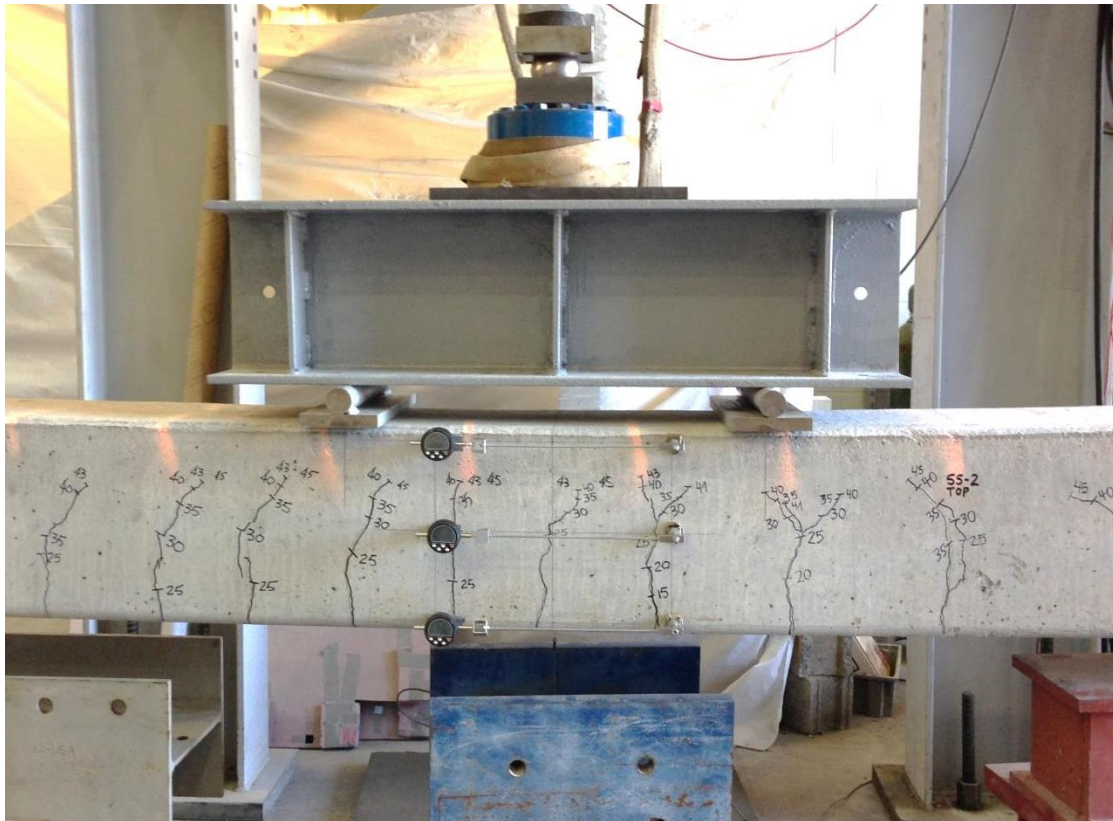
Figure H.24 Cracking pattern of top half of pile HSSS 2205 #2 before failure.

235

- Pile HSSS 2205 #2 – Bottom Half:
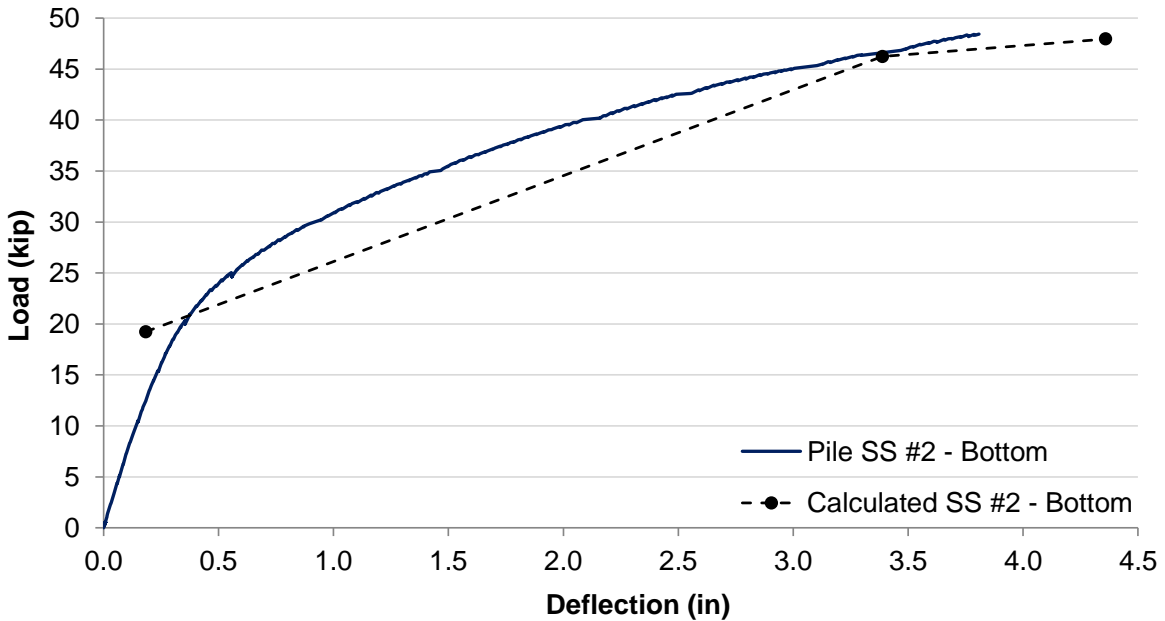
Figure H.25 Load-deflection curve for bottom half of pile HSSS 2205 #2, from flexure test. Dashed line shows calculations following ACI 318 requirements.

Figure H.26 Strain distributions of bottom half of pile HSSS 2205 #2.

Figure H.27 Moment-curvature curve for bottom half of pile HSSS 2205 #2. Dashed line shows calculations following ACI 318 requirements.

Figure H.28 Cracking pattern of bottom half of pile HSSS 2205 #2 before failure.

237

- Pile HSSS 2205 #3 – Top Half:

Figure H.29 Load-deflection curve for top half of pile HSSS 2205 #3, from flexure test. Dashed line shows calculations following ACI 318 requirements.

Figure H.30 Strain distributions of top half of pile HSSS 2205 #3.
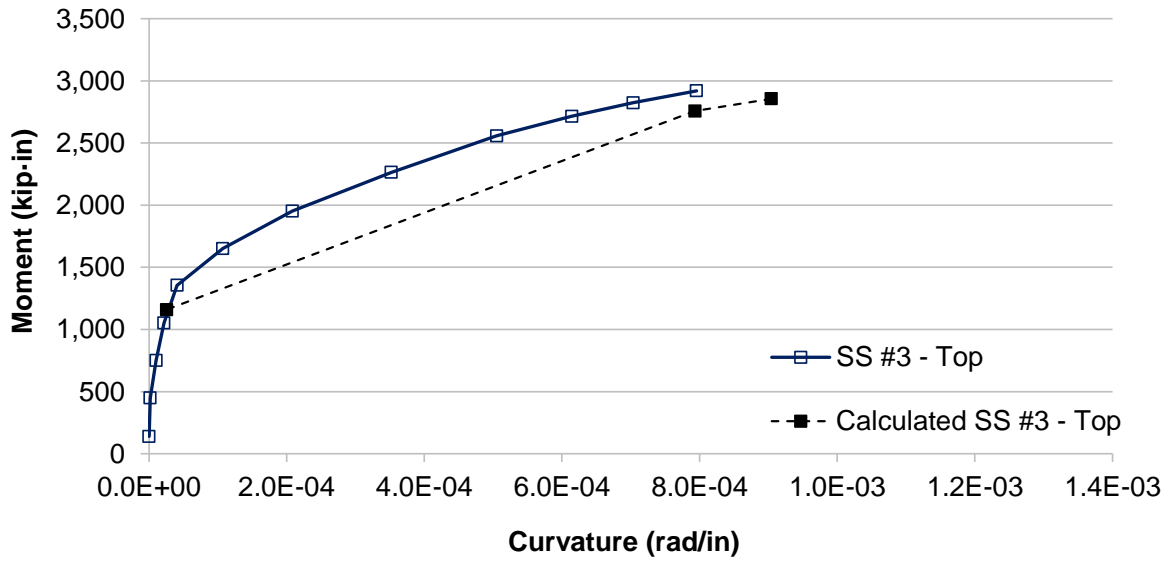
Figure H.31 Moment-curvature curve for top half of pile HSSS 2205 #3. Dashed line shows calculations following ACI 318 requirements.

Figure H.32 Cracking pattern of top half of pile HSSS 2205 #3 after failure.

239

- Pile HSSS 2205 #3 – Bottom Half:

Strain gauges failed at low loads for this pile; therefore, curvatures could not be measured, and moment-curvature plots could not be provided.
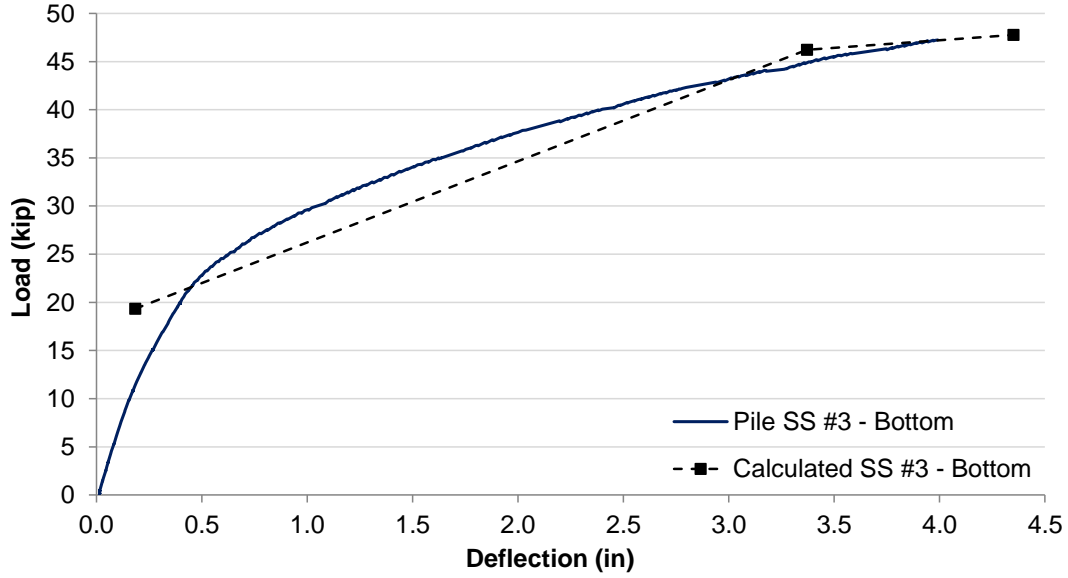
Figure H.33 Load-deflection curve for bottom half of pile HSSS 2205 #3, from flexure test. Dashed line shows calculations following ACI 318 requirements.

Figure H.34 Cracking pattern of bottom half of pile HSSS 2205 #3 after failure.

APPENDIX I: CALCULATION OF NOMINAL SHEAR STRENGTH

I.1 ACI 318 Nominal Shear Strength for Piles Using Conventional Steel.

– Piles AISI 1080, spiral wire spacing of 6 inches.

- Pile properties.

$f_c := 10800\text{psi}$ $\qquad$ $f_{pu} := 281.1\text{ksi}$ $\qquad$ $E_{ps} := 29400\text{psi}$ $\qquad$ $f_{se} := 195.7\text{ksi}$

$b_w := 16\text{in}$ $\quad$ $h := 16\text{in}$ $\quad$ $y_t := 8\text{in}$ $\quad$ $y_b := -8\text{in}$ $\quad$ $\text{Area} := b_w \cdot h = 256 \cdot \text{in}^2$

$A_{ps} := 1.386\text{in}^2$ $\quad$ $I_g := \dfrac{1}{12} b_w \cdot h^3$ $\quad$ $P_e := 270\text{kip}$ $\quad$ $e := -0\text{in}$ $\quad$ $w_{sw} := 21.667 \dfrac{\text{lbf}}{\text{in}}$

$L_1 := 311\text{in}$ $\quad$ $L_2 := 106\text{in}$ $\quad$ $L := L_1 + L_2 + 3\text{in} = 35 \cdot \text{ft}$ $\quad$ $x_1 := 31\text{in}$ $\quad$ $d := 0.8 \cdot h = 12.8 \cdot \text{in}$

$DL := w_{sw} \cdot L = 9100.14 \cdot \text{lbf}$ $\qquad$ $V_D := \dfrac{1}{L_1} \cdot \left[DL \cdot \left(\dfrac{L}{2} - L_2 \right) \right]$ $\qquad$ $V_D = 3.043 \cdot \text{kip}$

$P_L := 62.8\text{kip}$ $\qquad$ Value adjusted in order to have $V_n = V_D + V_L$

$F_{se} := P_e - 21.16\text{kip} = 248.84 \cdot \text{kip}$

$V_L := \dfrac{1}{L_1} \cdot \left[P_L \cdot (L_1 - x_1) \right]$ $\qquad$ $V_L = 56.54 \cdot \text{kip}$ $\qquad$ $V_p := 0\text{kip}$

$M_D := V_D \cdot x_1 - \dfrac{w_{sw} \cdot x_1^2}{2}$ $\qquad$ $M_D = 6.994 \cdot \text{kip} \cdot \text{ft}$ $\qquad$ $M_L := V_L \cdot x_1$ $\qquad$ $M_L = 146.062 \cdot \text{kip} \cdot \text{ft}$

$M_{cre} := \dfrac{-I_g}{y_b} \cdot \left(6 \cdot \sqrt{f_c \cdot \text{psi}} + \dfrac{F_{se}}{\text{Area}} + \dfrac{F_{se} \cdot e \cdot y_b}{I_g} + \dfrac{M_D \cdot y_b}{I_g} \right)$ $\qquad$ $M_{cre} = 83.776 \cdot \text{kip} \cdot \text{ft}$

241

- Web and flexural shear.

$$V_{ci} := \max\left(\left|0.6 \cdot \sqrt{f_c \cdot psi} \cdot b_w \cdot d\right| + \left|V_D\right| + \left|\frac{V_L \cdot M_{cre}}{M_L}\right|, \left|1.7\sqrt{f_c \cdot psi} \cdot b_w \cdot d\right|\right) \qquad V_{ci} = 48.243 \cdot kip$$

$$V_{cw} := \left(3.5\sqrt{f_c \cdot psi} + \frac{0.3 \cdot F_{se}}{Area}\right) \cdot b_w \cdot d + V_p \qquad V_{cw} = 134.21 \cdot kip$$

$$V_c := \min\left(V_{ci}, V_{cw}\right) = 48.243 \cdot kip$$

- Shear reinforcement.

$$A_v := 0.076 in^2 \qquad f_y := 70ksi \qquad sp := 6in$$

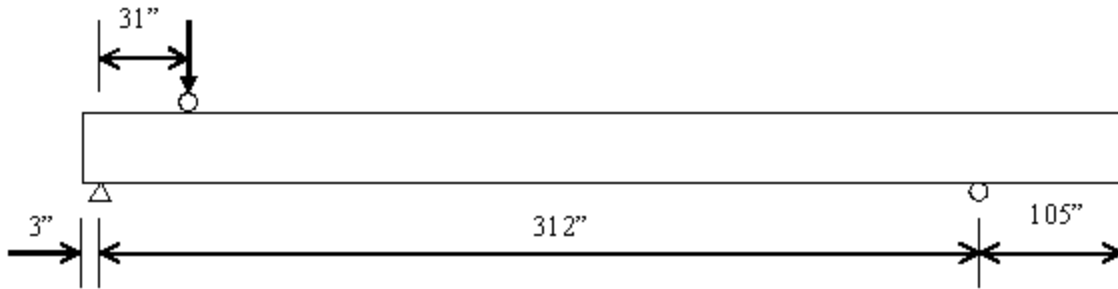$$V_s := \frac{A_v \cdot f_y \cdot d}{sp} = 11.349 \cdot kip$$

- Total shear.

$$V_n := V_c + V_s = 59.592 \cdot kip$$

I.2 ACI 318 Nominal Shear Strength for Piles Using Stainless Steel

– Piles HSSS 2205, spiral wire spacing of 6 inches.

- Pile properties.

$f_c := 10700\text{psi}$　　　$f_{pu} := 241.5\text{ksi}$　　　$E_{ps} := 23500\text{psi}$　　　$f_{se} := 147.1\text{ksi}$

$b_w := 16\text{in}$　　$h := 16\text{in}$　　$y_t := 8\text{in}$　　$y_b := -8\text{in}$　　$\text{Area} := b_w \cdot h = 256 \cdot \text{in}^2$

$A_{ps} := 1.848\text{in}^2$　$I_g := \dfrac{1}{12} b_w \cdot h^3$　$P_e := 270\text{kip}$　$e := -0\text{in}$　　$w_{sw} := 21.667 \dfrac{\text{lbf}}{\text{in}}$

$L_1 := 311\text{in}$　　$L_2 := 106\text{in}$　$L := L_1 + L_2 + 3\text{in} = 35 \cdot \text{ft}$　$x_1 := 31\text{in}$　$d := 0.8 \cdot h = 12.8 \cdot \text{in}$

$DL := w_{sw} \cdot L = 9100.14 \cdot \text{lbf}$　　$V_D := \dfrac{1}{L_1} \cdot \left[DL \cdot \left(\dfrac{L}{2} - L_2 \right) \right]$　　　$V_D = 3.043 \cdot \text{kip}$

$P_L := 61.2\text{kip}$　　　Value adjusted in order to have $V_n = V_D + V_L$

$F_{se} := P_e - 25.37\text{kip} = 244.63 \cdot \text{kip}$

$V_L := \dfrac{1}{L_1} \cdot \left[P_L \cdot \left(L_1 - x_1 \right) \right]$　　　　$V_L = 55.1 \cdot \text{kip}$　　　$V_p := 0\text{kip}$

$M_D := V_D \cdot x_1 - \dfrac{w_{sw} \cdot x_1^2}{2}$　　$M_D = 6.994 \cdot \text{kip} \cdot \text{ft}$　　$M_L := V_L \cdot x_1$　　$M_L = 142.341 \cdot \text{kip} \cdot \text{ft}$

$M_{cre} := \dfrac{-I_g}{y_b} \cdot \left(6 \cdot \sqrt{f_c \cdot \text{psi}} + \dfrac{F_{se}}{\text{Area}} + \dfrac{F_{se} \cdot e \cdot y_b}{I_g} + \dfrac{M_D \cdot y_b}{I_g} \right)$　　　$M_{cre} = 82.676 \cdot \text{kip} \cdot \text{ft}$

- Web and flexural shear.

$$V_{ci} := max\left(\left|0.6 \cdot \sqrt{f_c \cdot psi} \cdot b_w \cdot d\right| + \left|V_D\right| + \left|\frac{V_L \cdot M_{cre}}{M_L}\right|, \left|1.7 \sqrt{f_c \cdot psi} \cdot b_w \cdot d\right|\right) \qquad V_{ci} = 47.758 \cdot kip$$

$$V_{cw} := \left(3.5 \sqrt{f_c \cdot psi} + \frac{0.3 \cdot F_{se}}{Area}\right) \cdot b_w \cdot d + V_p \qquad V_{cw} = 132.86 \cdot kip$$

$$V_c := min\left(V_{ci}, V_{cw}\right) = 47.758 \cdot kip$$

- Shear reinforcement.

$$A_v := 0.08 in^2 \qquad f_y := 61 ksi \qquad sp := 6in$$

$$V_s := \frac{A_v \cdot f_y \cdot d}{sp} = 10.411 \cdot kip$$

- Total shear.

$$V_n := V_c + V_s = 58.168 \cdot kip$$

I.3 AASHTO LRFD Nominal Shear Strength for Piles Using Conventional Steel.

– Piles AISI 1080, spiral wire spacing of 6 inches.

- Pile properties.

$f_c := 10800psi$ $\quad\quad f_{pu} := 281.1ksi$ $\quad\quad E_{ps} := 29400psi$ $\quad\quad f_{se} := 195.7ksi$

$b_w := 16in$ $\quad h := 16in$ $\quad y_t := 8in$ $\quad y_b := -8in$ $\quad Area := b_w \cdot h = 256 \cdot in^2$

$A_{ps} := 1.386in^2$ $\quad I_g := \frac{1}{12} b_w \cdot h^3$ $\quad P_e := 270kip$ $\quad e := -0in$ $\quad w_{sw} := 21.667 \frac{lbf}{in}$

$L_1 := 311in$ $\quad L_2 := 106in$ $\quad L := L_1 + L_2 + 3in = 35 \cdot ft$ $\quad x_1 := 31in$ $\quad d := 0.8 \cdot h = 12.8 \cdot in$

$DL := w_{sw} \cdot L = 9100.14 \cdot lbf$ $\quad\quad V_D := \frac{1}{L_1} \cdot \left[DL \cdot \left(\frac{L}{2} - L_2 \right) \right]$ $\quad\quad V_D = 3.043 \cdot kip$

$P_L := 67.7kip$ $\quad\quad$ Value adjusted in order to have $V_n = V_D + V_L$

$F_{se} := P_e - 21.16kip = 248.84 \cdot kip$

$V_L := \frac{1}{L_1} \cdot \left[P_L \cdot (L_1 - x_1) \right]$ $\quad\quad V_L = 60.952 \cdot kip$ $\quad\quad V_p := 0kip$

$M_D := V_D \cdot x_1 - \frac{w_{sw} \cdot x_1^2}{2}$ $\quad\quad M_D = 6.994 \cdot kip \cdot ft$ $\quad\quad M_L := V_L \cdot x_1$ $\quad\quad M_L = 157.459 \cdot kip \cdot ft$

$M_{cre} := \frac{-I_g}{y_b} \cdot \left(0.24 \cdot \sqrt{f_c \cdot ksi} + \frac{F_{se}}{Area} + \frac{F_{se} \cdot e \cdot y_b}{I_g} + \frac{M_D \cdot y_b}{I_g} \right)$ $\quad\quad M_{cre} = 93.173 \cdot kip \cdot ft$

245

- Web and flexural shear.

$$V_{ci} := \max\left(\left| 0.02 \cdot \sqrt{f_c \cdot ksi} \cdot b_w \cdot d \right| + \left| V_D \right| + \left| \frac{V_L \cdot M_{cre}}{M_L} \right|, \left| 0.06 \sqrt{f_c \cdot ksi} \cdot b_w \cdot d \right| \right) \qquad V_{ci} = 52.571 \cdot kip$$

$$V_{cw} := \left(0.06 \sqrt{f_c \cdot ksi} + \frac{0.3 \cdot F_{se}}{Area} \right) \cdot b_w \cdot d + V_p \qquad V_{cw} = 100.1 \cdot kip$$

$$V_c := \min\left(V_{ci}, V_{cw} \right) = 52.571 \cdot kip$$

- Shear reinforcement.

$$A_v := 0.076 in^2 \qquad f_y := 70 ksi \qquad sp := 6 in$$

$$V_s := \frac{A_v \cdot f_y \cdot d}{sp} = 11.349 \cdot kip$$

- Total shear.

$$V_n := V_c + V_s = 63.92 \cdot kip$$

I.4 AASHTO LRFD Nominal Shear Strength for Piles Using Stainless Steel.

– Piles HSSS 2205, spiral wire spacing of 6 inches.

- Pile properties.

$f_c := 10700\text{psi}$ $\qquad$ $f_{pu} := 241.5\text{ksi}$ $\qquad$ $E_{ps} := 23500\text{psi}$ $\qquad$ $f_{se} := 147.1\text{ksi}$

$b_w := 16\text{in}$ $\quad$ $h := 16\text{in}$ $\quad$ $y_t := 8\text{in}$ $\quad$ $y_b := -8\text{in}$ $\quad$ $\text{Area} := b_w \cdot h = 256 \cdot \text{in}^2$

$A_{ps} := 1.848\text{in}^2$ $\quad$ $I_g := \dfrac{1}{12} b_w \cdot h^3$ $\quad$ $P_e := 270\text{kip}$ $\quad$ $e := -0\text{in}$ $\quad$ $w_{sw} := 21.667 \dfrac{\text{lbf}}{\text{in}}$

$L_1 := 311\text{in}$ $\quad$ $L_2 := 106\text{in}$ $\quad$ $L := L_1 + L_2 + 3\text{in} = 35 \cdot \text{ft}$ $\quad$ $x_1 := 31\text{in}$ $\quad$ $d := 0.8 \cdot h = 12.8 \cdot \text{in}$

$DL := w_{sw} \cdot L = 9100.14 \cdot \text{lbf}$ $\qquad$ $V_D := \dfrac{1}{L_1} \cdot \left[DL \cdot \left(\dfrac{L}{2} - L_2 \right) \right]$ $\qquad$ $V_D = 3.043 \cdot \text{kip}$

$P_L := 66\text{kip}$ $\qquad$ Value adjusted in order to have $V_n = V_D + V_L$

$F_{se} := P_e - 25.37\text{kip} = 244.63 \cdot \text{kip}$

$V_L := \dfrac{1}{L_1} \cdot \left[P_L \cdot (L_1 - x_1) \right]$ $\qquad$ $V_L = 59.421 \cdot \text{kip}$ $\qquad$ $V_p := 0\text{kip}$

$M_D := V_D \cdot x_1 - \dfrac{w_{sw} \cdot x_1^2}{2}$ $\qquad$ $M_D = 6.994 \cdot \text{kip} \cdot \text{ft}$ $\qquad$ $M_L := V_L \cdot x_1$ $\qquad$ $M_L = 153.505 \cdot \text{kip} \cdot \text{ft}$

$M_{cre} := \dfrac{-I_g}{y_b} \cdot \left(0.24 \cdot \sqrt{f_c \cdot \text{ksi}} + \dfrac{F_{se}}{\text{Area}} + \dfrac{F_{se} \cdot e \cdot y_b}{I_g} + \dfrac{M_D \cdot y_b}{I_g} \right)$ $\qquad$ $M_{cre} = 92.03 \cdot \text{kip} \cdot \text{ft}$

247

- Web and flexural shear.

$$V_{ci} := \max\left(\left| 0.02 \cdot \sqrt{f_c \cdot ksi} \cdot b_w \cdot d \right| + \left| V_D \right| + \left| \frac{V_L \cdot M_{cre}}{M_L} \right|, \left| 0.06 \sqrt{f_c \cdot ksi} \cdot b_w \cdot d \right| \right) \qquad V_{ci} = 52.066 \cdot kip$$

$$V_{cw} := \left(0.06 \sqrt{f_c \cdot ksi} + \frac{0.3 \cdot F_{se}}{Area} \right) \cdot b_w \cdot d + V_p \qquad V_{cw} = 98.91 \cdot kip$$

$$V_c := \min\left(V_{ci}, V_{cw} \right) = 52.066 \cdot kip$$

- Shear reinforcement.

$$A_v := 0.08 in^2 \qquad f_y := 61 ksi \qquad sp := 6 in$$

$$V_s := \frac{A_v \cdot f_y \cdot d}{sp} = 10.411 \cdot kip$$

- Total shear.

$$V_n := V_c + V_s = 62.477 \cdot kip$$

248

APPENDIX J: SUMMARY OF SHEAR TESTS

Table J.1 Experimental ultimate shear for piles using conventional steel.

Pile	Ultimate shear (kips)
1080 #1 – Top – 3-in.	86.6
1080 #1 – Top – 6-in.	85.7
1080 #1 – Bottom – 3-in.	87.2
1080 #1 – Bottom – 6-in.	84.6
1080 #2 – Top – 3-in.	89.7
1080 #2 – Top – 6-in.	92.5
1080 #2 – Bottom – 3-in.	84.8
1080 #2 – Bottom – 6-in.	92.9
Average 1080 – 3-in.	87.1 (2.0)[*]
Average 1080 – 6-in.	88.9 (4.4)[*]
Average 1080	88.0 (3.3)[*]

* Number in parenthesis shows standard deviation.

Table J.2 Experimental ultimate shear for piles using stainless steel.

Pile	Ultimate shear (kips)
HSSS 2205 #1 – Top – 3-in.	86.8
HSSS 2205 #1 – Top – 6-in.	93.4
HSSS 2205 #1 – Bottom – 3-in.	88.4
HSSS 2205 #1 – Bottom – 6-in.	89.0
HSSS 2205 #2 – Bottom – 3-in.	85.1
HSSS 2205 #2 – Bottom – 6-in.	102.0
HSSS 2205 #3 – Bottom – 3-in.	94.8
HSSS 2205 #3 – Bottom – 6-in.	89.4
Average HSSS 2205 – 3-in.	88.8 (4.3)[*]
Average HSSS 2205 – 6-in.	93.4 (6.0)[*]
Average HSSS 2205	91.1 (5.4)[*]

* Number in parenthesis shows standard deviation.

Note: The first four tests (piles HSSS #2 and #3, top halves, spacings 3-in. and 6-in.) were performed using wrong test configurations and their results were not considered for the analysis of the results. Initially, a load cell with 100-kips of capacity was used for the test; but this value was surpassed, and the actual failure load was not recorded properly. Also, a roller support originally was used for the support closer to the applied load which allowed lateral displacement of the pile, and resulted in a varying shear span during the test. This lateral displacement caused large errors in the deflection measurements due to the angle produced between the bottom of the pile and the position of the potentiometer. To correct the test set-up, two roller bars were installed between the load cell and the steel beam used to transfer the load to the pile. These rollers kept the steel beam in a correct orientation. Also, the end of the beam closest to the support was supported by a pin rather than a roller so that the shear span length remained constant.

APPENDIX K: AASHTO LRFD PRESTRESS LOSSES CALCULATION

- AASHTO Refined and AASHTO Lump-sum Methods:

Pile Information:

$f_c := 10.8 \text{ksi}$ $f_{ci} := 4.018 \text{ksi}$ Measured f_c at 1 day = 4.02 ksi (at SCP plant)

Measured f_c at 438 days = 10.81 ksi

$E_c := 7138 \text{ksi}$ $E_{ci} := 6138 \text{ksi}$ Measured E_c at 4 days = 6,138 ksi

Measured E_c at 445 days = 7,138 ksi

$h := 16 \text{in}$ $y_t := \dfrac{h}{2}$ $y_b := y_t$ $L_1 := 70 \text{ft}$ $\text{Area} := h^2$ $I := \dfrac{h^4}{12}$ $\text{cover} := 3.5 \text{in}$

$P_{jack} := 22.5 \text{kip}$ $\Delta f_{ANC} := 0 \text{ksi}$ $n := 12$

Duplex HSSS 2205 Strands Properties:

$f_{u.ss} := 241.5 \text{ksi}$ $E_{ps.ss} := 23500 \text{ksi}$ $f_{se.ss} := 0.6 \cdot f_{u.ss} = 144.9 \cdot \text{ksi}$ $A_{ps.ss} := 0.153 \text{in}^2$

AISI 1080 Steel Strands Properties:

$f_u := 281.1 \text{ksi}$ $E_{ps} := 29400 \text{ksi}$ $f_{se} := 0.7 \cdot f_u = 196.77 \cdot \text{ksi}$ $A_{ps} := 0.115 \text{in}^2$

Strands Configuration:

$e_{mid} := \dfrac{h - 2 \cdot \text{cover}}{6}$ $\text{bars} := \begin{pmatrix} 4 \\ 2 \\ 2 \\ 4 \end{pmatrix}$ $e_p := \begin{pmatrix} \dfrac{h}{2} - \text{cover} \\ e_{mid} \\ -e_{mid} \\ \text{cover} - \dfrac{h}{2} \end{pmatrix}$ $d_p := -e_p + \dfrac{h}{2}$

$P_i := P_{jack} \cdot \text{bars} = \begin{pmatrix} 90 \\ 45 \\ 45 \\ 90 \end{pmatrix} \cdot \text{kip}$ $P_1 := P_{i_0} + P_{i_1} + P_{i_2} + P_{i_3} = 270 \cdot \text{kip}$

Savannah RH: average annual high, according to the Southeast Regional Climate Center = 87%.

$RH := 75$

Note: AASHTO LRFD equation number is shown in parenthesis.

Elastic Shortening:

$$P_2 := 0.9\left(P_1 + \Delta f_{ANC} \cdot A_{ps}\right) = 243 \cdot kip \qquad e_2 := 0$$

$$f_2 := \frac{P_2}{n \cdot A_{ps}} = 176.087 \cdot ksi \qquad f_{2.ss} := \frac{P_2}{n \cdot A_{ps.ss}} = 132.353 \cdot ksi \qquad f_{cgp} := \frac{-P_2}{Area} = -0.949 \cdot ksi$$

$$\Delta f_{pES} := \frac{E_{ps}}{E_{ci}} \cdot f_{cgp} = -4.547 \cdot ksi \qquad \textbf{(5.9.5.2.3a-1)}$$

$$f_2 + \Delta f_{pES} = 171.54 \cdot ksi \quad < \quad 0.7 \cdot f_u = 196.77 \cdot ksi$$

$$\Delta f_{pES.ss} := \frac{E_{ps.ss}}{E_{ci}} \cdot f_{cgp} = -3.634 \cdot ksi \qquad \textbf{(5.9.5.2.3a-1)}$$

$$f_{2.ss} + \Delta f_{pES.ss} = 128.719 \cdot ksi \quad < \quad 0.7 \cdot f_{u.ss} = 169.05 \cdot ksi$$

- **AASHTO Refined Method.**

Shrinkage and Creep Losses:

$$V_2 := h^2 \qquad S_2 := 4 \cdot h \qquad k_s := \max\left(1.45 - 0.13\frac{1}{in}\frac{V_2}{S_2}, 1.0\right) \qquad \textbf{(5.4.2.3.2-2)}$$

$$k_{hs} := 2.0 - 0.014 \cdot RH = 0.95 \qquad t := 9125 \qquad \text{change time according to required} \\ \text{time span (days)}$$

$$\textbf{(5.4.2.3.3-2)}$$

$$k_f := \frac{5ksi}{1ksi + f_{ci}} = 0.996 \quad \textbf{(5.4.2.3.2-4)} \qquad k_{td} := \frac{t}{61 - 4 \cdot 4.5 + t} = 0.995 \quad \textbf{(5.4.2.3.2-5)}$$

$$\varepsilon_{sh} := -k_s \cdot k_{hs} \cdot k_f \cdot k_{td} \cdot 0.48 \cdot 10^{-3} = -4.522 \times 10^{-4} \qquad \textbf{(5.4.2.3.3-1)}$$

$$k_{hc} := 1.56 - 0.008 \cdot RH = 0.96 \qquad \psi_{tf.ti} := 1.9 \cdot k_s \cdot k_{hc} \cdot k_f \cdot k_{td} \cdot 3^{-0.118} = 1.589$$

$$\textbf{(5.4.2.3.2-3)} \qquad\qquad\qquad\qquad\qquad \textbf{(5.4.2.3.2-1)}$$

$$K_{id} := \frac{1}{1 + \dfrac{E_{ps}}{E_{ci}} \dfrac{A_{ps}}{Area} \left(1 + \dfrac{Area \cdot e_2 \cdot e_2}{I}\right) \cdot \left(1 + 0.7 \cdot \psi_{tf.ti}\right)} = 0.995 \qquad \textbf{(5.9.5.4.2a-2)}$$

$$K_{id.ss} := \frac{1}{1 + \dfrac{E_{ps.ss}}{E_{ci}} \dfrac{A_{ps.ss}}{Area} \left(1 + \dfrac{Area \cdot e_2 \cdot e_2}{I}\right) \cdot \left(1 + 0.7 \cdot \psi_{tf.ti}\right)} = 0.995 \qquad \textbf{(5.9.5.4.2a-2)}$$

253

$\Delta f_{pSR} := \varepsilon_{sh} \cdot E_{ps} \cdot K_{id} = -13.236 \cdot ksi$ $\qquad$ $\Delta f_{pSR.ss} := \varepsilon_{sh} \cdot E_{ps} \cdot K_{id.ss} = -13.232 \cdot ksi$

$$(5.9.5.4.2a\text{-}1)$$

$\Delta f_{pCR} := \dfrac{E_{ps}}{E_{ci}} \cdot f_{cgp} \cdot \psi_{tf.ti} \cdot K_{id} = -7.192 \cdot ksi$ $\qquad$ $\Delta f_{pCR.ss} := \dfrac{E_{ps}}{E_{ci}} \cdot f_{cgp} \cdot \psi_{tf.ti} \cdot K_{id.ss} = -7.19 \cdot ksi$

$$(5.9.5.4.2b\text{-}1)$$

Stress Relaxation:

$f_{py} := 0.94 \cdot f_u = 264.234 \cdot ksi$ $\qquad$ $K_L := 30$

$f_{py.ss} := 0.94 \cdot f_{u.ss} = 227.01 \cdot ksi$

$f_{pi} := f_2 + \Delta f_{pES} = 171.54 \cdot ksi$ $\quad > \quad 0.55 \cdot f_{py} = 145.329 \cdot ksi$

$f_{pi.ss} := f_{2.ss} + \Delta f_{pES.ss} = 128.719 \cdot ksi > 0.55 \cdot f_{py.ss} = 124.855 \cdot ksi$

$f_{pt} := f_{pi}$ $\qquad$ $f_{pt.ss} := f_{pi.ss}$

$\Delta f_{pRE} := \dfrac{-f_{pt}}{K_L} \cdot \left(\dfrac{f_{pt}}{f_{py}} - 0.55 \right) = -0.567 \cdot ksi$ $\qquad$ $(5.9.5.4.2c\text{-}1)$

$\Delta f_{pRE.ss} := \dfrac{-f_{pt.ss}}{K_L} \cdot \left(\dfrac{f_{pt.ss}}{f_{py.ss}} - 0.55 \right) = -0.073 \cdot ksi$ $\qquad$ $(5.9.5.4.2c\text{-}1)$

Total Stress Losses Refined Method - Conventional Steel:

$Losses := \Delta f_{pES} + \Delta f_{pSR} + \Delta f_{pCR} + \Delta f_{pRE} + \Delta f_{ANC}$ $\qquad$ $Losses = -25.541 \cdot ksi$

$f_s := f_2 + Losses = 150.546 \cdot ksi$

$F_{se} := f_s \cdot A_{ps}$ $\qquad$ $F_{se} = 17.313 \cdot kip$

$\varepsilon_{se} := \dfrac{Losses}{E_{ps}}$ $\qquad$ $\varepsilon_{se} = -8.6875 \times 10^{-4}$

Total Stress Losses Refined Method - Stainless Steel:

$$Losses_{ss} := \Delta f_{pES.ss} + \Delta f_{pSR.ss} + \Delta f_{pCR.ss} + \Delta f_{pRE.ss} + \Delta f_{ANC}$$

$$Losses_{ss} = -24.129 \cdot ksi$$

$$f_{s.ss} := f_{2.ss} + Losses_{ss} = 108.224 \cdot ksi$$

$$F_{se.ss} := f_{s.ss} \cdot A_{ps.ss}$$

$$F_{se.ss} = 16.558 \cdot kip$$

$$\varepsilon_{se.ss} := \frac{Losses_{ss}}{E_{ps.ss}}$$

$$\varepsilon_{se.ss} = -1.0268 \times 10^{-3}$$

- **AASHTO Lump-Sum Method.**

Shrinkage, Creep, and Stress Relaxation Losses:

$$\Delta f_{pR} := 2.4 ksi \qquad \gamma_h := 1.7 - 0.01 \cdot RH = 0.95 \qquad (5.9.5.3-2)$$

$$\gamma_{st} := k_f \qquad (5.9.5.3-3)$$

$$\Delta f_{pLT} := -\left(10 \cdot \frac{f_{pi} \cdot A_{ps}}{Area} \cdot \gamma_h \cdot \gamma_{st} + 12 \cdot \gamma_h \cdot \gamma_{st} \cdot ksi + \Delta f_{pR} \right) \qquad (5.9.5.3-1)$$

$$\Delta f_{pLT.ss} := -\left(10 \cdot \frac{f_{pi.ss} \cdot A_{ps.ss}}{Area} \cdot \gamma_h \cdot \gamma_{st} + 12 \cdot \gamma_h \cdot \gamma_{st} \cdot ksi + \Delta f_{pR} \right) \qquad (5.9.5.3-1)$$

Total Stress Losses Lump-Sum Method - Conventional Steel:

$$Losses_{LS} := \Delta f_{pES} + \Delta f_{pLT}$$

$$Losses_{LS} = -19.035 \cdot ksi$$

$$f_{s.LS} := f_2 + Losses_{LS} = 157.052 \cdot ksi$$

$$F_{se.LS} := f_{s.LS} \cdot A_{ps}$$

$$F_{se.LS} = 18.061 \cdot kip$$

$$\varepsilon_{se.LS} := \frac{Losses_{LS}}{E_{ps}}$$

$$\varepsilon_{se.LS} = -6.4745 \times 10^{-4}$$

255

Total Stress Losses Lump-Sum Method - Stainless Steel:

$$Losses_{LS.ss} := \Delta f_{pES.ss} + \Delta f_{pLT.ss}$$

$$Losses_{LS.ss} = -18.122 \cdot ksi$$

$$f_{s.LS.ss} := f_{2.ss} + Losses_{LS.ss} = 114.231 \cdot ksi$$

$$F_{se.LS.ss} := f_{s.LS.ss} \cdot A_{ps.ss}$$

$$F_{se.LS.ss} = 17.477 \cdot kip$$

$$\varepsilon_{se.LS.ss} := \frac{Losses_{LS.ss}}{E_{ps.ss}}$$

$$\varepsilon_{se.LS.ss} = -7.7113 \times 10^{-4}$$

APPENDIX L: INDIVIDUAL PRESTRESS LOSSES
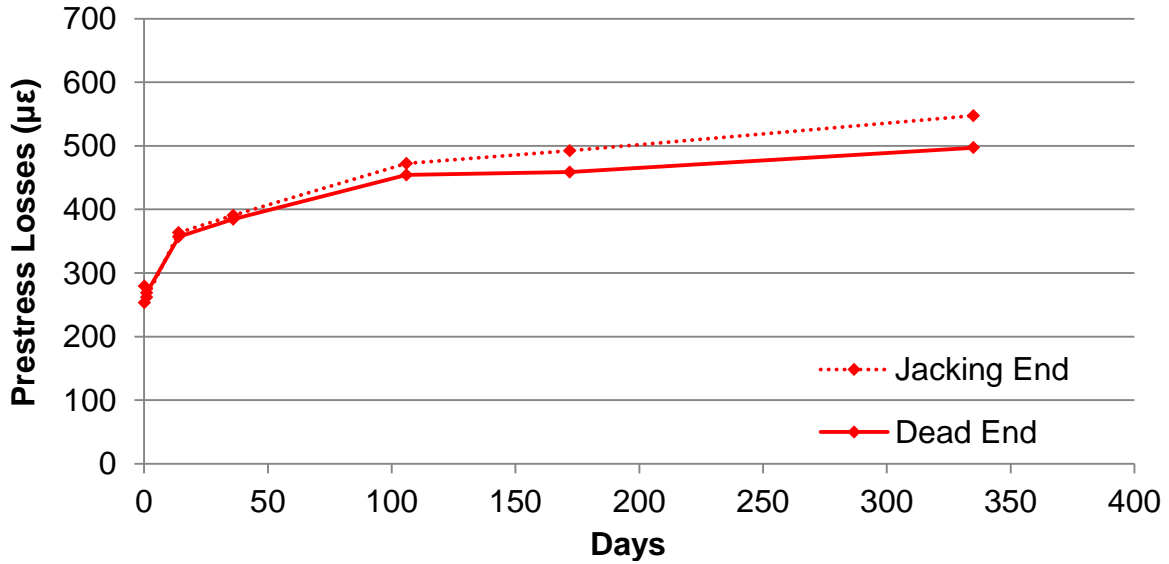
Figure L.1 Prestress losses of pile 1080 #1. Wires 3 and 4 correspond to vibrating wire sensors closer to the jacking end of the pile.
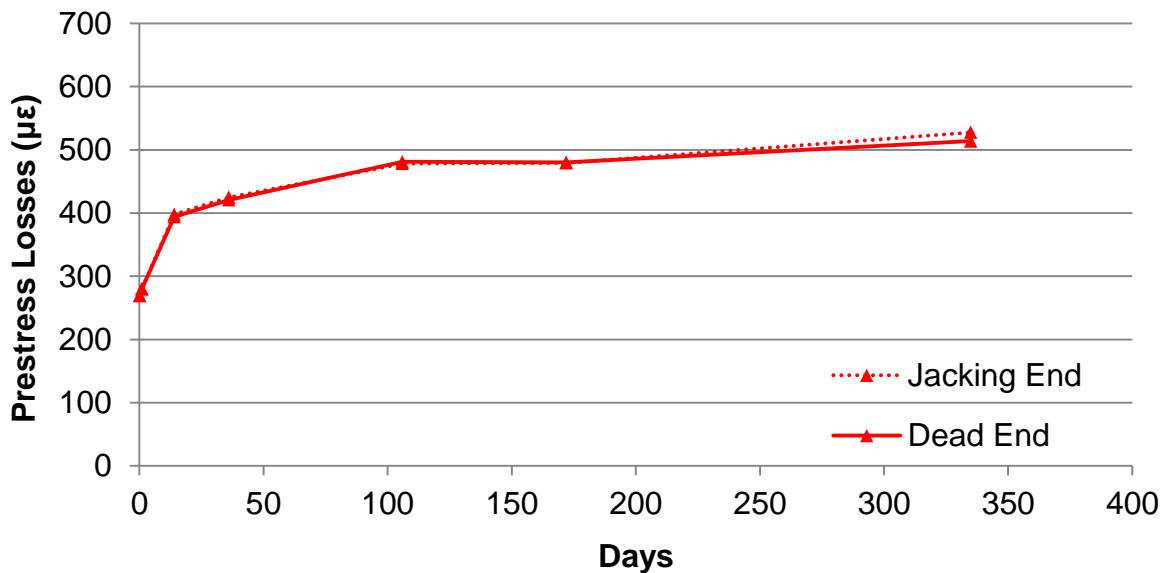
Figure L.2 Prestress losses of pile 1080 #2. Wires 3 and 4 correspond to vibrating wire sensors closer to the jacking end of the pile.
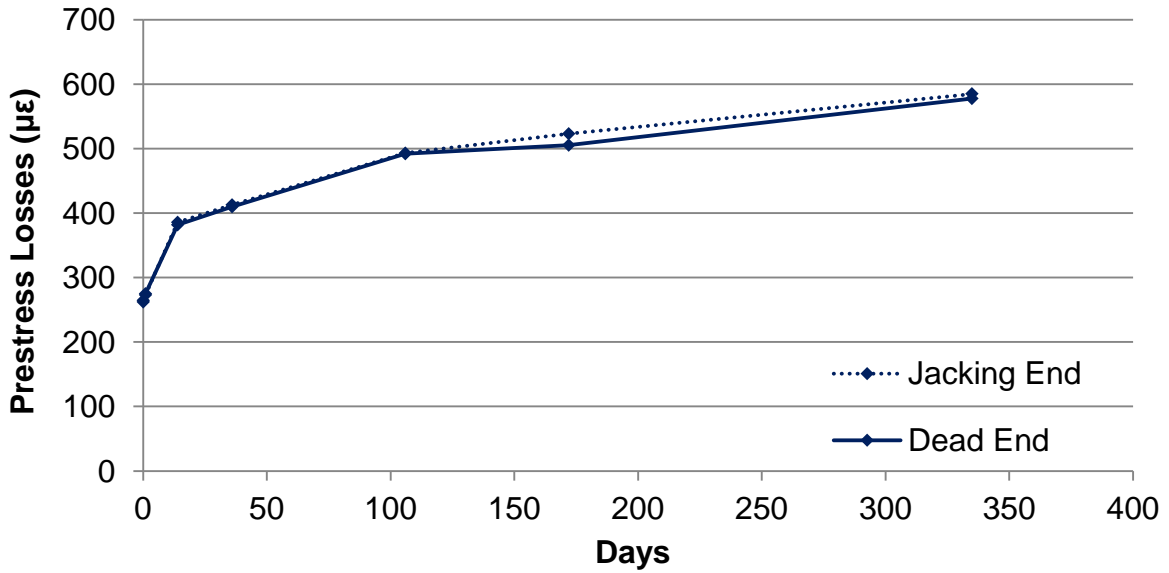
Figure L.3 Prestress losses of pile HSSS 2205 #1. Wires 3 and 4 correspond to vibrating wire sensors closer to the jacking end of the pile.
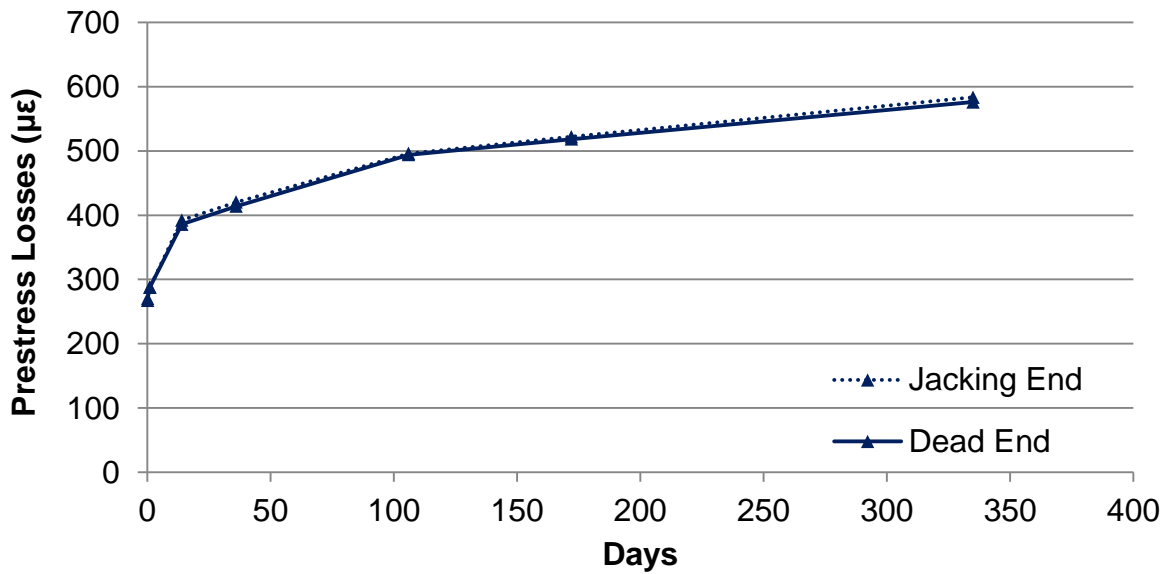
Figure L.4 Prestress losses of pile HSSS 2205 #2. Wires 3 and 4 correspond to vibrating wire sensors closer to the jacking end of the pile.
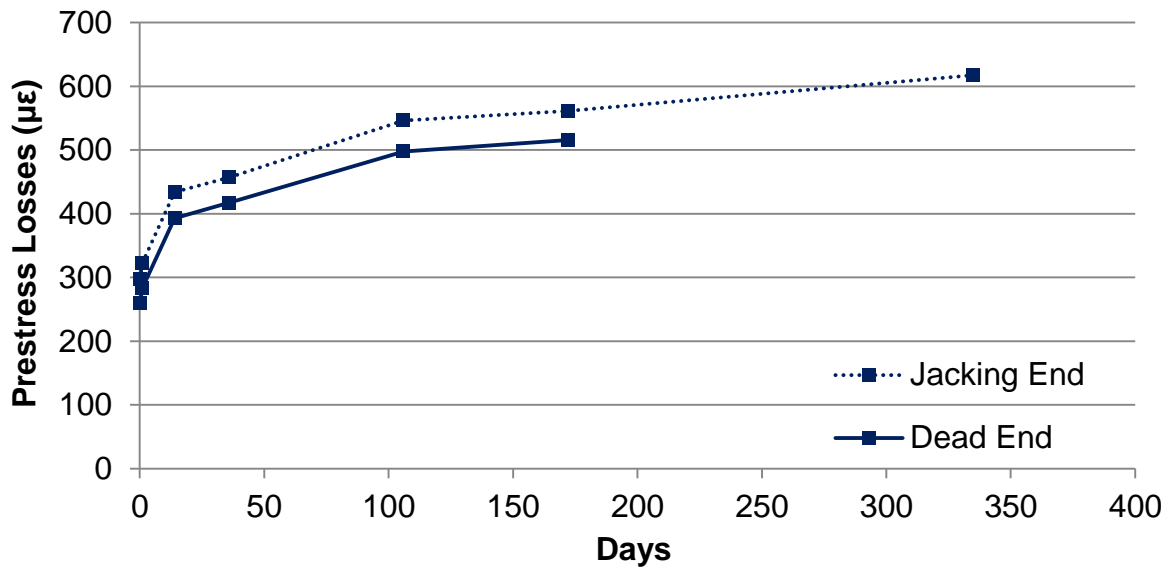
Figure L.5 Prestress losses of pile HSSS 2205 #3. Wires 3 and 4 correspond to vibrating wire sensors closer to the jacking end of the pile.

APPENDIX M: CONCRETE SURFACE STRAIN PROFILES
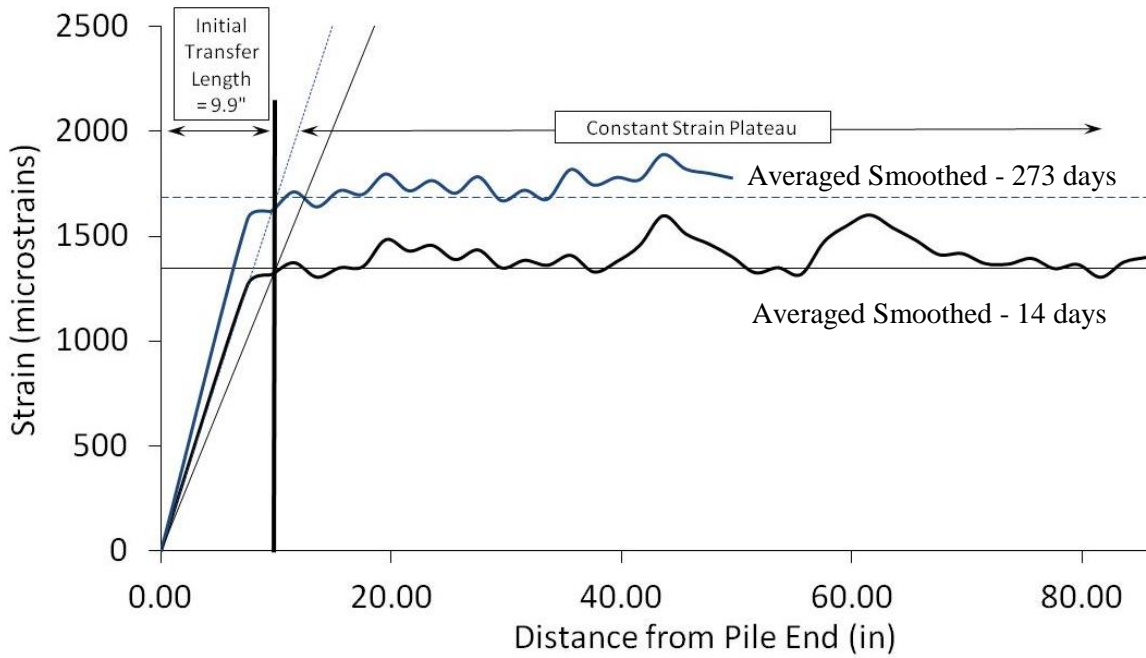
Figure M.1 Smoothed concrete surface strain profiles of pile 1080 #1, jacking end.
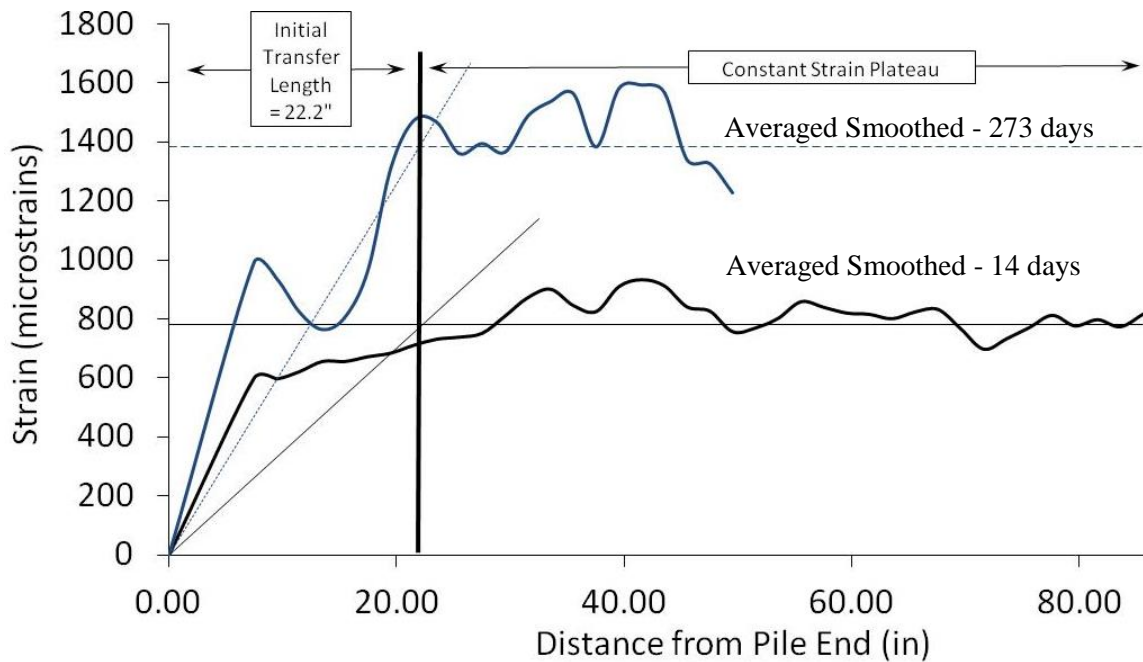
Figure M.2 Smoothed concrete surface strain profiles of pile 1080 #1, dead end.
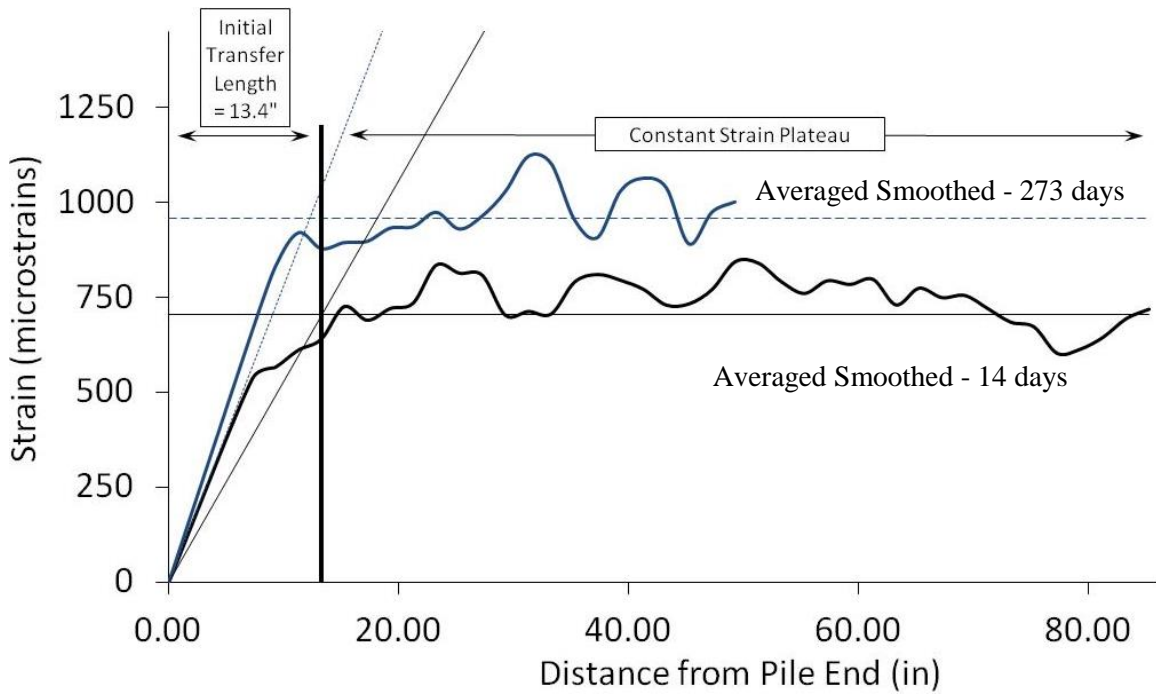
Figure M.3 Smoothed concrete surface strain profiles of pile 1080 #2, jacking end.
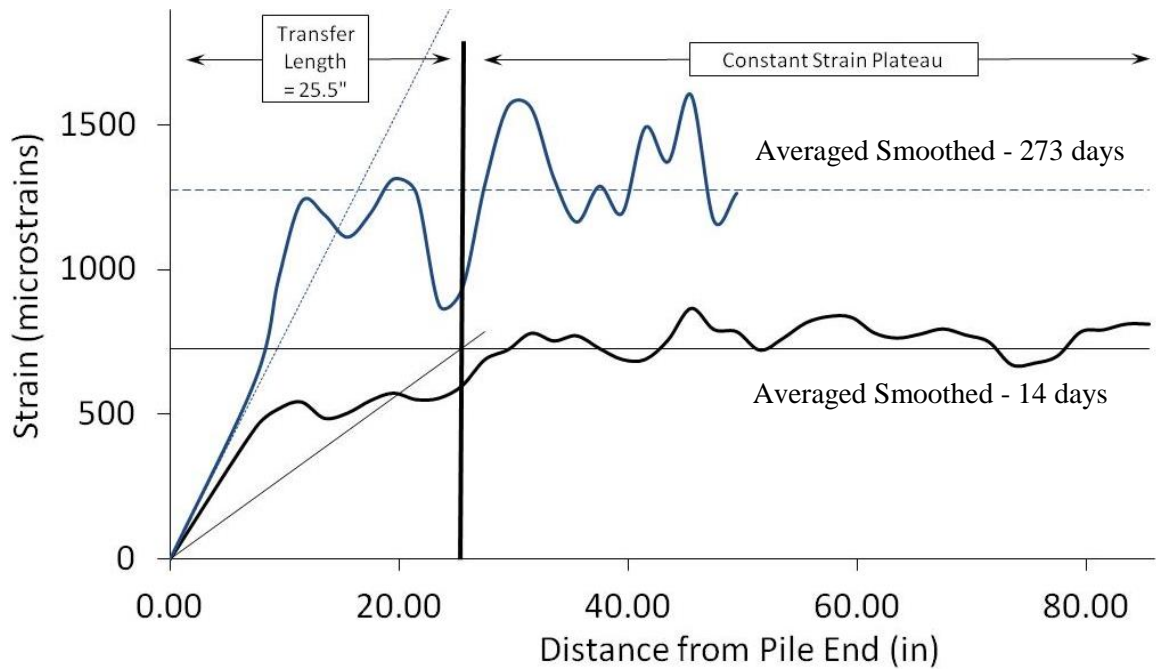
Figure M.4 Smoothed concrete surface strain profiles of pile 1080 #2, dead end.
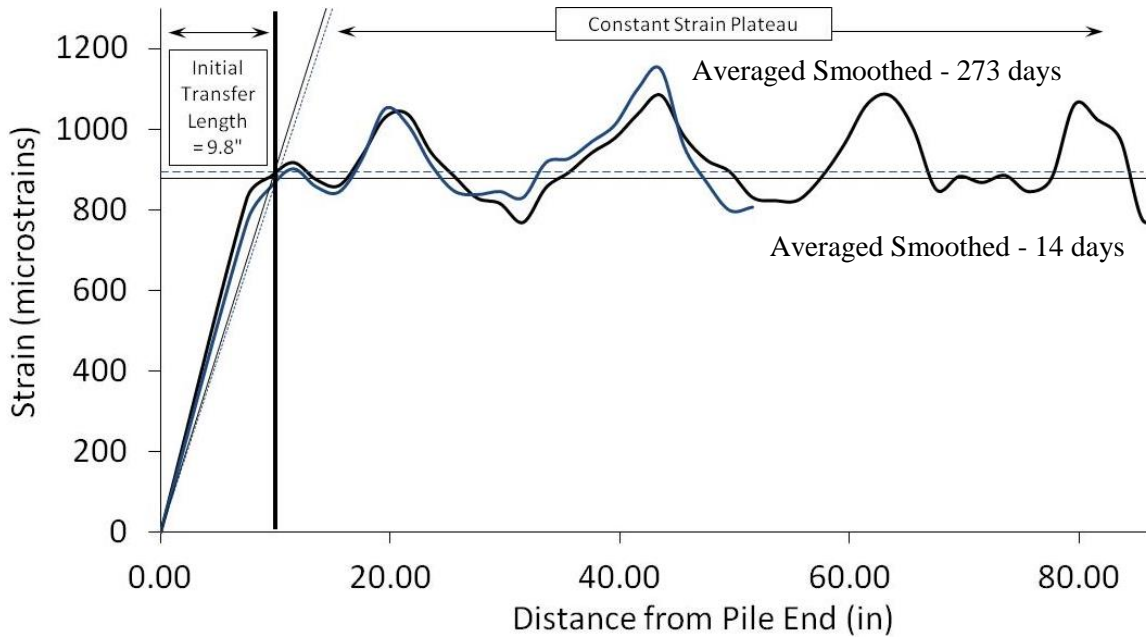
Figure M.5 Smoothed concrete surface strain profiles of pile HSSS 2205 #1, jacking end.
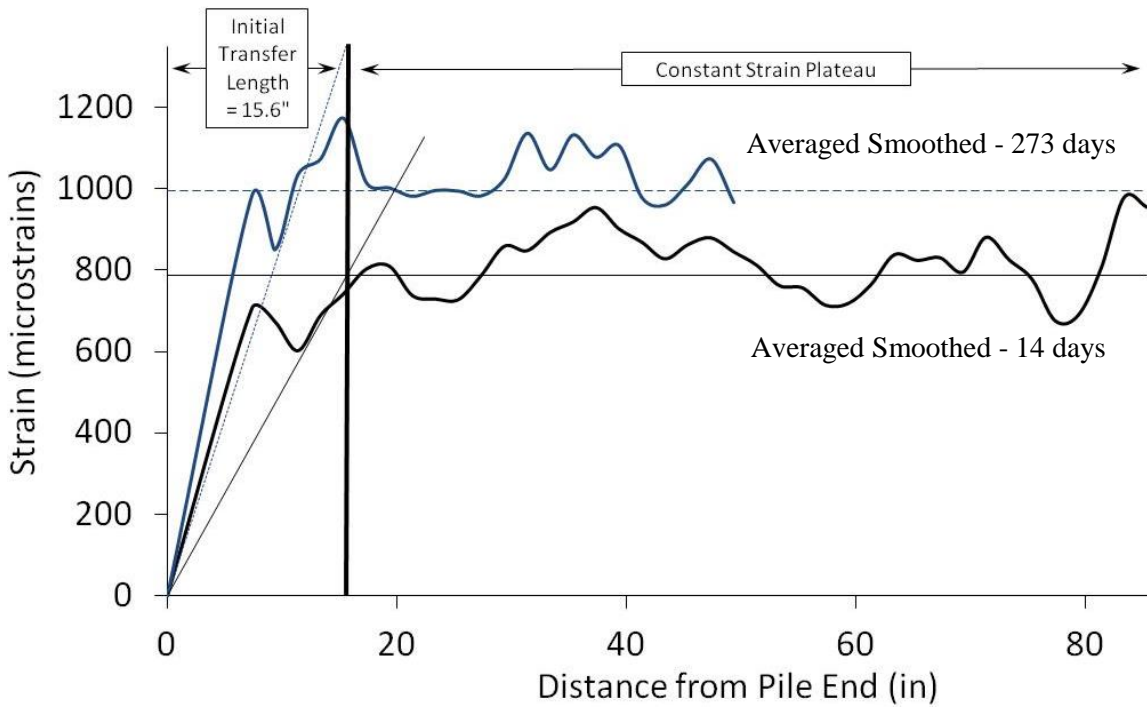
Figure M.6 Smoothed concrete surface strain profiles of pile HSSS 2205 #1, dead end.
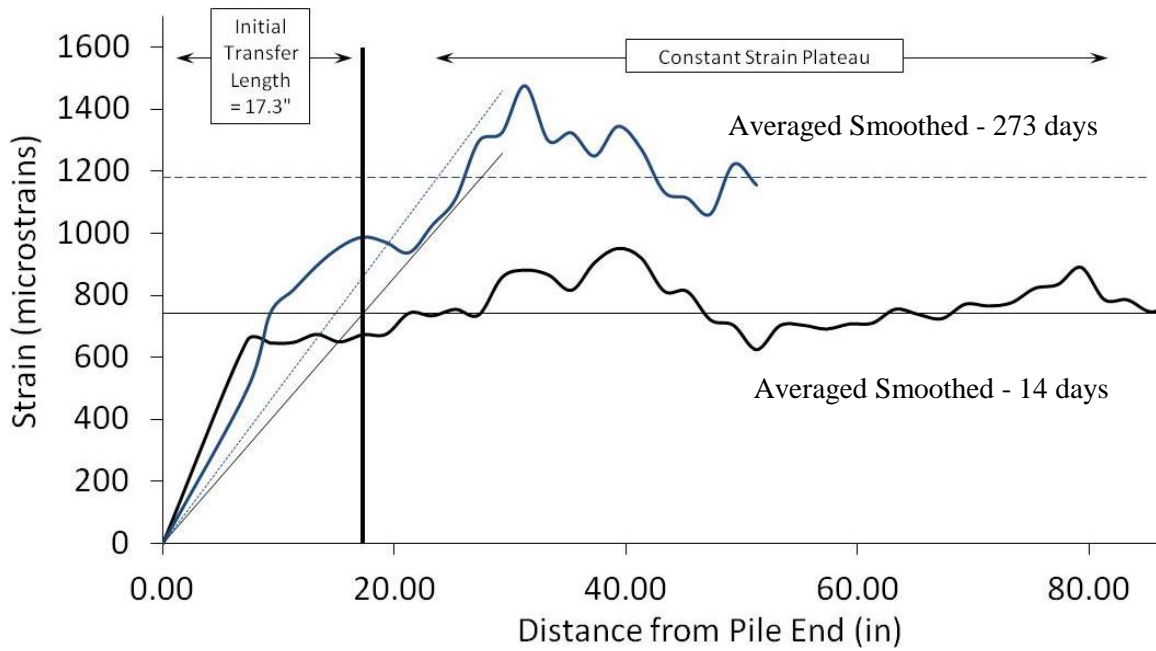
Figure M.7 Smoothed concrete surface strain profiles of pile HSSS 2205 #2, jacking end.
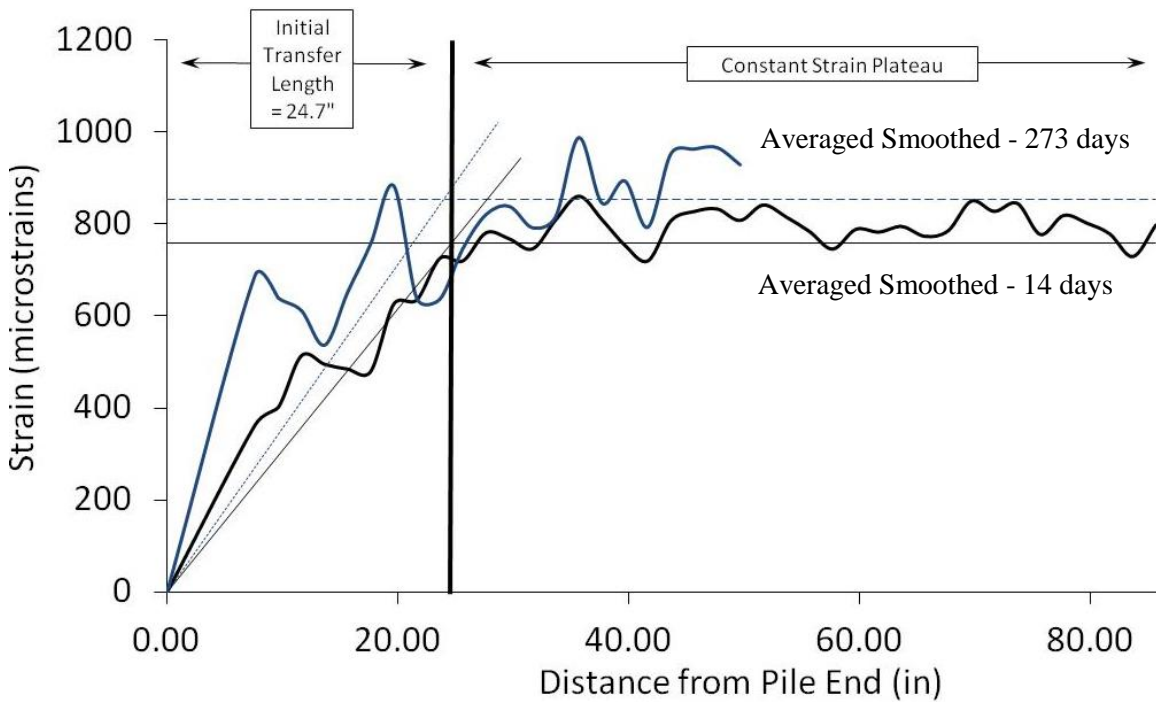
Figure M.8 Smoothed concrete surface strain profiles of pile HSSS 2205 #2, dead end.
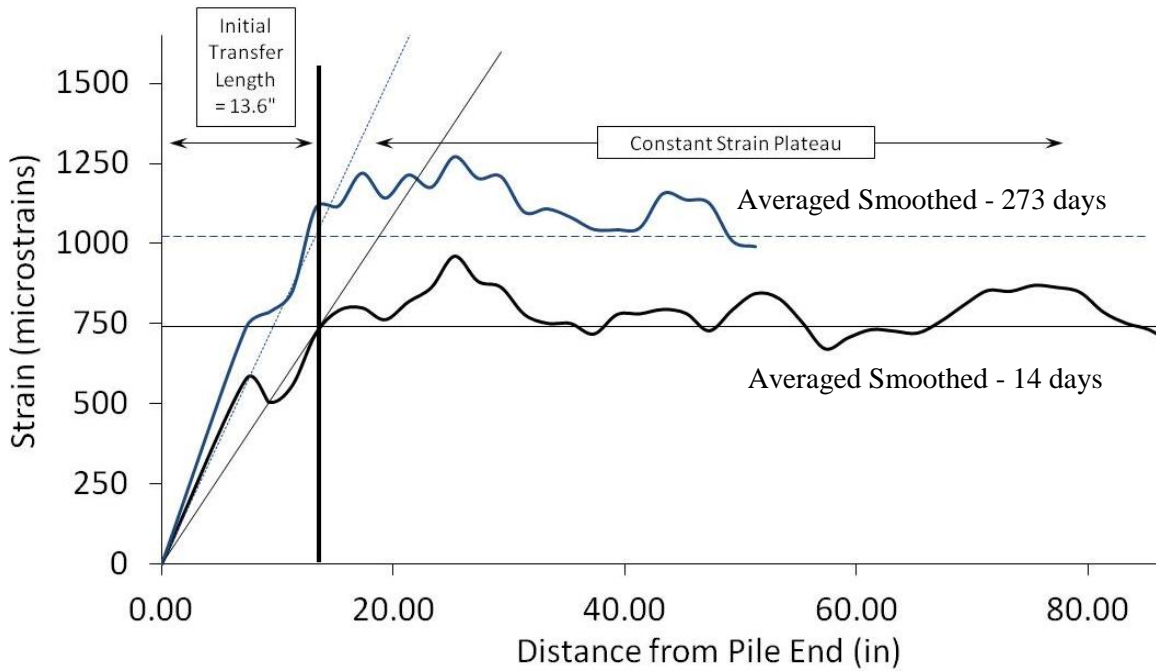
Figure M.9 Smoothed concrete surface strain profiles of pile HSSS 2205 #3, jacking end.
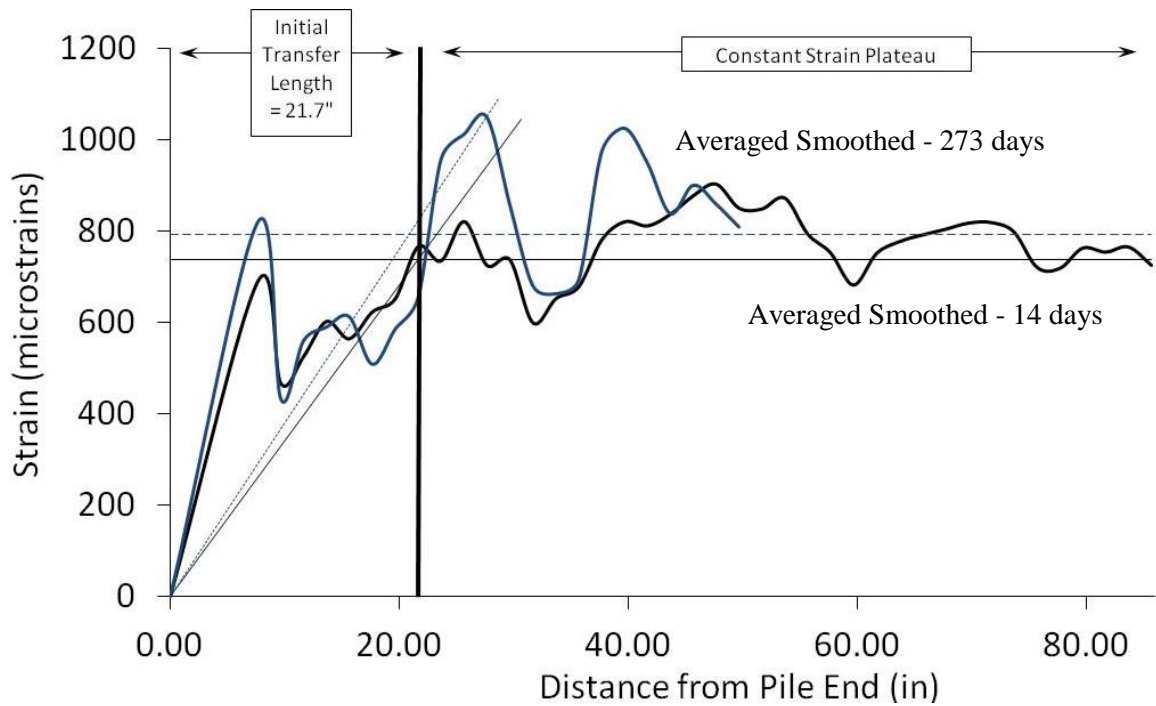
Figure M.10 Smoothed concrete surface strain profiles of pile HSSS 2205 #3, dead end.

264

APPENDIX N: DEVELOPMENT LENGTH TEST – INDIVIDUAL RESULTS

- Pile 1080 – Embedment length: 72 inches.
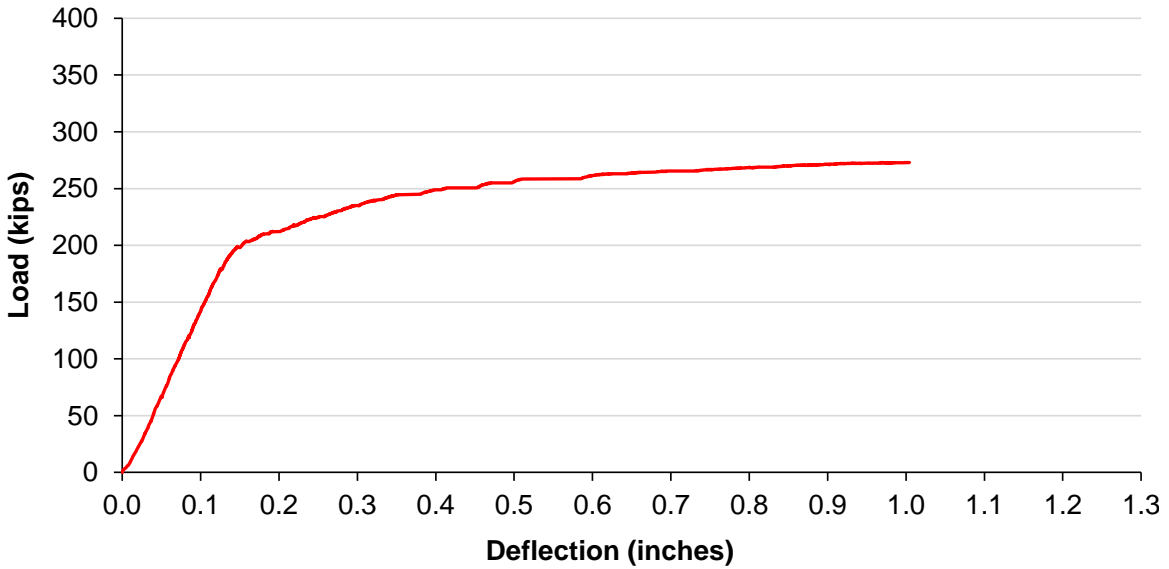
Figure N.1 Load-deflection curve for pile 1080 (l_e = 72-in.).
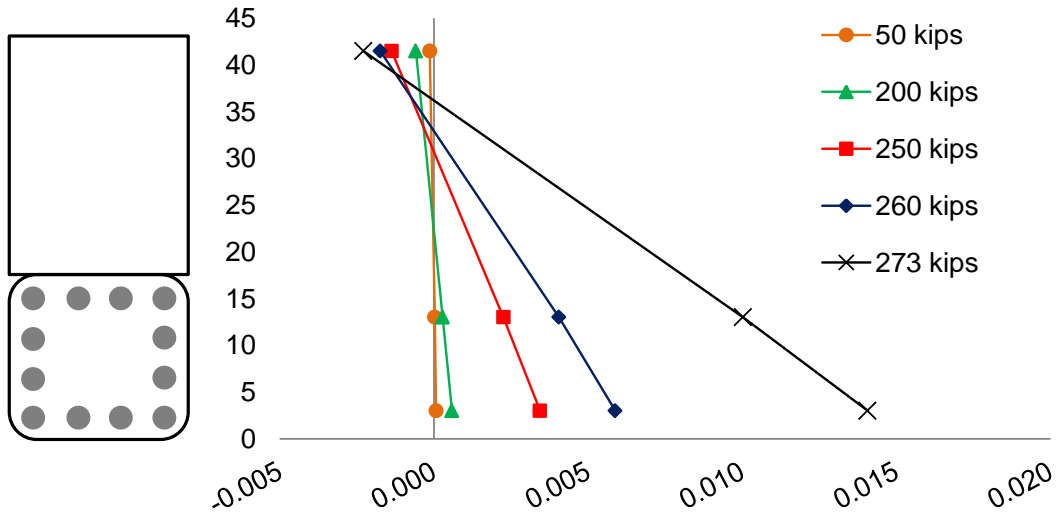
Figure N.2 Strain distribution for pile 1080 (l_e = 72-in.).
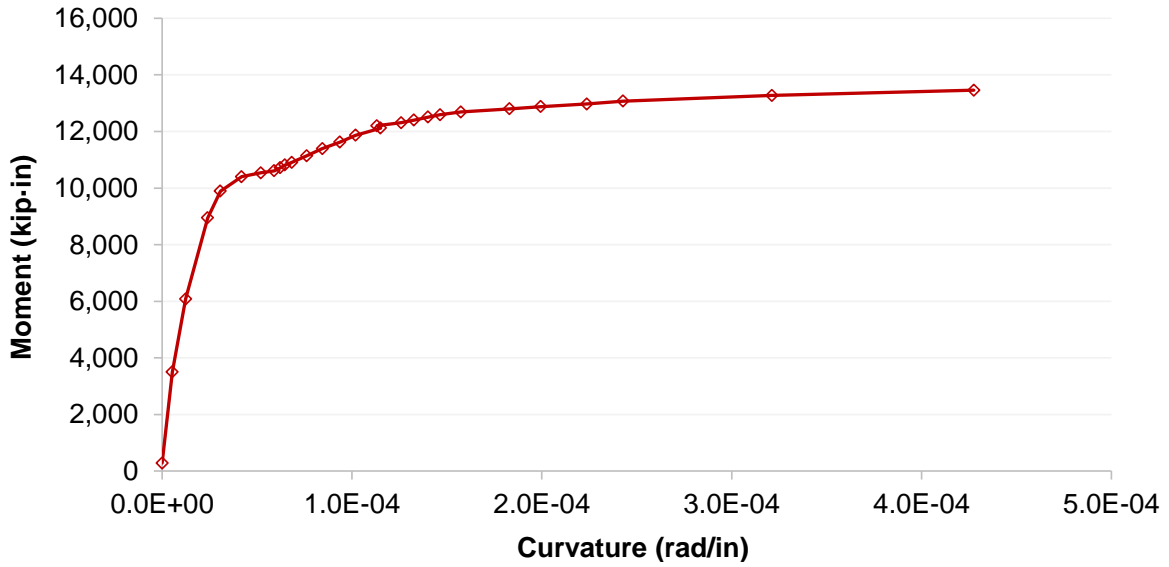
Figure N.3 Moment-curvature curve for pile 1080 (l_e = 72-in.).
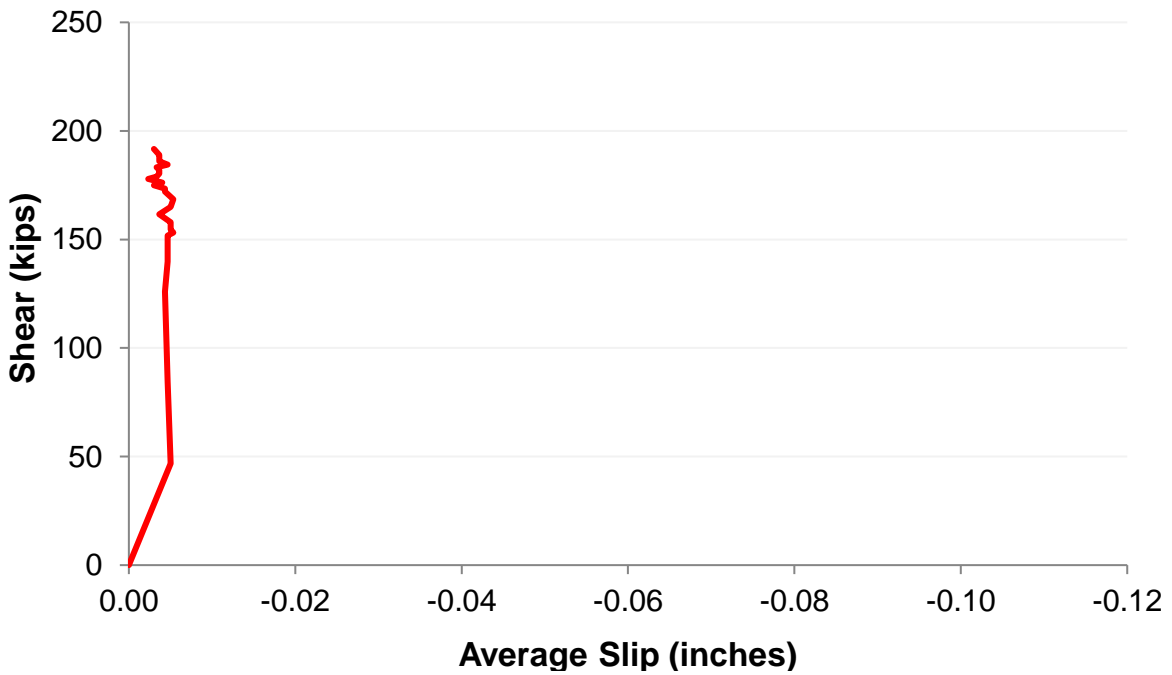
Figure N.4 Strand slip for pile 1080 (l_e = 72-in.).

- Pile 1080 – Embedment length: 61 inches.
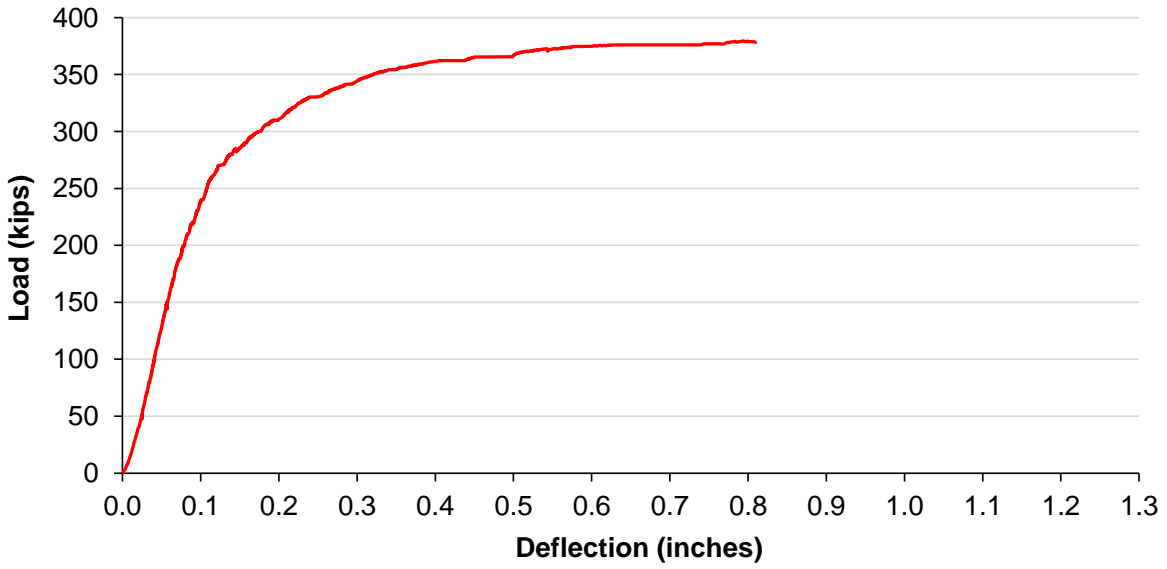
Figure N.5 Load-deflection curve for pile 1080 (l_e = 61-in.).
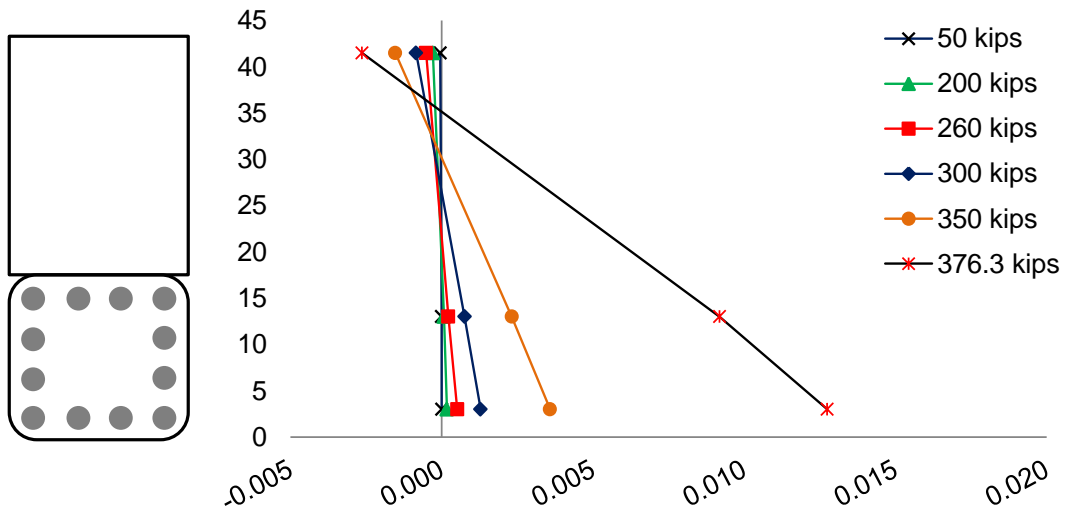
Figure N.6 Strain distribution for pile 1080 (l_e = 61-in.).
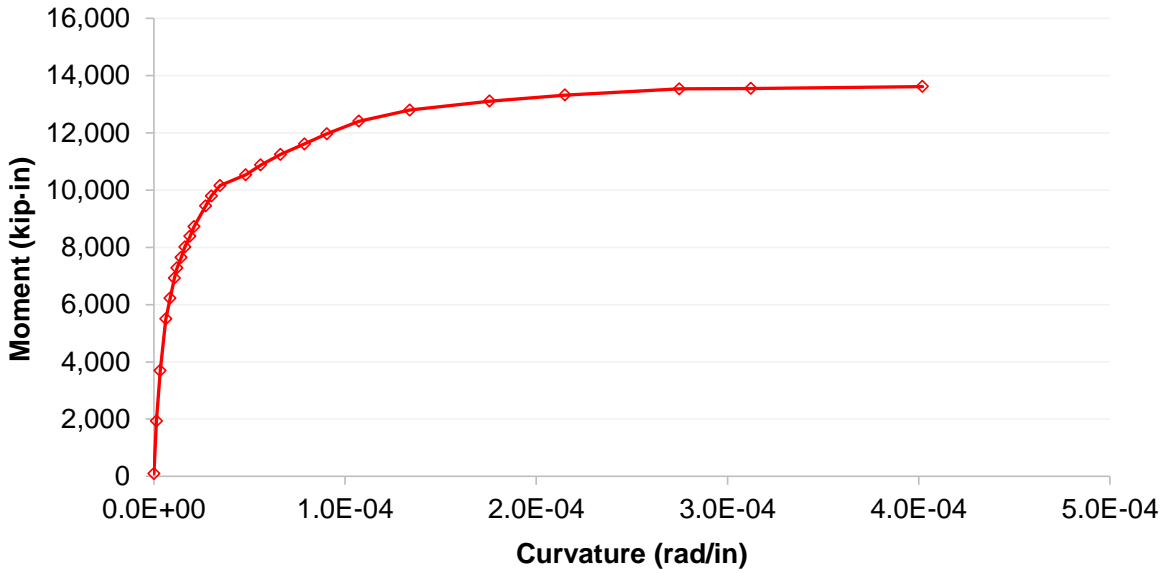
Figure N.7 Moment-curvature curve for pile 1080 (l_e = 61-in.).
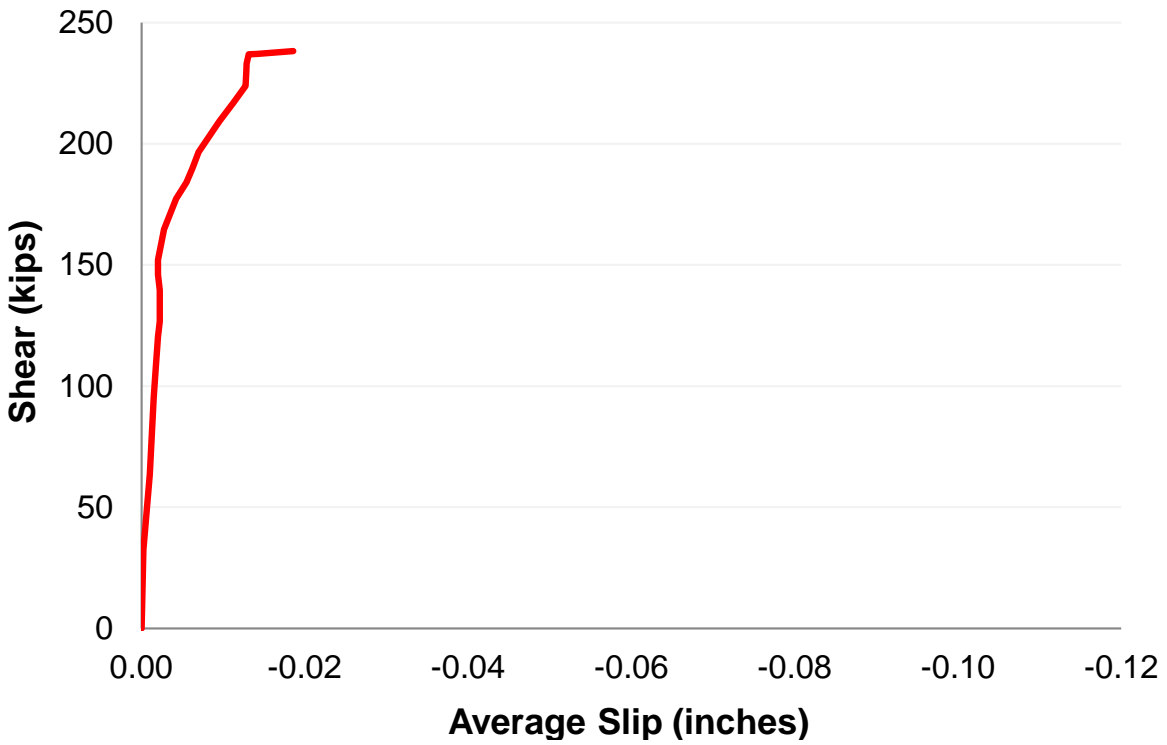
Figure N.8 Strand slip for pile 1080 (l_e = 61-in.).

- Pile 1080 – Embedment length: 57 inches.
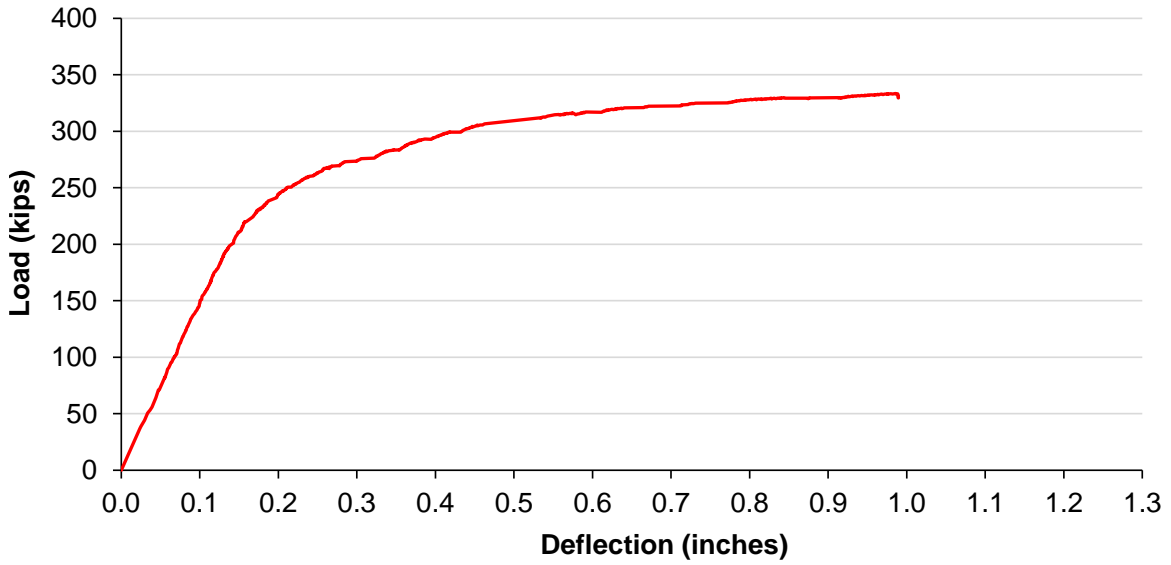
Figure N.9 Load-deflection curve for pile 1080 (l_e = 57-in.).
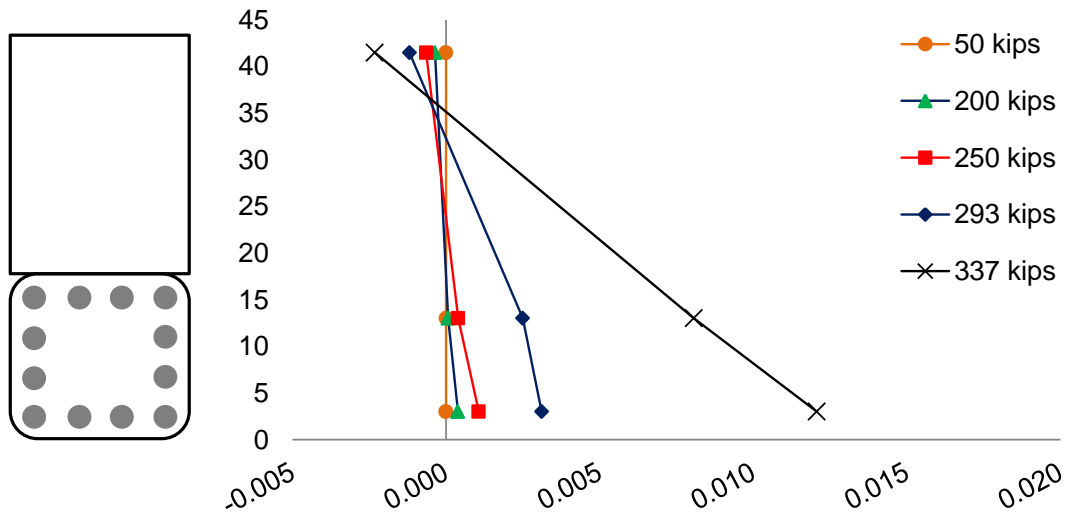
Figure N.10 Strain distribution for pile 1080 (l_e = 57-in.).
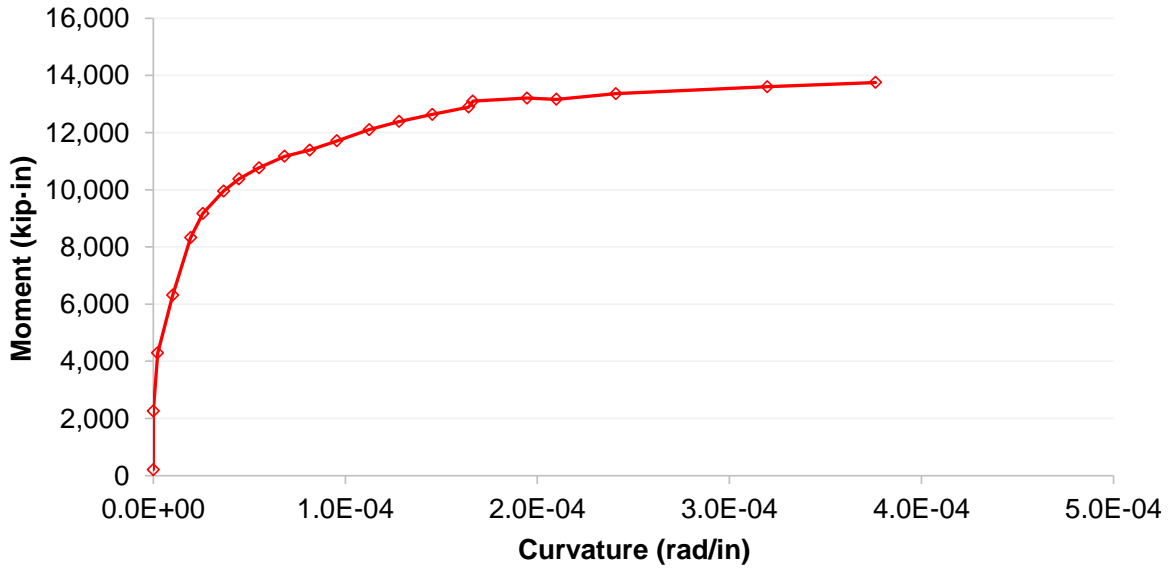
Figure N.11 Moment-curvature curve for pile 1080 (l_e = 57-in.).
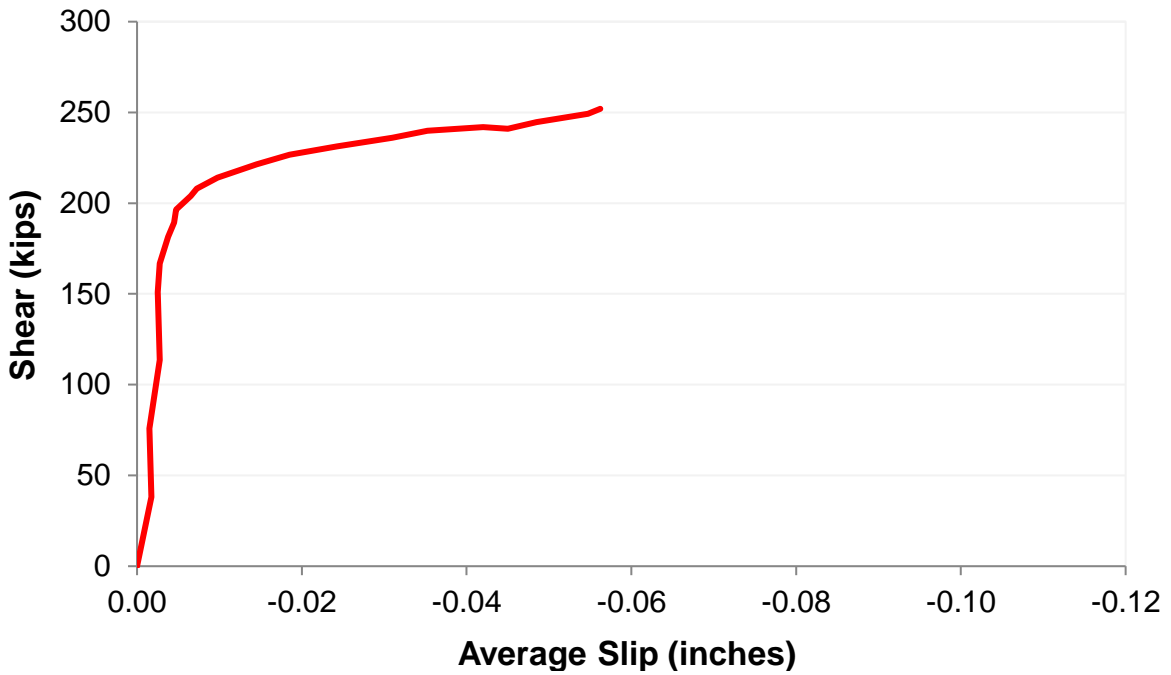
Figure N.12 Strand slip for pile 1080 (l_e = 57-in.).

- Pile 1080 – Embedment length: 53.5 inches.
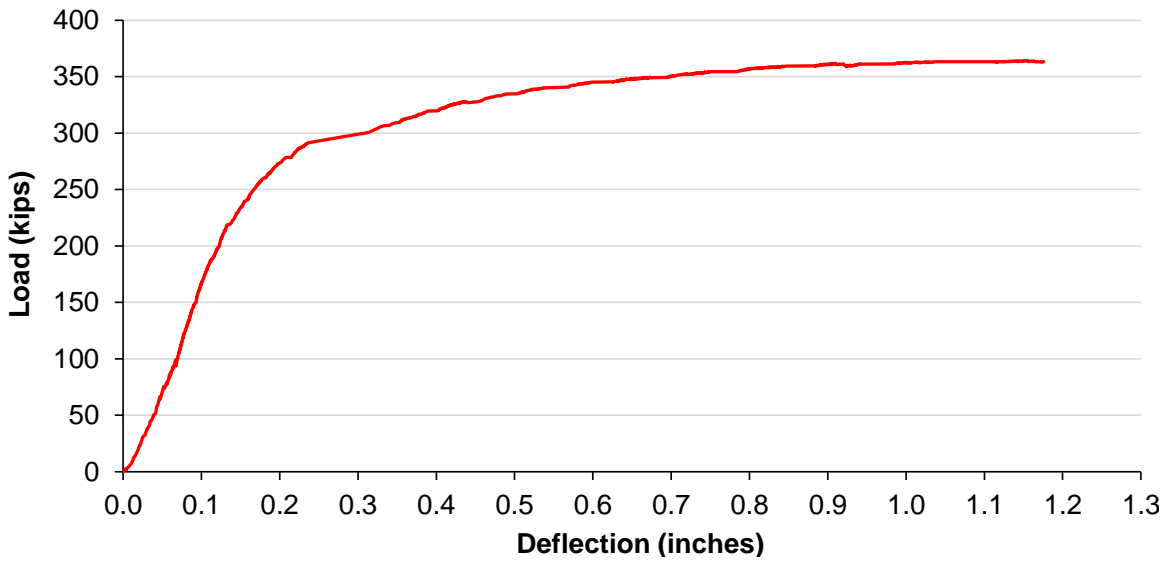
Figure N.13 Load-deflection curve for pile 1080 (l_e = 53.5-in.).
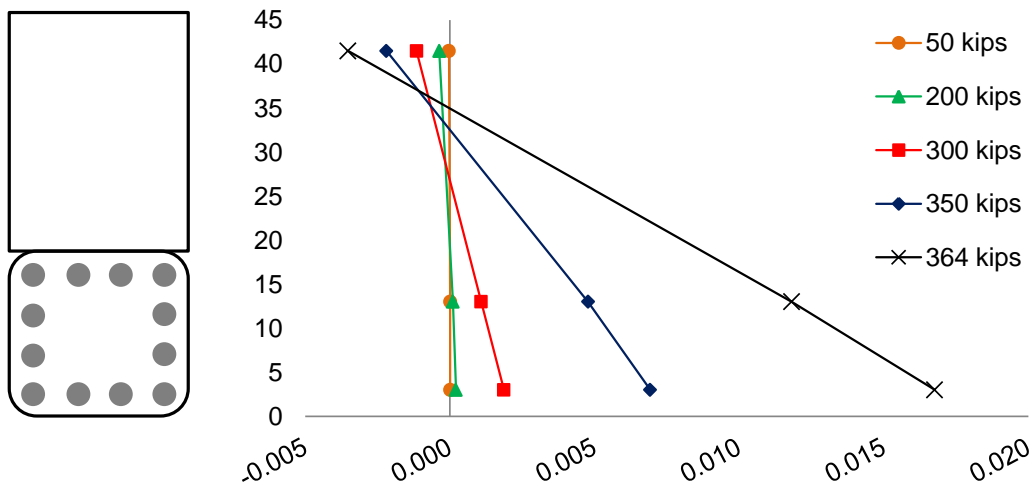
Figure N.14 Strain distribution for pile 1080 (l_e = 53.5-in.).

271
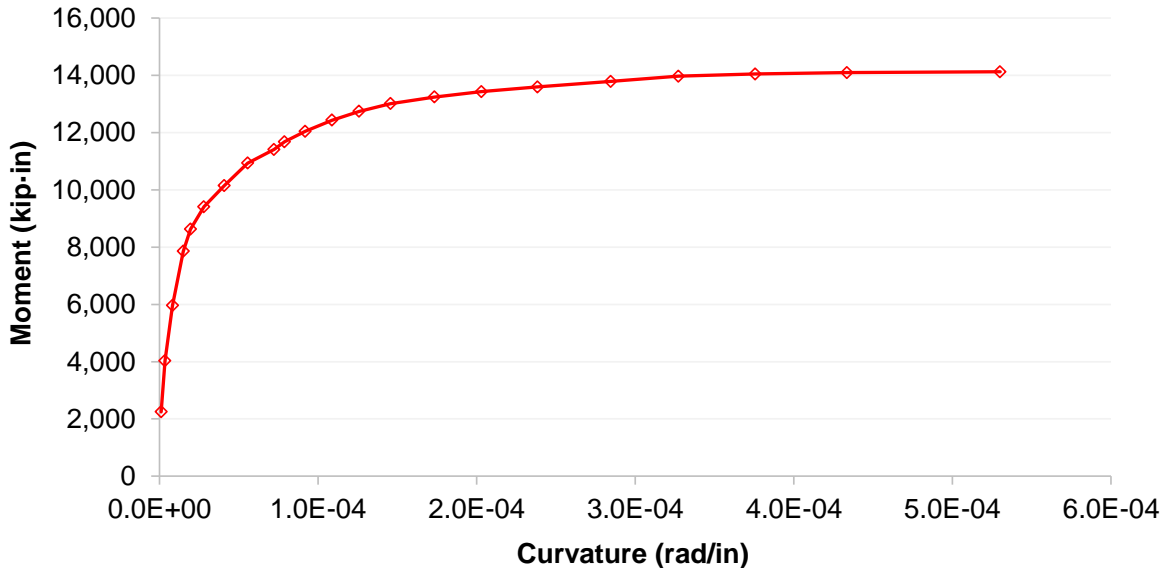
Figure N.15 Moment-curvature curve for pile 1080 (l_e = 53.5-in.).
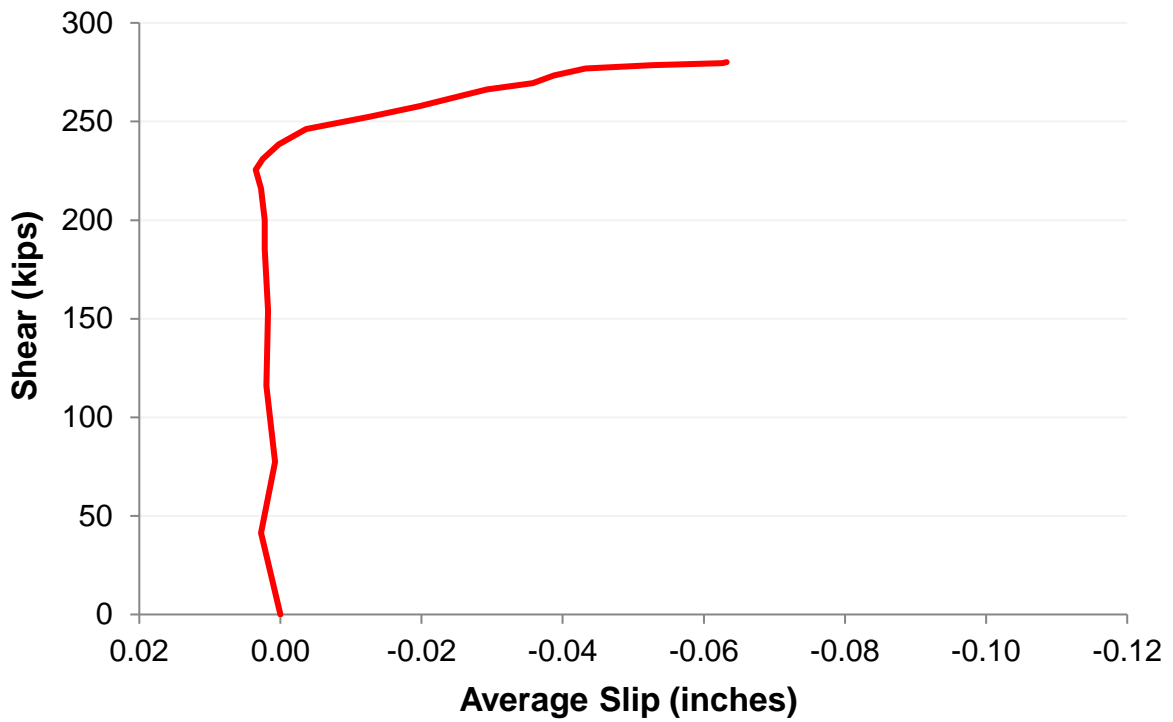
Figure N.16 Strand slip for pile 1080 (l_e = 53.5-in.).

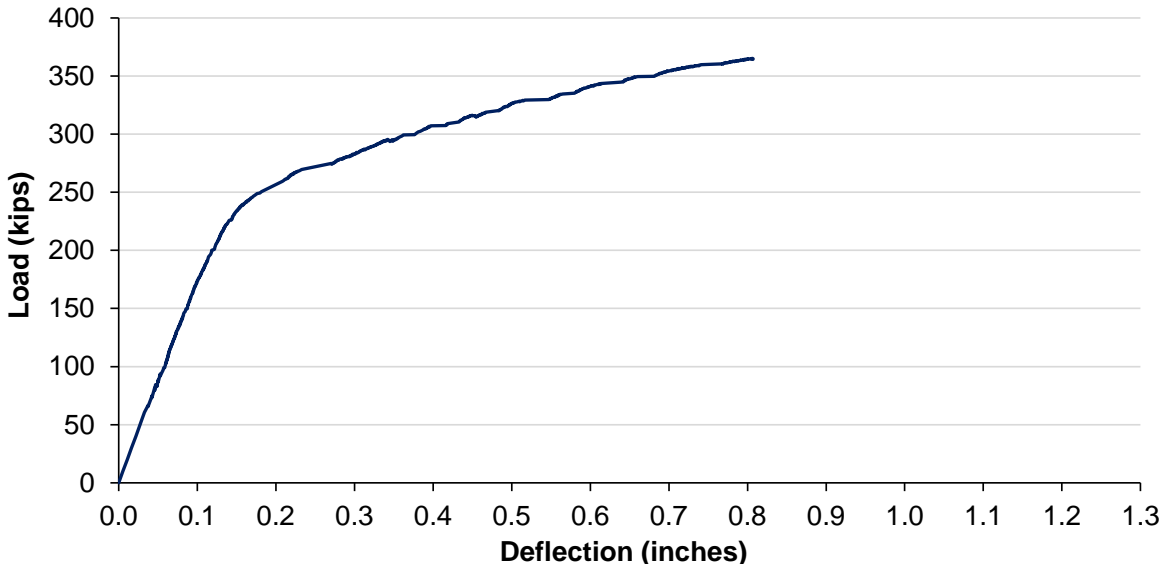**- Pile HSSS 2205 – Embedment length: 79.75 inches.**
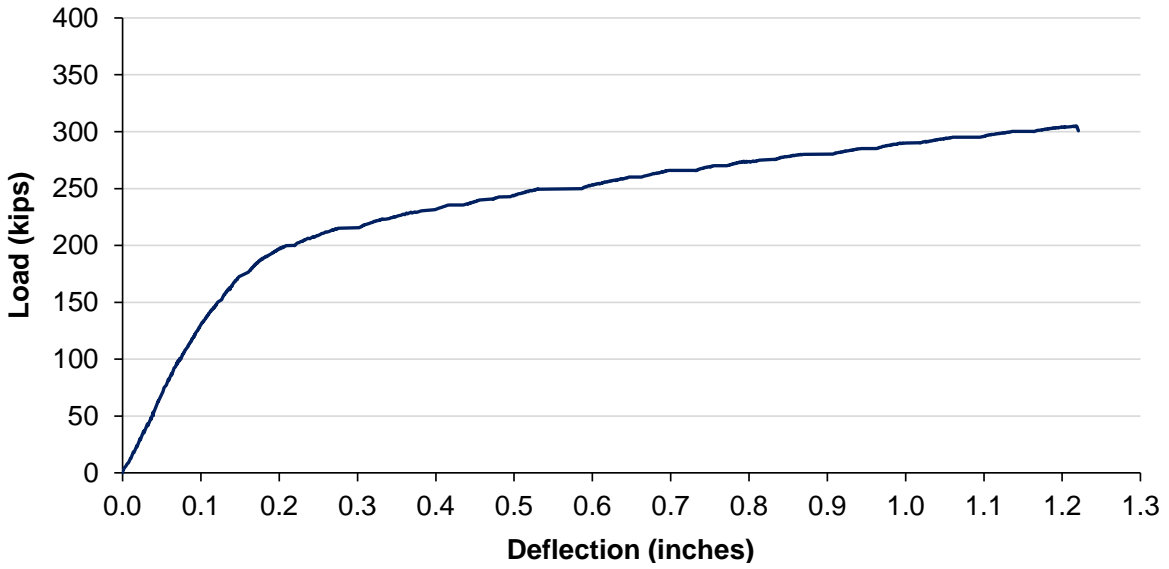
Figure N.17 Load-deflection curve for pile HSSS 2205 (l_e = 79.75-in.).
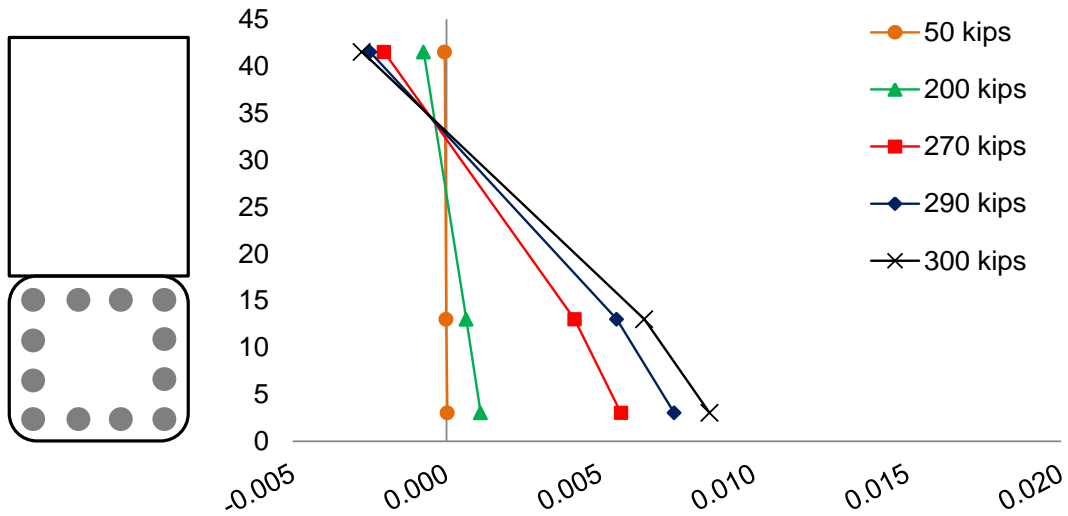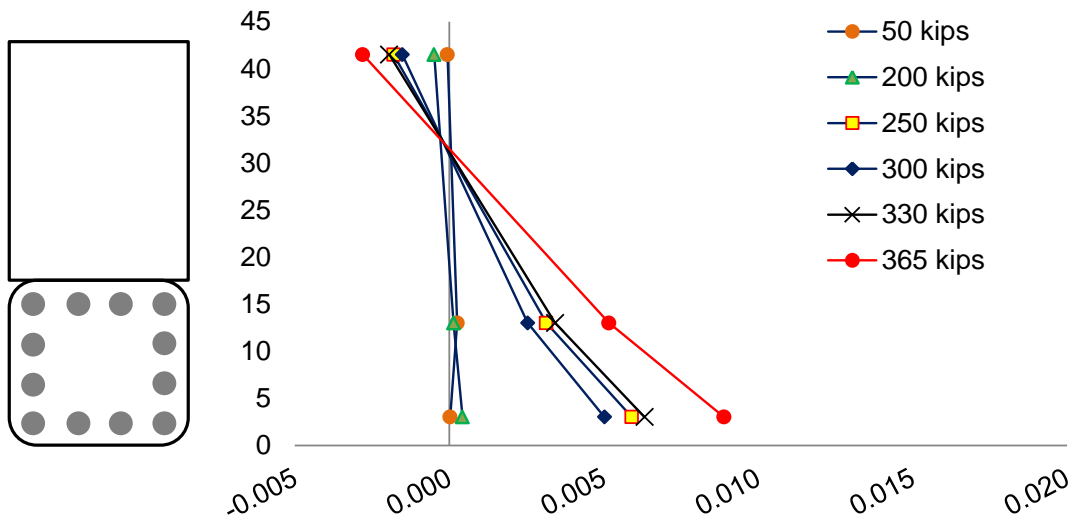

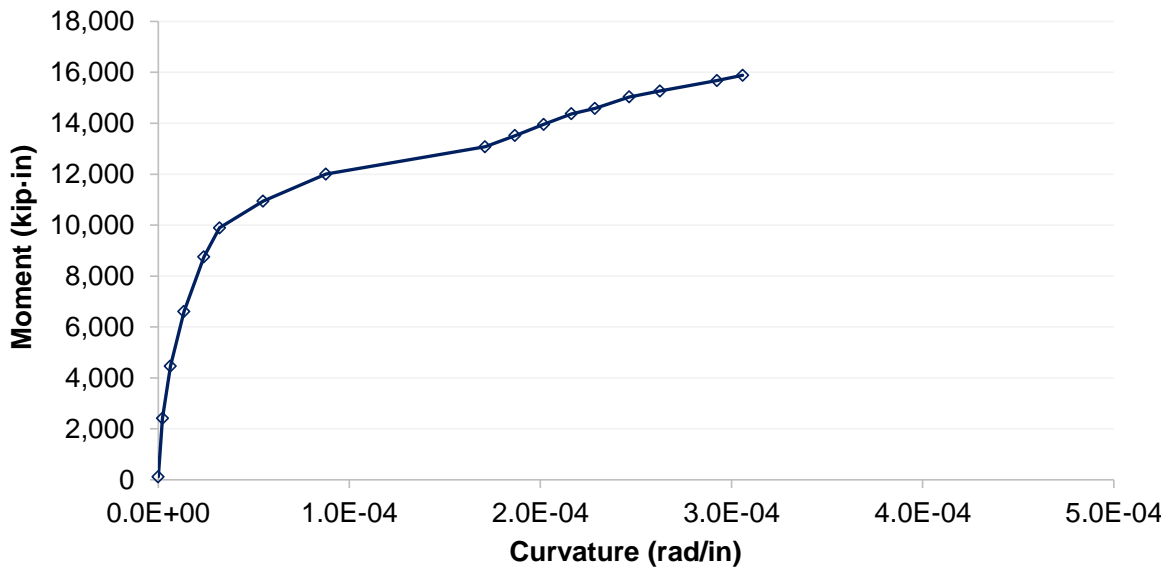**Figure N.18** Strain distribution for pile HSSS 2205 (l_e = 79.75-in.).

273
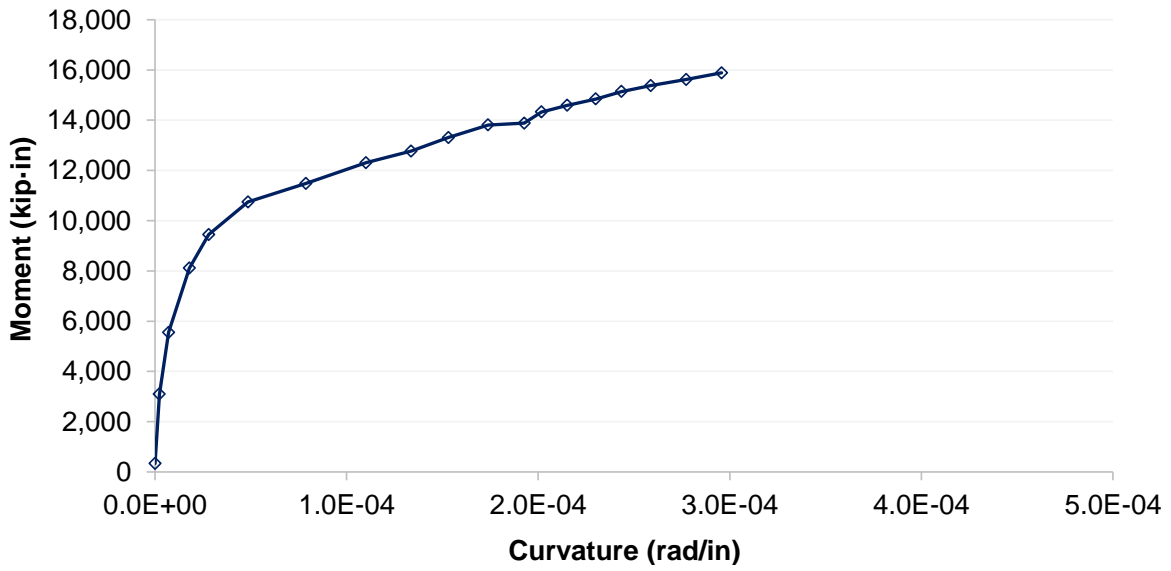
Figure N.19 Moment-curvature curve for pile HSSS 2205 (l_e = 79.75-in.).
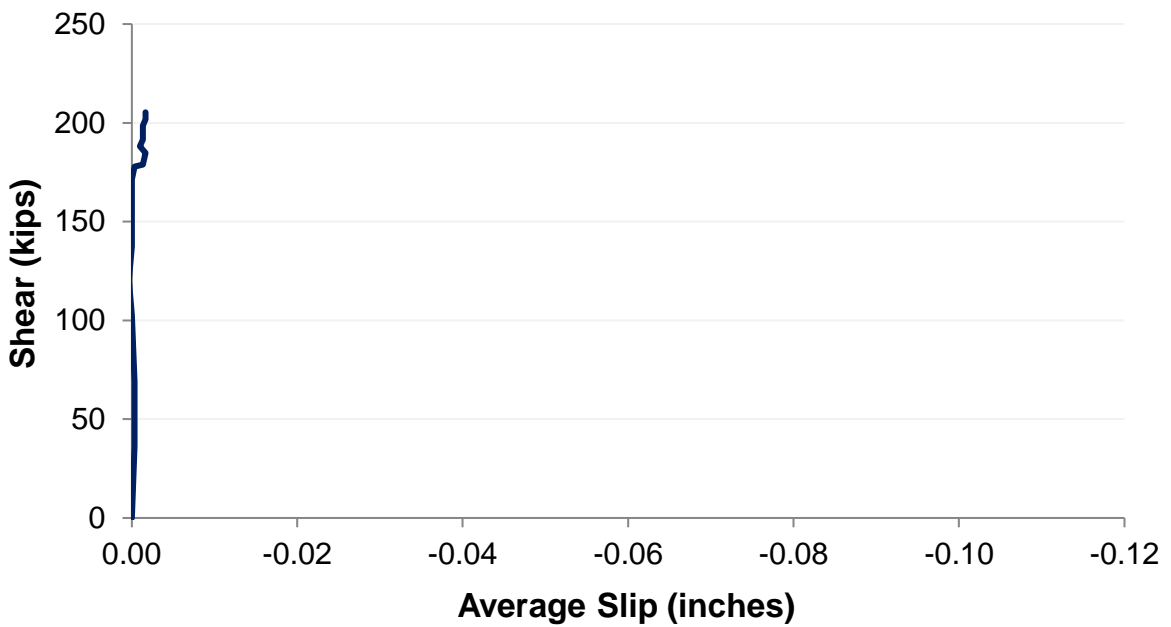
Figure N.20 Strand slip for pile HSSS 2205 (l_e = 79.75-in.).

- Pile HSSS 2205 – Embedment length: 69 inches.
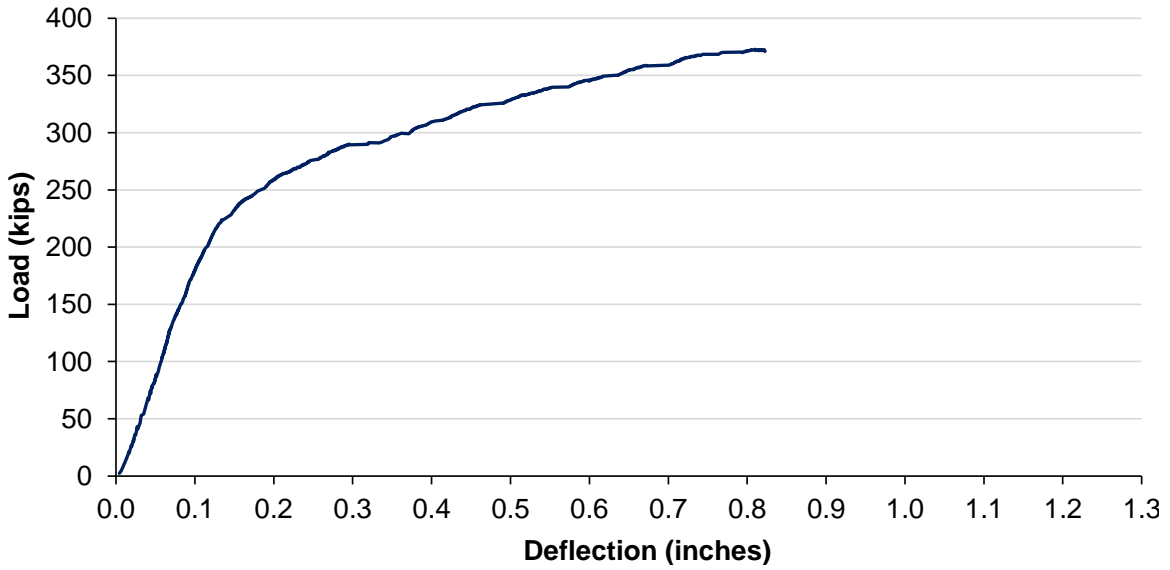
Figure N.21 Load-deflection curve for pile HSSS 2205 (l_e = 69-in.).
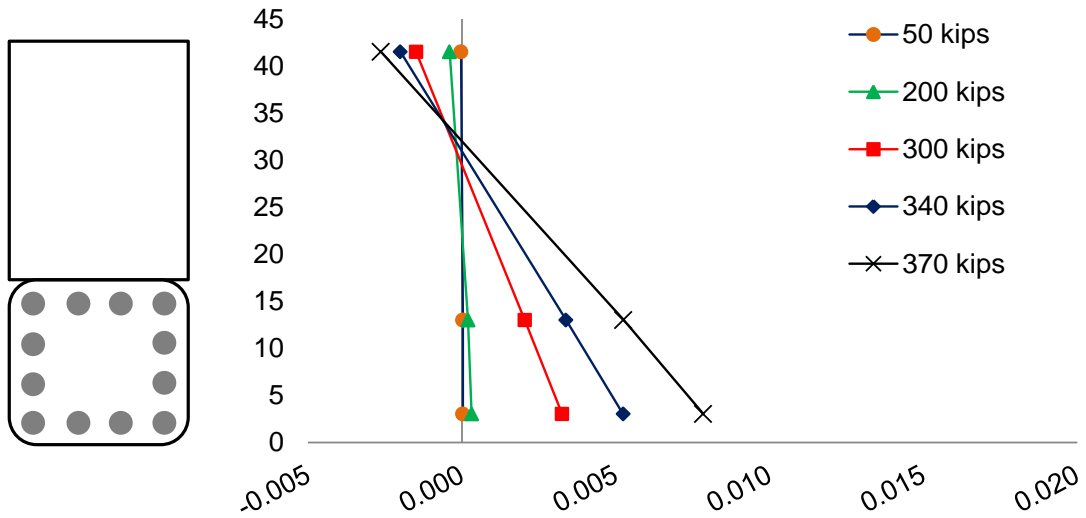
Figure N.22 Strain distribution for pile HSSS 2205 (l_e = 69-in.).
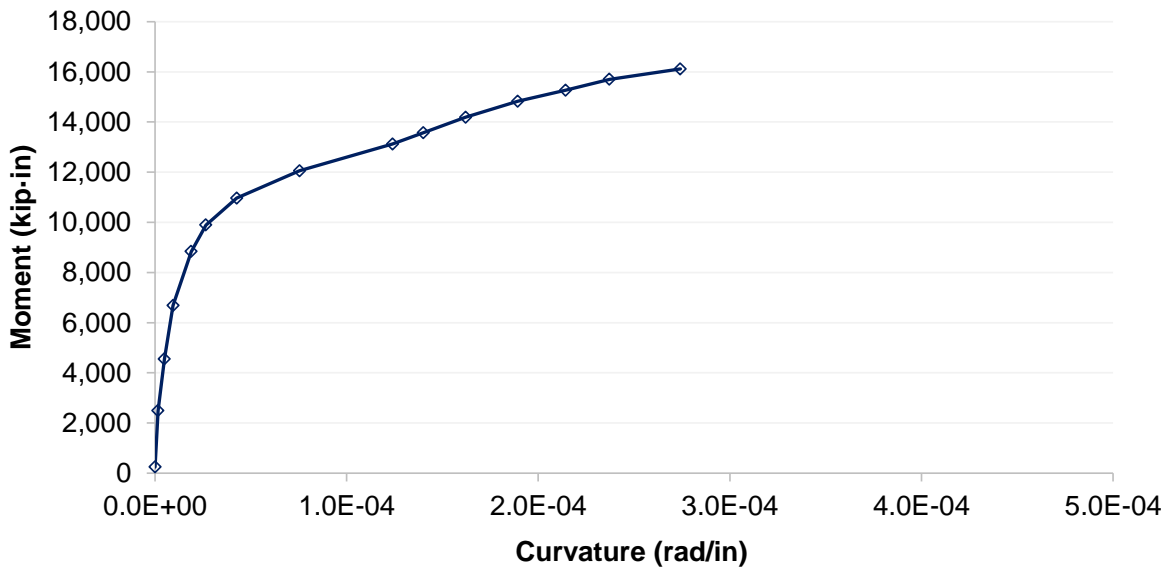
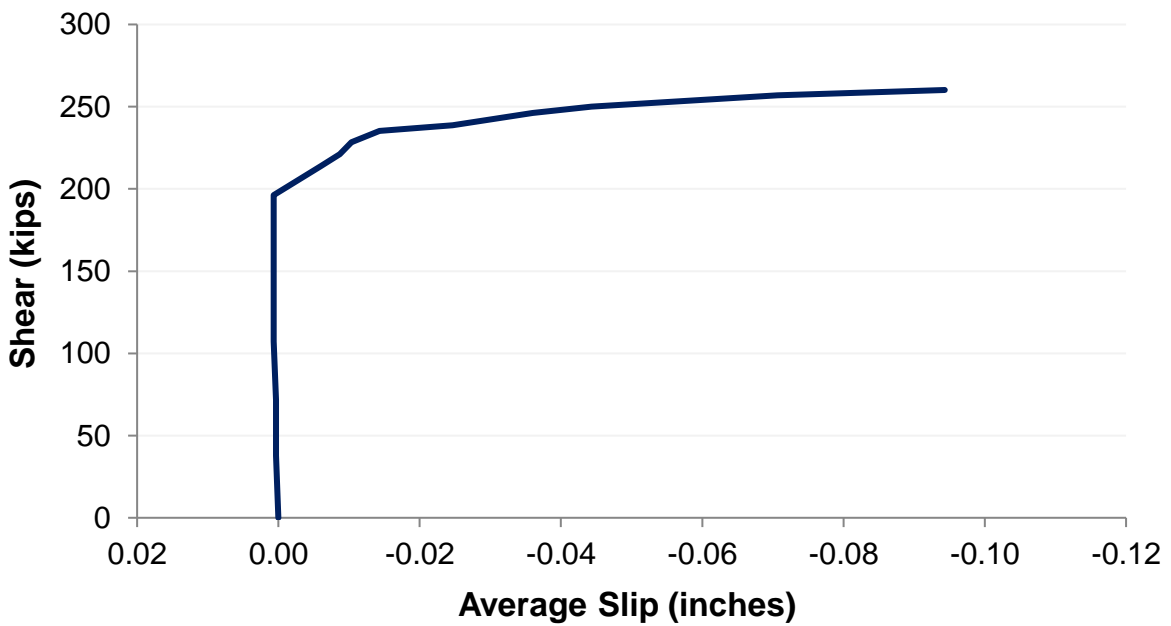**Figure N.23** Moment-curvature curve for pile HSSS 2205 (l_e = 69-in.).
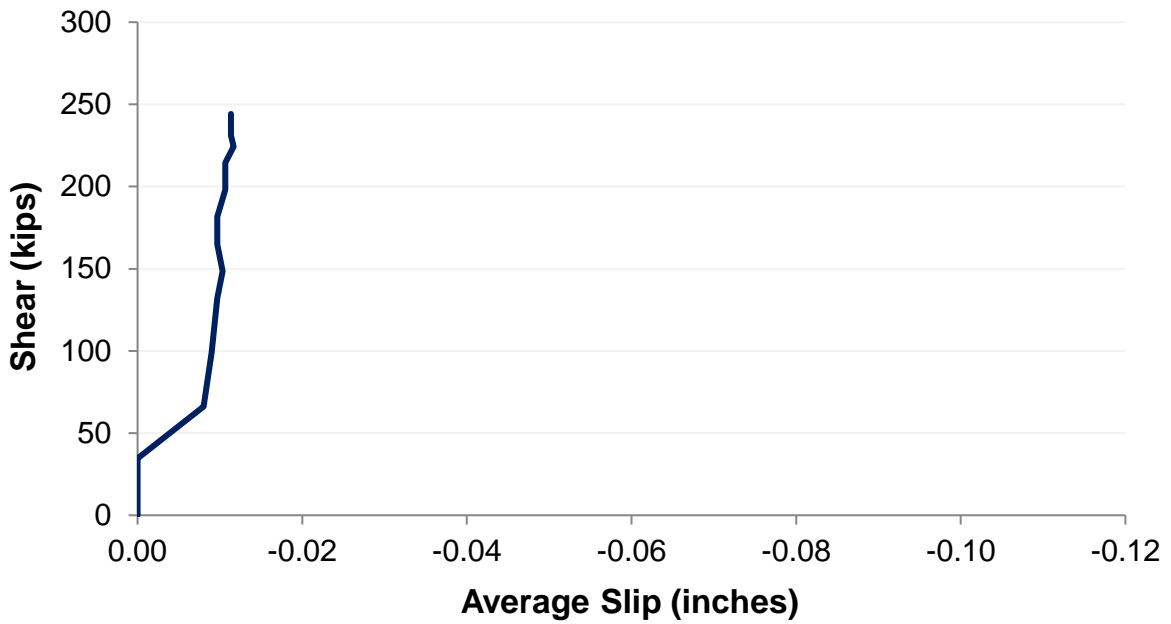
Figure N.24 Strand slip for pile HSSS 2205 (l_e = 69-in.).

- Pile HSSS 2205 – Embedment length: 61.75 inches.

Figure N.25 Load-deflection curve for pile HSSS 2205 (l_e = 61.75-in.).

Figure N.26 Strain distribution for pile HSSS 2205 (l_e = 61.75-in.).

Figure N.27 Moment-curvature curve for pile HSSS 2205 ($l_e = 61.75$-in.).

Figure N.28 Strand slip for pile HSSS 2205 ($l_e = 61.75$-in.).
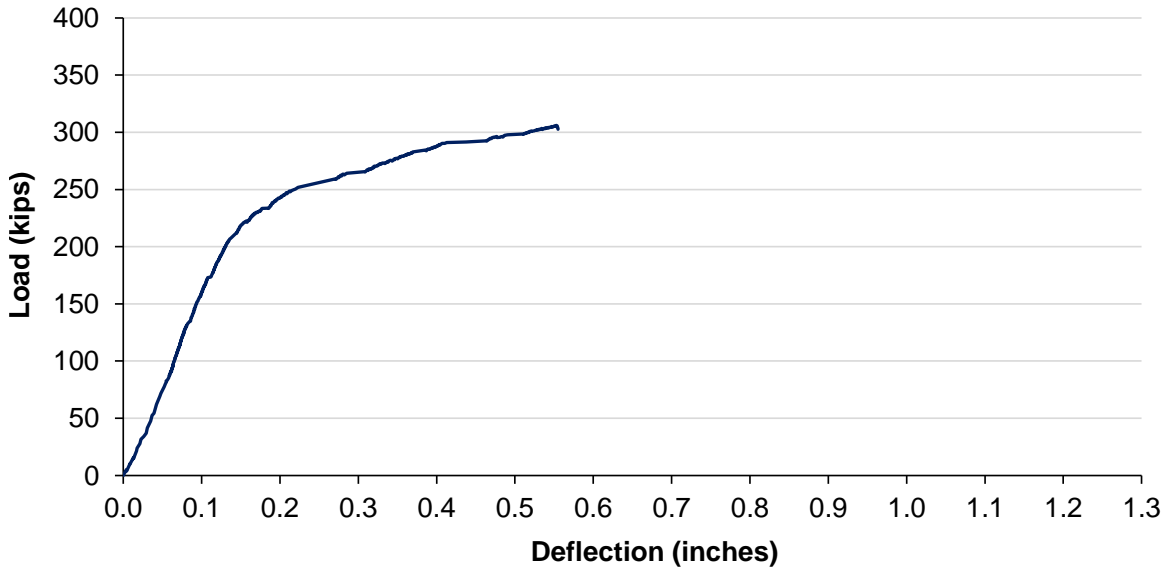
- Pile HSSS 2205 – Embedment length: 57 inches.

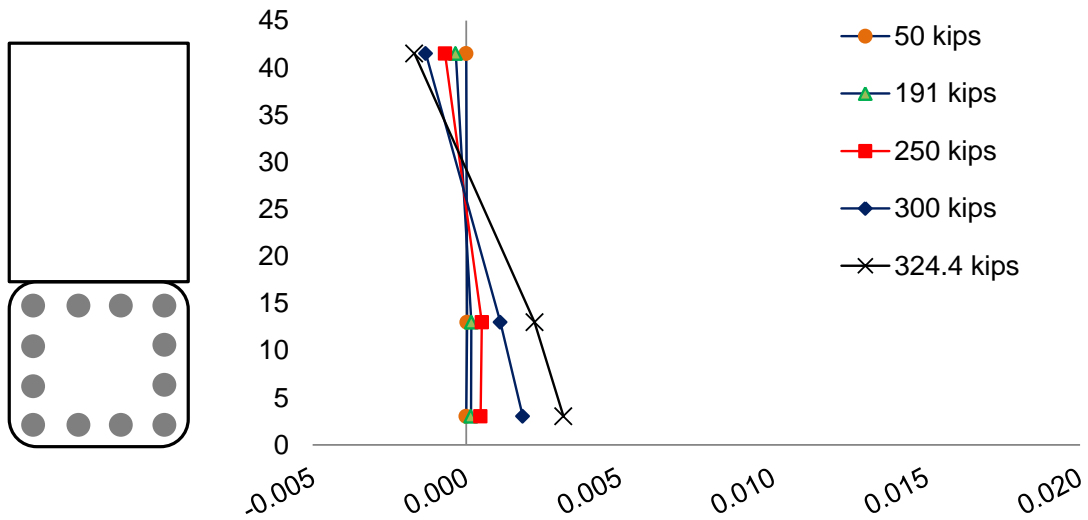**Figure N.29** Load-deflection curve for pile HSSS 2205 (l_e = 57-in.).

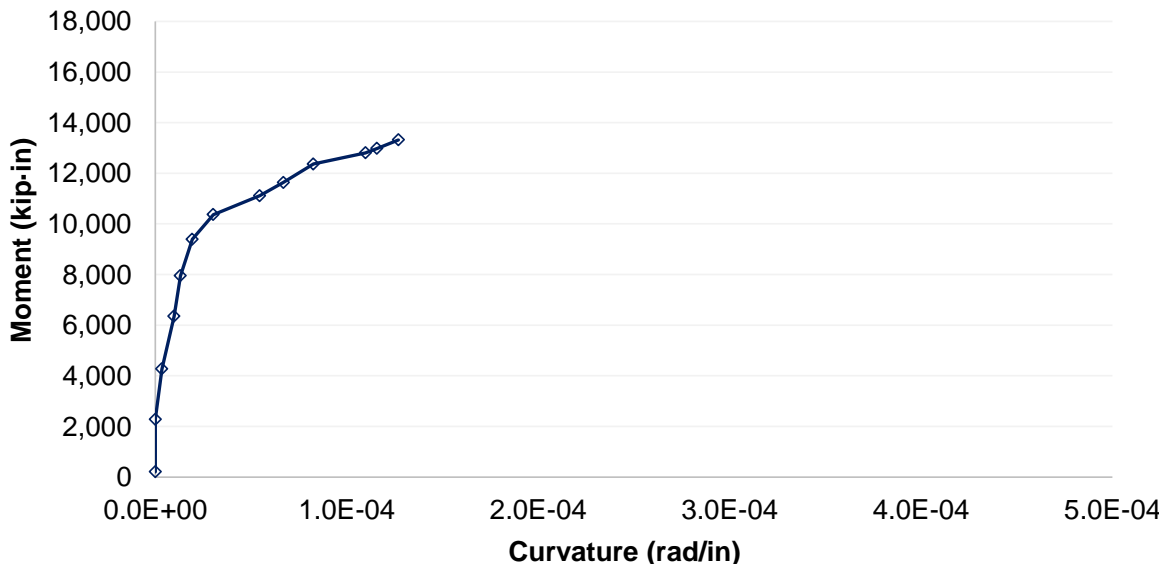**Figure N.30** Strain distribution for pile HSSS 2205 (l_e = 57-in.).

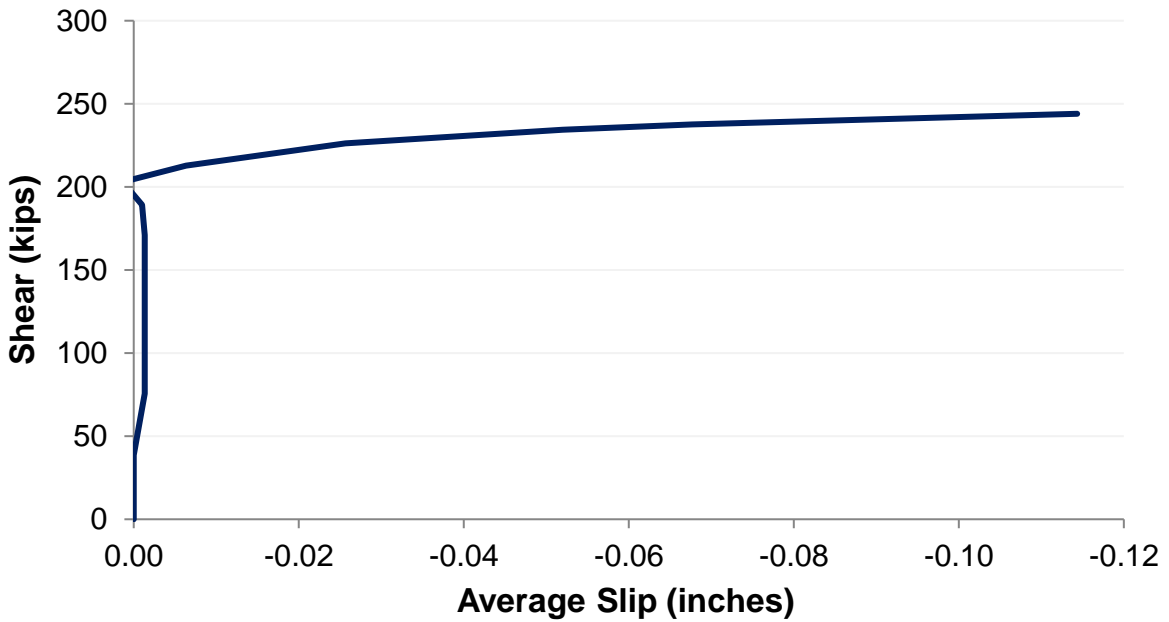**Figure N.31** Moment-curvature curve for pile HSSS 2205 (l_e = 57-in.).

Figure N.32 Strand slip for pile HSSS 2205 (l_e = 57-in.).